

GROWTH AND PHYSICAL-CHEMICAL PROPERTIES OF CARBON NANOTUBE ARRAYS FOR ENERGY CONVERSION DEVICES

By

Kudzai Mugadza

Submitted in fulfilment of the academic requirements for the degree of Master of Science
in the School of Chemistry and Physics, University of KwaZulu-Natal, Durban.

Supervisor: Prof V.O. Nyamori

Co-supervisors: Prof P.G. Ndungu

: Prof G.T. Mola

: Prof R.H. Simoyi

May 2015

Abstract

Energy demand has been on the increase globally whilst there has been continuous depletion of energy sources. This has prompted investigative research towards sustainable energy through the synthesis of carbon nanotubes (CNTs) for energy storage and conversion devices. Multiwalled carbon nanotubes (MWCNTs) were synthesised using two methods, the thermal chemical vapour deposition (CVD) method and purpose built non-equilibrium plasma-enhanced chemical vapour deposition (PECVD) method. The synthesis temperatures were 850 and 200 °C for CVD and PECVD. In non-equilibrium PECVD the low temperatures used retained the properties of indium tin oxide (ITO) coated glass substrate. MWCNTs synthesis involved the use of either, commercially available ferrocene or synthesised metal nanoparticle catalysts such as iron (Fe), cobalt (Co), nickel (Ni), nickel ferrite (NiFe), nickel cobaltite (NiCo) and cobalt ferrite (CoFe). The metal nanoparticles (MNPs) were synthesised using the co-precipitation method in the presence of hexadecylamine (HDA) as a surfactant. The MNPs and the MWCNTs were characterised using transmission electron microscopy (TEM), scanning electron microscopy (SEM), energy dispersive X-ray spectroscopy (EDX), Fourier transform infrared (FTIR) spectroscopy, thermogravimetric analysis (TGA) and Raman spectroscopy. Growth, physical and chemical properties of the MWCNTs were studied. The synthesised MWCNTs were used as part of the electrode material in organic solar cells (OSC), where poly(3,4-ethylenedioxythiophene) polystyrene sulfonate (PEDOT: PSS) was used as an electron transporter and poly-3-hexyl thiophene (P3HT) as an electron donor. The OSC performance was tested in a solar simulator.

Mono-dispersed MNPs, in the diameter range 3-10 nm, were successfully synthesised. HDA was suitable as both surfactant and reducing agent and it aided the formation of mono-dispersed MNPs. EDX confirmed the presence of typical metals such as Fe, Ni and Co, and the oxygen peak which correlated with the FTIR characteristic metal oxide bonds. The presence of the carbon peak correlated with TGA which showed the decomposition profile of the organic coating. All the CVD methods produced MWCNTs with non-equilibrium PECVD producing vertically aligned MWCNTs directly on the substrate. In non-equilibrium PECVD, liquefied petroleum gas (LPG) and acetylene were successfully used to synthesise MWCNTs at low temperatures. Typical hollow tubular structures of MWCNTs were observed using TEM. These observations correlated morphology from SEM which showed “spaghetti like” structures in the case of thermal CVD and vertical tubular structures in the case of non-equilibrium PECVD. This correlated well with the thermal stability

studies of the MWCNTs which showed the characteristic peak for MWCNTs. In addition, Raman spectroscopy showed typical MWCNTs bands, G-band and D-band due to graphitic carbon vibrations and defects respectively and the graphitic nature of the synthesised MWCNTs. The non-equilibrium PECVD, LPG synthesised, MWCNTs were tested in OSC. Positive results that showed dependency on the metal catalyst used during synthesis were observed. The Fe synthesised MWCNTs gave the highest efficiency, 0.116%, among the single metal catalysed MWCNTs followed by Co (0.012%) and Ni with 0.003%. CoFe synthesised MWCNTs also gave the best efficiency (0.009%) among mixed metal catalysed MWCNTs. Therefore, the synthesised MWCNTs gave positive results as part of the electrode material, however, with low efficiencies.

Preface

The experimental work presented in this dissertation was carried out in the School of Chemistry and Physics, University of KwaZulu-Natal, Durban, from August 2013 to April 2015, under the supervision of Prof P.G. Ndungu, Prof V.O. Nyamori, Prof G. Mola and Prof R.H Simoyi.

The studies represent original work by the author and have not otherwise been submitted in any form for any degree or diploma to any tertiary institution. Where use has been made of the work of others it is duly acknowledged in the text.

Declaration–Plagiarism

I, Kudzai Mugadza declare that:

1. The research reported in this thesis, except where otherwise indicated, and is my original research.
2. This thesis has not been submitted for any degree or examination at any other university.
3. This thesis does not contain other persons' data, pictures, graphs or other information, unless specifically acknowledged as being sourced from other persons.
4. This thesis does not contain other persons' writing, unless specifically acknowledged as being sourced from other researchers. Where other written sources have been quoted, then:
 - a. Their words have been re-written but the general information attributed to them has been referenced
 - b. Where their exact words have been used, then their writing has been placed in italics and inside quotation marks, and referenced.
5. This thesis does not contain text, graphics or tables copied and pasted from the Internet, unless specifically acknowledgements and the source being detailed in the thesis and in the References sections.

Signed.....

Declaration- Presentations and publications

Oral presentations

1. Kudzai Mugadza, Vincent O. Nyamori, and Patrick G. Ndungu, “PECVD synthesis of multiwalled carbon nanotubes: direct growth on substrate”, at the South African Chemical Institute Postgraduate Colloquium, University of KwaZulu-Natal (Pietermaritzburg), 23 September 2014.

Poster presentations

1. Kudzai Mugadza, Vincent O. Nyamori, and Patrick G. Ndungu, “Low temperature synthesis of multiwalled carbon nanotubes”, at the G2C2 Global Green Chemistry 2nd International Symposium and workshop , V&A Waterfront and Aquarium, Cape town, 24 to 26 August 2014.
2. Kudzai Mugadza, Vincent O. Nyamori, Genene T. Mola, Reuben H. Simoyi and Patrick G. Ndungu, “Effect of catalyst on multiwalled carbon nanotubes quality towards application”, at the College of Agriculture, Engineering and Science Postgraduate research day, University of KwaZulu-Natal (Westville), 27 October 2014.

Publications

1. Kudzai Mugadza, Vincent O. Nyamori, Genene T. Mola, Reuben H. Simoyi and Patrick G. Ndungu, “Low temperature synthesis of multiwalled carbon nanotubes: Effect of catalyst on multiwalled carbon nanotubes quality towards application” (manuscript in preparation).

Acknowledgements

I would like to express my sincere gratitude and appreciation to my supervisors Prof. Nyamori, Prof. Ndungu, Prof. Mola and Prof. Simoyi for their constructive advice, sound motivations and overwhelming ideas. This dissertation would not have been a success without their help, time and effort which they put into training me during the course of the project.

I wish to extend many thanks and appreciation to the following:

- ❖ Prof Martincgh, Dr. Owaga and Dr. Nombona for timely suggestions during the course of the research.
- ❖ Mr. E. Chekure, Mr. Nudkum and Mr. G. Moodley for their necessary technical suggestions.
- ❖ Dr. El Hardy for assistance during the solar cell experiments.
- ❖ Labmates and friends, G. Keru, E. Mombeshora, E. Njogu, N. Ngidi, N. Charmane, B. Gumbi, W. Munzeiwa, F. Makururu, B. Tapa, M. Goboza, E. Maronedze and P. Magazini, for their constant association which was most cherished.
- ❖ UKZN for funding the project. The School of Chemistry and Physics for the space and allowing the project to run.
- ❖ My family Charity, Shelter, Pamela, Elizabeth, and Lilliosa Mugadza, all my nieces (Nyasha, Tadel, Tashar and Brian Jnr) and my grandmother Mrs C. Sandy for their continuous moral support and patience throughout the whole study.
- ❖ The God Almighty for making this journey a success.

Table of contents

| Title | Page |
|--|-------------|
| Abstract | II |
| Preface | IV |
| Declaration Plagiarism | V |
| Declaration Presentations and publications | VI |
| Oral presentations | VI |
| Poster presentations | VI |
| Publications | VI |
| Acknowledgements | VII |
| Table of contents | VIII |
| List of tables | XII |
| List of figures | XIV |
| List of abbreviations | XVIII |

Chapter One: Introduction

| | |
|--|----|
| 1.1 Background of study | 1 |
| 1.1.1 Population growth and the looming energy crises | 4 |
| 1.2 Motivation | 6 |
| 1.3 Aim of the project | 9 |
| 1.3.1 Research questions | 9 |
| 1.4 Thesis outline | 10 |
| References | 12 |

Chapter Two: Literature review

| | |
|---|----|
| 2.1 Energy and resources | 16 |
| 2.1.1 Renewable energy | 17 |
| 2.2 Nanoscience and nanotechnology | 20 |
| 2.2.1 Carbon nanomaterials | 21 |

| | | |
|----------------|--|----|
| 2.3 | CNT synthesis methods | 26 |
| 2.3.1 | Arc discharge | 26 |
| 2.3.2 | Laser ablation | 27 |
| 2.3.3 | Chemical vapour deposition | 29 |
| 2.3.3.1 | Plasma-enhanced chemical vapour deposition | 30 |
| 2.4 | Factors affecting CNT synthesis | 32 |
| 2.4.1 | Catalysts | 33 |
| 2.4.1.1 | Iron, cobalt and nickel | 34 |
| 2.4.1.2 | Bimetallic catalyst | 34 |
| 2.4.2 | Carbon sources | 35 |
| 2.4.2.1 | Liquefied petroleum gas | 37 |
| 2.4.2.2 | Acetylene | 37 |
| 2.5 | Mechanism of CNT growth using CVD | 38 |
| 2.6 | Organic solar cells | 42 |
| 2.6.1 | Types of organic solar cells | 43 |
| 2.7 | Characterisation techniques | 44 |
| 2.7.1 | Scanning electron microscopy | 44 |
| 2.7.2 | Transmission electron microscopy | 46 |
| 2.7.3 | X-Ray diffraction | 48 |
| 2.7.4 | Raman spectroscopy | 48 |
| 2.7.5 | Fourier transform infra-red spectroscopy | 50 |
| 2.7.6 | Thermogravimetric analysis | 52 |
| 2.8 | Application and growth on substrates | 53 |
| 2.9 | Summary and conclusions | 54 |
| | References | 55 |

Chapter Three: Experimental

| | | |
|--------------|---|----|
| 3.1 | General procedures | 71 |
| 3.1.1 | Chemicals, reagents, solvents and gases | 71 |
| 3.2 | Instrumentation | 72 |
| 3.3 | Catalyst synthesis | 73 |
| 3.3.1 | Thermal decomposition | 74 |

| | | |
|----------------|---|----|
| 3.3.2 | Co-precipitation | 75 |
| 3.4 | Reactor set-up for the synthesis of CNT forests | 77 |
| 3.4.1 | Single-furnace set-up | 77 |
| 3.4.2 | Double-furnace set up | 78 |
| 3.4.3 | Non-equilibrium plasma reactor set-up | 79 |
| 3.5 | Synthesis of MWCNTs | 81 |
| 3.5.1 | Single-furnace approach | 82 |
| 3.5.1.1 | Ferrocene-toluene | 82 |
| 3.5.1.2 | LPG | 83 |
| 3.5.2 | Double-furnace approach | 84 |
| 3.5.3 | Non-equilibrium plasma-enhanced CVD approach | 84 |
| 3.5.3.1 | Preparation of the substrate | 85 |
| 3.5.3.2 | Non-equilibrium PECVD procedure | 86 |
| 3.6 | Characterisation | 86 |
| 3.6.1 | Transmission electron microscopy | 87 |
| 3.6.2 | Scanning electron microscopy | 87 |
| 3.6.3 | Electron dispersive X-ray spectroscopy | 87 |
| 3.6.4 | Fourier transform infrared spectroscopy | 88 |
| 3.6.5 | Thermogravimetric analysis | 88 |
| 3.6.6 | Raman spectroscopy | 88 |
| | References | 89 |

Chapter Four: Synthesis of metal nanoparticles

| | | |
|----------------|----------------------------|-----|
| 4.1 | Introduction | 90 |
| 4.1.1 | Thermal decomposition | 90 |
| 4.1.1.1 | SEM and EDX | 91 |
| 4.1.1.2 | TEM | 96 |
| 4.1.2 | Co-precipitation | 97 |
| 4.1.2.1 | SEM and EDX | 98 |
| 4.1.2.2 | TEM | 102 |
| 4.1.2.3 | FTIR spectroscopy | 105 |
| 4.1.2.4 | Thermogravimetric analysis | 107 |

| | | |
|--------------|---------------------------------------|-----|
| 4.1.3 | Summary of the MNPs synthesis methods | 109 |
| | References | 110 |

Chapter Five: MWCNTs synthesis and application

| | | |
|----------------|--|-----|
| 5.1 | MWCNTs synthesis using thermal CVD | 114 |
| 5.1.1 | Single-furnace synthesis of MWCNTs using Liquefied petroleum gas | 117 |
| 5.1.2 | Double-furnace synthesis of MWCNTs using Liquefied petroleum gas | 120 |
| 5.1.3 | Comparison of the thermal CVD approaches | 122 |
| 5.2 | Non-equilibrium PECVD | 124 |
| 5.2.1 | Optimisation | 124 |
| 5.2.1.1 | Structural characterisation | 126 |
| 5.2.2 | Synthesis of aligned MWCNTs using LPG and acetylene | 128 |
| 5.2.2.1 | Structural characterisation of the synthesised MWCNTs | 128 |
| 5.2.2.2 | Comparison of the MWCNTs synthesised | 132 |
| 5.2.2.3 | Raman analysis | 133 |
| 5.2.2.4 | Summary of the synthesised MWCNTs | 134 |
| 5.3 | Organic solar cells | 134 |
| 5.3.1 | Cell fabrication | 135 |
| 5.3.2 | Device preparation | 135 |
| 5.3.3 | Results and discussion | 136 |
| 5.3.4 | Summary of the OSC | 138 |
| | References | 139 |

Chapter Six: Conclusions and future work

| | | |
|------------|----------------------------|-----|
| 6.1 | Summary of thesis chapters | 142 |
| 6.2 | Conclusions | 143 |
| 6.3 | Future work | 145 |
| | Appendices | 146 |

List of tables

Chapter Two

| | | |
|-----|---|----|
| 2.1 | Dimensional classification of carbon structures | 23 |
| 2.2 | Parameters influencing plasma treatment during synthesis | 31 |
| 2.3 | Various common carbon sources used in plasma design synthesis of CNTs | 36 |

Chapter Three

| | | |
|-----|---|----|
| 3.1 | Chemicals, reagents, solvents and gases supplier and purity/grades as used | 72 |
| 3.2 | Experimental instruments, model, software version and use in research | 73 |
| 3.3 | Concentrations of catalyst precursors as used | 74 |
| 3.4 | Masses of single metal precursors dissolved in ethanol (50 mL) with 1 g HDA | 74 |
| 3.5 | Furnace temperature rate ramps and purpose | 74 |
| 3.6 | Masses of mixed metal precursors dissolved in ethanol (50 mL) with 1 g HDA | 75 |

Chapter Four

| | | |
|-----|--|-----|
| 4.1 | Summary of the main peaks of the HDA as analysed using FTIR | 106 |
| 4.2 | Summary of FTIR peaks assigned to the co-precipitation synthesised metal nanoparticles | 107 |

Chapter Five

| | | |
|-----|--|-----|
| 5.1 | Summary of the observed SCNMs and the challenges at different LPG synthesis temperatures | 118 |
| 5.2 | Representative SEM and TEM sample images of the LPG SCNMs samples | 119 |
| 5.3 | Comparison of the D- and G-bands from Raman analysis, and average tube diameter of tubes from TEM of the CVD methods | 124 |
| 5.4 | Summary of non-equilibrium variables used for method optimisation | 126 |
| 5.5 | Representative images of the various SCNMs observed at different $T_{(MAX)}$ using Iron | 127 |

| | | |
|------------|---|-----|
| | catalyst | |
| 5.6 | A summary of the mean diameters of the synthesised MWCNTs using LPG and acetylene with a variety of catalysts | 132 |
| 5.7 | Comparison of the I_D/I_G in Raman analysis with respect to the MWCNTs diameters for the LPG and acetylene carbon sources | 133 |
| 5.8 | Measured cell parameters for all MWCNTs samples | 138 |

List of figures

Chapter One

- | | | |
|-----|---|---|
| 1.1 | Energy source consumption from the 19 th to the 21 st century | 3 |
| 1.2 | World population growth statistics | 5 |

Chapter Two

- | | | |
|------|---|----|
| 2.1 | Global energy potential | 17 |
| 2.2 | Illustration of the mechanism involved in (a) the concentrating solar power and (b) photovoltaic system | 19 |
| 2.3 | The structure of the carbon nanoforms (a) graphene, (b) fullerenes, (c) CNTs and (d) graphite | 22 |
| 2.4 | The structural forms of carbon nanotubes and the nature of their tube ends | 23 |
| 2.5 | The conformations in which graphene can roll up | 24 |
| 2.6 | Arch discharge set-up | 26 |
| 2.7 | Laser ablation set-up | 28 |
| 2.8 | Illustration of the CVD set-up for CNT synthesis | 29 |
| 2.9 | FeNi phase diagram | 35 |
| 2.10 | Summary of the steps involved during PECVD | 39 |
| 2.11 | Carbon nanotubes growth models; (a) tip growth and (b) base growth | 40 |
| 2.12 | Illustration of the structure of an organic solar cell | 43 |
| 2.13 | SEM column (a) schematic presentation and (b) actual picture of the instrument | 45 |
| 2.14 | TEM column (a) actual picture and (b) schematic presentation of the instrument | 47 |
| 2.15 | Raman (a) spectroscope instrument and (b) basic components for analysis | 49 |
| 2.16 | A typical Raman spectra indicating CNT characteristic bands | 50 |
| 2.17 | FTIR spectroscopy (a) picture of the instrument and (b) block diagram for steps involved in analysis | 51 |
| 2.18 | A schematic diagram for the TGA instrument for analysis | 52 |

Chapter Three

| | | |
|-----|--|----|
| 3.1 | Schematic co-precipitation method illustration | 77 |
| 3.2 | Photograph of (a) gas and carbon source injection port attached to a syringe pump (b) gas outlet exhaust system and (c) complete CVD set-up for MWCNTs | 78 |
| 3.3 | Photographic illustration of the double-furnace set-up where FN stands for furnace | 79 |
| 3.4 | Schematic illustration of the non-equilibrium PECVD | 80 |
| 3.5 | (a) Whole non-equilibrium PECVD and (b) magnification of the reactor set-up for MWCNTs where full trough element (FTE) ceramic heaters were used | 81 |
| 3.6 | ITO substrate in a boat | 83 |
| 3.7 | Schematic illustration of the double furnace set-up | 84 |
| 3.8 | Schematic presentation of the 30 x 30 mm treated ITO substrate | 86 |

Chapter Four

| | | |
|-----|--|-----|
| 4.1 | Iron nanoparticles on ITO substrates synthesized using the thermal decomposition method at (a) 400, (b) 500 and (c) 600 °C with inserts of respective EDX spectra | 92 |
| 4.2 | Nickel nanoparticles on ITO substrates synthesized using the thermal decomposition method at (a) 400, (b) 500 and (c) 600 °C with inserts of respective EDX spectra | 93 |
| 4.3 | Cobalt nanoparticles on ITO substrates synthesized using the thermal decomposition method at (a) 400, (b) 500 and (c) 600 °C with inserts of respective EDX spectra | 94 |
| 4.4 | Cobalt-iron nanoparticles on ITO substrates synthesized using the thermal decomposition method at (a) 400, (b) 500 and (c) 600 °C with inserts of respective EDX spectra | 95 |
| 4.5 | TEM images of nanoparticles synthesized when the thermal decomposition method was used at 400 °C; (a) iron, (b) nickel, (c) cobalt and (d) cobalt-iron | 97 |
| 4.6 | SEM images of co-precipitation synthesised metal nanoparticles (a) iron, (b) cobalt, (c) nickel, (d) cobalt-iron, (e) nickel-cobalt and (f) nickel-iron | 99 |
| 4.7 | EDX spectra of co-precipitation synthesised metal nanoparticles (a) iron, (b) cobalt, (c) nickel, (d) cobalt-iron, (e) nickel-cobalt and (f) nickel-iron | 100 |

| | | |
|-------------|--|-----|
| 4.8 | EDX spectra of co-precipitation synthesised metal nanoparticles with the atomic weight % of (a) iron, and (b) cobalt-iron | 101 |
| 4.9 | Representative CoFe false colour maps indicating the distribution of the metals in the synthesised MNPs using co-precipitation method | 102 |
| 4.10 | TEM images of co-precipitation synthesised metal nanoparticles; (a) iron, (b) cobalt, (c) nickel, (d) cobalt-iron, (e) nickel-cobalt and (f) nickel-iron | 103 |
| 4.11 | Histograms for the sizes of co-precipitation synthesised metal nanoparticles; (a) iron, (b) cobalt, (c) nickel, (d) cobalt-iron, (e) nickel-cobalt and (f) nickel-iron | 104 |
| 4.12 | Hexadecylamine IR spectrum as analysed using ATR instrument | 105 |
| 4.13 | Comparison of the IR spectra for HDA and co-precipitation synthesised MNPs | 106 |
| 4.14 | TGA of all the metal nanoparticles synthesised by the co-precipitation method in nitrogen; (a) single metals and (b) mixed metals | 108 |
| 4.15 | DTG profiles of all the metal nanoparticles synthesised by the co-precipitation method in nitrogen; (a) single metals and (b) mixed metals | 108 |

Chapter Five

| | | |
|------------|---|-----|
| 5.1 | The synthesised MWCNTs SEM images at (a) low, (b) medium and (c) high magnification with (d) EDX spectrum at 850 °C with the use of ferrocene and toluene in the thermal CVD method | 115 |
| 5.2 | Representative TEM image of the synthesised MWCNTs at 850 °C with the use of ferrocene and toluene in the thermal CVD method | 116 |
| 5.3 | ITO melted and stuck substrate in a quartz boat using LPG at 800 °C, the insert shows the state before synthesis | 117 |
| 5.4 | Representative SEM-EDX images of MWCNTs synthesised with the double furnace approach using LPG as the carbon source at 800/400 °C; (a) SEM and (b) EDX | 121 |
| 5.5 | Representative TEM images of MWCNTs synthesised with the double furnace approach using LPG as the carbon source at 800/400 °C (a) low and (b) high magnification | 122 |
| 5.6 | Thermal profiles (i) TGA and (ii) DTGA for the thermal CVD approaches using (a) LPG single furnace, (b) LPG double furnace and (c) ferrocene-toluene approach | 123 |
| 5.7 | Photographic illustration of the ITO-plasma orientation in the reactor chamber | 125 |

| | | |
|-------------|---|-----|
| | where (a) complete set-up, (b) an aerial view and (c) enlarged ITO-plasma area | |
| 5.8 | Representative images indicating the different views of the MWCNTs as observed using SEM for CoFe catalyst using LPG as the carbon source; (a) aerial view on substrate, (b) scrapped off aerial view and (c) scrapped off side views | 129 |
| 5.9 | EDX spectra of MWCNTs synthesised using various catalysts and LPG as the carbon source (a) Fe, (b) Co, (c) Ni, (d) CoFe, (e), NiCo and (f) NiFe | 130 |
| 5.10 | TEM images representing the various MWCNT structures using LPG where (a) Fe, (b) Co, (c) Ni, (d) CoFe, (e), NiCo and (f) NiFe are the catalysts used | 131 |
| 5.11 | Schematic diagram of the layer arrangement in OSC | 136 |
| 5.12 | Comparison of current against voltage (J/V) plots in (a') dark and (b') illumination using MWCNTs prepared with (a) Fe, (b) Co, (c) Ni, (d) CoFe, (e) NiCo and (f) NiFe as catalysts | 137 |

List of abbreviations

| Abbreviation | Full name |
|---------------------|---|
| Ar | Argon |
| CNF | Carbon nanofibers |
| CNT | Carbon nanotube |
| CVD | Chemical vapour deposition |
| Co | Cobalt |
| CoFe | Cobalt ferrite |
| DCPECVD | Direct current plasma-enhanced chemical vapour deposition |
| D-Band | Disorder-band |
| EDX | Energy dispersive X-ray spectroscopy |
| FTIR | Fourier transform infra-red spectroscopy |
| G-Band | Graphitic-band |
| HDA | Hexadecylamine |
| HRTEM | High resolution transmission electron microscopy |
| ITO | Indium tin oxide |
| IEA | International Energy Agency |
| LPG | Liquefied petroleum gas |
| MNPs | Metal nanoparticles |
| MPECVD | Microwave plasma-enhanced chemical vapour deposition |
| Mtoe | Million tonnes of oil equivalent |
| MWCNTS | Multiwalled carbon nanotubes |
| 1-D | One-dimensional |
| OSC | Organic solar cells |
| PECVD | Plasma-enhanced chemical vapour deposition |
| PEDOT:PSS | Poly(3,4-ethylenedioxythiophene) polystyrene sulfonate |
| P3HT | Poly-3-hexyl thiophene |
| RPECVD | Remote plasma-enhanced chemical vapour deposition |
| SEM | Scanning electron microscopy |
| TW | Terawatt |
| TGA | Thermogravimetric analysis |
| TEM | Transmission electron microscopy |

| | |
|----------|---|
| 2-D | Two-dimensional |
| UN | United Nations |
| VACNTs | Vertically aligned carbon nanotubes |
| VAMWCNTs | Vertically aligned multiwalled carbon nanotubes |
| wt. % | Weight percent |
| 0-D | Zero dimensional |

Chapter One

INTRODUCTION

This chapter provides a detailed overview of the background of the study highlighting the importance of the work undertaken. Basically, energy is one of the most important fundamental aspects of life; nothing can exist without energy. The ability of animals to move, growth and vegetation, lighting of cities and mobility of vehicles, among others, all depend on energy. The sun provides light and warmth during the day, and is responsible for plant growth through photosynthesis. These plants constitute part of animal and humankind prey as well as the source of oxygen for respiration. Once the animals and humankind feed they have the capacity to do work and reproduce. Once there is reproduction, the population increases. As the population is increasing, there is need for better agricultural productivity, food availability, improvement in the public health, sanitation and hygiene. This in turn, in modern times, is exerting pressure on the energy resources because all of these processes sorely depend on energy. Therefore, the increased energy demands lead to inadequate energy supply. It is this energy shortage which brings about the need to look at alternative sources of energy available and the possible ways to develop sustainable energy supply. Detailed explanation concerning the current population statistics and the relative effect to the energy availability is provided in this chapter. Possible ways of overcoming the energy demand are also discussed.

1.1 Background

Chemical energy transformations are a basic function of all living things. The different energy conversions within an ecosystem are responsible for sustaining the ecosystem. Considering the planet earth as an ecosystem, the cycle of the energy transformations between living (plants and animals) and non-living (sun, earth, seas, machines etc.) things maintains the planet. Energy needs were relatively moderate before the Industrial revolution. In the early years, energy form came from the sun in the form of heat and light all day long. Transport relied on muscles of horses and wind power, and work depended on the animals, water and wind.¹ In ancient Egypt, wind propelled boats along the Nile River. In China, wind was used for windmills to pump water and grain grinding. All the processes involved in wind and rain formation are driven by the energy from the sun. Although the

sun was and still is the powerhouse of energy, humankind could not harness solar energy effectively. Solar energy could not be used during winter or rainy seasons. Therefore, they developed other sources of energy such as fire. Fire was discovered as another alternative source of heat and light as well as food preparation.² The fire came mainly from burned wood, straw and dried dung.³ The use of fire brought about changes from the Stone to Iron Age, where it was utilised for the moulding of pots and bricks, copper, bronze and iron into useful hand tools. Therefore, the invention of useful hand tools brought about changes in the agricultural practises as well as the lifestyles.⁴ Firewood became scarce as deforestation overtook reforestation, thus coal came in handy.² The use of coal, oil and natural gas lead to Industrial revolution.⁵ During this era the 18th to 19th centuries, there was a great transition from the hand tools to heavy special purpose machinery, new chemical and iron production processes and low cost automobiles that were developed.⁶ It was also during the Industrial revolution that mass production of goods and services improved. Therefore, this led to a significant change in society's energy use.

Globally, since the 1st and 2nd Industrial revolutions, there has been a continuous increase in energy demand.⁶ It has been estimated by the International Energy Agency (IEA) forecasts that the world primary energy demand will increase by 1.5% per year from just over 12,000 million tonnes of oil equivalent (Mtoe) to 16,800 Mtoe. This is an overall increase of about 40% between 2013 and 2030.⁷ The world energy outlook (WEO) global per capita energy consumption statistics are presented in **Figure 1.1**.

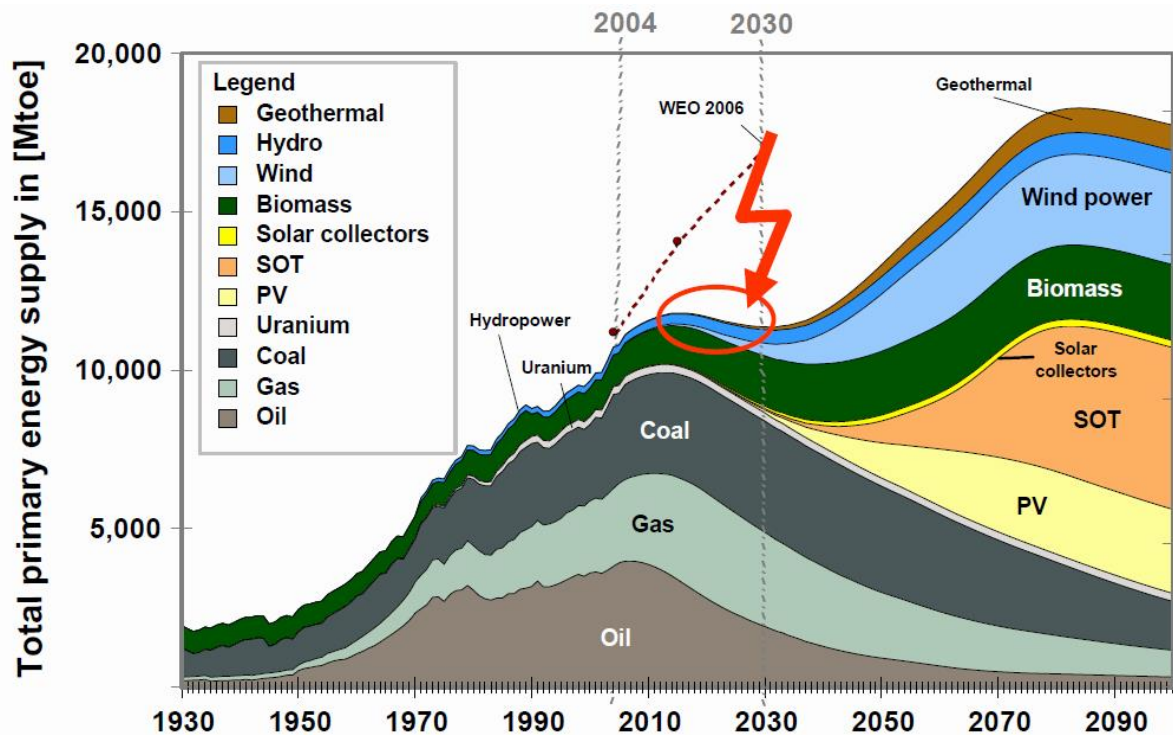


Figure 1.1: Energy source consumption from the 19th to the 21st century⁸

In **Figure 1.1**, the fossil fuel energy supply shows a gradual increase from the 19th century and an estimated maximum supply in the 21st century from around 2004 to around 2015. This observation is attributed to the mid-19th century Industrial revolution where coal was the major energy source.⁵ Around the beginning of the 20th century there was a major shift towards higher energy sources i.e. oil and gas. A rapid energy supply decrease in these non-renewable sources is expected beyond 2030. This is attributed to the depletion and exhaustion of the fossil fuel reserves in the late 20th century. Apart from the decline in the production of energy, extraction of energy from fossil fuels disturbs the natural ecosystems significantly.⁹ The associated challenges include, land degradation, pollution, and introduction of health related problems like the respiratory diseases, lung cancer, and the production of acid rain amongst other negative environmental impacts.¹⁰ For these reasons, the renewable energy source supply is postulated to show a steady increase from around 2030 with the maximum supply expected around 2080. This is attributed to the postulated development in alternative and sustainable energy sources i.e. geothermal,¹¹ wind,¹² biomass¹³ and solar energy.¹⁴ This in turn has therefore seen the development and exploitation of different forms of energy based on cost and accessibility to the energy resources.¹⁵

Energy security concerns, environmental impact, sustainability, affordable energy services and the need to increase accessibility to economically viable energy options, especially where they lack in developing countries forms the basis of the reasons to consider during the energy development process.¹⁴ Several key factors affect energy development especially in developing nations. This includes, heavy on-going investments in infrastructure development, and refurbishment of aging infrastructures coupled with uncertainties and capital risk factors associated with renewable technologies.¹³ Therefore, in order to develop sustainable energy supply, there are several factors for consideration. These factors include; making sure there is a positive and strong social economic development, because most developing and industrial societies would be unable to maintain their economic growth and subsistence.⁹ Hence, the need for a greater probability of a reliable, abundant energy supply that caters for all the economic sectors, domestic and industrial scales, as well as meets the growing population.¹⁶

1.1.1 Population growth and the looming energy crises

The number of people living within a particular area, whether it is a country or defined geographical region, at a particular time, defines a population.¹⁷ The estimated world population statistics report a decline of 5% of Europe's population from 2012 to 2050, and a 7% rise in the sub-Saharan Africa region, over the same time frame. Therefore, as a result of the differences in the population growth, almost all population growth is centred in the developing regions.¹⁸ According to the United Nations Population Division (UNPD), in 2050, the population in these developing regions will be approximately double what the population was in 2000 (**Figure 1.2**).¹⁷ The growth of the population significantly affects the economic development process in a contradicting way. It can either stimulate or restrain growth and development. Generally, considering developing countries, rapid population growth presents an obstacle to the growth in the standard of living.¹⁹ On the other hand, this could also translate to positive competitions and new innovations.

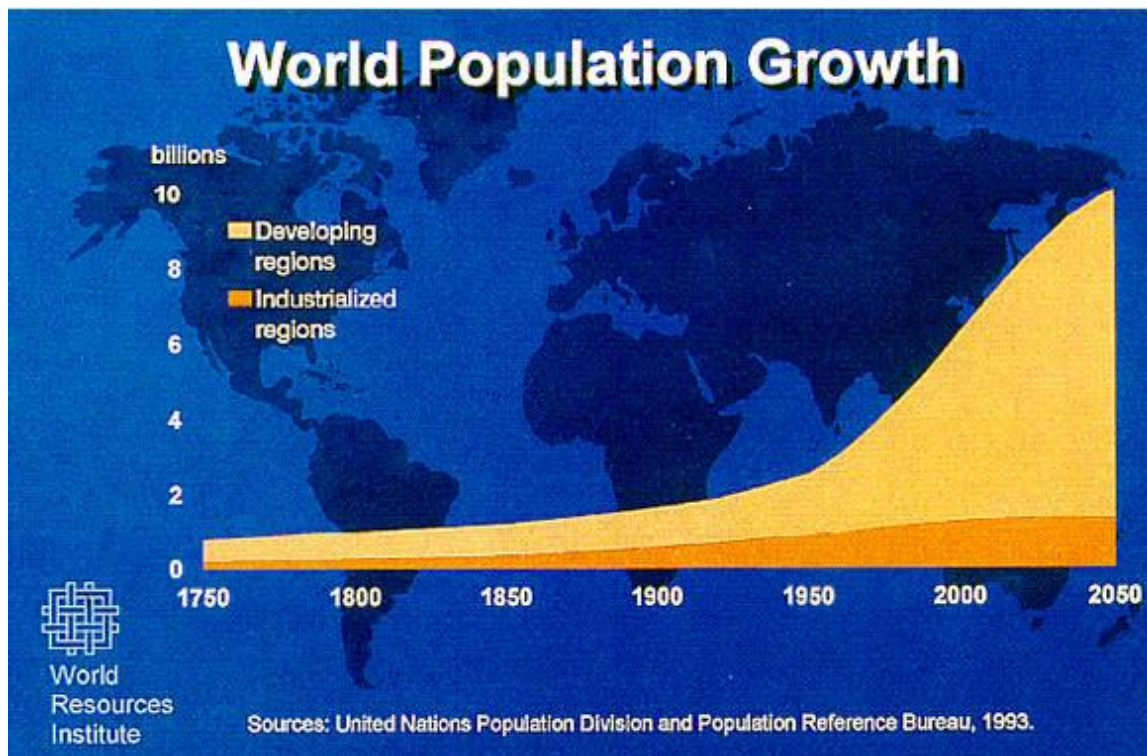


Figure 1.2: World population growth statistics¹⁷

In many cases, it is in these developing regions that there is high commercial and industrial productivity, which puts strains in energy supply chains.²⁰ The other factors that contribute to high energy demand are industrialisation and the human reliance on energy based devices. Industrialisation has an impact especially in emerging markets, since operations in factories, and the production of goods requires significant amounts of energy. The energy is typically in the form of both electricity, which itself is primarily produced from burning fossil fuels and petroleum-based fuels. The finished goods are then moved to the consumers where there will be intense use of energy during the day to day activities, and the majority of the energy used is derived from fossil fuels. An increase in the standard of living can often lead to a greater reliance on energy based devices, where the advancement in technology plays a major role. For instance, the end users have increased their interests in the use of mobile phones, washing machines, computers, light bulbs and cars.²¹ Constant use of these characteristic devices strains the energy supply chain.

The negative interaction in the energy supply chain causes an energy crisis. The energy crisis is a situation where the world's demands on the limited natural resources that are used to power industrial society are diminishing as the demand rises.¹² Several factors account for the depletion of the natural resources; fossil fuels currently supplying the energy are facing exhaustion, and the

strong population growth which is exceeding the carrying capacities.¹⁰ The energy crisis situation has been occurring since the 1970's where the oil and petroleum economic cartel (OPEC) in Arab countries placed a trading ban on their oil sales. In short, the world is currently facing an energy crisis because the dwindling finite fossil fuels cannot meet the fast growing population energy demands. In an effort to address the energy crisis, various forms of energy storage and conversion devices have become the subject of intense research and development. These devices include batteries, supercapacitors, concentrating solar power systems and solar cells. Typical devices are designed in such a way that focuses on cost and efficiency relative to pollution.

Nanotechnology and the fabrication of nanomaterials with an improved capacity to store and convert energy seems to be rather appealing since these devices have found use in many applications which include measurement and sensing devices,²² and therapeutic systems.²³ Nanomaterials are amongst the emerging technological advances being researched on their ability to fabricate energy storage and conversion devices. Amongst these nanomaterials are carbon based nanomaterials, these include graphene and carbon nanotubes (CNTs) among others. The CNTs are known to have unique characteristics, and this includes the nature of them being very light, strong and resilient, and also, possessing electrical and optical properties.²⁴ Such properties are considered to qualify the CNTs for fabricating high rated lighting and solar collection devices.

1.2 Motivation

Implementation and utilization of renewable energy technologies is associated with several advantages. Amongst the advantages; there is reliability and localization, energy security, alternative and diversified energy supply, opportunities to create new wealth and an insignificant negative impact on the environment, since little or no carbon footprints are produced.⁹ Solar energy is amongst the various popular options for renewable sources of energy available. Solar energy has some major advantages associated with it. The advantages become very significant especially when considering the developing nations in the tropical regions in sub Saharan Africa. In fact most of the African region receives sunshine all year round. This also implies that Africa, by virtue of location in the tropics, has some of the highest solar insolation-receiving regions on the planet. In the tropics solar radiation mostly strikes the ground at an angle of 90° almost throughout the year.²⁵

Most areas in Africa receive an average of greater than 2 500 hours of sunshine per year, with average solar-radiation levels ranging between 4.5 and 6.5 kWh/m² in one day. All together, the earth receives approximately 120,000 TW every hour from the sun, and the estimated global energy requirement per year is approximately 16 TW.^{26,27} This therefore suggests that harnessing at least 0.01% of the energy received by the earth per hour will be able to meet and surpass the global energy requirement per year. However, the main challenge is on how to harness this energy. Basing from the perspective of the basic photosynthesis processes where light, captured by the chlorophyll pigments and converted to chemical energy in a series of events,²⁸ is stored for future use. Similar processes are required for the conversion of solar energy to chemical or potential energy. Therefore, the main methods used for light harvesting in order to produce electric energy, are the concentrating solar power²⁹ and the solar photovoltaics (SPV).³⁰ Concentrating solar power (CSP) utilises computer controlled mirrors to trap thermal energy and convert it to heat transfer fluid and produce steam. Once the heat produced is recovered it turns into steam which then drives the turbines thus producing electricity.²⁹ In the organic photovoltaics, electromagnetic radiation is converted directly into electricity through the photo excitation of the electrons in donor molecules. The transfer of these excited electrons to electrodes generates electricity.³¹ CSP faces many challenges, for instance, the need for higher levels of irradiance, reliable access to water for cooling, and that it is restricted to installation in specific areas unlike the SPV that can be installed almost anywhere where CSP can be installed.²⁹ The SPV is the most preferred method when considering the developing areas in the southern Africa region. Hence, when it comes to project financing, the CSP challenges may push investors more towards SPV than to CSP.

SPV generate electric energy by making use of solar cells for the conversion of energy. Solar cells are made up of materials which possesses semiconducting properties.³² When this material is struck by sunlight, photo excitation of the electrons occurs, and is turned into electrical currents. There are several types of solar cells available for the process depending on the material used for fabrication. These include inorganic and organic solar cells (OSC).³² Inorganic solar cells are silicon based and can be monocrystalline,³³ polycrystalline³⁴ or amorphous.³⁵ These types of solar cells are made from very reliable and advanced processing technologies. They have been reported to have high efficiency rates.³⁰ However, they are very expensive to manufacture as they require huge labour and facilities investments.³² This is not favourable when looking at developing nations where there is need for a combination of efficient and low cost manufactured devices. The OSC counter parts become a considerable option. These are associated with low charge carrier mobility which is responsible for their lower efficiency rates. However, they are made up of polymers, small organic molecules or a

combination of both, with or without incorporation of nanomaterials.³¹ These properties give them an affinity for chemical modification thus creating a potential for large scale manufacturing.

Numerous studies have focused on the fabrication of reliable energy conversion devices such as OSC. In order for the resulting materials to faithfully address the global energy demand, the efficiency of the devices has been set as one priority. Efforts to improve the solar cell efficiencies started with the development of the photovoltaic cells from a single layer to bilayer through to bulk heterojunction solar cells.³¹ Considerable efforts to improve performance in absorption of electrons by the key components of the active layer started with the introduction of conducting metal layers such as fluorine tin oxide (FTO)³⁶ and indium tin oxide (ITO) layers.³⁷ This brought an increase in the efficiencies, however, not comparable to the silicon based cells. Research interests developed the ITO materials and introduced a layer of CNTs over the top. The CNTs were suitable candidate materials for the purpose because they displayed excellent performance in other related fields such as fuel cells³⁸ and light emitting diodes.³⁹ CNTs have the ability to create percolation paths through their hetero-structure, while providing electron-hole dissociation sites.³⁷ This increases the electron mobility and therefore enhances a change in the efficiency. However, the main challenge is the orientation of the CNTs on the ITO. Randomly oriented CNTs have cross linking problems,⁴⁰ while aligned CNTs are associated with improved electrical conductance.⁴¹ This is attributed to the ability of the internal walls of the vertically aligned CNTs to participate in electrical transport without cross linkage problems.⁴¹ The production of these vertically aligned CNTs in a bundle manner maximises the surface area and therefore enhances cell performance. World-wide research focus has been on the synthesis of CNTs using several techniques. The main method used for commercial synthesis of CNTs is the thermal chemical vapour deposition (CVD).⁴² The thermal CVD technique utilises high temperatures in the range 500-1100 °C.⁴³ These temperatures are not suitable for direct substrate growth when considering using substrates with very low strain points. These temperatures lead to the destruction of substrate properties. Among the various CVD methods is the plasma-enhanced chemical vapour deposition (PECVD). This method makes use of the plasma which overcomes the high temperatures and provides suitable growth of CNTs directly on the substrate. However, not much studies have been done on the production of CNTs which are vertically aligned and dense directly on the substrate using lower temperatures. Therefore, the growth and physical-chemical properties of carbon nanotube arrays directly on the substrate form the basis of this study.

1.3 Aim of the project

The main objective of this work was to synthesise vertically aligned multiwalled carbon nanotubes (MWCNTs) directly on the ITO substrate, as an electrode material for organic solar cells using non-equilibrium PECVD approach. The work focuses on, enhancing solar cell applicability, maximisation of the electrode surface area characteristics and investigating the electrical properties.

In order to achieve this, several milestones had to be reached.

- ✓ Synthesis of mono-dispersed metal catalysts with controlled size distribution.
- ✓ Synthesis of MWCNTs with the synthesised catalysts using CVD methods.
- ✓ Optimisation of the PECVD operating parameters such as reaction time, temperature, carbon sources and gas flow rates, such that vertically aligned MWCNTs can be synthesised.
- ✓ Use of different carbon sources to synthesize MWCNTs.
- ✓ Application of the synthesised vertically aligned MWCNTs in organic solar cells.

1.3.1 Research questions

The specific aims and objectives of this work are better presented as questions surrounding the research.

- a. Is it possible to synthesise metal nanoparticles (MNPs) of Fe, Co, Ni, NiFe, NiCo and CoFe which are mono-dispersed using hexadecylamine (HDA) as the reducing agent as well as the surfactant?
- b. Is it possible to grow MWCNTs using the synthesised MNPs? What is the effect of particle size on the structure of the MWCNTs?
- c. Is it possible to grow MWCNTs at temperatures below 300 °C using a tailor made non-equilibrium plasma-enhanced chemical vapour deposition method? Does growth occur directly on the substrate? What is the resulting growth orientation?
- d. What is the effect of other process parameters, such as carbon source, gas flow rate, reaction time and temperature?
- e. What is the effect of the synthesised CNTs when applied to organic solar cells?
- f. Is it possible to characterise the CNTs and MNPs, and relate their properties to its application, with reference to organic solar cells?

1.4 Thesis outline

Chapter One

This chapter presents the introduction, background, motivation, aims, objectives and the thesis outline of this work.

Chapter Two

This chapter focuses on the literature review. The review of the synthesis methods available, includes the previous studies done elsewhere, characterisation techniques, the properties of the CNTs and the application in energy devices.

Chapter Three

In this chapter detailed methods of synthesising the catalysts and the MWCNTs are given. The chemicals, solvents, gases and instrumentation involved during synthesis and characterisation is also provided and discussed in detail. Catalysts consisting of single metals (Fe, Co, and Ni), mixtures of metals (CoFe, NiCo and NiFe) and MWCNTs were synthesised. The synthesised MNPs and MWCNTs were mainly characterised using TEM, SEM, TGA, FTIR and Raman spectroscopy.

Chapter Four

This chapter focuses on the results and discussion of the synthesised metal nanoparticle catalysts. The size and morphology of the synthesised catalysts were discussed.

Chapter Five

A detailed description of the synthesised MWCNTs and their application in solar cells, solar cell set-up, and the solar cell efficiencies is provided in this chapter. Explanation of the solar cell experiments is provided and the short circuit current (IV) curves discussed.

Chapter Six

This chapter gives the overall summary and conclusions of all the thesis chapters and the experimental procedure results. It also gives the recommendation for future work.

Appendices

Supplementary information is provided here.

References

- (1) Underwood, W. J.; McGlone, J. J.; Swanson, J.; Anderson, K. A.; Anthony, R. Agricultural Animal Welfare. *Laboratory Animal Welfare, Academic Press* **2014**, 233-278.
- (2) Albertyn, R.; Rode, H.; Millar, A. J.; Peck, M. D. The domestication of fire: the relationship between biomass fuel, fossil fuel and burns. *Burns : Journal of the International Society for Burn Injuries* **2012**, *38*, 790-795.
- (3) Mlekuž, D. The materiality of dung: the manipulation of dung in Neolithic Mediterranean caves. *Documenta Praehistorica* **2009**, *36*, 219.
- (4) Dumpe, B.; Stivrins, N. Organic inclusions in Middle and Late Iron Age (5th–12th century) hand-built pottery in present-day Latvia. *Journal of Archaeological Science* **2015**, *57*, 239-247.
- (5) Spear, B. Coal – Parent of the Industrial Revolution in Great Britain: The early patent history. *World Patent Information* **2014**, *39*, 85-88.
- (6) Tepper, A.; Borowiecki, K. J. Accounting for breakout in Britain: The industrial revolution through a Malthusian lens. *Journal of Macroeconomics* **2015**, *44*, 219-233.
- (7) Administration, U. S. Energy Information. *International Energy Outlook 2013*, 25 July **2013**.
- (8) SourceOECD: *World energy outlook*; OECD/IEA, **2006**.
- (9) Spalding-Fecher, R.; Winkler, H.; Mwakasonda, S. Energy and the world summit on sustainable development: what next? *Energy Policy* **2005**, *33*, 99-112.
- (10) Farhat, A. A.; Ugursal, V. I. Greenhouse gas emission intensity factors for marginal electricity generation in Canada. *International Journal of Energy Research* **2010**, *34*, 1309-1327.
- (11) Haehnlein, S.; Bayer, P.; Blum, P. International legal status of the use of shallow geothermal energy. *Renewable and Sustainable Energy Reviews* **2010**, *14*, 2611-2625.
- (12) Saidur, R.; Islam, M. R.; Rahim, N. A.; Solangi, K. H. A review on global wind energy policy. *Renewable and Sustainable Energy Reviews* **2010**, *14*, 1744-1762.
- (13) Posten, C.; Schaub, G. Microalgae and terrestrial biomass as source for fuels—A process view. *Journal of Biotechnology* **2009**, *142*, 64-69.
- (14) Solangi, K. H.; Islam, M. R.; Saidur, R.; Rahim, N. A.; Fayaz, H. A review on global solar energy policy. *Renewable and Sustainable Energy Reviews* **2011**, *15*, 2149-2163.

- (15) Kamat, P. V. Meeting the Clean Energy Demand: Nanostructure architectures for solar energy conversion. *Journal of Physical Chemistry: C* **2007**, *111*, 2834-2860.
- (16) Asif, M.; Muneer, T. Energy supply, its demand and security issues for developed and emerging economies. *Renewable and Sustainable Energy Reviews* **2007**, *11*, 1388-1413.
- (17) Division, U. N. P. World population prospects: the 1994 revision. *United Nations* **1995**, 145.
- (18) Nejat, P.; Jomehzadeh, F.; Taheri, M. M.; Gohari, M.; Abd. Majid, M. Z. A global review of energy consumption, CO₂ emissions and policy in the residential sector (with an overview of the top ten CO₂ emitting countries). *Renewable and Sustainable Energy Reviews* **2015**, *43*, 843-862.
- (19) Cohen, B. Urbanization in developing countries: Current trends, future projections, and key challenges for sustainability. *Technology in Society* **2006**, *28*, 63-80.
- (20) Lee, C. C. The causality relationship between energy consumption and GDP in G-11 countries revisited. *Energy Policy* **2006**, *34*, 1086-1093.
- (21) Mitcheson, P. D.; Yeatman, E. M.; Rao, G. K.; Holmes, A. S.; Green, T. C. Energy harvesting from human and machine motion for wireless electronic devices. *Proceedings of the IEEE* **2008**, *96*, 1457-1486.
- (22) Nossol, E.; Gorgatti, Z. A. J. Transparent films from carbon nanotubes/Prussian blue nanocomposites: preparation, characterization, and application as electrochemical sensors. *Journal of Material Chemistry*. **2012**, *22*, 1824-1833.
- (23) Bianco, A. Carbon nanotubes for the delivery of therapeutic molecules. *Expert opinion on drug delivery* **2004**, *1*, 57-65.
- (24) Park, Y. J.; Kim, H. J.; Han, L. T.; Zoukarniev, A. Z.; Min, K. W.; Baek, C. W.; Jeong, T. W.; Chung, D. S.; Park, S. H.; Choi, J. H.; Song, B. K.; Kang, H. S.; Heo, J. N.; Lee, J. H.; Jin, Y. W.; Kim, J. M. Density control of carbon nanotubes for field emission display by control of catalytic layer diffusion. *Technical Digest of the 18th International Vacuum Nanoelectronics Conference* **2005**, 358-359.
- (25) Gopinathan, K. K. Estimating the diffuse fraction of hourly global solar radiation in Southern Africa. *International Journal of Solar Energy* **1989**, *7*, 39-45.
- (26) Outlook, A. E. Energy Information Administration. *Department of Energy* **2010**.
- (27) Lewis, N. S.; Nocera, D. G. Powering the planet: Chemical challenges in solar energy utilization. *Proceedings of the National Academy of Sciences* **2006**, *103*, 15729-15735.

- (28) ByungáYoon, K. Energy and environment policy case for a global project on artificial photosynthesis. *Energy & Environmental Science* **2013**, *6*, 695-698.
- (29) Wang, C.; Abdul-Rahman, H.; Rao, S. A new design of luminescent solar concentrator and its trial run. *International Journal of Energy Research* **2010**, *34*, 1372-1385.
- (30) Green, M. A.; Emery, K.; Hishikawa, Y.; Warta, W.; Dunlop, E. D. Solar cell efficiency tables (Version 45). *Progress in Photovoltaics: Research and Applications* **2015**, *23*, 1-9.
- (31) Somani, P. R.; Savita, P. S.; Masayoshi U. Toward organic thick film solar cells: three dimensional bulk heterojunction organic thick film solar cell using fullerene single crystal nanorods. *Applied Physics Letters* **2007**, *91*, 173503-173503.
- (32) Mohammad, B. A. comparison of organic solar cells and inorganic solar cells. *International Journal of Renewable and Sustainable Energy* **2014**, *3*, 53.
- (33) Choi, S. J.; Yu, G. J.; Kang, G. H.; Lee, J. C.; Kim, D.; Song, H. The electrical properties and hydrogen passivation effect in mono crystalline silicon solar cell with various pre-deposition times in doping process. *Renewable Energy* **2013**, *54*, 96-100.
- (34) Xue, C.; Rao, J.; Varlamov, S. A novel silicon nanostructure with effective light trapping for polycrystalline silicon thin film solar cells by means of metal-assisted wet chemical etching. *Physica Status Solidi: A* **2013**, *210*, 2588-2591.
- (35) Misra, S.; Yu, L.; Foldyna, M.; I Cabarrocas, P. R. High efficiency and stable hydrogenated amorphous silicon radial junction solar cells built on VLS-grown silicon nanowires. *Solar Energy Materials and Solar Cells* **2013**, *118*, 90-95.
- (36) Lee, M. M.; Teuscher, J.; Miyasaka, T.; Murakami, T. N.; Snaith, H. J. Efficient hybrid solar cells based on meso-superstructured organometal halide perovskites. *Science* **2012**, *338*, 643-647.
- (37) Capasso, A.; Salamandra, L.; Di, C. A.; Bell, J. M.; Motta, N. Low-temperature synthesis of carbon nanotubes on indium tin oxide electrodes for organic solar cells. *Beilstein Journal of Nanotechnology*. **2012**, *3*, 524-532.
- (38) Wang, C.; Waje, M.; Wang, X.; Tang, J. M.; Haddon, R. C.; Yan, Y. Proton exchange membrane fuel cells with carbon nanotube based electrodes. *Nano letters* **2004**, *4*, 345-348.
- (39) Zhang, D.; Ryu, K.; Liu, X.; Polikarpov, E.; Ly, J.; Tompson, M. E.; Zhou, C. Transparent, conductive, and flexible carbon nanotube films and their application in organic light-emitting diodes. *Nano Letters* **2006**, *6*, 1880-1886.

- (40) Wang, C.; Gao, E.; Wang, L.; Xu, Z. Mechanics of network materials with responsive crosslinks. *Comptes Rendus Mécanique* **2014**, *342*, 264-272.
- (41) Zhu, L.; Sun, Y.; Hess, D. W.; Wong, C. P. Well-aligned open-ended carbon nanotube architectures: an approach for device assembly. *Nano letters* **2006**, *6*, 243-247.
- (42) Nxumalo, E. N.; Nyamori, V. O.; Coville, N. J. CVD synthesis of nitrogen doped carbon nanotubes using ferrocene/aniline mixtures. *Journal of Organometallic Chemistry* **2008**, *693*, 2942-2948.
- (43) Lee, Y. T.; Park, J.; Choi, Y. S.; Ryu, H.; Lee, H. J. Temperature-dependent growth of vertically aligned carbon nanotubes in the range 800-1100 °C. *Journal of Physical Chemistry: B* **2002**, *106*, 7614-7618.

Chapter Two

LITERATURE REVIEW

This chapter presents an overview of the energy demand, energy sources and the alternative ways to meet the energy demand. Conventional technologies used for the conversion and storage of energy are discussed herein. Carbon nanotubes are discussed as a form of advancement in the technology of energy conversion and storage devices. The main focus is on growth and physicochemical properties of vertically aligned carbon nanotubes directly on the substrate.

2.1 Energy and resources

Energy is the ability of any system to do work.¹ A system is comprised of many properties, and among them, the property which depreciates when the system is properly functional is energy. The various forms of energy, such as kinetic and potential energy, can only be converted from one form to another depending on the type of the operating system. Considering an ecosystem, such as the earth, living organisms require energy to survive. Particularly, humankind and animals obtain energy from food and oxygen. When these animals and plants die they decay over a long period of time, 35-40 years and they become buried geological organic matter. This organic matter when converted from its original state forms part of the energy which is required for most day to day activities of humankind. Statistically it was noted that the world uses about 16 TW of energy per year.² The consumption of energy is escalating at an alarming rate universally. This is due to the rapid economic expansion worldwide, world population growth and an ever increasing human reliance on energy consuming appliances (as discussed in **Chapter One**). According to 2011 energy statistics, by 2050 the world will need to double its energy supply.^{3,4} Therefore, there has been serious considerations to look at the energy sources available in order to meet the energy demand.⁵ Fossil fuels are being used as the major source of energy supply, and the demand is growing. Hence, renewable energy sources have become a necessary component for sustainable growth and development.

2.1.1 Renewable energy

Over the past years, mankind has been tirelessly exploring the earth in search of sustainable energy. Currently 90% of the world's energy supply and consumption is being generated from fossil fuels and these are getting depleted as they are being overexploited to match the energy demand (**Figure 2.1**).⁴ Limited viability and environmental concerns have since surfaced as the major challenges that the energy grid is facing.⁶ For instance, the extraction, processing and generation of energy is marred by different drawbacks e.g. land degradation,⁷ respiratory diseases,⁸ greenhouse gases,^{9,10} and acid rain.^{6,11} Hence, it has become imperative that there be development of some form of sustainable energy sources.

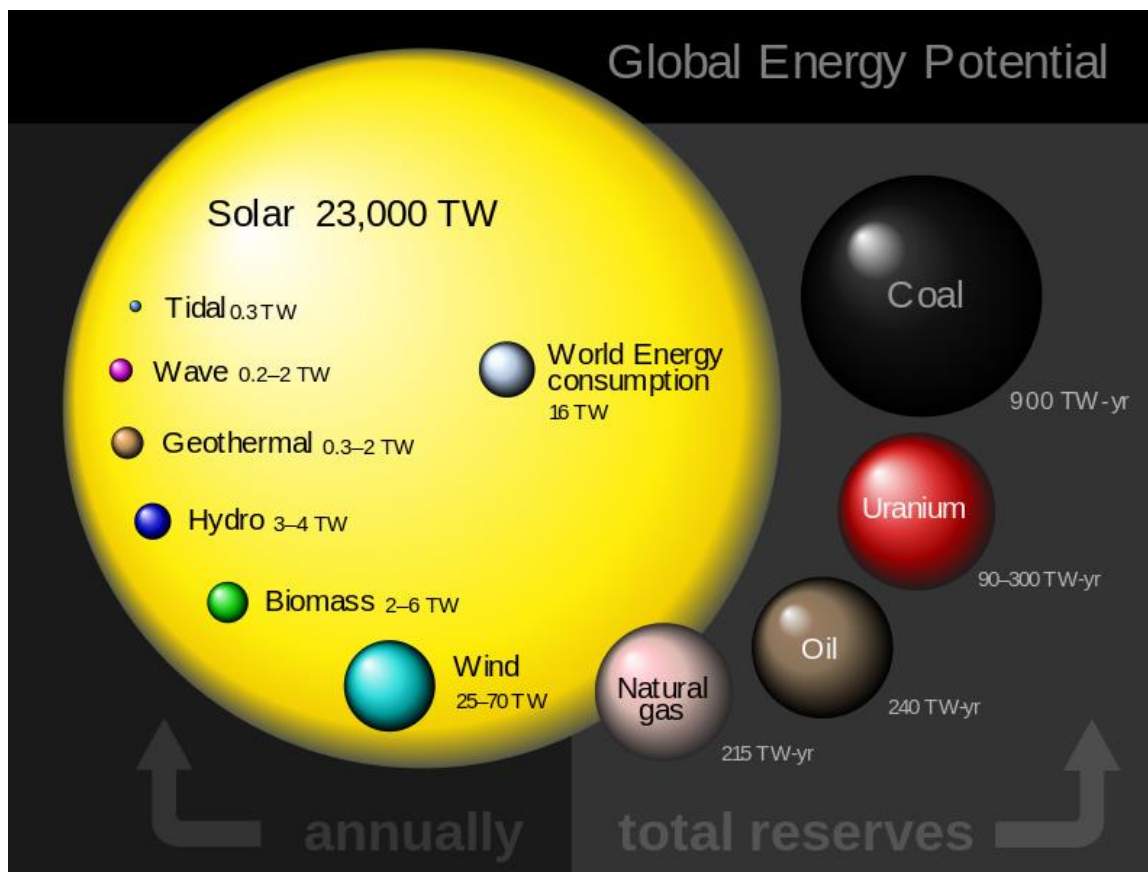


Figure 2.1: Global energy potential¹²

Energy sources can be classified into two general types, i.e. renewable and non-renewable sources. Renewable energy sources are the most desirable, and this is attributed to their ability to replenish at a rate that does not put them to extinction using natural processes.^{13,14} Hydropower, geothermal,

wind power and solar power are the predominant sources of renewable energy being utilized presently.¹⁵

Hydropower is the largest form of renewable energy in use and is tailed by biomass. Hydropower is the energy utilised from water in motion, once harnessed it is converted directly to electricity. The water cycle is a continuous process which involves natural recycling of the water thus considered renewable. Water is stored in a reservoir; it flows through a tunnel that is connected to the reservoir. As the water flows it passes through turbine gates where the pressure of the water is responsible for the spinning of the turbines. Once the turbines turn the generator becomes activated hence, the hydro turbine produces electricity.¹⁶⁻¹⁸

Geothermal power involves the use of steam turbines to generate electricity. Underground water is heated to form steam. The steam is pressurised and passed through a steam turbine. The steam turbine then uses electromagnetic induction to convert thermal energy to electricity.¹⁹ The main challenge associated with hydrothermal energy is that it is only suitable for areas prone to volcanic eruptions, i.e. Iceland, Indonesia and Philippines, where there are multi volcanic islands. It is also found in Kenya due to the Africa's rift valley and the Ring of fire in Japan where the four tectonic plates converge.^{17,20}

Wind power makes use of the kinetic energy of the wind. Wind turbines are placed on towers and as the wind blows, it forcefully turns the turbines. The turbines in turn activate the wind generators thus producing electricity.^{3,18}

These, hydropower, geothermal and wind power, energy sources are renewable and supply clean energy. However, they entail large capital investments amongst other disadvantages which include; noise production from wind turbines, and distraction of both terrestrial and underground habitats during the anchoring of the windmill. In this regard, these primary energy generation systems have become a less preferred option for energy generation. This leaves solar energy as an attractive technology since it does not require a massive set-up like wind and hydrothermal power stations.

All life on earth is supported by the sun and the sun is the primary source for almost every other form of energy in use.^{18,21} The power from the sun is in vast and inexhaustible supplies. The earth

receives 120 000 TW of energy from the sun per hour.² Globally, the energy demand per year is around 16 TW. Based on the abundance of the solar supply, it is a mystery why solar still provides less than 2% of the global energy. *Solar power* generates electricity as a result of sunlight collection and conversion. The main challenge is to harness the energy from the sun. Electricity generation is through various technological pathways. However, the main technologies are the concentrating solar power (CSP) and the photovoltaic systems (PV) (**Figure 2.2**). The CSP indirectly converts sunlight into electricity. The technology utilises an array of tracking reflectors (heliostats) to focus a large area of sunlight into a small beam of high temperature heat. A working fluid is heated by the concentrated sunlight and is used to drive turbines that generate electrical power (**Figure 2.2 (a)**).

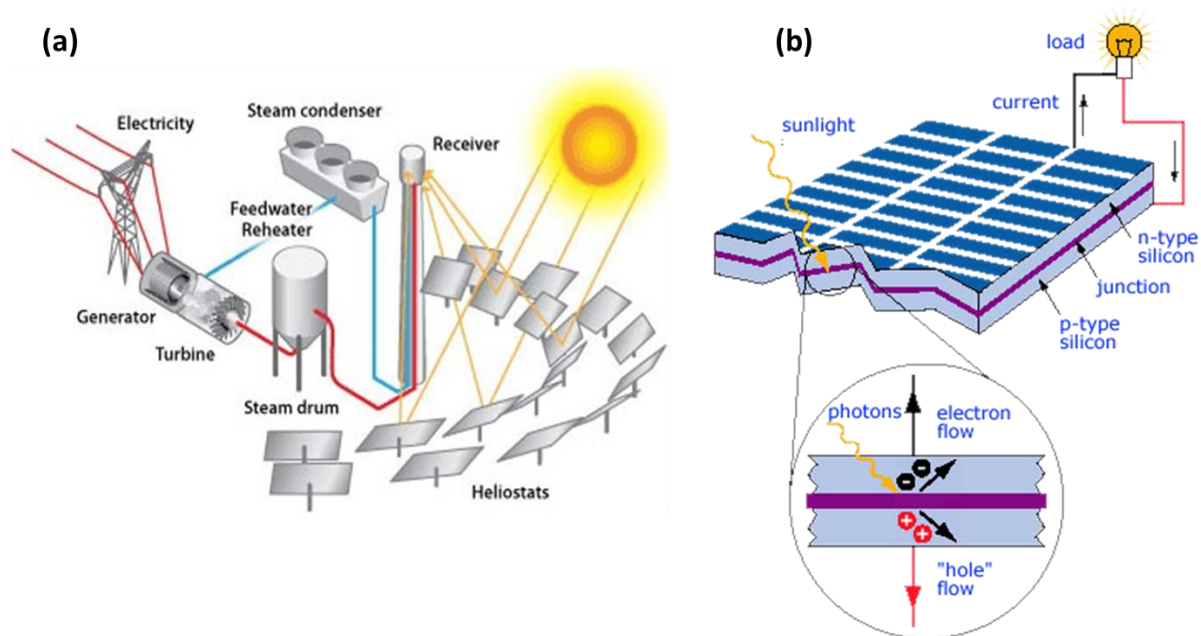


Figure 2.2: Illustration of the mechanism involved in (a) the concentrating solar power and (b) photovoltaic system¹⁴

The PV system uses the photovoltaic effect to convert sunlight into electric current. To accomplish the absorption of solar photons the process requires the use of semiconductors. The PV cell therefore consists of n- and p- type semiconductors. When sunlight hits the PV cells, negatively and positively charged electrons are generated simultaneously. The negatively charged electrons are attracted to the n-type semiconductor while the positively charged electrons are attracted to the p-type semiconductor.¹³ When a load (light bulb etc.) is connected to the PV cell, electric current flows between the two electrodes thus electricity is generated. Considerable efforts to enhance the

harvesting of the solar energy are still under study.¹⁴ Amongst the technologies towards reliable and sustainable energy supplies is nanotechnology which is a concept under nanoscience.²²

2.2 Nanoscience and nanotechnology

The concept of nanotechnology utilises dimensions and tolerance of less than 100 nm at molecular scale.²³ Nanotechnology refers to the design, characterization, production, and application of materials, devices and systems by controlling shape and size at the nanoscale.²⁴ Generally, nanotechnology provides many advantages in specified fields of interest. This technology has contributed immensely in the betterment of the life on the globe. For instance, the development of technological paper towels has been found to accelerate the removal of harmful air components.²⁵ Aligned carbon nanotube (CNT) sheets were either stacked parallel to each other or in a cross-ply position and were incorporated between micro-fibre polypropylene non-woven fabrics to produce filters with high efficiency particulate air level efficiency. The filters (nanofabrics), show higher absorptivity, 20 times more than the micro-fibres without the CNTs.²⁶ In addition, there has been advancement towards nanotechnology-enabled sensors to recognise harmful agents present in the air and soil in agriculture sector. This was achieved by fabricating a highly sensitive electrochemiluminescence immunosensor for transgenic *Bacillus thuringiensis* soybean Cr1Ac protein detector. The device utilised gold (Au) coated iron oxide (Fe_3O_4) nanoparticles to detect the transgenic protein microbial contamination from non-transgenic plants.²⁷ These sensors would also assist farmers in identifying the best possible places to grow crops as much as they become aware of unsatisfactory yields.^{28,29}

Nanotechnologies have also been applied in cosmetic and beauty products through enhancing antioxidant and anti-microbial properties.³⁰ Silver (Ag) synthesised nanoparticles were investigated on microorganisms, along with the skin permeability and the cytotoxicity in human keratinocytes. Their investigation was done under ultra violet B-irradiation. In this case, an excellent potential of Ag nanoparticles for use as a preservative in cosmetics was reported to be; very effective at low concentrations, unable to readily penetrate the skin barrier, and possessing no detrimental effects on keratinocytes.³¹ Therefore, nanotechnology has opened up new lines of study in material science and engineering. Looking at energy, nanotechnology is advancing to provide major improvements in the way useful energy is generated. This is considered to be achievable through fabricating and

introducing new materials particularly carbon nanomaterials for efficient energy conversion and storage.²²

In a drive to improve flexibility, energy density and conductivity in supercapacitors, carbon paper with high-volumetric capacitance in flexible supercapacitors has been reported. The fabrication involve vacuum-assisted filtration of aqueous suspension of phenolic nanofibers and graphene oxide, followed by a one-step thermal treatment.³² In another study to enhance the high energy density storage devices, integrated supercapacitors with extended operation voltage were fabricated. The graphene-polyaniline based electrodes reported by Chen and co-workers showed very high specific and volumetric capacitance. Their electrodes were fabricated by direct electrode deposition in a separator process which involved vacuum filtration, ion exchange and capillary compression.³³ On the other hand, carbon nanomaterials are also being applied in energy conversion devices. Single walled carbon nanotubes have been incorporated as part of the electrode material in bulk heterojunction solar cells to improve efficiency. Flexible transparent conducting electrodes were fabricated using printed films of single-walled carbon nanotube networks on plastic.³⁴ However synthesis of such carbon nanomaterials for use in energy conversion systems amongst others, seem to be contradicting the goal to scale up energy supply because of high temperatures often involved. Hence, synthesis of unique carbon nanomaterials with different morphology and dimensions using economically favourable temperature conditions is still a promising avenue.

2.2.1 Carbon nanomaterials

Carbon nanomaterials are nanoscale in various dimensions ranging from 1-3 dimensions. These carbon nanomaterials can exist in definite forms and shapes depending on the dimensional phase.³⁵ The common types of nanomaterials include quantum dots, fullerenes and CNTs.³⁶ Carbon fibre structures that were hollow and graphitic were first published by Radushkevich in 1952.³⁷ Since then, research on carbon nanomaterials has been ongoing. In 1976, a hollow carbon fibre was published by Endo *et.al.*³⁸ More evidence on fibrous carbon was published in 1978.³⁹ Further results in multi-layer tubular crystal structures were provided by Soviet scientists in 1981 and subsequent years. In 1985, Kroto and co-workers discovered the Buckminster fullerenes.⁴⁰ The discovery of fullerenes in 1985 triggered research on other allotropes of carbon. Since then, carbon nanomaterials have been a key research area.

The hybridization of the carbon atoms and overall morphological arrangement plays an important role in determining the identity of these types of nanomaterials. For instance, fullerenes are a product of highly symmetrical (icosahedral symmetry), molecular clusters of carbon atoms, comprising of a carbon atom bonded to three others forming sp^2 hybrids, and are also zero dimensional (0-D). Structurally, fullerenes consist of 20 hexagonal and 12 pentagonal rings. These are responsible for their icosahedral symmetry and closed cage structure **(Figure 2.3)**.⁴¹ Another allotrope of carbon is graphene. Graphene is a two dimensional (2-D) monoatomic layer of graphite, **(Figure 2.3)**, which is also a sp^2 hybridized carbon nanomaterial form. The hybridised carbon atoms form three in-plane pi-bonds per atom which in turn lead to the hexagonal planar layer, which is responsible for the displayed honeycomb atomic arrangement.⁴² A graphene layer when rolled up forms a one dimensional (1-D) structure and is referred to as a carbon nanotube (CNT) **(Figure 2.3)**.⁴³

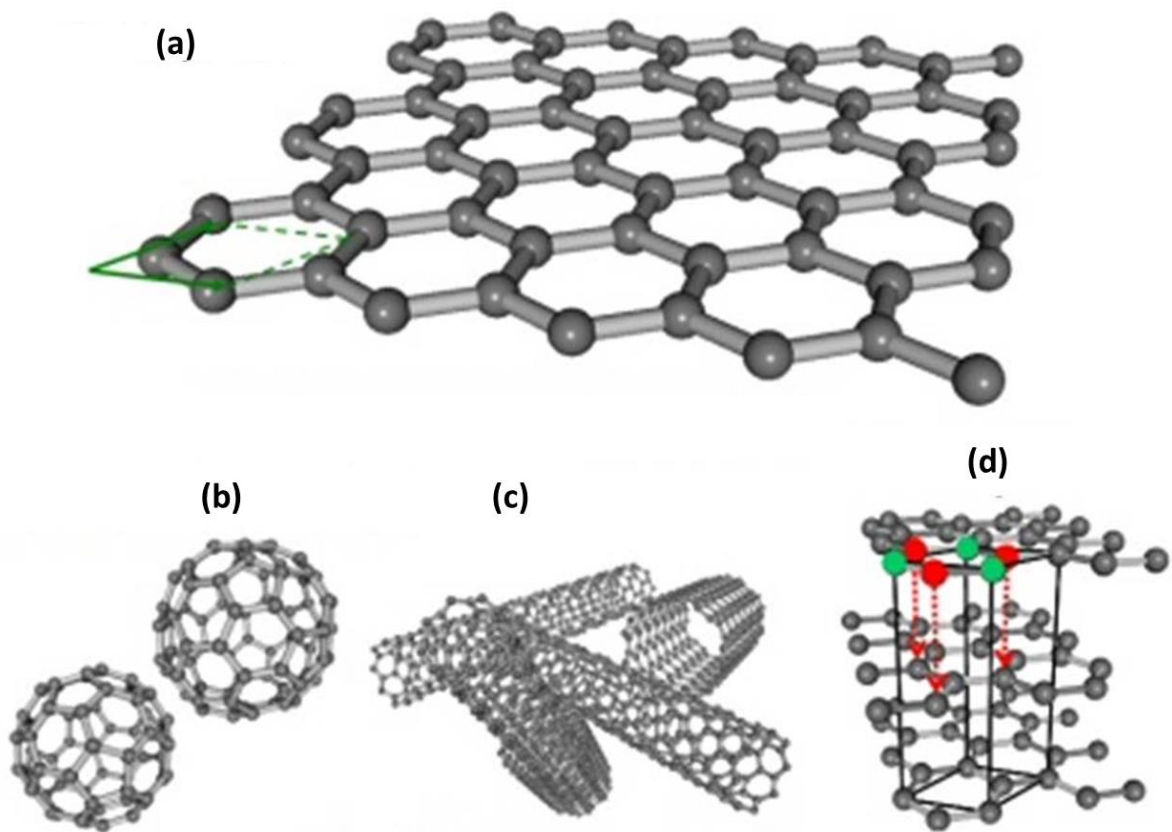


Figure 2.3: The structure of the carbon nanoforms (a) graphene, (b) fullerenes, (c) CNTs and (d) graphite^{41,43}

Carbon nanostructures are classified according to their unique geometrical arrangements. The major classification criteria currently in use are dimensions as indicated by the **Table 2.1**.⁴⁴

Table 2.1: Dimensional classification of carbon nanostructures

| Classification | Size/nm | Examples |
|----------------|---------|--|
| 0-D | <100 | Bucky balls (C_{70} , C_{76} , C_{84}) |
| 1-D | < 100 | Nanorods, nanowires |
| 2-D | < 100 | Tubes and fibres |
| 3-D | < 100 | Quantum dots, particles |

The class of 2-D carbon based nanostructures consist of nanofibers and nanotubes. The CNTs have single, double or multi walls, with open or closed ends (**Figure 2.4**). The number of walls is a result of the number of graphene layers rolled together, i.e. one, two or many.⁴³

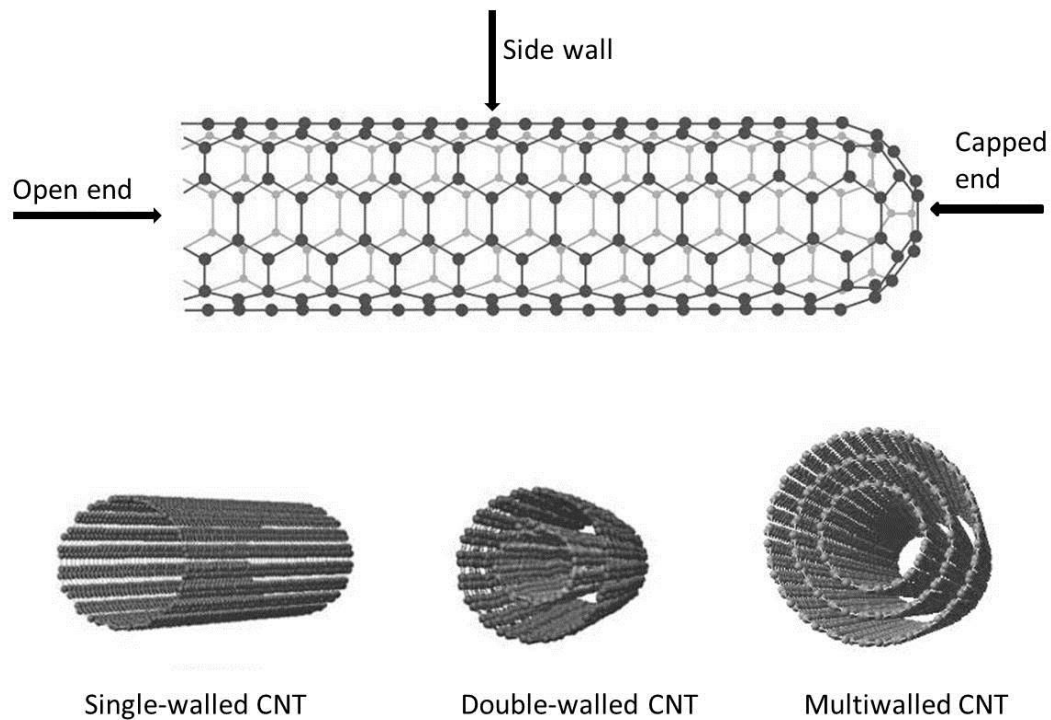


Figure 2.4: The structural forms of carbon nanotubes and the nature of their tube ends

The way the graphene layer is rolled is represented with the indices n and m . These indices present the number of unit vectors along the two directions in the graphene crystal lattice. Considering tube axis (T), where a_1 and a_2 are lattice vectors, the chiral vector (c_h) is represented by the equation:

$$c_h = na_1 + ma_2 \quad (\text{Equation 2.1})$$

The c_h defines the manner in which graphene can be curled to form tubular structures with different conformations. When $m=0$, the resulting tubes are zigzag at a chiral angle of 0° , whilst if $n=m$ an arm chair conformation results at 30° chiral angle (Figure 2.5).⁴⁵

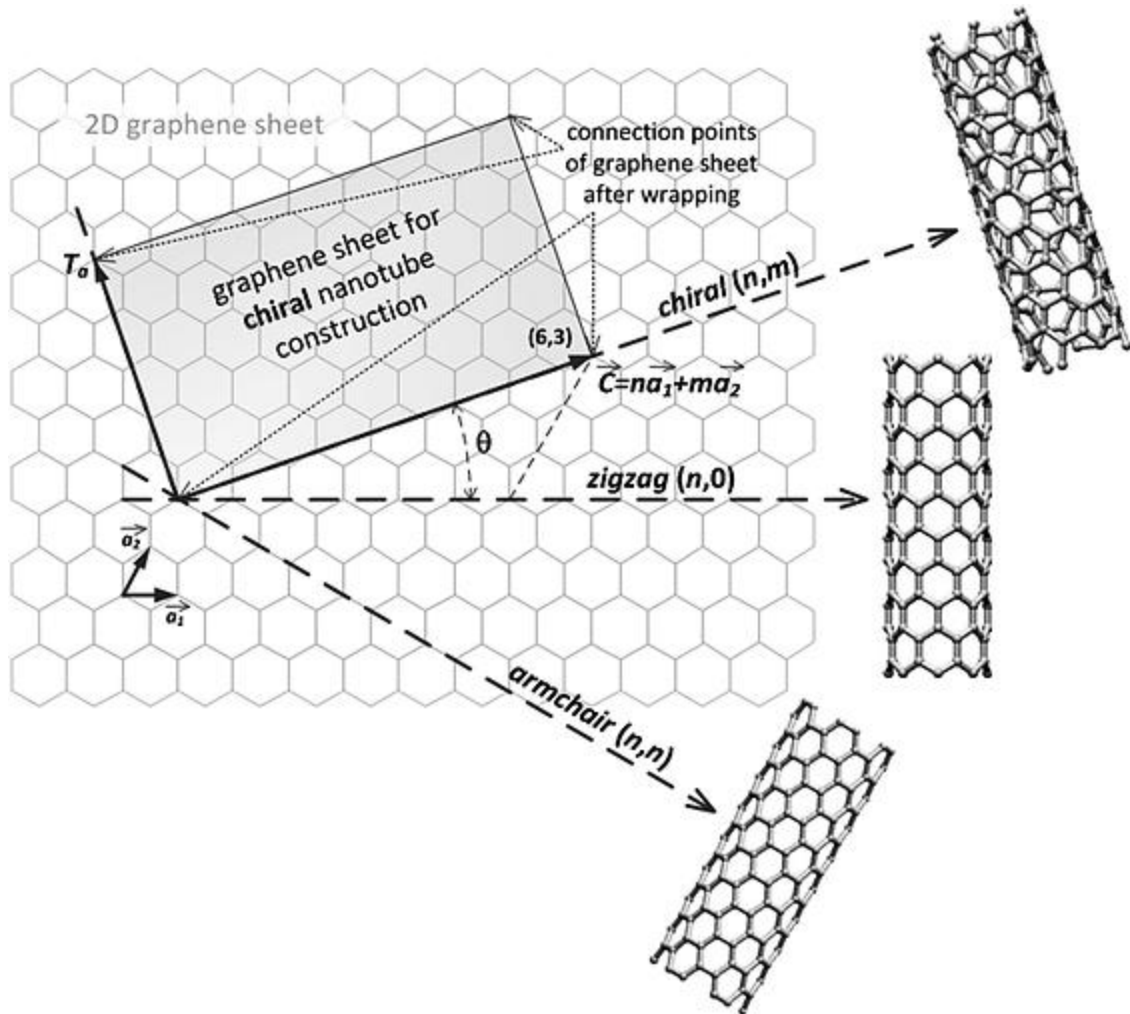


Figure 2.5: The conformations in which graphene can roll up⁴⁶

Properties of CNTs responsible for their uniqueness such as; thermal,⁴⁷ electronic,⁴⁸ optical⁴⁹ and magnetic,⁴⁸ all depend on the chirality. Considering electronic properties, if n, m values satisfy the equation:

$$n - m = 3j \quad (\text{Equation 2.2})$$

Where; j is an integer, the resulting tubes are metallic and can function as conductive wires. When, n, m satisfies **Equation 2.3** or **2.4**:

$$n - m = 3j + 1 \quad \text{(Equation 2.3)}$$

$$n - m = 3j + 2 \quad \text{(Equation 2.4)}$$

the tubes are semiconducting and can therefore be used as gate materials in transistors.⁵⁰ The band structure of the CNTs with n, m indices can be easily calculated⁵¹ and a plot can be drawn to show the relationship between CNT diameter and its band gap energy.⁴⁵ The curvature of the CNT wall is found to be responsible for the reduction of the band gap of the CNTs by hybridization, and also modification of the energies of the electronic states responsible for transitions in the visible energy range.⁵¹ The magnetic field have strong effects on the electronic structure and bulk properties of CNTs. The magneto resistance of pure CNTs is sensitive to the electronic structure and external magnetic field such that the weak field magneto susceptibility is predicted to increase proportionally with the CNT radius. The susceptibility can be diamagnetic or paramagnetic depending on helicity of the CNT, the field direction and Fermi energies.⁴⁸

These properties makes the CNT suitable for a wide range of applications such as energy storage devices,⁵² catalysis,⁵³ field emission⁵⁴ and gas sensing, since their discovery by Iijima in 1991.⁵⁵ CNTs provide increased electrical and mechanical integrity which enhances rate capability and life cycle of energy related devices.⁵⁶ Considerable efforts with outstanding progress to utilize these properties have been achieved.²³ For instance in batteries, CNTs are proved to be the most effective for decreasing resistance and improving electrochemical behaviour of the composite cathode. To demonstrate this, CNTs were incorporated as conductive additives at reduced weight loading jointly with lithium cobalt oxide (LiCoO_2) as the active material and a lanthanum 132 (LA132) binder. The mixed slurry was spread onto a 10 μm -thick Al foil to form an electrode.⁵⁷ Therefore, due to these properties displayed by the CNTs, it is imperative to look at the methods available for the synthesis of CNTs.

2.3 CNT synthesis methods

Several synthesis methods are available for the production of CNTs.⁵⁸⁻⁶⁰ Respective methods produce exceptional CNT materials. However, there are three core techniques considered; arc discharge,⁶¹ laser ablation⁶² and chemical vapour deposition (CVD).^{35,59}

2.3.1 Arc discharge

Arc discharge, was the first acknowledged CNT synthesis technique for producing either MWCNTs or SWCNTs. Arc discharge is the electrical dissociation of a gas to generate plasma. Basically the technique involves the use of two electrodes, cathode and anode, which are made from high-pure graphite. To vaporise the electrodes, a direct current is passed through the gap between the electrodes in an atmosphere consisting of Helium.⁶³ **Figure 2.6** shows a schematic set-up to further explain the technique.⁶³ Deposits are formed at the cathode and definite carbon products rely on the process parameters.

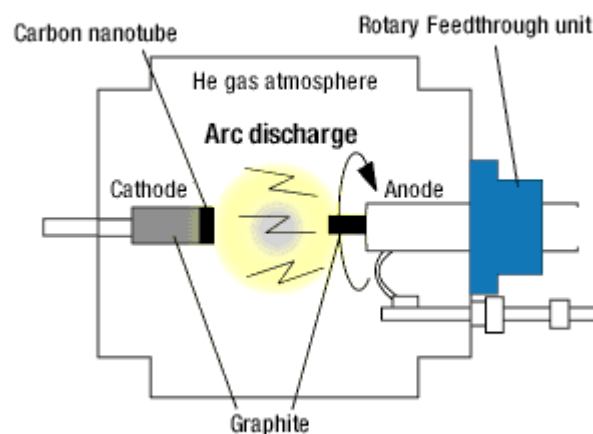


Figure 2.6: Arc discharge set-up⁶³

The power supply source of the arc could be direct current (DC),⁶⁴ alternating current (AC)⁶⁵ or pulsed arc discharge.⁶¹ These show deviations in the manner in which the products are formed. In DC and pulsed arc discharges, the products form at the cathode, whilst in AC the products forms anywhere within the chamber. Since the initiation of utilising this synthesis approach, there has

been technological advancement in the process in order to improve the yield, quality and size of the CNTs.⁶⁶ Ebbesen and Ajayan reported a large-scale synthesis of MWCNTs by means of a modified standard arc-discharge system.³⁵ They operated with a potential of 18 volts of DC between two thin graphite rods in helium atmosphere, 500 Torr. A maximum of 75% yield was recorded. The TEM image analysis revealed that their samples consisted of nanotubes of two or more concentric carbon shells with diameters between 2 and 20 nm. In another study by Journet and co-workers, large-scale SWCNTs were synthesised.⁶⁷ A helium atmosphere of 660 mbar and a current of 100 A with 30 voltage power was used. To one end of the anode, a hole filled with bimetallic catalytic particles of NiCo, CoY or NiY and graphite was drilled. SEM analysis showed that 80% of the product was twinned carbon ropes, while HR-TEM showed that the diameters were between 5 and 20 nm.⁶⁷ Bethune and co-workers synthesised the nanotubes in a similar way.⁶⁸ They used thin anode electrodes with holes filled with combinations of pure metal powders of Fe, Ni, or Co collectively with graphite. The electrodes were vaporized with a current of 95–105 A, in 100–500 Torr of Helium. TEM image analysis showed that only the cobalt-catalysed nanotubes had single-atomic-layer walls with uniform diameters of 1.2 nm. In order to upgrade the process, different atmospheric conditions were employed. Liquid atmospheres were introduced; were the CNTs would float on the surface of the liquid upon synthesis. The readily used liquids included deionised water,⁶⁹ NaCl,⁷⁰ liquid N₂⁷¹ and He.⁷² To further improve the technique, Zhao and Liu applied six anodes and intensified the CNT yield.⁷³ Numerous methods comprising of pivoting the carbon cathode for a consistent micro discharge,⁷⁴ dropping the disk revolution speed⁷⁵ and sloping the cathode and anode at an angle of 30 °C⁷⁶ were devoted to improve the yield. Therefore, in this Arc discharge technique, the CNTs produced are normally long and straight with decent crystalline structures but difficult to purify because they contain carbon particles and even amorphous carbon.³⁵

2.3.2 Laser ablation

The processing technique involved in the laser ablation is almost similar to arc discharge. However, differences include the involvement of higher temperatures and energy supplied by a laser hitting a graphite pellet which contains catalyst material in the laser ablation technique. Graphite is the carbon source which is vaporised using a high laser power. The laser ablation method produces CNTs and by products like fullerenes, graphitic polyhedrons with closed metal particles and amorphous carbon depending on the reaction parameters, for instance addition of metal catalyst. To further illustrate this method, **Figure 2.7** shows the reactor set-up.⁷⁷

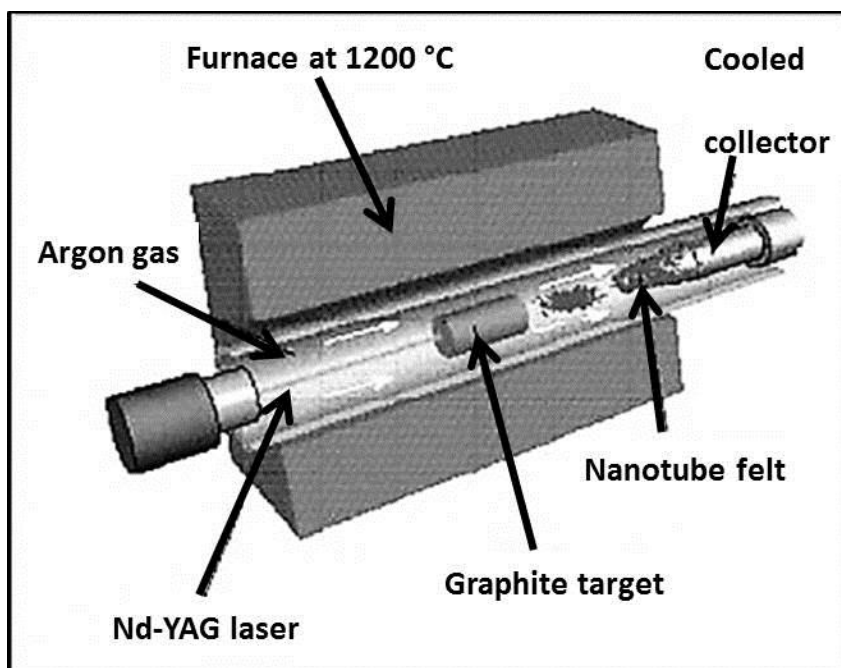


Figure 2.7: Laser ablation set-up⁷⁷

In a study conducted by Guo and co-workers, high yields of SWCNTs, above 70%, were recorded.⁷⁷ This group used laser-ablation to vaporise the graphite rods with insignificant metal catalyst quantities i.e. Ni and Co at 1200 °C. The TEM image analysis showed that the synthesized nanotubes had notable uniform diameters in the range 5–20 nm.⁷⁸ This laser ablation technique produces a high yield of the carbon materials, SWCNTs, with good diameter control, and few defects. Nevertheless, the method is a cost intensive technique, which entails pricey lasers and elevated power.^{77,78}

Both the arc discharge and the laser ablation techniques have the advantage of high percentage yields exceeding 70%. The major shortcomings are: the consistency on evaporation of carbon atoms from solid graphite targets at temperatures higher than 3 000 °C and producing CNTs which are tangled and mixed with undesirable carbon and catalyst variety. Hence, it turns out to be challenging to purify and acquire assembled structures suitable for versatile applications.⁷⁹ Therefore, chemical vapour deposition technique becomes considerable synthesis method.

2.3.3 Chemical vapour deposition

Chemical vapour deposition (CVD) technique is a process used to synthesise high quality, high-purity bulk materials and powders, as well as fabricating composite materials via infiltration techniques. In CVD a hydrocarbon source is decomposed at suitable temperatures, and with the aid of a catalyst, carbon nanomaterials are formed. This process is associated with challenges during synthesis. The major disadvantage of the CVD is that the nature of the precursor should be volatile. Therefore, this limits the range of applicable catalyst precursors. However, CVD advantages outweigh disadvantages. Advantages of CVD include; relatively high deposition rates, deposition of a variety of materials and deposition with very high purity. This makes CNT purification easier after synthesis. Basically, the CVD process involves flowing precursor gas molecules into a hot chamber containing substrate material. The volatile precursors react and decompose on the substrate resulting in the deposition of a thin film of carbon structures on the substrate surface. The process is associated with the production of volatile by-products that are exhausted out of the chamber along with unreacted precursor gases (**Figure 2.8**).⁸⁰

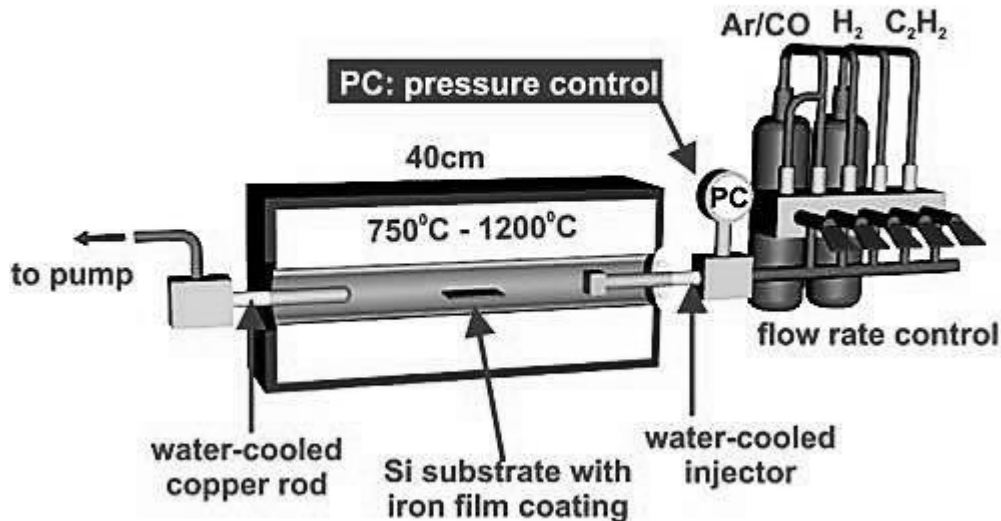


Figure 2.8: Illustration of the CVD set-up for CNT synthesis⁸⁰

The CVD process is performed in hot and cold-wall reactors, at pressures from sub-torr total to above-atmospheric pressures, with and without carrier gases, and at temperatures ranging from 200-1100 °C. The CVD can be enhanced such that deposition rates can be increased or deposition

temperatures can be lowered. There are a variety of enhanced CVD processes, which involve the use of plasmas, ions, photons, lasers, hot filaments, or combustion reactions.⁸⁰ The range of CVD products includes spheres, fibres and CNTs.

The greatest challenge faced in the CNT synthesis is the preparation of finely dispersed CNTs that are well aligned, densely populated, and intended for electronic device related applications. The efficient synthesis of vertically oriented nanotubes has been demonstrated by using the CVD techniques, as compared to arc discharge and laser ablation techniques.^{59,60,81} In the CVD process, the size and distribution of the active catalyst are reported to play a key role in the determination of the height and alignment of the CNT array, wall number and diameter. In order to control these properties, studies focussing on the catalyst preparation method as well as the pre-treatment methods have been conducted.⁸²

In this method, usually very high temperatures 500-1100 °C are employed during synthesis.⁸³ These high temperatures are difficult to reduce because the activation of the catalysts requires high process temperatures. The high temperatures are responsible for the catalyst bond breaking. Therefore, resulting in the formation of small metal nanoparticles for CNT catalysis.⁸⁴ Despite the fact that the method has a high level of growth control, high temperatures above 500 °C, restricts the range of possible substrates for growth of the CNTs.⁸⁵ To address this problem, alternative substrate friendly methods should be employed; this then develops subsidiary CVD methods. These subsidiary methods lead to the grouping and classification of the CVD methods. The CVD technique is classified according to the operating procedure, the means by which chemical reactions are initiated and physical characteristics of vapour.⁸⁶ Amongst the types are thermal CVD and plasma methods.

2.3.3.1 Plasma-enhanced chemical vapour deposition

Plasma is ionized gas, which consist of electrons, ions, charged and neutral radicals, in addition to the atoms and molecules of the precursor gas. The concentration of ions and charged species is remarkably very low when compared to the concentrations of neutral species. Therefore this result in the plasma being weakly ionized.⁸⁰ It is the effective dissociation of precursor gas species in the gas phase which is responsible for reducing the amount of heat supplied to the growth substrate, where in thermal CVD precursor dissociation usually occurs. Therefore, the main purpose of the

plasma is to overcome high deposition temperatures that are responsible for degrading the substrate materials.⁸⁵ There are various ways to supply the necessary energy to a neutral gas in order to generate plasma. The type of source used to generate the gas discharge is one key feature which distinguishes the different plasma methods.^{87,88} Some of the most common types include direct current plasmas (dc plasma), capacitively coupled plasmas (CCPs), inductively coupled plasmas (ICPs) and microwave plasmas (MWPs). These plasmas are characterised with temperatures of radical, ions, and neutral species that are much lower than the electron temperature. This creates a very strong thermal non-equilibrium and leads to unique possibilities to utilize electron-impact reactions, thus substantially enhancing chemical reactions in the gas phase. **Table 2.2** summarises the factors that influence plasma treatment.⁸⁹

Table 2.2: Parameters influencing plasma treatment during synthesis⁸⁹

| Plasma | Substrate | Reactor | Materials flow | Energy input |
|--|---|---|--|---|
| <ul style="list-style-type: none"> • Type and degree of gas dissociation • Residence time of the active species • Homo/heterogeneous reactions • Ion bombardment and radiation | <ul style="list-style-type: none"> • Material • Dimension • Morphology • Quantity • Temperature • Potential | <ul style="list-style-type: none"> • Gas leading system • Inner wall • Electrode material, configuration and temperature | <ul style="list-style-type: none"> • Monomers • Carrier gas • Pressure flow (total/partial) • Gas background | <ul style="list-style-type: none"> • Frequency • Power density • Duration • pulse |

To control these parameters several factors are considered. For instance, plasma is affected by the type and degree of dissociation of the feed gas and by what means the active species perform throughout the glow. Measurement, amount and morphology of the substrate directly influence plasma treatment. Certain substrates are extremely susceptible as contrasted to others. Wang and Moore reported the use of PECVD to be a more efficient and very reliable method for the low temperature production of CNTs.⁹⁰ This was attributed to the fact that the synthesis parameters such as carbon source, gas species, plasma source and the reaction temperature can be controlled easily.⁹⁰

Plasma generation occurs when energy is supplied to a neutral gas causing the formation of charged species. This happens when electrons or photons with sufficient energy collide with the neutral atoms and molecules in the feed gas.^{91,92} Low-temperature, low-pressure and non-equilibrium

plasma discharges are the most common in nanoscale fabrication. Such plasmas are operated using different power delivery mechanisms. For instance, in broad pressure ranges the operation uses a variety of gas compositions and excitation sources. At higher pressures, above 0.1 atm, the species collision rates are higher, thus, they tend to thermalize. The temperatures of the electrons (T_e), ions (T_i), and neutrals (T_n) are very close to each other ($T_e \sim T_i \sim T_n$) therefore, all the species find themselves in thermal equilibrium. Whereas, for non-equilibrium systems, the electron temperature is much higher than the ion and neutral temperature i.e. ($T_e \gg T_i, T_n$). The inelastic collisions of the electrons with the precursor molecules are responsible for the formation of chemically active species that participate in the reactions leading to the formation of a film. The surface chemistry is changed by the bombardment of the surfaces with active species (ions, electrons and neutrals).⁹³

The types of plasma sources are coupled with a technique, e.g. CVD, referred to as hybrid systems. Some common CVD plasma hybrid techniques include, microwave plasma-assisted CVD (MPCVD), direct current plasma-enhanced CVD (DCPECVD) and radio frequency plasma-enhanced CVD (RFPECVD). In PECVD, not only can the growth temperatures be dramatically reduced but also the CNTs usually become pure and vertically aligned.^{84,94,95} Studies have reported that the low temperature synthesis of CNTs by PECVD is the most useful method for the direct deposition of the CNTs onto substrates. The deposition favours substrates with the low melting points.^{87,89,94} Therefore, it is important to look at the factors that affect the synthesis CNT structures.

2.4 Factors affecting CNT synthesis

The growth and production of CNTs is influenced by several input parameters. These parameters include catalyst nanoparticle, carbon precursors, substrate, reaction time and temperature. A brief overview of the parameters; the catalyst, provide a template for the nucleation and growth of the nanotube, allows for the diffusion of the carbon intermediates and their chemical interaction, and it helps the dissociation of the carbon containing molecules. Carbon precursor is the source of the carbon responsible for the tube growth. Reaction time and temperature determines where optimum growth occurs. Pyrolysis time and temperature have a greater effect on the CNT growth, increasing heat treatment time initiates growth for lower temperatures and vice versa.⁵⁸

2.4.1 Catalysts

Metal catalysts used are in the nanometre size ranges, *i.e.* with their length, width, as well as thickness in the range 1-100 nm. Metal nanoparticles are used in the synthesis of CNTs mainly because the catalysts decompose the hydrocarbon molecules, allow diffusion of carbon intermediates and their chemical interaction provides a template for CNT nucleation and sustains growth.⁹⁶ The selection of the catalyst influences the growth and morphology of the synthesised CNTs. These metal catalyst possess unique characteristics which include, high surface area to volume ratio, greater surface energy, short range ordering and increased number of kinks as compared to the bulk equivalents.⁹⁷ Amongst these properties the smaller size of the metal catalyst is required such that it enables the decomposition of the hydrocarbon at lower temperatures.⁹⁸ Therefore, the choice of the method of synthesising the metal nanoparticles is very crucial for effective catalysis. Key considerations include, a method which is reproducible, controls the shape of the particles, yields mono-disperse metallic nanoparticles, and which utilises a one pot reaction is ideal for the synthesis of the metal nanoparticles.⁹⁹

Many methods for fabrication of nanoparticles have been developed. These range from lithographic technologies to chemical methods.¹⁰⁰ Various chemical methods have been adopted for the preparation of metal oxides nanoparticles. These include gas-phase methods¹⁰¹, sol gel methods¹⁰², evaporative decomposition of solution¹⁰³, wet chemical synthesis and co-precipitation methods.^{104,105} However, it is difficult to obtain nanoparticles with a low degree of agglomeration without the use of very stringent control over the various processing parameters. One of the ways to control agglomeration is through the use of a surfactant and organometallic precursors.¹⁰⁰ Of late, organometallic precursors have been found to be much more suitable for the production of the mono dispersed nanoparticles with controlled sizes, surface coordination and which are crystalline.¹⁰⁰ Among the various techniques developed for the synthesis of the metals and their oxides, thermal decomposition and co-precipitation methods have been found to produce stable mono-dispersed nanoparticles.¹⁰⁶ In comparison with the other conventional methods these methods are faster, economical and environmentally friendly. Transition metals are most often used to catalyse the growth of CNTs.

2.4.1.1 Iron, cobalt and nickel

There are several catalytic metal nanoparticles that have been reported in literature to produce better CNTs.⁵⁸ Transition metals such as Fe, Co and Ni have been successfully used for the synthesis of CNTs.^{96,107} Metal nanoparticles synthesized from these transition metals are among the most promising materials particularly for use in catalysis, magnetic fluids and information storage. Transition metals (Fe, Co and Ni), have higher melting points and lower equilibrium vapour pressures which enables them to suit catalysis of several hydrocarbon species during synthesis. In addition, Fe, Co and Ni catalysts possess high solubility of carbon, higher carbon diffusion rates and they form meta-stable carbides.^{96,108,109} These properties are responsible for the growth of the crystalline tubular structures. Latest reports have considered that these magnetite's of Fe have stronger adhesion with the growing CNTs and hence are more efficient in forming high-curvature and low diameter CNTs.^{107,110} However, the selectivity and activity of the single metal catalysts for the synthesis of CNTs can be poor. Therefore, this affects the structure of the CNTs produced. A convenient way that has been used to overcome this problem is to use bimetallic catalysts

2.4.1.2 Bimetallic catalyst

Bimetallic catalysts contain a mixture of two catalytic particles. The combination of metals provides good selectivity for CNT synthesis. The greatest advantage associated with the use of the bimetallic catalyst is that the melting point of the mixture is lower than that of single metals.¹¹¹ Considering the FeNi phase diagram (**Figure 2.9**),¹¹² the FeNi alloy system with 50% atomic fraction of Fe has a melting point lower than that of pure Fe. Therefore, this essentially provides the need for a bimetallic catalyst which could theoretically provide a good environment for low temperature growth of CNTs as well as enhance the carbon diffusion.⁹⁰ Furthermore, in another study which employed bimetallic catalysts of Fe-M (M=Pd, Mo, Ni) it was reported that the bimetallic catalysts lowered the decomposition temperature of the carbon source, methane. Overall, a high conversion rate of methane into pure hydrogen and high MWCNT production was achieved.¹¹³ In another report from Wang and co-workers, same concentrations and thickness of Ni and FeNi nanoparticles were used for synthesis.⁹⁰ It was observed that Ni films produced carbon nanofibers whilst FeNi films produced MWCNTs. This observation led to a conclusion that the activity of the pure Ni catalyst is lower than that of the alloy. Halonen *et al.* studied the catalytic activity of Co, Ni and Fe for low temperature growth of MWCNTs.¹¹⁴ They reported that growth occurred at 400 °C using a

bimetallic CoFe and at 500 °C when using a single metal catalyst. However, for efficient catalysis during synthesis of CNTs, use of a good carbon source enhances the metal catalytic activity.

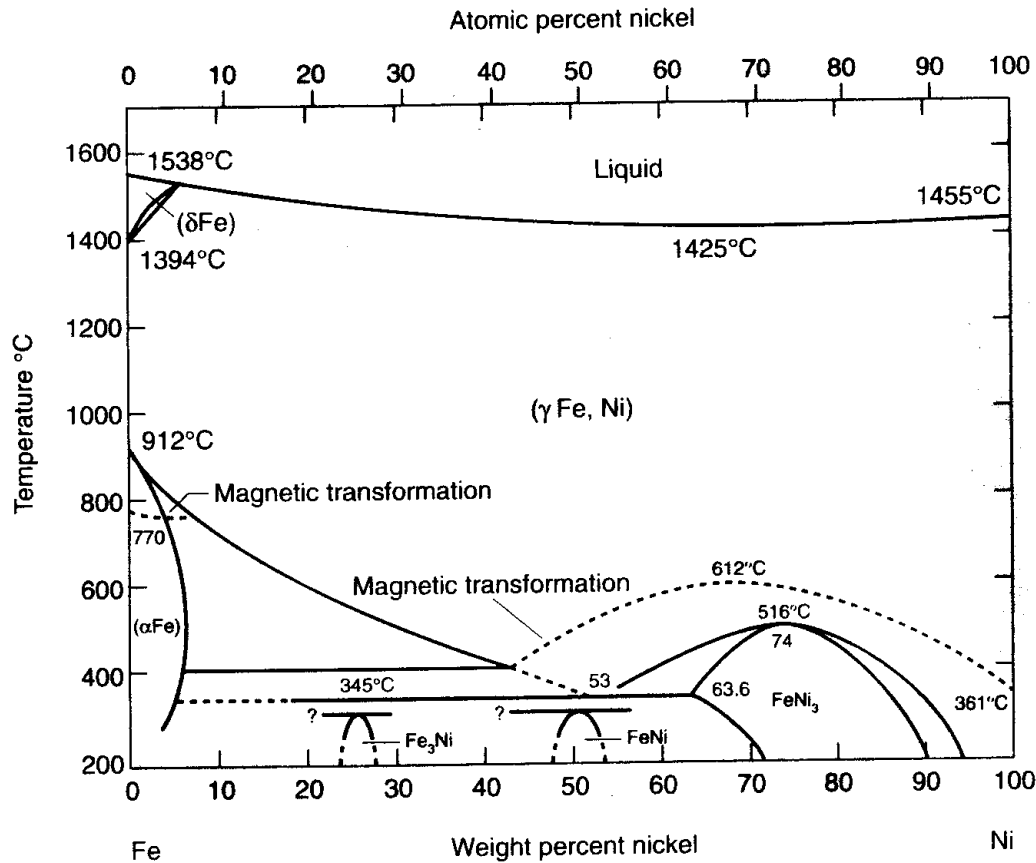


Figure 2.9: FeNi phase diagram¹¹²

2.4.2 Carbon sources

In the synthesis of CNTs, the CNTs grow from a carbon source. The carbon source can be any chemical source that contains carbon. The chemical source can either be a lighter (methane, ethylene, acetylene) or heavy (benzene, toluene, and xylene) hydrocarbon. Each synthetic method (e.g. thermal CVD or PECVD) show some preference on the type of the hydrocarbon feedstock used.¹¹⁵ For instance, in thermal CVD, cyclic aromatic hydrocarbons (toluene, benzene) are used due to their high decomposition temperatures. Whilst in PECVD, methane and other low molecular weight carbon feedstock are preferred. The hydrocarbon source should be supplied in excess of the catalyst in such a way that the ratio of the carbon to the catalyst becomes greater, to prevent the high levels of contamination from metal impurities.⁵⁸ The molecular structure of the carbon

precursors has a detrimental effect on the overall morphology of the CNTs grown. For instance, when the carbon source contains nitrogen or boron the resulting CNTs are bamboo shaped due to the incorporation of the heteroatoms into the CNT backbone.¹¹⁶ When considering the carbon precursors, a careful selection is required with much attention to the vapour pressure and the intended type of CNTs (MWCNTs or SWCNTs) to be produced. Overall, this will assist in the production of quality CNTs. Considering CVD, aromatic hydrocarbons, xylene, toluene, benzene, naphthalene are the mainly carbon precursors in use along with ferrocene.¹¹⁷ This selection is due to the similarity in chemical structures and the fact that ferrocene is soluble in most of these aromatic hydrocarbons.¹¹⁸ However, when considering PECVD, much preference is given to the lighter hydrocarbon sources such as, acetonitrile, ethylene, acetylene, and alkanes.¹¹⁹⁻¹²¹ This choice is because the heavier hydrocarbons tend to deposit in the low temperature zone of the reactor wall. The lighter hydrocarbons tend to decompose into atomic carbons, linear dimmers/trimmers of carbon upon exposure to heat to produce straight and hollow CNTs. The CVD of lighter hydrocarbon gases turns out to be prominent because of its comparative simplicity, ease of control and low cost.^{82,122,123} **Table 2.3** shows the commonly used carbon precursors for the CNT synthesis.

Table 2.3: Various common carbon sources used in plasma design synthesis of CNTs

| Plasma source | Precursor | Gas ratio | Ref |
|---------------|---|------------------------------------|---|
| Helicon | CH ₄ | | Sato <i>et al.</i> ¹²⁴ |
| ICP* | CH ₄ | | Wang <i>et al.</i> ¹²⁵ |
| ICP | CH ₄ /Ar | 16.4 : 14 | Hiramatsu <i>et al.</i> ¹²⁶ |
| TM-MW* | CH ₄ /Ar | 1 : 8 | Wang <i>et al.</i> ¹²⁷ |
| TM-MW | CH ₄ /N ₂ | | Soin <i>et al.</i> ¹²⁸ |
| TM-MW | CH ₄ /N ₂ | | Shang <i>et al.</i> ¹²⁹ |
| TM-MW | C ₂ H ₂ /N ₂ /Ar | 0.5% C ₂ H ₂ | Teii <i>et al.</i> ¹³⁰ |
| ICP | CH ₄ /H ₂ | 2 : 3 | Zhu <i>et al.</i> ¹³¹ |
| TM-MW | CH ₄ /H ₂ /Ar | 1 : 1 : 20 | Zeng <i>et al.</i> ¹³² |
| DC glow* | CH ₄ /H ₂ | 3–8% CH ₄ | Krivchenko <i>et al.</i> ¹³³ |
| DC glow | CH ₄ /H ₂ | 8 : 92 | Zheng <i>et al.</i> ⁹¹ |
| TM-MW | C ₂ H ₂ /NH ₃ | >1 : 1 | Chuang <i>et al.</i> ¹³⁴ |

*ICP = inductively coupled plasma, TM-MW = transverse magnetic-microwave and DC glow = direct current glow

In some cases the hydrocarbon sources can be used along with diluents to improve CNT quality and yield. For instance, in order to avoid oxidation, an inert atmosphere is employed. Nitrogen, helium and argon are the most extensively used gases to ensure inert atmospheric condition during

synthesis.¹³⁵ These gases are sometimes changed with hydrogen gas to reduce the oxygen content in the reaction environment.¹³¹ The flow rate of the hydrocarbon source is usually maintained below that of the inert atmosphere.¹³⁶ However, in general, the flow rate of the gases determines the rate of formation and has an influence on the length, diameter and type of the carbon nanomaterials formed. Therefore, the choice of the hydrocarbon source forms a key component in the synthesis of CNTs.

2.4.2.1 Liquefied petroleum gas

The liquefied petroleum gas (LPG) is a cheaper fuel which is readily available. LPG contains traces of sulphur in concentrations of hundreds ppm. Despite the fact that the gas contain sulphur which may attribute to catalyst poisoning, LPG is much preferred for the synthesis of CNTs.¹¹⁷ Prokudina's study reported the synthesis of agglomerated CNTs from LPG.¹¹⁷ In the study there was no information about the sulphur content that was reported. In another study, 13 ppm of sulphur in LPG was reported. The method involved the use of FeMo bimetallic catalyst supported on Al₂O₃ to synthesise CNTs. The study gave agglomerated CNTs from the decomposition of LPG and there was no information reported on the catalyst poison from sulphur.¹³⁷ The probability of the catalyst poison can be eliminated through hydrodesulphurisation processes in the reactor. Therefore this will eliminate the production of defected CNTs.¹³⁸ Despite causing catalyst poisoning, the presence of sulphur is reported to reduce the diameter of the CNTs thereby improving the conductivity properties.^{117,139}

2.4.2.2 Acetylene

Acetylene has been the most widely used hydrocarbon in the production of CNTs.^{60,120,140,141} Comparing acetylene with other hydrocarbons, under the same reaction temperature, acetylene is more reactive. Quality CNTs are synthesised, this is mainly due to the high chances of preventing carbon nanoshells from forming. These carbon nanoshells are responsible for poisoning catalytic centres hence producing defected tubes.¹⁴¹ Molecular beam experiments have demonstrated that acetylene is the most active growth precursor and the primary growth precursor in both hydrocarbon and alcohol feed stocks.^{120,142,143} Rapid growth of vertically aligned CNTs (VACNTs) was achieved using atmospheric-pressure CVD of C₂H₂ in hydrogen balanced in argon using an Fe catalyst film.¹⁴⁴

2.5 Mechanism of CNT growth using CVD

Several parameters influence the growth of the CNTs. Apart from catalysts and carbon sources (factors discussed in **Section 2.4**), temperature, pressure, nature of diluents (H_2 , Ar or N_2 etc.), substrate and flow rate also influence growth of CNTs. In cases where plasma is used, the nature of the plasma power source, input power and pressure are also considered.¹⁴⁵ Another factor to be considered is the nature of catalyst, how it is deposited and pre-treated, and metal under layer support also referred to as diffusion barrier. Collectively all these species responsible for the growth of CNTs brings about the mechanism of growth.

In preparation for synthesis using PECVD, plasma initiation occurs followed by plasma stabilisation for 30-60 seconds. Once the plasma is stabilised precursors are added. The plasma is responsible for dissociation of any precursors present, and in some cases any carrier gas used. Typically with carbon nanostructures, hydrocarbons are used along with carrier gases such as mixtures of hydrogen and argon, thus, the plasma will result in the ionisation of the hydrocarbon (C_2H_2 , CH_4 and LPG) and the H_2 /Ar to produce reactive radicals.¹⁴⁶ There are various active species produced by the plasma, electrons produce whole molecule radicals ($C_2H_2^+$, CH_4^+) and ions produce smaller molecule radicals (H^+ , C^+ , CH^+ , CH_2^+ and CH_3^+) at relatively low temperatures.⁸⁵ There are intensive ongoing investigations pertaining to the composition of the plasma species. The series of events that occurs thereafter are summarised into five major steps. The flow chart in **Figure 2.10** summarises the five steps of events that occur during the reaction.⁵⁸ It is these steps which then determine the mechanism of the reaction based on the rate determining steps.

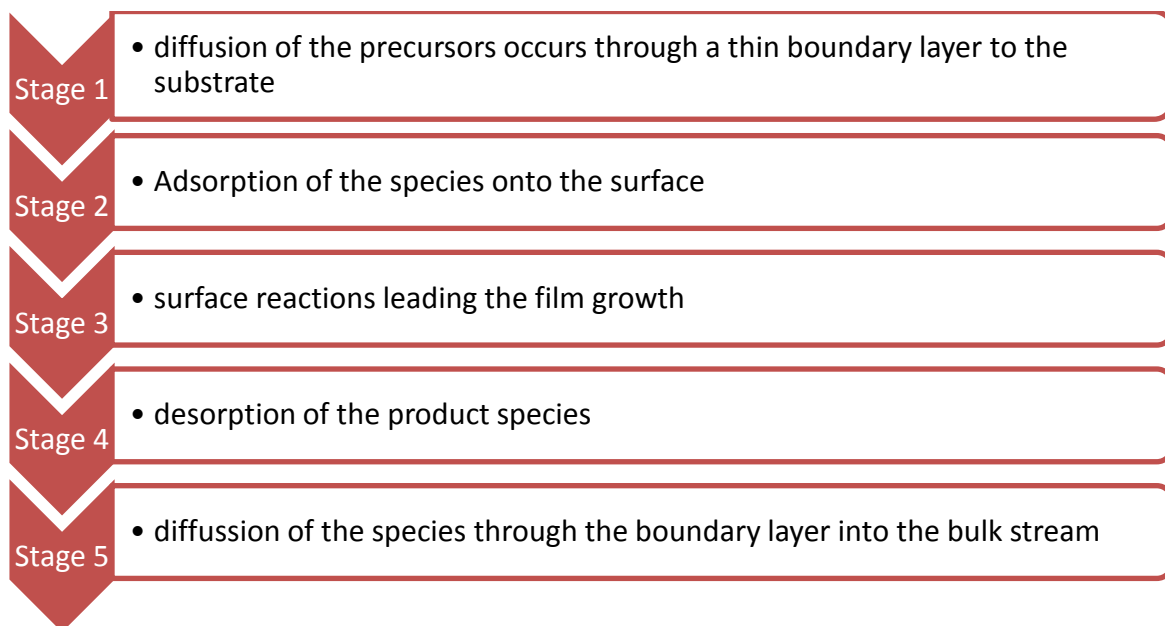


Figure 2.10: Summary of the steps involved during PECVD

There are various substrates which include silicon, glass, polymers or ITO, that are used for plasma synthesis of CNTs. Most of these substrates have low thermal stabilities thus they find use in plasma based reactions. These substrates are either coated with thin films of catalytic nanoparticles or in the case of floating catalysts the substrates are not coated.⁸⁰ The H^+ generated from the dissociation of the precursor is responsible for the surface reduction of the catalyst nanoparticles or metal oxides in cases where catalytic metals had been oxidised. Hence, the diffusion of the precursors occurs through the catalyst thin boundary layer to the nanoparticle surface. The active species becomes adsorbed to the nanoparticle surface where positive ion bombardment of the surface provides energy for the reduction and desorption processes. The reduction process occurs on the surface of the metal catalysts and this enhances the catalyst activity, selectivity and wetting ability. Once a supersaturated state is attained, carbon precipitates in a crystalline cylindrical structure preceding to the growth of a carbon layer. The growth of the cylindrical structure pursues either approach of the two forms likely. Initially, if the particle is adhered intensely to the surface, then the carbon precipitates from the upper surface of the particle. The carbon filament will then continue to grow as the particle is attached to the substrate. This growth model is referred to as the base growth.¹⁴⁷ The other scenario in which the particle is insecurely adhered to the surface, carbon precipitation occurs from underneath the surface of the particle. In this case, the carbon filament persists to grow as it thrusts the particle upwards. This growth model is known as tip growth and here the catalyst particle is noticed at the top end of the carbon filament.^{108,140,148} **Figure 2.11** shows the two growth models.

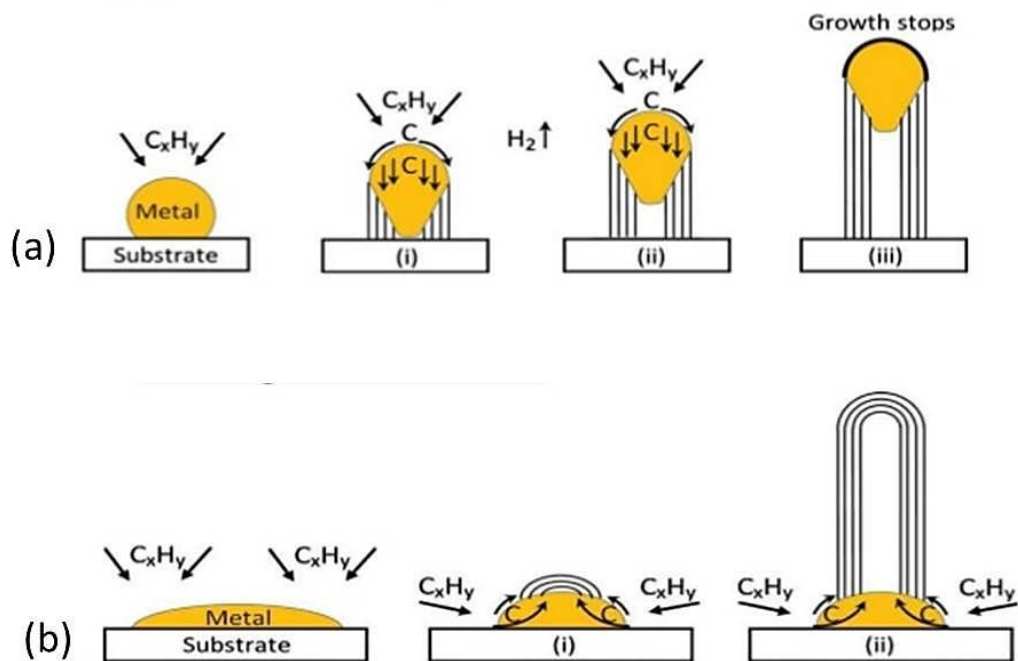


Figure 2.11: Carbon nanotubes growth models (a) tip growth and (b) base growth¹⁰⁸

There are many studies that report the effect of the plasma electric field on the CNTs.^{149,150} These studies show that the CNTs in the PECVD are more vertically aligned in comparison with the CNTs from the thermal CVD.^{84,151}

In a study by Chowalla and co-workers, growth properties of VACNTs were examined against the Ni-catalyst thickness.¹⁵² The method involved use of DCPECVD and they concluded that growth rate, diameter and density of the resulting carbon structures are controlled by the thickness of the catalyst layer. The growth mechanism reported by Wang and Moore using sputtered 8 nm thin films of Ni and NiFe as catalysts on glass substrates with methane as the carbon source produced carbon nanofibers (CNFs) and CNTs respectively. The method used RFPECVD at 140 °C and 180 °C. The growth mechanism was based upon deposition parameters, the structure of the catalyst, flow rate, gas composition, substrate temperature and the plasma power. They concluded that the alloy of NiFe catalyst was more efficient for the catalysis of CNT formation as compared to the Ni catalyst.⁹⁰

Insignificant methane dissociation was signified using mass spectrometry in a thermal CVD reactor employed at a temperature of 900 °C.¹⁵³ Furthermore, replications of the same procedure showed that densities of methyl radical and atomic hydrogen were comparatively negligible. Therefore, this

indicated that the CNT growth solely depended on the hydrocarbon-catalyst interactions when considering thermal CVD. Minute quantities of methyl radicals together with their extraordinary sticking co-efficient are accountable for the observed dangling amorphous carbon on top of the CNTs films and a gradual assembling with time on the reactor tube walls. As opposed to thermal CVD, in PECVD methods that utilise methane, substantial quantities of hydrogen and methyl radicals together with neutrals like C_2H_4 and C_2H_6 forms part of the gas phase composition.⁸⁵ The ultraviolet absorption measurements show that at low atmospheric pressures, around 10^{13} cm^{-3} methane radical densities are detected, and the values escalate in conjunction with pressure as well as input power. While methane prolongs as the chief carbon-generating species in the reaction chamber following decomposition, its mole fraction extremely declines in a blend consisting of H_2/CH_4 . The massive decomposition creates extra carbon-generating species which includes methanimine, hydrogen cyanide and to some point methane on top of the methyl and other radicals bound to emanate. Altogether these species have different catalysis rates on the particle surface in comparison to the hydrocarbon input, overall influencing growth features.¹⁵⁴

In a study conducted by Teo *et al.*, they investigated the importance of plasma heating in the growth of CNT or CNF.¹⁵¹ In their study, they obtained a substrate temperature of $700 \text{ }^\circ\text{C}$ exclusive of any additional outside heating system using a dc discharge. They employed a pressure of 12 mbar and the ratio of $C_2H_2:NH_3$ flow was maintained at 54:200 sccm, coupled with a plasma input power of 200 W. Contrary to this, a combination of plasma and an outside heater, tungsten, under the substrate podium involved only 66 W to achieve an equivalent substrate temperature. Confirmation of the temperature measurements and probable low temperature growth mechanism were presented by Hoffman *et al.*⁹⁴ They used nickel catalyst to investigate the dependence of temperature on the growth rate and structure of the as grown CNTs. Their group managed to synthesise MWCNTs at a temperature of $120 \text{ }^\circ\text{C}$ using dc- discharge consisting $C_2H_2:NH_3$ at a pressure of 1.5 mbar. They used a cathode voltage of 600 V coupled with 30 mA current flow for an 18 W plasma power supply. A thermocouple was used to assess the temperature of the wafer and template markers.

CNTs growth using low temperature requires a mechanism which is discrete from the established rationalization regularly attained resulting from primary works regarding carbon fibres.^{140,155} In accordance to the primary growth models, diffusion of the carbon across the catalyst particles in their molten states signifies the rate controlling phase.^{154,156} The process is usually sustained by the resemblance of the activation energy for growth by thermal CVD and the volume diffusion of carbon.

At low temperatures, 120 °C and room temperature, the mechanism does not apply. Lower temperature ranges may not be sufficient for melting the catalytic particles. The evidence was observed in Ni bunches that stayed concrete under low temperatures.¹⁵⁷ A 0.23 eV activation energy for MWCNTs using PECVD is in essence nearer to 0.3 eV for the surface diffusion of carbon atoms on polycrystalline nickel.^{94,158} This led to the conclusion that the activation energy required for the growth was lower than the one from thermal CVD. This in turn shows that growth occurs by surface reactions of the carbon on the catalyst involved and this is postulated to be the rate determining stage in PECVD operating under low temperature for CNT growth.⁹⁴ Previous studies on CNT production using PECVD have been mainly focused on growth of CNTs, mechanisms, properties in relation to catalysts and not much has been done on the how to control the density and space of vertically aligned CNTs, which then drives the motivation for this study. Once the CNTs are grown they need to be characterised so as to ascertain their structures in relation to their functions and application.¹⁵⁹

2.6 Organic solar cells

CNTs have been reported to be useful in the development of low cost renewable energy sources such as in solar cells. There are several types of solar cells which include dye sensitised solar cells (DSSCs), hybrid solar cells and organic solar cells (OSC). OSC utilise solar energy via the photovoltaic effect which converts light directly to electrical energy using portable packages. Amongst other advantages, solar cells possess low weight, flexible and semi-transparent properties and are associated with low environmental impact. However, OSC are associated with low efficiencies especially when compared to silicon based solar cells. The silicon based solar cells have efficiencies between 10-28%.^{160,161} whilst OSC have efficiencies between 5-11%.^{161,162} These low efficiencies are attributed to low material stability and poor strength which in turn is responsible for the easy degradation of OSC with time. These factors (mechanical, environmental stability and efficiencies) are the major challenges that hinder the widespread use of OSC when compared with inorganic solar cells.³⁴ Hence, it is imperative to look at the morphology and structural composition of the OSC.

OSC consist of organic materials which act as electron donor and acceptor material (**Figure 2.12**). These organic materials have the ability to transport electric current and absorb light in the ultra violet-visible region of the solar spectrum. This is attributed to; the nature of the carbon hybridisation (sp^2 hybridisation) and the strong absorption co-efficiencies of the organic semi-

conductors. However, the organic semi-conductors have high band gap and relatively small diffusion length for photo-generated excitons. During solar energy conversion process, a strong electric field is required to dissociate the photo-generated excitons into free charge carriers. However, the photon induced generated excitons have high binding energies which are likely to favour recombination. Therefore, these organic material components need to have high stabilities, good film morphologies and large hole/electron mobility in order to maximise charge transport.¹⁶³ Hence, this presents the need to thoroughly look at the fabrication of the OSC and, where necessary revise the components of the key active layers that absorbs and release electrons amongst other things.

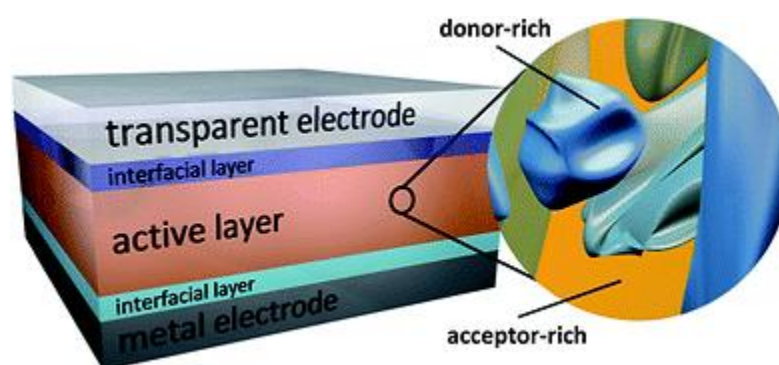


Figure 2.12: Illustration of the structure of an organic solar cell¹⁶³

The OSC have been reported to have different device designs which include bulk heterojunction, bilayer and single layer.

2.6.1 Types of organic solar cells

The range of OSC design has improved from Single layer to Bilayer, which was then followed by the introduction of bulk and graded heterojunction organic photovoltaic cells. The first generation of OSC was formed based on single organic layers sandwiched between two metal electrodes of different work function. The devices showed good rectification, which was attributed to the electron and hole injection to π^* and π orbitals respectively. These devices displayed very low power conversion efficiencies, less than 0.1%. In an effort to improve the efficiencies, the single layer was then replaced with bilayer. In this device, two organic layers with specific(n- and p-type) electron/hole transporting properties were sandwiched between electrodes.¹⁶³ The interface between the p- and n-type organic semiconductors creates an additional exciton dissociation sites

for the generation of free charges. As the need to improve the power conversion efficiencies kept on growing, a three layer p-i-n device was developed. The device consisted of a co-deposited interlayer between the p-type, hole conducting, and the n-type, electron conducting, layers. The incorporation of the fullerene to the conjugated polymers made a significant change in the efficiencies. It was observed that when the conjugated polymers were optically excited, there was a pronounced photo induction electron transfer to the fullerene molecules. This highly increased the photo conductivity. The observation led to the development of the polymer-fullerene bilayer heterojunction and the bulk heterojunction devices. These devices incorporated the fullerene and fullerene derivatives. Since then, there was a significantly improvement of the performance of the OSC.¹⁶⁰ Amongst these materials CNTs are incorporated. The CNTs have been explored for applications where low sheet resistance and high optical transparency in the visible and infrared spectral range are essential.¹⁶⁰ A layer of CNTs has been used as anode material either mixed with a polymer or alone. This has since improved the performance of the OSC. However, the introduction of the CNTs resulted in different characteristic properties associated with the synthesised tubes. As a result, it is important to look at the techniques available to characterise properties of the synthesised CNTs.

2.7 Characterisation techniques

Metal catalyst particles show differences in their size distribution, elemental composition, organic matter coating and morphology, therefore, thorough characterisation to determine the specific properties associated with each catalyst is required. On the other hand the CNTs have unique properties (morphology, optical and electronic properties) which distinguish them from any other carbon containing material. Therefore, in order to investigate the structural and morphological characterisation, there are several techniques used. These techniques include scanning electron microscopy (SEM), energy dispersive X-ray spectroscopy (EDX), transmission electron microscopy (TEM), X-Ray diffraction (XRD), Fourier transform infra-red (FTIR), thermogravimetric analysis (TGA), and Raman spectroscopy.

2.7.1 Scanning electron microscopy

Electron microscopes were developed due to limitations of light microscopes which are limited by the light of physics. Knoll invented the SEM in the 1930s and there have been further technological

improvements to date.¹⁶⁴ SEM is the most widely used analysis technique for nanomaterials. SEM provides information about the sample topography (texture), morphology (particle shape and size), composition (elements and compounds amount) and crystallographic information (arrangement of atoms). Three-dimensional sample images are produced. SEM produces three-dimensional sample images. The technique utilises a focussed beam of high-energy electrons, produced by a source into a probe, to scan across the surface of a sample in a raster scan pattern.¹⁶⁵ The electrons interact with the atoms at the surface of the sample. The accelerated electrons have high kinetic energy which they tend to lose during deceleration. This energy dissipation is observed as various emission signals (secondary electrons, photons, back-scattered electrons, continuum X-rays, diffracted back scattered electrons and visible light). The signals are captured, detected and passed to the display. Secondary electrons are responsible for the morphological/topological contrast while backscattered electrons are responsible for compositional (distribution of different elements in sample).¹⁶⁶ **Figure 2.13** shows the components of the SEM responsible for analysis.

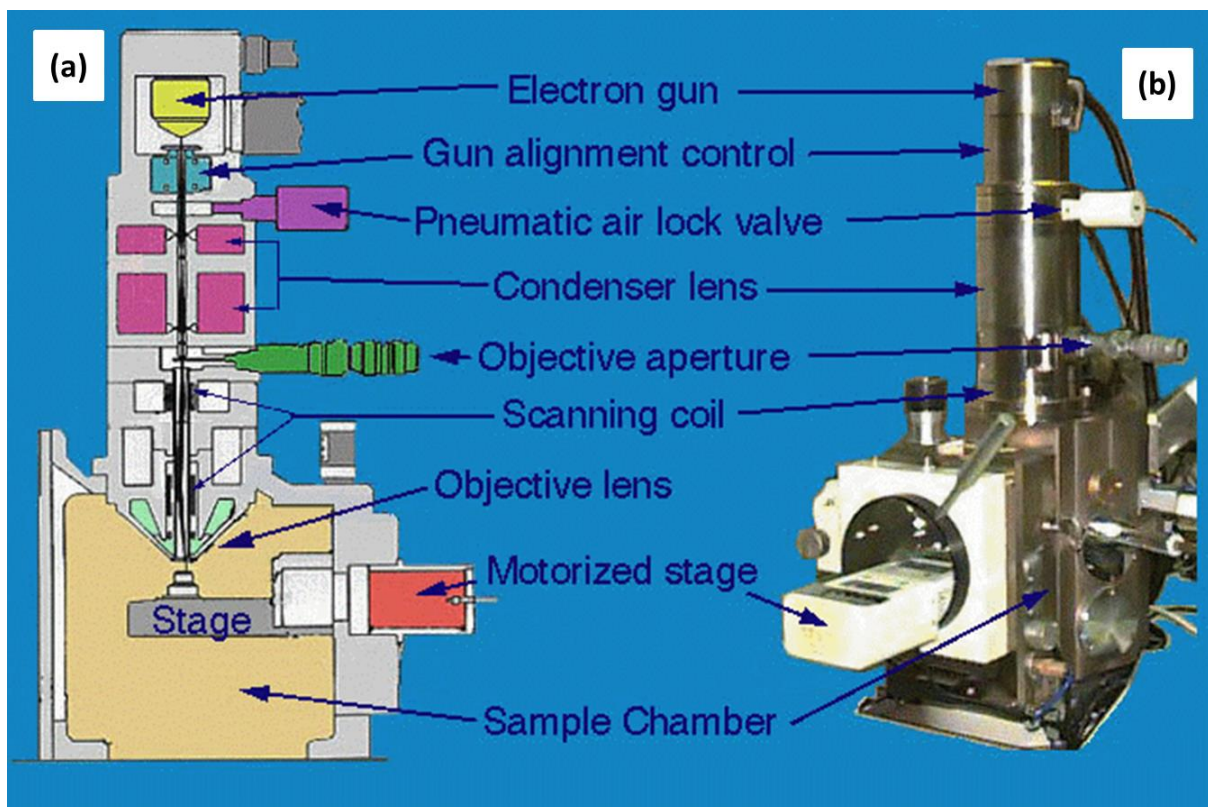


Figure 2.13: SEM column (a) schematic presentation and (b) actual picture of the instrument¹⁶⁶

In order to analyse a sample, an electron gun is responsible for the discharge of monochromatic electrons. The electron beam is concentrated by the first condenser lens, such that it forms the

beam, regulates the quantity of current, and eliminate the high angle electrons from the beam with the assistance of the condenser aperture. The electrons are moulded into a narrow, compact consistent beam using the second condenser lens. Additional eradication of the elevated angle electrons from the beam is achievable through an objective aperture. A collection of coils is employed to peruse the ray in a grid style residing on specified points for a time phase influenced by the scan velocity. The objective lens focuses the perusing beam on top of the sample desired. Once the beam hits the sample, interactions occur inside the sample and numerous electrons are detected. Identified signal comprises data concerning the sample under examination.¹⁶⁶

There are several types of SEM which include conventional, variable pressure and field emission SEMs. Field emission SEM has an intense electron source, small beam volume, escalates the effective magnification range for surveillance (imaging up to 500,000X) and can perform high resolution imaging with very low accelerating voltages. When attached to EDX, X-ray radiation can be detected.¹⁶⁷ Sample preparation depends with the material type since SEM can analyse a wide range of materials (geological specimens, biological specimens, metals etc.). CNT sample preparation involves mounting the sample on metallic stubs using double-sticky carbon tape and placing the stub on the sample holder ready for analysis.

2.7.2 Transmission electron microscopy

Gommes and co-workers developed the TEM method in order to characterize MWCNTs.¹⁶⁸ Further morphological analysis is provided by TEM. The quality of the sample in terms of crystal structure, defects, and crystal phases is provided.¹⁶⁹ The existence of amorphous material in and around the structures is also part of the data generated. When considering the CNTs, the length, diameter, the number of walls and the nature of the tube end, is part of the sample information obtained. TEM characterise the microstructure of materials with very high spatial resolution. A high electron beam is transmitted through a very thin sample to image and analyse the microstructure of the materials with an atomic scale resolution.¹⁷⁰ **Figure 2.14** shows the basic inner column operation for TEM.

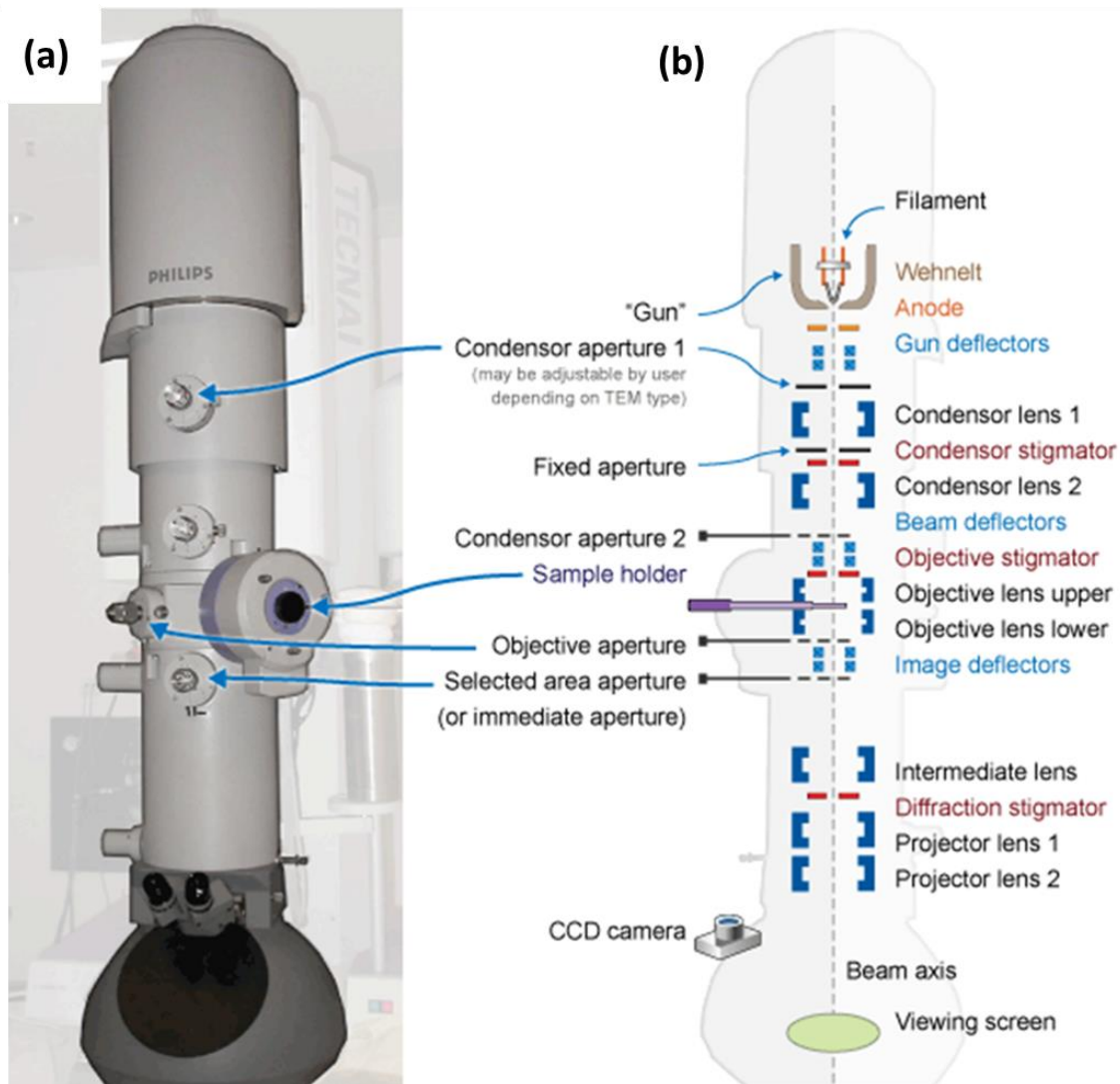


Figure 2.14: TEM column (a) actual picture and (b) schematic presentation of the instrument¹⁷⁰

In TEM, the electron gun generates an electron beam. The electron beam is permitted into an ultra-thin sample, interacting with the sample along the way. The size and intensity of the beam are controlled. An image is formed from the interaction of the electrons and the sample. The image is magnified in the objective lens and focussed onto imaging device or detected by a sensor such as CCD camera. In this technique, the side with nanoparticles should be facing down in the sample holder and high resolution images are possible due to the small de Broglie electron wavelength. The operating principle is the same as for SEM, where an electron beam is produced from the virtual source, passes through the first condenser lens, second condenser lens then aperture of the sample and to the projector lens. When under high resolution (HR-TEM), intershell spacing can be observed. Intershell spacing varies the CNT diameter but, ranges from 0.34-0.39 nm.¹⁷¹ When comparing with graphite interplanar distance (0.336 nm) the values are greater and this can be attributed to the

curvature of the graphene sheets modified by the tube radius. The information provided on fringe spacing (d-spacing) should correspond to the data on the XRD.¹⁷²

2.7.3 X-Ray diffraction

This technique applies to any sample that is polycrystalline. The technique is not sample destructive, it is used to obtain information on the interlayer spacing, the structural strain and impurities. Diameters and chirality distributions are also observed as well as various number of layers for MWCNTs. However, CNTs possess numerous alignments contrasted to the X-ray incident beam. Thus in turn leading to a numerical description of CNTs.¹⁷³ X-rays focussed on a sample secured on the axis of the sample holder are diffracted by the sample. Alterations in the diffracted X-ray intensities are measured, recorded and plotted against the rotation angles of the sample. A computer examination of the peak locations and intensities related with this pattern permits qualitative analysis, lattice constant or stress determination of the sample. The peak angles and outlines can be utilised to ascertain particle diameters and extent of crystallinity.¹⁷²

2.7.4 Raman spectroscopy

Raman spectroscopy is a structural characterisation technique, which is suitable for the analysis of all allotropes of carbon (fullerenes, carbon nanotubes, amorphous carbon, polycrystalline carbon etc.), insensitive to the chemical composition of the carbon allotropes. The technique is highly sensitive to chemical bond lengths, strengths and arrangements. Raman spectroscopy provides not only unique vibrational and crystallographic information, but also unique information about physical properties that are relevant to electrons and phonons.^{172,174} The technique utilises inelastic scattering of the monochromatic light, normally from a laser source (**Figure 2.15**). Photons are irradiated on molecules, and become absorbed. The frequencies of the photons found in the monochromatic light change to high-energy states upon interaction with the molecules. The molecule then absorbs and re-emits the laser light. The Raman effect is then seen when the frequency of the re-emitted photons is shifted up/down in comparison with the original monochromatic frequency (**Figure 2.15**).¹⁷²

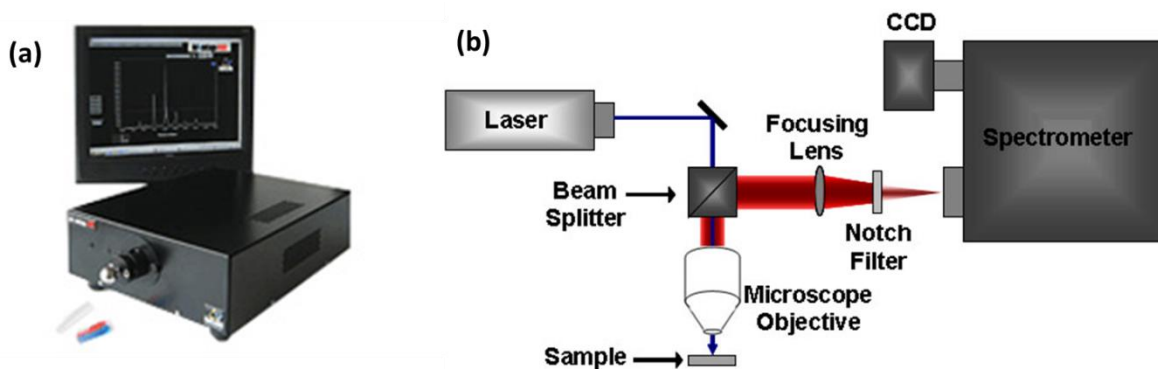


Figure 2.15: Raman (a) spectroscopy instrument and (b) basic components for analysis¹⁷²

Since all allotropic configurations of carbon are active, the type of the carbon determines the location, breadth and relative intensity of the bands.¹⁷⁵ The greatest characteristic of CNT topographies are summarized in **Figure 2.16**. These include; (i) A low-frequency peak around 200 cm^{-1} . This can also be observed as a bunch of peaks for polydisperse samples when resonating conditions are met. This peak, radial breathing mode (RBM), is characteristic of the SWCNT diameter assigned to an A_{1g} “breathing” mode of the tubes; (ii) A large structure (1350 cm^{-1}) assigned to residual disordered graphite (D-band). This is attributed to disordered defects or ion interaction between graphitic walls; (iii) A high-frequency peak usually located around the middle of 1500 and 1600 cm^{-1} known as the graphitic band (G-band). The G-band is distinctive of CNTs, corresponding to a splitting of the E_{2g} stretching mode of graphite; (iv) A second order noticed mode between 2450 and 2650 cm^{-1} assigned to the first overtone of the D mode frequently entitled G'' mode; (v) A combination mode of the D and G modes between 2775 and 2950 cm^{-1} .¹⁷⁶

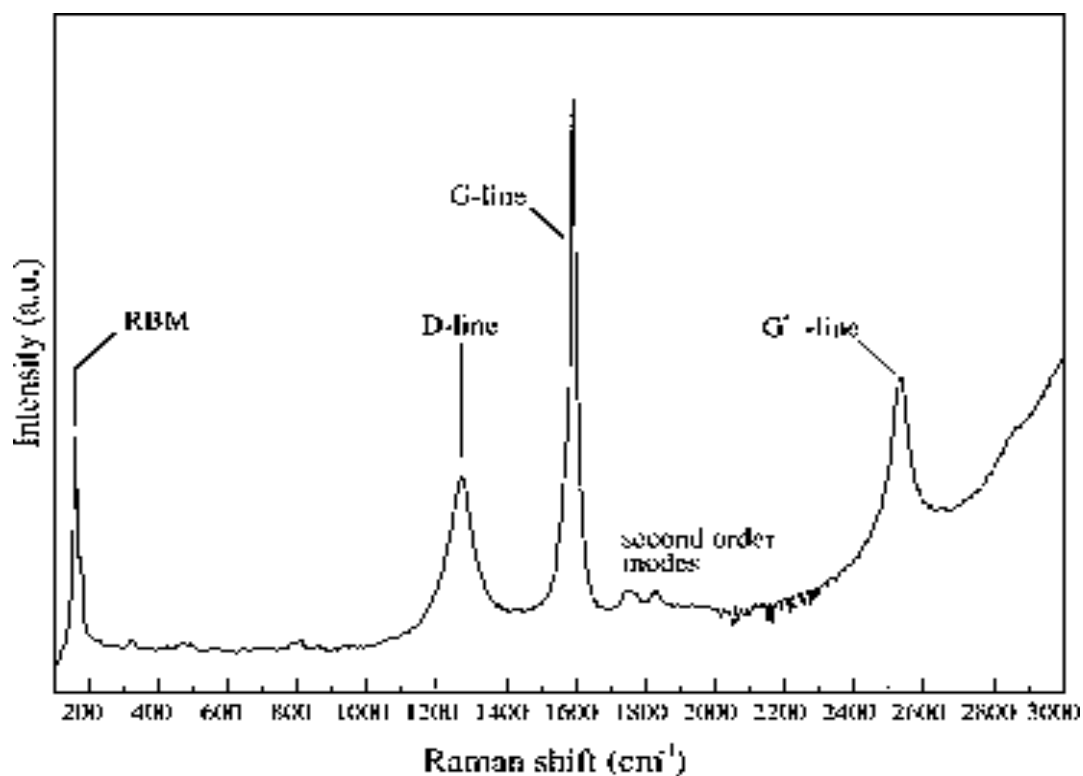


Figure 2.16: A typical Raman spectra indicating MWCNT characteristic bands¹⁷⁶

In MWCNTs the ratio of the D-band to the G-band (I_D/I_G) is used to estimate defect content and inter-defect distance. The ratio indicates the overall graphitic nature of the MWCNTs i.e. provide a measure of how the MWCNT carbon bond structure would deviate from the ideal sp^2 hybridised structure of graphite. In smaller diameter MWCNTs where sp^2 to sp^3 ratio is high, R is higher than the expected. Therefore the R ratio of I_D/I_G increases due to an increase in curvature as the diameter becomes smaller and defect sites increase.¹⁷⁶

2.7.5 Fourier transform infrared spectroscopy

Infrared (IR) radiation lies between the visible and microwave portions of the electromagnetic spectrum. This is because IR waves have wavelengths longer than visible and shorter than microwaves, and have frequencies which are lower than visible and higher than microwaves. The primary source of IR radiation is thermal radiation which is produced by the motion of atoms and molecules in an object. The FTIR technique provides information on the molecular structure of all types of samples i.e. solids, liquids or gas. Basically, an absorption measurement of different IR frequencies by a sample positioned in the path of an IR beam is provided. The main goal is the

identification of the presence of certain chemical functional groups in the sample.¹⁷⁷ In this technique, the IR radiation is passed through a sample and it initiates the excitation of the vibrations of the covalent bonds within the molecules of the sample. The vibrations are the stretching or the bending modes. The sample contains different functional groups and these groups absorb different IR frequencies.¹⁷² Some of the IR radiation is absorbed by the sample and some is transmitted. The resulting spectrum represents the molecular absorption and transmission, creating a molecular fingerprint of the sample. FTIR spectroscopy is preferred over dispersive or filter methods of IR spectral analysis because it is a non-destructive technique which provides a precise measurement method which requires no external calibration amongst several advantages. FTIR can be used to determine the quality or consistency of a sample, and the amount of components in a mixture. **Figure 2.17** shows the FTIR instrument and a block diagram summarising the steps involved.

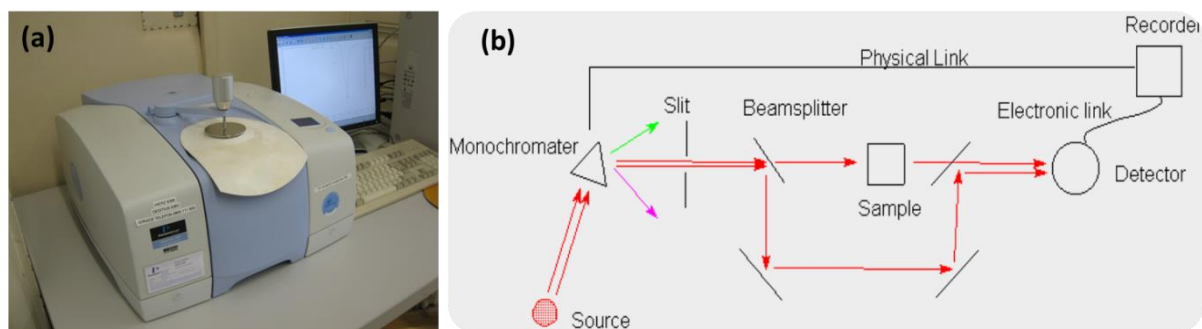


Figure 2.17: FTIR (a) picture of the instrument and (b) block diagram for steps involved in analysis¹⁷⁷

The source radiates IR from a radiant black-body supply. The IR beam navigates past an aperture. The aperture regulates the quantity of energy posed to the sample and finally to the detector. The beam goes in the interferometer where spectral encryption transpires. There after the subsequent interferogram signal departs the interferometer. The beam then penetrates the sample compartment where it is transmitted past or reflected off the surface of the sample, varying on the nature of examination transpiring. This is where precise frequencies of energy, which are exceptionally distinctive of the sample, are absorbed. Eventually the beam elapses to the detector for ultimate quantification. Custom made detectors are employed to quantify the distinct interferogram signal. Quantified signal is recorded and transmitted to the computer upon which Fourier transformation occurs. The ultimate IR spectrum is subsequently displayed to the operator for elucidation and any additional data manipulation.¹⁷⁸

2.7.6 Thermogravimetric analysis

TGA provides information of the thermal stability of the sample. In TGA, empty aluminium or platinum pans are used as sample holders. One empty pan is used as the reference material while the other pan is for the sample to be analysed. The sample is heated in either reducing or oxidising conditions (air, N₂, CO₂, He, Ar, etc.) at a controlled rate. The temperature is increased at a constant rate for a known initial weight of the substance and the changes in weights are recorded as a function of temperature at different time interval.¹⁷⁹ The mass of the sample is plotted against the temperature or time accordingly to demonstrate thermal variations in the material. This includes loss of solvent and plasticizers in polymers, water of hydration in inorganic materials and the disintegration of the material.¹²³ The graph of change in mass against temperature is referred to as thermogravimetric curve (TG) or thermogram. TG curves of pure substances provide a fingerprint of that substance, it helps to determine the extent of purity of samples and the mode of their transformations within specified range of temperatures.¹⁸⁰ In a typical TG curve, thermal stability is deduced from the oxidation temperatures of a sample. In CNTs, the oxidation temperature is a result of carbon-carbon bond-length, curvature and strains. **Figure 2.18** shows a block diagram for the TGA instrument.

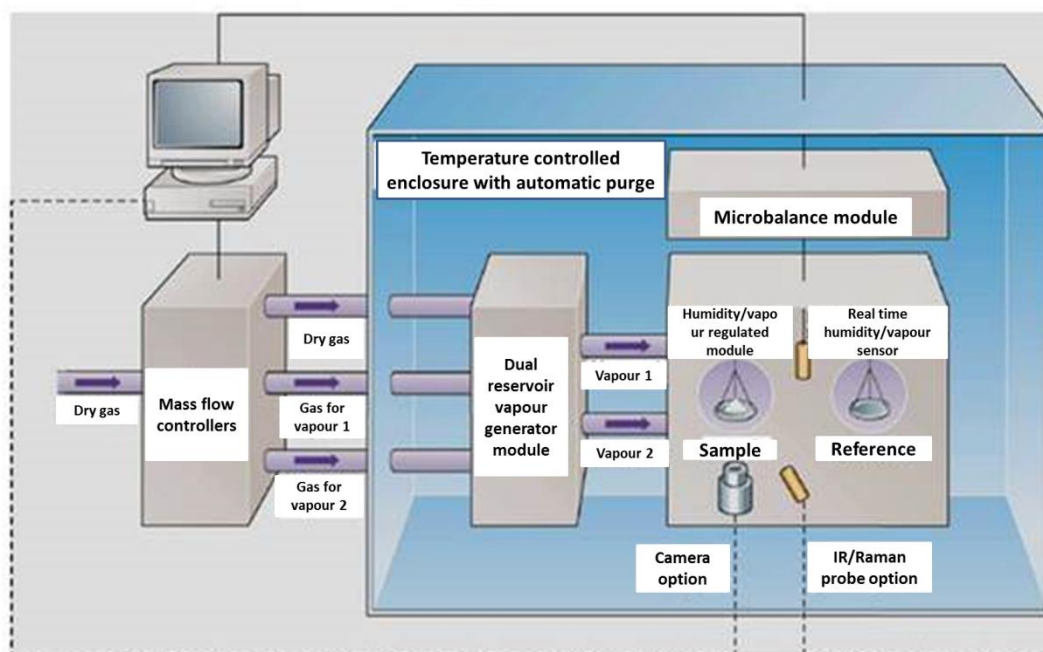


Figure 2.18: A schematic diagram for the TGA instrument for analysis¹⁸⁰

Basically, a known sample weight (ideally small weight) is taken in a crucible to a furnace controlled thermobalance which is enclosed by a furnace. The furnace temperature is raised slowly so that the temperature gives linearity with time. A platinum/platinum-rhodium thermocouple is used to monitor the sample temperature. The changes in weight are recorded from the beam deflection.

2.8 Application and growth on substrates

CNTs have persuaded vast awareness as thermal controlling materials for microelectronic wrapping, electrode constituents for application in energy storage cells and supercapacitors, field emission (FE) electron reserves for application in flat panel displays, e-beam lithography equipment, X-ray supplies, and vacuum microwave amplifiers. This is attributed to the extraordinary aspect proportion, minute apex area, satisfactory chemical consistency, low co-efficient of thermal expansion, distinguished thermal and electrical conductivity, and excellent mechanical strength.¹⁸¹

In an effort to acquire improved electrical properties of the aligned CNT arrays in such purposes, it is essential to produce CNT forests directly onto conductive substrates like metals or amalgams.¹⁸² Direct growth technique of CNTs on metal substrate mainly reduces the contact resistance and forms an ohmic assembly between CNTs and metal substrate, which is vital for electronic devices.^{89,183} Miller *et al.* reported growth of MWCNTs directly on ITO glass coated substrate using the CVD as considerable area semi-transparent electrodes for OSC applications.¹⁸⁴ They concluded that the rate of CNT growth on ITO is considerably decreased as contrasted to that of silicon dioxide and glass substrates, which enables an extreme extent of control over CNT height. They demonstrated the effective capacity of the nanostructured semi-transparent substrate as an interpenetrating hole-removing electrode in bulk-heterojunction OSC. They also concluded that the limpidity of the electrode is maximum at elongated wavelengths, rendering it appropriate to the solar spectrum.

In an effort to improve the electrical performance of ITO coated glass, a controlled layer of MWCNTs was directly deposited on top of the ITO film. The coated ITO was applied as anodes for OSC based on poly-3-hexylthiophene (P3HT) and phenyl-C61-butyric acid methyl ester (PCBM). The MWCNT-developed electrodes were reported to increase the charge-carrier extension from the photoactive composite. This was attributed to the extra percolation paths offered by the CNTs.¹⁸⁵ The work function of the as-adjusted ITO surfaces was measured by the Kelvin probe technique to be 4.95 eV.

Thus ensuing enhanced equivalent to the HOMO level of the P3HT. This is in turn anticipated to intensify the hole transport and collection at the anode. Therefore, it substantially raises the charge/discharge rate and open-circuit voltage especially in the test cells constructed using MWCNT-based electrodes.^{56,186} In another study, Pasquier and co-workers, described implementation of SWCNT thin layers as transparent and conducting electrodes for hole collection in P3HT: PCBM organic photovoltaics.¹⁸⁷ They reported a power conversion efficiency of 1%, with a fill factor of 0.3 and a short-circuit current of 6.5 mA/cm² under 100 mW/cm² polychromatic white light illumination measured in air.

2.9 Summary and conclusions

Renewable energy sources are the way to go for sustainable energy. Solar energy is amongst the promising renewable energy sources. Solar PV systems, particularly OSC, are considered to be a reliable method for harnessing the energy from the sun in low cost light packages. Nanotechnology has opened up new pathways for improvements in OSC fabrication so as to enhance the power conversion efficiencies. MWCNTs are amongst the promising materials in the OSC fabrication. The incorporation of MWCNTs in bulk heterojunction OSC is a promising way to improve the life cycle and strength of the OSC. Synthesis of MWCNTs by CVD methods produces high purity and high yield products. However, PECVD produces well aligned MWCNTs at low temperatures. The low temperatures favor the direct deposition on ITO substrate without destroying the substrate properties. Synthesis of the MWCNTs requires efficient metal catalysts (Fe, Co and Ni) and low hydrocarbon feedstock (LPG and acetylene) amongst other controllable factors such as temperature and gas flow rate. Various physical and chemical properties of the synthesized metal catalysts and MWCNTs are characterized using techniques that provide information from the nanoscale level. These include SEM, TEM, FTIR and Raman spectroscopy. The unique properties of each nanomaterial are responsible for the characteristic information obtained from each instrumental technique.

References

- (1) *The American Heritage® Science Dictionary* Published by Houghton Mifflin **2002**.
- (2) Vesborg, P. C. K.; Jaramillo, T. F. Addressing the terawatt challenge: scalability in the supply of chemical elements for renewable energy. *Royal Society of Chemistry Advances* **2012**, *2*, 7933.
- (3) Jacobson, M. Z.; Delucchi, M. A. Providing all global energy with wind, water, and solar power, Part I: Technologies, energy resources, quantities and areas of infrastructure, and materials. *Energy Policy* **2011**, *39*, 1154-1169.
- (4) Lewis, N. S.; Nocera, D. G. Powering the planet: Chemical challenges in solar energy utilization. *Proceedings of the National Academy of Sciences* **2006**, *103*, 15729-15735.
- (5) Administration, U. S. E. I. *International Energy Outlook 2013*, released 25 July **2013**.
- (6) Barnwal, B. K.; Sharma, M. P. Prospects of biodiesel production from vegetable oils in India. *Renewable and Sustainable Energy Reviews* **2005**, *9*, 363-378.
- (7) Demirbas, A.; Sahin, D. A.; Hilal, D. A. Global energy sources, energy usage, and future developments. *Energy Sources* **2004**, *26*, 191-204.
- (8) Dincer, I. Environmental issues: I-energy utilization. *Energy Sources* **2001**, *23*, 69-81.
- (9) Balat, M. Energy and greenhouse gas emissions: A global perspective. *Energy Sources, Part B* **2006**, *1*, 157-170.
- (10) Kaygusuz, K. Energy and environmental issues relating to greenhouse gas emissions for sustainable development in Turkey. *Renewable and Sustainable Energy Reviews* **2009**, *13*, 253-270.
- (11) Mann, M. E.; Bradley, R. S.; Hughes, M. K. Global-scale temperature patterns and climate forcing over the past six centuries. *Nature* **1998**, *392*, 779-787.
- (12) Perez, R.; Perez, M. A-fundamental-look-at the-planetary-energy-reserves. *IEA/SHC Solar update* **2009**, 1-3.
- (13) Malik, M.; Dincer, I.; Rosen, M. A. Development and analysis of a new renewable energy-based multi-generation system. *Energy* **2015**, *79*, 90-99.
- (14) Onar, O. C.; Khaligh, A.: Chapter 2 - Energy Sources. *Alternative Energy in Power Electronics. Butterworth-Heinemann: Boston* **2015**; 81-154.

- (15) Asif, M.; Muneer, T. Energy supply, its demand and security issues for developed and emerging economies. *Renewable and Sustainable Energy Reviews* **2007**, *11*, 1388-1413.
- (16) Kishor, N.; Saini, R.; Singh, S. A review on hydropower plant models and control. *Renewable and Sustainable Energy Reviews* **2007**, *11*, 776-796.
- (17) Cheong, I. P.A.; Johari, M.; Said, H.; Treagust, D. F. What do you know about alternative energy? Development and use of a diagnostic instrument for upper secondary school science. *International Journal of Science Education* **2015**, *37*, 210-236.
- (18) Jacobson, M. Z.; Delucchi, M. A. A path to sustainable energy by 2030. *Scientific American* **2009**, *301*, 58-65.
- (19) DiPippo, R. *Geothermal power plants: principles, applications, case studies and environmental impact*. Butterworth-Heinemann, **2012**.
- (20) Saar, M. O. Review: Geothermal heat as a tracer of large-scale groundwater flow and as a means to determine permeability fields. *Hydrogeology Journal* **2011**, *19*, 31-52.
- (21) Delucchi, M. A.; Jacobson, M. Z. Providing all global energy with wind, water, and solar power, Part II: Reliability, system and transmission costs, and policies. *Energy Policy* **2011**, *39*, 1170-1190.
- (22) Azad Malik, M.; Revaprasadu, N.; Ramasamy, K. Nanomaterials for solar energy. Nanoscience: Nanostructures through chemistry. *The Royal Society of Chemistry*, **2013**, *1*, 29-59.
- (23) Dresselhaus, M. S.; Thomas, I. L. Alternative energy technologies. *Nature* **2001**, *414*, 332-337.
- (24) Ramsden, J. J. Chapter 1 - What is nanotechnology? *Applied Nanotechnology*. William Andrew Publishing: Oxford, **2014**; *2*, 3-12.
- (25) Yildiz, O.; Bradford, P. D. Aligned carbon nanotube sheet high efficiency particulate air filters. *Carbon* **2013**, *64*, 295-304.
- (26) Garde, K.; Kosaraju, K.; Ravari, S. B.; Aravamudhan, S. Toward Understanding Toxicity of Engineered Nanomaterials. *Nanoscience and Nanoengineering: Advances and Applications* **2014**, 243.
- (27) Li, J.; Xu, Q.; Wei, X.; Hao, Z. Electrogenerated chemiluminescence immunosensor for bacillus thuringiensis Cry1Ac based on Fe₃O₄@Au nanoparticles. *Journal of Agricultural and Food Chemistry* **2013**, *61*, 1435-1440.

- (28) Joseph, T.; Morrison, M. Nanotechnology in agriculture and food: a nanoforum report. *Nanoforum Organisation* **2006**.
- (29) Srilatha, B. Nanotechnology in agriculture. *Journal of Nanomedicine & Nanotechnology* **2011**.
- (30) Malanowski, N.; Heimer, T.; Luther, W.; Werner, M. Growth market nanotechnology: an analysis of technology and innovation. *John Wiley & Sons* **2008**.
- (31) Kokura, S.; Handa, O.; Takagi, T.; Ishikawa, T.; Naito, Y.; Yoshikawa, T. Silver nanoparticles as a safe preservative for use in cosmetics. *Nanomedicine: Nanotechnology, Biology and Medicine* **2010**, *6*, 570-574.
- (32) Ma, C.; Wang, X.; Ma, Y.; Sheng, J.; Li, Y.; Li, S.; Shi, J. Carbon nanofiber/graphene composite paper for flexible supercapacitors with high volumetric capacitance. *Materials Letters* **2015**, *145*, 197-200.
- (33) Chen, W.; Xia, C.; Alshareef, H. N. Graphene based integrated tandem supercapacitors fabricated directly on separators. *Nano Energy* **2015**, *15*, 1-8.
- (34) Rowell, M. W.; Topinka, M. A.; McGehee, M. D.; Prall, H.-J.; Dennler, G.; Sariciftci, N. S.; Hu, L.; Gruner, G. Organic solar cells with carbon nanotube network electrodes. *Applied Physics Letters* **2006**, *88*, 233501-233506.
- (35) Ebbesen, T. W.; Ajayan, P. M. Large-scale synthesis of carbon nanotubes. *Nature* **1992**, *358*, 220-222.
- (36) Longmire, M.; Choyke, P. L.; Kobayashi, H. Clearance properties of nano-sized particles and molecules as imaging agents: considerations and caveats. **2008**.
- (37) Radushkevich, L.; Lukyanovich, V. About the structure of carbon formed by thermal decomposition of carbon monoxide on iron substrate. *Journal of Physics and Chemistry*. **1952**, *26*, 88-95.
- (38) Oberlin, A.; Endo, M.; Koyama, T. High resolution electron microscope observations of graphitized carbon fibers. *Carbon* **1976**, *14*, 133-135.
- (39) Wiles, P. G.; Abrahamson, J. Carbon fibre layers on arc electrodes—I: Their properties and cool-down behaviour. *Carbon* **1978**, *16*, 341-349.
- (40) Kroto, H. W.; Heath, J. R.; O'Brien, S. C.; Curl, R. F.; Smalley, R. E. C 60: buckminsterfullerene. *Nature* **1985**, *318*, 162-163.

- (41) Yadav, B.; Kumar, R. Structure, properties and applications of fullerenes. *International Journal of Nanotechnology and Applications* **2008**, 15-24.
- (42) Meyer, J. C.; Geim, A. K.; Katsnelson, M.; Novoselov, K.; Booth, T.; Roth, S. The structure of suspended graphene sheets. *Nature* **2007**, 446, 60-63.
- (43) Dai, H. Carbon nanotubes: opportunities and challenges. *Surface Science* **2002**, 500, 218-241.
- (44) Aliofkhazraei, M.; Sabour R. A. Synthesis and processing of nanostructured films, and introduction to and comparison with plasma electrolysis. *Fabrication of Nanostructures by Plasma Electrolysis* **2010**, 1-22.
- (45) Kataura, H.; Kumazawa, Y.; Maniwa, Y.; Umezumi, I.; Suzuki, S.; Ohtsuka, Y.; Achiba, Y. Optical properties of single-wall carbon nanotubes. *Synthetic metals* **1999**, 103, 2555-2558.
- (46) Prasek, J.; Drbohlavova, J.; Chomoucka, J.; Hubalek, J.; Jasek, O.; Adam, V.; Kizek, R. Methods for carbon nanotubes synthesis—review. *Journal of Materials Chemistry* **2011**, 21, 15872-15884.
- (47) Zhang, W.; Zhu, Z.; Wang, F.; Wang, T.; Sun, L.; Wang, Z. Chirality dependence of the thermal conductivity of carbon nanotubes. *Nanotechnology* **2004**, 15, 936.
- (48) Lu, J. P. Novel magnetic properties of carbon nanotubes. *Physical review letters* **1995**, 74, 1123.
- (49) Bachilo, S. M.; Strano, M. S.; Kittrell, C.; Hauge, R. H.; Smalley, R. E.; Weisman, R. B. Structure-assigned optical spectra of single-walled carbon nanotubes. *Science* **2002**, 298, 2361-2366.
- (50) Mistry, K. S.; Larsen, B. A.; Blackburn, J. L. High-yield dispersions of large-diameter semiconducting single-walled carbon nanotubes with tunable narrow chirality distributions. *Applied Chemical Society Nano* **2013**, 7, 2231-2239.
- (51) Reich, S.; Thomsen, C.; Ordejón, P. Electronic band structure of isolated and bundled carbon nanotubes. *Physical Review B* **2002**, 65, 155411.
- (52) Saito, S. Carbon nanotubes for next-generation electronics devices. *Science* **1997**, 278, 77-78.
- (53) Ombaka, L. M.; Ndungu, P. G.; Nyamori, V. O. Pyrrolic nitrogen-doped carbon nanotubes: physicochemical properties, interactions with Pd and their role in the selective hydrogenation of nitrobenzophenone. *Royal Society of Chemistry Advances* **2015**, 5, 109-122.

- (54) Tans, S. J.; Verschueren, A. R. M.; Dekker, C. Room-temperature transistor based on a single carbon nanotube. *Nature* **1998**, *393*, 49-52.
- (55) Iijima, S. Helical microtubules of graphitic carbon. *Nature* **1991**, *354*, 56–58
- (56) Capasso, A.; Salamandra, L.; Di, C. A.; Bell, J. M.; Motta, N. Low-temperature synthesis of carbon nanotubes on indium tin oxide electrodes for organic solar cells. *Beilstein Journal. Nanotechnology*. **2012**, *3*, 524-532.
- (57) Guoping, W.; Qingtang, Z.; Zuolong, Y.; Meizheng, Q. The effect of different kinds of nano-carbon conductive additives in lithium ion batteries on the resistance and electrochemical behavior of the LiCoO₂ composite cathodes. *Solid State Ionics* **2008**, *179*, 263-268.
- (58) Lim, S. H.; Lin, J. Synthesis of carbon nanotubes. *Pan Stanford Publishing Pte. Ltd* **2011**, 31-72.
- (59) Chuang, C. M.; Sharma, S. P.; Ting, J. M.; Lin, H. P.; Teng, H.; Huang, C. W. Preparation of sea urchin-like carbons by growing one-dimensional nanocarbon on mesoporous carbons. *Diamond Related Material* **2008**, *17*, 606-610.
- (60) Li, W. Z.; Xie, S. S.; Qian, L. X.; Chang, B. H.; Zou, B. S.; Zhou, W. Y.; Zhao, R. A.; Wang, G. Large-scale synthesis of aligned carbon nanotubes. *Science*, **1996**, *274*, 1701-1703.
- (61) Sugai, T.; Yoshida, H.; Shimada, T.; Okazaki, T.; Shinohara, H.; Bandow, S. New synthesis of high-quality double-walled carbon nanotubes by high-temperature pulsed arc discharge. *Nano Letters* **2003**, *3*, 769-773.
- (62) Chen, C.; Chen, W.; Zhang, Y. Synthesis of carbon nano-tubes by pulsed laser ablation at normal pressure in metal nano-sol. *Physica E: Low-dimensional Systems and Nanostructures* **2005**, *28*, 121-127.
- (63) Iijima, S.; Ichihashi, T. Single-shell carbon nanotubes of 1-nm diameter. *Nature* **1993**, 603-605.
- (64) Shi, Z.; Lian, Y.; Zhou, X.; Gu, Z.; Zhang, Y.; Iijima, S.; Li, H.; Yue, K. T.; Zhang, S.-L. Production of single-wall carbon nanotubes at high pressure. *The Journal of Physical Chemistry B* **1999**, *103*, 8698-8701.
- (65) Matsuura, T.; Taniguchi, K.; Watanabe, T. A new type of arc plasma reactor with 12-phase alternating current discharge for synthesis of carbon nanotubes. *Thin Solid Films* **2007**, *515*, 4240-4246.

- (66) Arora, N.; Sharma, N. N. Arc discharge synthesis of carbon nanotubes: Comprehensive review. *Diamond and Related Materials* **2014**, *50*, 135-150.
- (67) Journet, C.; Maser, W.; Bernier, P.; Loiseau, A.; de La Chapelle, M. L.; Lefrant, D. I. S.; Deniard, P.; Lee, R.; Fischer, J. Large-scale production of single-walled carbon nanotubes by the electric-arc technique. *Nature* **1997**, *388*, 756-758.
- (68) Bethune, D.; Klang, C.; De Vries, M.; Gorman, G.; Savoy, R.; Vazquez, J.; Beyers, R. Cobalt-catalysed growth of carbon nanotubes with single-atomic-layer walls. *Nature* **1993**, 605-607.
- (69) Lange, H.; Sioda, M.; Huczko, A.; Zhu, Y. Q.; Kroto, H. W.; Walton, D. R. M. Nanocarbon production by arc discharge in water. *Carbon* **2003**, *41*, 1617-1623.
- (70) Wang, S.-D.; Chang, M.-H.; Lan, K. M.-D.; Wu, C.-C.; Cheng, J.-J.; Chang, H.-K. Synthesis of carbon nanotubes by arc discharge in sodium chloride solution. *Carbon* **2005**, *43*, 1792-1795.
- (71) Cui, S.; Scharff, P.; Siegmund, C.; Spiess, L.; Romanus, H.; Schawohl, J.; Risch, K.; Schneider, D.; Klötzer, S. Preparation of multiwalled carbon nanotubes by DC arc discharge under a nitrogen atmosphere. *Carbon* **2003**, *41*, 1648-1651.
- (72) Sugai, T.; Omote, H.; Bandow, S.; Tanaka, N.; Shinohara, H. Production of fullerenes and single-wall carbon nanotubes by high-temperature pulsed arc discharge. *The Journal of Chemical Physics* **2000**, *112*, 6000-6005.
- (73) Zhao, T.; Liu, Y. Large scale and high purity synthesis of single-walled carbon nanotubes by arc discharge at controlled temperatures. *Carbon* **2004**, *42*, 2765-2768.
- (74) Jong Lee, S.; Koo Baik, H.; Yoo, J.; Hoon Han, J. Large scale synthesis of carbon nanotubes by plasma rotating arc discharge technique. *Diamond and Related Materials* **2002**, *11*, 914-917.
- (75) Joshi, R.; Engstler, J.; Nair, P. K.; Haridoss, P.; Schneider, J. J. High yield formation of carbon nanotubes using a rotating cathode in open air. *Diamond and Related Materials* **2008**, *17*, 913-919.
- (76) Ando, Y.; Zhao, X.; Hirahara, K.; Suenaga, K.; Bandow, S.; Iijima, S. Arc plasma jet method producing single-wall carbon nanotubes. *Diamond and Related Materials* **2001**, *10*, 1185-1189.
- (77) Guo, T.; Nikolaev, P.; Thess, A.; Colbert, D.; Smalley, R. Catalytic growth of single-walled nanotubes by laser vaporization. *Chemical physics letters* **1995**, *243*, 49-54.

- (78) Thess, A.; Lee, R.; Nikolaev, P.; Dai, H.; Petit, P.; Robert, J.; Xu, C.; Lee, Y. H.; Kim, S. G.; Rinzler, A. G. Crystalline ropes of metallic carbon nanotubes. *Science-AAAS-Weekly Paper Edition* **1996**, *273*, 483-487.
- (79) Popov, V. Carbon nanotubes: properties and application. *Materials Science and Engineering: R: Reports* **2004**, *43*, 61-102.
- (80) Caglar, B. Production of carbon nanotubes by PECVD and their applications to supercapacitors. *Universitat de Barcelona* **2010**.
- (81) Pan, Z. W.; Xie, S. S.; Chang, B. H.; Wang, C. Y.; Lu, L.; Liu, W.; Zhou, W. Y.; Li, W. Z.; Qian, L. X. Very long carbon nanotubes. *Nature* **1998**, *394*, 631-632.
- (82) Singh, C.; Shaffer, M. S.; Windle, A. H. Production of controlled architectures of aligned carbon nanotubes by an injection chemical vapour deposition method. *Carbon* **2003**, *41*, 359-368.
- (83) Ahmad, M.; Anguita, J. V.; Stolojan, V.; Carey, J. D.; Silva, S. R. P. Efficient coupling of optical energy for rapid catalyzed nanomaterial growth: High-quality carbon nanotube synthesis at low substrate temperatures. *American Chemical Society Applied Materials and Interfaces* **2013**, *5*, 3861-3866.
- (84) Merkulov, V. I.; Lowndes, D. H.; Wei, Y. Y.; Eres, G.; Voelkl, E. Patterned growth of individual and multiple vertically aligned carbon nanofibers. *Applied Physics Letters* **2000**, *76*, 3555-3557.
- (85) Meyyappan, M.; Delzeit, L.; Cassell, A.; Hash, D. Carbon nanotube growth by PECVD: a review. *Plasma Sources Science and Technology* **2003**, *12*, 205.
- (86) Hampden-Smith, M. J.; Kudas, T. T. Chemical vapor deposition of metals: Part 1. An overview of CVD processes. *Chemical Vapor Deposition* **1995**, *1*, 8-23.
- (87) Lieberman M. A. Principals of Plasma Discharges and Materials Processing; *Wiles: New York*, **1994**.
- (88) Popov, O. A. High density plasma sources: design, physics and performance. *Noyes Publications: Park Ridge, New Jersey*, **1995**.
- (89) Sato, H.; Sakai, T.; Suzuki, A.; Kajiwara, K.; Hata, K.; Saito, Y. Growth control of carbon nanotubes by plasma-enhanced chemical vapor deposition. *Vacuum* **2008**, *83*, 515-517.

- (90) Wang, H.; Moore, J. J. Low temperature growth mechanisms of vertically aligned carbon nanofibers and nanotubes by radio frequency-plasma-enhanced chemical vapor deposition. *Carbon* **2012**, *50*, 1235-1242.
- (91) Zheng, J.; Yang, R.; Xie, L.; Qu, J.; Liu, Y.; Li, X. Plasma-Assisted Approaches in Inorganic Nanostructure Fabrication. *Advanced Materials* **2010**, *22*, 1451-1473.
- (92) Wang, Q.; Wang, X.; Chai, Z.; Hu, W. Low-temperature plasma synthesis of carbon nanotubes and graphene based materials and their fuel cell applications. *Chemical Society Reviews* **2013**, *42*, 8821-8834.
- (93) Nozaki, T.; Ohnishi, K.; Okazaki, K.; Kortshagen, U. Fabrication of vertically aligned single-walled carbon nanotubes in atmospheric pressure non-thermal plasma CVD. *Carbon* **2007**, *45*, 364-374.
- (94) Hofmann, S.; Ducati, C.; Robertson, J.; Kleinsorge, B. Low-temperature growth of carbon nanotubes by plasma-enhanced chemical vapor deposition. *Applied Physics Letters* **2003**, *83*, 135-137.
- (95) Le Poche, H.; Dijon, J.; Goisard de Monsabert, T. Radio-frequency plasma system to selectively grow vertical field-aligned carbon nanofibers from a solid carbon source. *Carbon* **2007**, *45*, 2904-2916.
- (96) Lee, C. J.; Park, J.; Yu, J. A. Catalyst effect on carbon nanotubes synthesized by thermal chemical vapor deposition. *Chemical Physics Letters* **2002**, *360*, 250-255.
- (97) Schmid, G. M. D.; Emst, H.; Fuchs, H. Miniaturization and material properties. *Europaische Akademien* **2003**.
- (98) Teo, K. B.; Singh, C.; Chhowalla, M.; Milne, W. I. Catalytic synthesis of carbon nanotubes and nanofibers. *Encyclopedia of nanoscience and nanotechnology* **2003**, *1*, 10.
- (99) Amiens, C.; Chaudret, B.; Ciuculescu-Pradines, D.; Colliere, V.; Fajerweg, K.; Fau, P.; Kahn, M.; Maisonnat, A.; Soulantica, K.; Philippot, K. Organometallic approach for the synthesis of nanostructures. *New Journal of Chemistry* **2013**, *37*, 3374-3401.
- (100) Green, M. Organometallic based strategies for metal nanocrystal synthesis. *Chemical Communications* **2005**, 3002-3011.
- (101) Gordon, W. O. Metal Oxide Nanoparticles: Optical Properties and Interaction with Chemical Warfare Agent Simulants. *Virginia Polytechnic Institute and State University* **2006**.

- (102) Zhang, J.; Jin, M.; Xiao, F.; Li, C.; Jin, X. Martensitic transformation in Fe–Ni nanoparticles prepared by a sol–gel process. *Materials Letters* **2012**, *80*, 152-154.
- (103) D’Souza, L.; Richards, R. Synthesis of metal-oxide nanoparticles: Liquid–solid transformations. *Synthesis, Properties, and Applications of Oxide Nanomaterials* **2007**, 81-117.
- (104) Derakhshi, P.; Khorrami, S.; Lotfi, R. An investigation on synthesis and morphology of nickel doped cobalt ferrite in presence of surfactant at different calcination temperature by co-precipitation route. *World Applied Sciences Journal* **2012**, *16*, 156-159.
- (105) Altavilla, C.; Ciliberto, E. Inorganic Nanoparticles: synthesis, applications, and perspectives-an overview. *CRC Press* **2011**, 1-15.
- (106) Altavilla, C.; Leone, C.; Sannino, D.; Sarno, M.; Ciambelli, P. Synthesis of monodispersed MFe_2O_4 (M=Fe, Co, Ni) ferrite nanoparticles: effect of reaction temperature on particle size. *CRC Press* **2009**, *1*, 143-146.
- (107) Kim, N. S.; Bae, S. Y.; Park, J. The catalytic effect on vertically aligned carbon nanotubes. *Material Research Society*. **2003**, *800*, 105-110.
- (108) Kumar, M.; Ando, Y.: Chemical Vapor Deposition of Carbon Nanotubes: A Review on Growth Mechanism and Mass Production. *Journal of Nanoscience and Nanotechnology* **2010**, *10*, 3739-3758.
- (109) Kiang, C. H. Carbon rings and cages in the growth of single-walled carbon nanotubes. *Journal of Chemistry Physics*. **2000**, *113*, 4763-4766.
- (110) Ding, F.; Larsson, P.; Larsson, J. A.; Ahuja, R.; Duan, H.; Rosén, A.; Bolton, K. The importance of strong carbon-metal adhesion for catalytic nucleation of single-walled carbon nanotubes. *Nano letters* **2008**, *8*, 463-468.
- (111) Kumar, M.; Ando, Y. Gigas growth of carbon nanotubes. *Defence Science Journal* **2008**, *58*, 496-503.
- (112) Massalski, T. B.; Okamoto, H.; Subramanian, P.; Kacprzak, L. Binary alloy phase diagrams; *ASM international*, **1990**.
- (113) Parthangal, P. M.; Cavicchi, R. E.; Zachariah, M. R. A generic process of growing aligned carbon nanotube arrays on metals and metal alloys. *Nanotechnology* **2007**, *18*.
- (114) Halonen, N.; Sápi, A.; Nagy, L.; Puskás, R.; Leino, A. R.; Mäklin, J.; Kukkola, J.; Tóth, G.; Wu, M. C.; Liao, H. C.; Su, W. F.; Shchukarev, A.; Mikkola, J. P.; Kukovecz, A.; Kónya, K.; Kordás, K. Low-temperature growth of multi-walled carbon nanotubes by thermal CVD. *Physica Status Solidi (B) Basic Research* **2011**, *248*, 2500-2503.

- (115) Nessim, G. D.; Seita, M.; Plata, D. L.; O'Brien, K. P.; Hart, A. J.; Meshot, E. R.; Reddy, C. M.; Gschwend, P. M.; Thompson, C. V. Precursor gas chemistry determines the crystallinity of carbon nanotubes synthesized at low temperature. *Carbon* **2011**, *49*, 804-810.
- (116) Keru, G.; Ndungu, P. G.; Nyamori, V. O. Nitrogen-Doped Carbon Nanotubes Synthesised by Pyrolysis of (4-[[pyridine-4-yl)methylidene]amino]phenyl)ferrocene. *Journal of Nanomaterials* **2013**, *2013*, 1-7.
- (117) Huang, J.; Zhang, Q.; Wei, F.; Qian, W.; Wang, D.; Hu, L. Liquefied petroleum gas containing sulfur as the carbon source for carbon nanotube forests. *Carbon* **2008**, *46*, 291-296.
- (118) Fahlman, B. D. Low temperature synthesis of carbon nanotubes by catalytic decomposition of halogenated hydrocarbons *American Chemical Society*, **2004**, *10*, 29.
- (119) Fleaca, C. T.; Morjan, I.; Rodica, A.; Dumitrache, F.; Soare, I.; Gavrilă-Florescu, L.; Sandu, I.; Dutu, E.; Le Normand, F.; Faerber, J. Oriented carbon nanostructures grown by hot-filament plasma-enhanced CVD from self-assembled Co-based catalyst on Si substrates. *Physica E- Low-Dimensional Systems & Nanostructures* **2012**, *44*, 1024-1027.
- (120) Xiang, R.; Einarsson, E.; Okawa, J.; Miyauchi, Y.; Maruyama, S. Acetylene-accelerated alcohol catalytic chemical vapor deposition growth of vertically aligned single-walled carbon nanotubes. *Journal of Physical Chemistry: C* **2009**, *113*, 7511-7515.
- (121) Benedikt, J. Plasma-chemical reactions: low pressure acetylene plasmas. *Journal of Physics: D: Applied Physics* **2010**, *43*, 043001-043021.
- (122) See H.C. A review of carbon nanotube synthesis via fluidized-bed chemical vapor deposition. *Industrial Engineering Chemical Research* **2007**, *46*, 997-1012.
- (123) Escobar, M.; Moreno, M. S.; Candal, R. J.; Marchi, M. C.; Caso, A.; Polosecki, P. I.; Rubiolo, G. H.; Goyanes, S. Synthesis of carbon nanotubes by CVD: Effect of acetylene pressure on nanotubes characteristics. *Applied Surface Science* **2007**, *254*, 251-256.
- (124) Sato, G.; Morio, T.; Kato, T.; Hatakeyama, R. Fast growth of carbon nanowalls from pure methane using helicon plasma-enhanced chemical vapor deposition. *Japanese Journal of Applied Physics* **2006**, *45*, 5210.
- (125) Wang, J.; Zhu, M.; Outlaw, R. A.; Zhao, X.; Manos, D. M.; Holloway, B. C. Synthesis of carbon nanosheets by inductively coupled radio-frequency plasma-enhanced chemical vapor deposition. *Carbon* **2004**, *42*, 2867-2872.

- (126) Hiramatsu, M.; Shiji, K.; Amano, H.; Hori, M. Fabrication of vertically aligned carbon nanowalls using capacitively coupled plasma-enhanced chemical vapor deposition assisted by hydrogen radical injection. *Applied Physics Letters* **2004**, *84*, 4708-4710.
- (127) Wang, Z.; Shoji, M.; Ogata, H. Carbon nanosheets by microwave plasma-enhanced chemical vapor deposition in CH₄-Ar system. *Applied Surface Science* **2011**, *257*, 9082-9085.
- (128) Soin, N.; Roy, S. S.; Lim, T. H.; McLaughlin, J. A. D. Microstructural and electrochemical properties of vertically aligned few layered graphene (FLG) nanoflakes and their application in methanol oxidation. *Materials Chemistry and Physics* **2011**, *129*, 1051-1057.
- (129) Shang, N. G.; Papakonstantinou, P.; McMullan, M.; Chu, M.; Stamboulis, A.; Potenza, A.; Dhesi, S. S.; Marchetto, H. Catalyst-free efficient growth, orientation and biosensing properties of multilayer graphene nanoflake films with sharp edge planes. *Advanced Functional Materials* **2008**, *18*, 3506-3514.
- (130) Teii, K.; Shimada, S.; Nakashima, M.; Chuang, A. T. H. Synthesis and electrical characterization of n-type carbon nanowalls. *Journal of Applied Physics* **2009**, *106*, 084303.
- (131) Zhu, M. Y.; Outlaw, R. A.; Bagge-Hansen, M.; Chen, H. J.; Manos, D. M. Enhanced field emission of vertically oriented carbon nanosheets synthesized by C₂H₂/H₂ plasma-enhanced CVD. *Carbon* **2011**, *49*, 2526-2531.
- (132) Zeng, L.; Lei, D.; Wang, W.; Liang, J.; Wang, Z.; Yao, N.; Zhang, B. Preparation of carbon nanosheets deposited on carbon nanotubes by microwave plasma-enhanced chemical vapor deposition method. *Applied Surface Science* **2008**, *254*, 1700-1704.
- (133) Krivchenko, V. A.; Dvorkin, V. V.; Dzbanovsky, N. N.; Timofeyev, M. A.; Stepanov, A. S.; Rakhimov, A. T.; Suetin, N. V.; Vilkov, O. Y.; Yashina, L. V. Evolution of carbon film structure during its catalyst-free growth in the plasma of direct current glow discharge. *Carbon* **2012**, *50*, 1477-1487.
- (134) Chuang, A. T. H.; Boskovic, B. O.; Robertson, J. Freestanding carbon nanowalls by microwave plasma-enhanced chemical vapour deposition. *Diamond and Related Materials* **2006**, *15*, 1103-1106.
- (135) Jung, Y.; Song, J.; Huh, W.; Cho, D.; Jeong, Y. Controlling the crystalline quality of carbon nanotubes with processing parameters from chemical vapor deposition synthesis. *Chemical Engineering Journal* **2013**, *228*, 1050-1056.

- (136) Acomb, J. C.; Wu, C.; Williams, P. T. Effect of growth temperature and feedstock:catalyst ratio on the production of carbon nanotubes and hydrogen from the pyrolysis of waste plastics. *Journal of Analytical and Applied Pyrolysis* **2015**.
- (137) Zhang, Q.; Liu, Y.; Huang, J.; Qian, W.; Wang, Y.; Wei, F. Synthesis of single-walled carbon nanotubes from liquefied petroleum gas. *Nanotechnology* **2008**, *3*, 95-100.
- (138) Wang, W.; Turn, S. Q.; Keffer, V.; Douette, A. Parametric study of autothermal reforming of LPG. *American. Chemical. Society., Division of Fuel Chemistry* **2004**, *49*, 142-143.
- (139) Zhang, Q.; Huang, J.; Wei, F.; Xu, G.; Wang, Y.; Qian, W.; Wang, D. Large scale production of carbon nanotube arrays on the sphere surface from liquefied petroleum gas at low cost. *Chinese Science Bulletin* **2007**, *52*, 2896-2902.
- (140) Baker, R. T. K.; Barber, M. A.; Harris, P. S.; Feates, F. S.; Waite, R. J. Nucleation and growth of carbon deposits from the nickel catalyzed decomposition of acetylene. *Journal of Catalysis* **1972**, *26*, 51-62.
- (141) Soneda, Y.; Duclaux, L.; Beguin, F. Synthesis of high quality multi-walled carbon nanotubes from the decomposition of acetylene on iron-group metal catalysts supported on MgO. *Carbon* **2002**, *40*, 965-969.
- (142) Eres, G.; Kinkhabwala, A. A.; Cui, H.; Geohegan, D. B.; Poretzky, A. A.; Lowndes, D. H. Molecular Beam-Controlled Nucleation and Growth of Vertically Aligned Single-Wall Carbon Nanotube Arrays. *Journal of Physical Chemistry: B* **2005**, *109*, 16684-16694.
- (143) Zhong, G.; Hofmann, S.; Yan, F.; Telg, H.; Warner, J. H.; Eder, D.; Thomsen, C.; Milne, W. I.; Robertson, J. Acetylene: A Key Growth Precursor for Single-Walled Carbon Nanotube Forests. *Journal of Physical Chemistry: C* **2009**, *113*, 17321-17325.
- (144) Hart, A. J.; Slocum, A. H. Rapid growth and flow-mediated nucleation of millimeter-scale aligned carbon nanotube structures from a thin-film catalyst. *Journal of Physical Chemistry: B* **2006**, *110*, 8250-8257.
- (145) Hesamzadeh, H.; Ganjipour, B.; Mohajerzadeh, S.; Khodadadi, A.; Mortazavi, Y.; Kiani, S. PECVD-growth of carbon nanotubes using a modified tip-plate configuration. *Carbon* **2004**, *42*, 1043-1047.
- (146) Somers, W.; Bogaerts, A.; van Duin, A. C. T.; Neyts, E. C. Interactions of plasma species on nickel catalysts: A reactive molecular dynamics study on the influence of temperature and surface structure. *Applied Catalysis B* **2014**, *154-155*, 1-8.

- (147) Baker, R. T. K.; Waite, R. J. Formation of carbonaceous deposits from the platinum-iron catalyzed decomposition of acetylene. *Journal of Catalysis* **1975**, *37*, 101-105.
- (148) Aqel, A.; Abou El-Nour, K. M. M.; Ammar, R. A. A.; Al-Warthan, A. Carbon nanotubes, science and technology part (I) structure, synthesis and characterization. *Arabian Journal of Chemistry*. **2012**, *5*, 1-23.
- (149) Bower, C.; Zhu, W.; Jin, S.; Zhou, O. Plasma-induced alignment of carbon nanotubes. *Applied Physics Letters* **2000**, *77*, 830-832.
- (150) Delzeit, L.; McAninch, I.; Cruden, B. A.; Hash, D.; Chen, B.; Han, J.; Meyyappan, M. Growth of multiwall carbon nanotubes in an inductively coupled plasma reactor. *Journal of Applied Physics* **2002**, *91*, 6027-6033.
- (151) Teo, K. B. K.; Hash, D. B.; Lacerda, R. G.; Rupesinghe, N. L.; Bell, M. S.; Dalal, S. H.; Bose, D.; Govindan, T. R.; Cruden, B. A.; Chhowalla, M.; Amaratunga, G. A. J.; Meyyappan, M.; Milne, W. I. The significance of plasma heating in carbon nanotube and nanofiber growth. *Nano Letters* **2004**, *4*, 921-926.
- (152) Chhowalla, M., K. B. K.; Teo, C.; Ducati, N. L.; Rupesinghe, G. A. J.; Amaratunga, A. C.; Ferrari, D.; Roy, J.; Robertson W. I. Growth process conditions of vertically aligned carbon nanotubes using plasma enhanced chemical vapor deposition. *Journal of Applied Physics* **2001**, *90*, 10, 5308-5317.
- (153) Franklin, N. R.; Dai, H. An enhanced CVD approach to extensive nanotube networks with directionality. *Advanced Mater.* **2000**, *12*, 890-894.
- (154) Park, Y. J.; Han, I. T.; Kim, H. J.; Woo, Y. S.; Lee, N. S.; Jin, Y. W.; Jung, J. E.; Choi, J. H.; Jung, D. S.; Park, C. Y.; Kim, J. M. Effect of catalytic layer thickness on growth and field emission characteristics of carbon nanotubes synthesized at low temperatures using thermal chemical vapor deposition. *Japanese Journal of Applied Physics, Part 1: Regular Papers and Short Notes and Review Papers* **2002**, *41*, 4679-4685.
- (155) Tibbetts, G. G. Carbon fibers produced by pyrolysis of natural gas in stainless steel tubes. *Applied Physics Letters* **1983**, *42*, 666-668.
- (156) Hou, H.; Schaper, A. K.; Jun, Z.; Weller, F.; Greiner, A. Large-scale synthesis of aligned carbon nanotubes using FeCl₃ as floating catalyst precursor. *Chemistry of Materials* **2003**, *15*, 580-585.

- (157) Neyts, E. C.; Bogaerts, A. numerical study of the size-dependent melting mechanisms of nickel nanoclusters. *Journal of Physical Chemistry: C* **2009**, *113*, 2771-2776.
- (158) Ducati, C.; Alexandrou, I.; Chhowalla, M.; Amaratunga, G. A. J.; Robertson, J. Temperature selective growth of carbon nanotubes by chemical vapor deposition. *Journal of Applied Physics* **2002**, *92*, 3299-3303.
- (159) Rinzler, A.; Liu, J.; Dai, H.; Nikolaev, P.; Huffman, C.; Rodriguez-Macias, F.; Boul, P.; Lu, A. H.; Heymann, D.; Colbert, D. Large-scale purification of single-wall carbon nanotubes: process, product, and characterization. *Applied Physics A: Materials Science & Processing* **1998**, *67*, 29-37.
- (160) Hoppe, H.; Sariciftci, N. S. Organic solar cells: An overview. *Journal of Material Research*. **2004**, *19*, 1924-1945.
- (161) Green, M. A.; Emery, K.; Hishikawa, Y.; Warta, W.; Dunlop, E. D. Solar cell efficiency tables (Version 45). *Progress in Photovoltaics: Research and Applications* **2015**, *23*, 1-9.
- (162) Luo, J.; Fang, B.; Wanjala, B. N.; Njoki, P. N.; Loukrakpam, R.; Yin, J.; Mott, D.; Lim, S.; Zhong, C. J. Nanoparticled for fuel cell applications. *American Chemical Society* **2011**, 159-184.
- (163) Arici, E. Inorganic nanoparticles for photovoltaic applications. *American Chemical Society* **2011**, 185-211.
- (164) Joy, D. C.; Joy, C. S. Low voltage scanning electron microscopy. *Micronanotechnology* **1996**, *27*, 247-263.
- (165) Drouin, D.; Couture, A. R.; Joly, D.; Tastet, X.; Aimez, V.; Gauvin, R. A fast and easy-to-use modeling tool for scanning electron microscopy and microanalysis users. *Scanning* **2007**, *29*, 92-101.
- (166) Suga, M.; Asahina, S.; Sakuda, Y.; Kazumori, H.; Nishiyama, H.; Nokuo, T.; Alfredsson, V.; Kjellman, T.; Stevens, S. M.; Cho, H. S.; Cho, M.; Han, L.; Che, S.; Anderson, M. W.; Schüth, F.; Deng, H.; Yaghi, O. M.; Liu, Z.; Jeong, H. Y.; Stein, A.; Sakamoto, K.; Ryoo, R.; Terasaki, O. Recent progress in scanning electron microscopy for the characterization of fine structural details of nano materials. *Progress in Solid State Chemistry* **2014**, *42*, 1-21.
- (167) Yu, M.; Dyer, M. J.; Skidmore, G. D.; Rohrs, H. W.; Lu, X.; Ausman, K. D.; Von Ehr, J. R.; Ruoff, R. S. Three-dimensional manipulation of carbon nanotubes under a scanning electron microscope. *Nanotechnology* **1999**, *10*, 244.

- (168) Gommès, C.; Blacher, S.; Masenelli-Varlot, K.; Bossuot, C.; McRae, E.; Fonseca, A.; Nagy, J. B.; Pirard, J. P. Image analysis characterization of multi-walled carbon nanotubes. *Carbon* **2003**, *41*, 2561-2572.
- (169) Jiang, N.; Wang, H. X.; Zhang, H.; Sasaoka, H.; Nishimura, K. Characterization and surface modification of carbon nanowalls. *Journal of Materials Chemistry* **2010**, *20*, 5070-5073.
- (170) Wang, Z. L. New development for transmission electron microscopy for nanotechnology. *Advanced Materials* **2003**, *15*, 1497-1514.
- (171) Eba, R. Characterization of Carbon Nanotubes. *INTECH Open Access Publisher*, **2013**.
- (172) Belin, T.; Epron, F. Characterization methods of carbon nanotubes: a review. *Material Science and Engineering: B* **2005**, *119*, 105-118.
- (173) Dresselhaus, M. S.; Avouris, P. Introduction to carbon materials research. Carbon nanotubes *Springer* **2001**, 1-9.
- (174) Dresselhaus, M.; Jorio, A.; Saito, R. Characterizing graphene, graphite, and carbon nanotubes by Raman spectroscopy. *Material Physics* **2010**, *1*, 89-108.
- (175) Jorio, A.; Pimenta, M.; Souza Filho, A.; Saito, R.; Dresselhaus, G.; Dresselhaus, M. Characterizing carbon nanotube samples with resonance Raman scattering. *New Journal of Physics* **2003**, *5*, 139.
- (176) Costa, S.; Borowiak-Palen, E.; Kruszynska, M.; Bachmatiuk, A.; Kalenczuk, R. J.; Characterization of carbon nanotubes by Raman spectroscopy. *Mater Science* **2008**, *26*, 433-441.
- (177) Kim, U. J.; Furtado, C. A.; Liu, X.; Chen, G.; Eklund, P. C. Raman and IR spectroscopy of chemically processed single-walled carbon nanotubes. *Journal of the American Chemical Society* **2005**, *127*, 15437-15445.
- (178) Ramos, J. M.; de M. Cruz, M. T.; Costa, A. C., Jr.; Versiane, O.; Tellez Soto, C. A. Fourier transform infrared spectrum: vibrational assignments using density functional theory and natural bond orbital analysis of the bis(guanidoacetate)nickel(II)complex. *ScienceAsia* **2011**, *37*, 247-255.
- (179) Brown, M. E.: Introduction to thermal analysis: techniques and applications. *Springer Science & Business Media* **2001** , 1.
- (180) Yoe, J. H. Inorganic Thermogravimetric Analysis. *Journal of the American Chemical Society* **1963**, *85*, 3905-3905.

- (181) Iijima, S. Helical microtubules of graphitic carbon. *Nature* **1991**, *354*, 56-58.
- (182) Ren, L.; Wang, S. Organic solar cell with carbon nanotube anode. *American Society of Mechanical Engineers* **2010**, *2*, 425-430.
- (183) Kim, S. M.; Gangloff, L. Growth of carbon nanotubes (CNTs) on metallic underlayers by diffusion plasma-enhanced chemical vapour deposition (DPECVD). *Physics* **2009**, *41*, 1763-1766.
- (184) Miller, A. J.; Hatton, R. A.; Chen, G. Y.; Silva, S. R. P. Carbon nanotubes grown on In₂O₃:Sn glass as large area electrodes for organic photovoltaics. *Applied Physics Letters* **2007**, *90*, 023105.
- (185) Agrawal, S.; Frederick, M. J.; Lupo, F.; Victor, P.; Nalamasu, O.; Ramanath, G. Directed growth and electrical-transport properties of carbon nanotube architectures on indium tin oxide films on silicon-based substrates. *Advanced Functional Material* **2005**, *15*, 1922-1926.
- (186) Ren, Z. F.; Huang, Z. P.; Xu, J. W.; Wang, J. H.; Bush, P.; Siegel, M. P.; Provencio, P. N. Synthesis of large arrays of well-aligned carbon nanotubes on glass. *Science* **1998**, *282*, 1105-1107.
- (187) Pasquier, A. D.; Unalan, H. E.; Kanwal, A.; Miller, S.; Chhowalla, M. Conducting and transparent single-wall carbon nanotube electrodes for polymer-fullerene solar cells. *Applied Physics Letters* **2005**, *87*, 203511.

Chapter Three

EXPERIMENTAL

This chapter provides details on the experimental work which was carried out to synthesize and characterise vertically-aligned multi-walled carbon nanotubes (MWCNTs). The step by step procedures from the synthesis of metal nanoparticles that were used as catalysts to the synthesis of the MWCNTs is provided. All chemicals, reagents, gases, instruments and characterisation techniques used during the project are all listed and briefly discussed herein. Thus, a comprehensive description is given in the respective subsequent sections within this chapter.

3.1 General procedures

The common laboratory glassware used in this project, (**Appendix A**) were washed with scrubbing using a detergent in water. Thorough cleaning was done using acetone, then finally rinsed in deionised water and dried in an oven at 120-150 °C for at least 30 minutes.

3.1.1 Chemicals, reagents, solvents and gases

All chemicals used in these experiments were obtained from commercial sources and were used as received without further purification. The purity of the surfactant was 90% and the other inorganic precursor reagents had a purity that was not less than 98%. The solvents were used as chemically pure (CP) or analytical (AR) grade (**Table 3.1**).

Table 3.1: Chemicals, reagents, solvents and gases supplier and purity/grades as used

| Chemical name | Chemical formula | Supplier | Grade/Purity (%) |
|--------------------------------|--|---|-------------------|
| Acetone | $(\text{CH}_3)_2\text{CO}$ | Protea Chemicals, South Africa | AR/100 |
| Ammonium solution | NH_4OH | Associated Chemical Enterprises, South Africa | CP/25 |
| Cobaltous chloride | $\text{CoCl}_2 \cdot 6\text{H}_2\text{O}$ | Rochelle Chemicals, South Africa | AR/99 |
| Double deionised water | H_2O | UKZN | |
| Ferrocene | $\text{Fe}(\text{C}_2\text{H}_5)_2$ | Merck, Germany | AR/98 |
| Hexadecylamine | $\text{CH}_3(\text{CH}_2)_{15}\text{NH}_2$ | Capital Lab Supplies, South Africa | Technical/90 |
| Iron chloride hexahydrate | $\text{FeCl}_3 \cdot 6\text{H}_2\text{O}$ | Associated Chemical Enterprises, South Africa | AR/99 |
| Isopropanol | $\text{C}_3\text{H}_7\text{OH}$ | Saarchem, South Africa | AR/99.5 |
| Nickel chloride hexahydrate | $\text{NiCl}_2 \cdot 6\text{H}_2\text{O}$ | Saarchem, South Africa | AR/98 |
| Toluene | $\text{C}_6\text{H}_5\text{CH}_3$ | Saarchem, South Africa | AR/99 |
| Acetylene | C_2H_2 | Afrox, South Africa | High purity |
| Argon | Ar | Afrox, South Africa | Ultra high purity |
| Hydrogen balanced in argon | 10% H_2 in Ar | Afrox, South Africa | Ultra high purity |
| Liquefied petroleum gas | $\text{C}_3\text{H}_8 \cdot \text{C}_4\text{H}_{10}$ (60:40) | Afrox, South Africa | |

3.2 Instrumentation

A general summary of the several instruments, model, software versions and brief usage in the experimental procedure is given in **Table 3.2**. Detailed explanation is provided in subsequent sections detailing how the instruments were used.

Table 3.2: Experimental instruments, model, software version and use in research

| Instrument | Model | Supplier/specification version | Use in research |
|---|--------------------------------------|--|--|
| Analytical balance | Ohaus PA214 | Precision weighing balances 0.1 mg | Weighing reagents and samples |
| Centrifuge | Labofuge 200, GmbH | Thermo scientific | Separating by centrifugation |
| Digital ultrasonic heater | UD150SH-6L | Shalom laboratories | Ultrasonic mixing of reagents and solutions |
| Hot plate | MS-H PRO ⁺ | LAB smart | Maintaining reaction temperature |
| Fourier transform Infrared spectrometer | Perkin Elmer Spectrum 100 | Perkin Elmer Multimedia spectrum | Elemental bonds peaks |
| Raman spectrometer | Delta Nu Advantage 532 TM | 2D CCD- detector | Determination of the graphitic nature of MWCNTs |
| Scanning electron microscope | JEOL JSM 6100 | Zeiss Smart SEM version 5.03.06. | Morphology of MNPs and MWCNTs |
| Thermal analyser | Q series (Q600) | TA instruments Universal Analysis 2000 | Determining the thermal stability of the samples |
| Transmission electron microscope | JEOL JEM 1010 | Mega view 3 camera, image J | Determination of size and distribution of the MNPs or MWCNTs |

3.3 Catalyst synthesis

The catalysts were synthesised using two different methods namely, thermal decomposition and co-precipitation method. The outcomes of the methods were compared and optimised. The in-depth synthesis details of each method are described in the **Section 3.3.1** and **3.3.2**. A constant concentration of each catalyst precursor was prepared throughout each method as shown in **Table 3.3**.

Table 3.3: Concentrations of catalyst precursors as used

| Reagent | No of moles | Concentration (M) |
|--|-------------|-------------------|
| $\text{FeCl}_3 \cdot 6\text{H}_2\text{O}$ | 0.01/0.005 | 0.2/0.1 |
| $\text{CoCl}_2 \cdot 6\text{H}_2\text{O}$ | 0.005 | 0.1 |
| $\text{CH}_3(\text{CH}_2)_{15}\text{NH}_2$ | 0.002 | 0.08 |
| $\text{NiCl}_2 \cdot 6\text{H}_2\text{O}$ | 0.005 | 0.1 |
| NH_4OH | 0.00625 | 0.25 |

3.3.1 Thermal decomposition

The catalysts were prepared as single metals namely, Fe, Co and Ni, and as metal mixtures, i.e. CoFe, NiFe and NiCo. In this work the method employed involved formation of metal nanoparticles on indium tin oxide (ITO) glass substrate. The actual masses of the precursors dissolved in ethanol solvent with the surfactant hexadecylamine (HDA) used are presented in **Table 3.4 and 3.6**.

Table 3.4: Masses of single metal precursors dissolved in ethanol (50 mL) with 1 g HDA

| Precursor | Active metal | Mass/g |
|---|--------------|--------|
| $\text{FeCl}_3 \cdot 6\text{H}_2\text{O}$ | Fe | 1.352 |
| $\text{CoCl}_2 \cdot 6\text{H}_2\text{O}$ | Co | 1.190 |
| $\text{NiCl}_2 \cdot 6\text{H}_2\text{O}$ | Ni | 1.880 |

The metal salt, iron chloride hexahydrate ($\text{FeCl}_3 \cdot 6\text{H}_2\text{O}$) (1.352 g) was dissolved in ethanol (50 mL). The ethanol/salt solution was mixed by sonication for 5 minutes. The surfactant, HDA (1.000 g), was added to the mixture and further sonicated for 5 minutes. A 30 x 30 x 0.7 mm ITO glass substrate with a resistivity of 15 ohms was immersed in the prepared solution and then placed in a quartz boat. The quartz boat was placed in the hot zone of a furnace. The furnace was ramped to the desired temperatures for different purposes as presented in **Table 3.5**.

Table 3.5: Furnace temperature rate ramps and purpose

| Temperature ramp (°C) | Rate (°C/minute) | Hold time (minute) | Purpose |
|--------------------------|------------------|--------------------|--|
| Ambient - 80 | 5 | 10 | Drying solution on ITO |
| 80 - 150 | 2 | 10 | Allow decomposition of precursor molecules |
| 150 - T_{MAX}^* | 20 | 30 | Synthesis temperature |

* T_{MAX} is the maximum reaction temperature 400, 500 or 600 °C, all reactions were carried out at T_{MAX}

The catalyst synthesis temperature treatment involved Ar flowing at 100 mL/minute. Once the target temperature (T_{MAX}) was archived, synthesis was allowed for 30 minutes. Thereafter, the furnace temperature was allowed to cool to room temperature.

A similar procedure was used for mixed metal (CoFe, NiCo and NiFe) catalysts. The difference was that instead of making an individual metal solution, a second metal precursor was added. **Table 3.6** shows the masses of the precursors used.

Table 3.6: Masses of mixed metal precursors dissolved in ethanol (50 mL) with 1 g HDA

| Precursor | Active metal | Mass/g |
|--|--------------|---|
| CoCl₂·6H₂O : FeCl₃·6H₂O | CoFe | 2.703 (FeCl ₃ ·6H ₂ O) : 1.190 (CoCl ₂ ·6H ₂ O) |
| NiCl₂·6H₂O : CoCl₂·6H₂O | NiCo | 2.380 (CoCl ₂ ·6H ₂ O) : 1.880 (NiCl ₂ ·6H ₂ O) |
| NiCl₂·6H₂O : FeCl₃·6H₂O | NiFe | 2.703 (FeCl ₃ ·6H ₂ O) : 1.880 (NiCl ₂ ·6H ₂ O) |

The metal salt (FeCl₃·6H₂O) (2.703 g) was dissolved in ethanol (50 mL). In a separate beaker cobalt chloride (CoCl₂·6H₂O) (1.190 g) was dissolved in ethanol (50 mL). The salt solutions were mixed together and sonicated for 5 minutes. HDA (1.000 g), was added to the mixture and further sonicated for 5 minutes. An ITO glass substrate was immersed in the prepared solution and then placed in a quartz boat. The quartz boat was placed in the hot zone of a furnace. The furnace was ramped to the desired temperatures using the temperature ramps in **Table 3.5**. The catalyst synthesis temperature treatment involved Ar flowing at 100 mL/minute. Once the target temperature (T_{MAX}) was archived, synthesis was allowed for 30 minutes. Thereafter, the furnace temperature was allowed to cool to room temperature.

3.3.2 Co-precipitation

This method utilises the formation of nanoparticles in solution. In this case, the procedure was divided into two phases, firstly, preparation of the surfactant and, secondly, the preparation of the catalyst solution mixture. The synthesis procedure was based on a method used by Choi and co-workers.¹ The same precursor masses were used as shown in **Tables 3.4** (single metal) and **3.6** (mixed metal).

In brief, HDA (0.5 g) was dissolved in acetone (25 mL). The mixture was ultra-sonicated for 20 minutes until a homogeneous mixture was obtained, then stored in a beaker for further use. In a 100 mL beaker, $\text{FeCl}_3 \cdot 6\text{H}_2\text{O}$ (1.352 g) was dissolved in 50 mL of deionised water. The solution (20 mL) was transferred into a three-necked round-bottomed flask. The mixture was ultra-sonicated for 5 minutes and thereafter placed onto a hot plate. To the mixture, an NH_4OH (20 mL) solution was added dropwise. The pH of the solution was maintained at 11, with the dropwise addition of the precipitating agent (NH_4OH) while heating the solution at 80 °C under vigorous stirring (300 rpm). The precipitation temperature was maintained constant within ± 1 °C using an oil bath. After 10 minutes, the prepared HDA (5 mL) was added when stirring for 5 minutes. An additional NH_4OH (5 mL) was added and the solution was further stirred for 5 minutes. Thereafter, four aliquots of HDA (5 mL) were added at 5 minutes interval. After the addition of the last aliquot of HDA, growth was allowed for 30 minutes, at a constant temperature of 80 °C. The mixture was consistently stirred during this step in order to produce a stable suspension. This was followed by cooling, the contents in a round-bottomed flask, to room temperature under running water. The precipitates were centrifuged at 2500 rpm for 20 minutes, washed with ethanol (6 mL) and acetone (10 mL) sequentially several times, until a colourless supernatant was obtained which was also an indication of the removal of the excess surfactant. The final products were stored as a concentrated mixture in a refrigerator at temperatures below 5 °C to avoid fusion of the particles. The procedure was repeated for Co and Ni catalysts.

The same procedure was followed for the mixtures of CoFe, NiFe and NiCo catalysts. The metal chloride salts were dissolved in deionised water as individual solutions. The co-precipitation method and deposition of the catalysts is summarised in **Figure 3.1**.

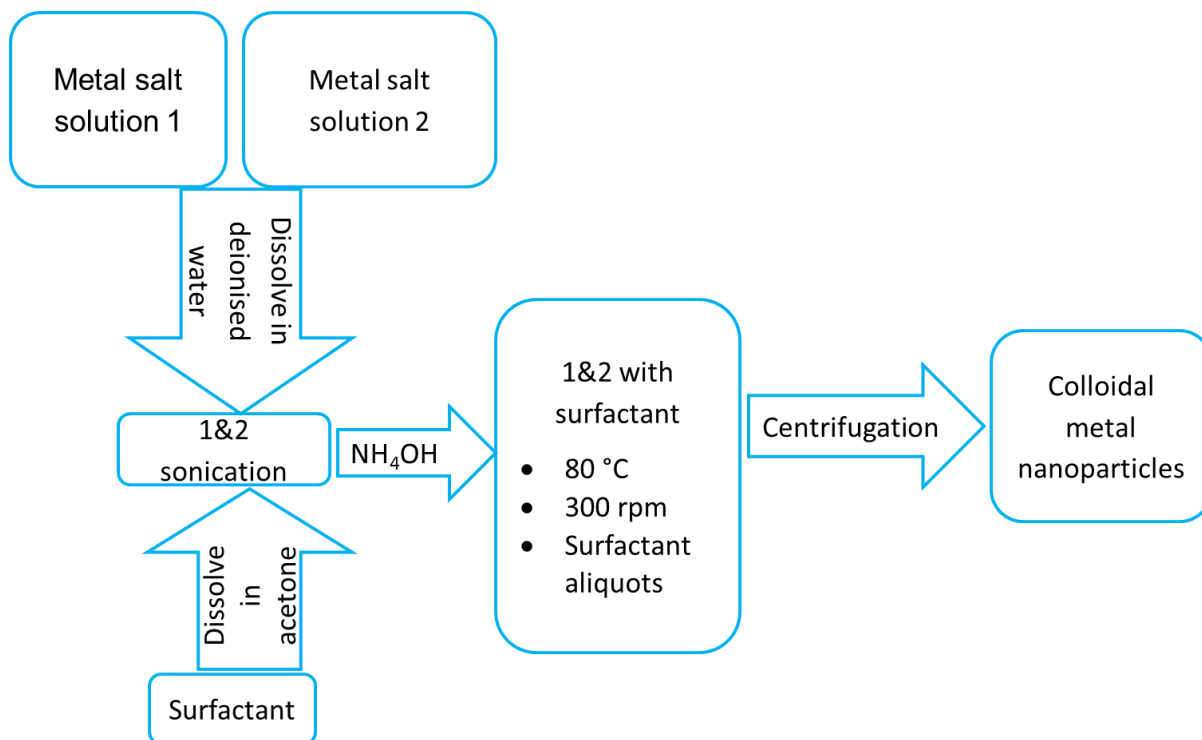


Figure 3.1: Schematic co-precipitation method illustration

3.4 Reactor set-up for the synthesis of CNT forests

Three approaches were used, whereby the first two were based on thermal CVD methods while the third approach was based on a non-equilibrium PECVD method. The reactor designs are explained in detail in each sub section below.

3.4.1 Single-furnace set-up

A horizontal tube furnace, single Elite Thermal Systems Limited, model TSH12/50/610 fitted with a main zone furnace controller Eurotherm 2416 and an oven temperature controller Eurotherm 2116 was used. The reactor vessel used was a quartz tube with an inner diameter of 27 mm and length 850 mm. The reactor vessel was placed inside the furnace with the vessel ends equidistant from the edges of the furnace. One end of the quartz reactor vessel was fitted with a quartz water-cooled injection port, through the use of a ground glass joint, **(Figure 3.2 (a))** and the other end was closed with a glass cold finger **(Figure 3.2 (b))**. Hooks and elastic bands were used to seal the ends firmly to

withstand high pressure build up during the synthesis process. The cold finger was responsible for the gas exhaust while the injection point was the gas inlet point. A New Era systems syringe pump, NE-300 was used to inject the solutions. The photograph in **Figure 3.2 (c)** shows the reaction set-up for the single-furnace.

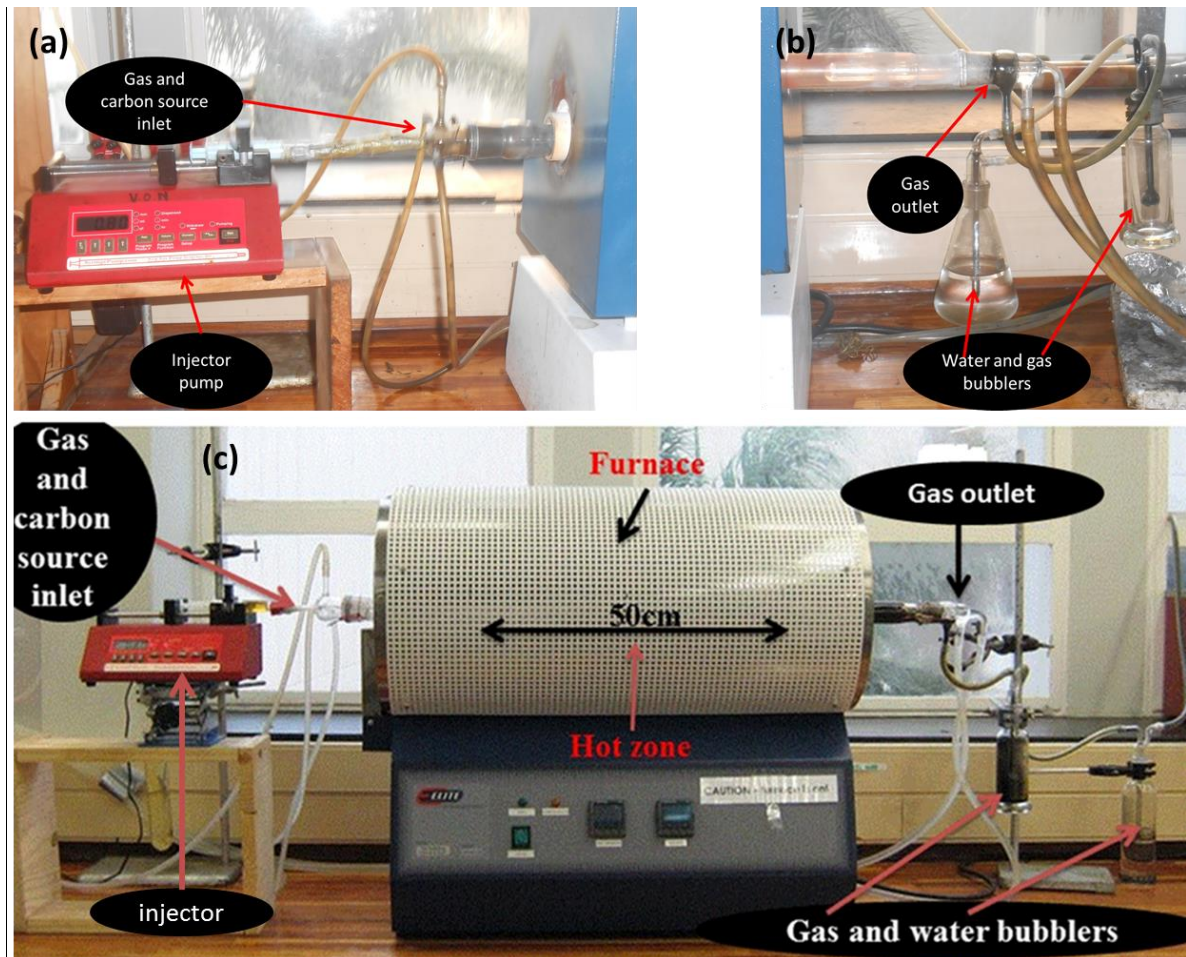


Figure 3.2: Photograph of (a) gas and carbon source injection port attached to a syringe pump (b) gas outlet and exhaust system and (c) complete CVD set-up for MWCNTs

3.4.2 Double-furnace set-up

The reaction set-up utilised two furnaces joined together as close as possible without leaving a gap in between. The Elite Thermal Systems Limited furnace described in **Section 3.4.1** above was used as the high temperature furnace. The lower temperature furnace was a Labofum, model TUB 002, with a fitted temperature controller CAHO P961. A longer quartz tube, diameter 27 mm and length 1600 mm was used as the reactor vessel. The reactor vessel passed through all the furnaces with the

vessels ends at an equidistant of either furnace ends. The system was closed to prevent the atmospheric oxygen from being part of the system with the use of a glass cold finger and a quartz glass injection point as explained in **Section 3.4.1** for the single-furnace. The photograph in **Figure 3.3** shows the double-furnace set-up.

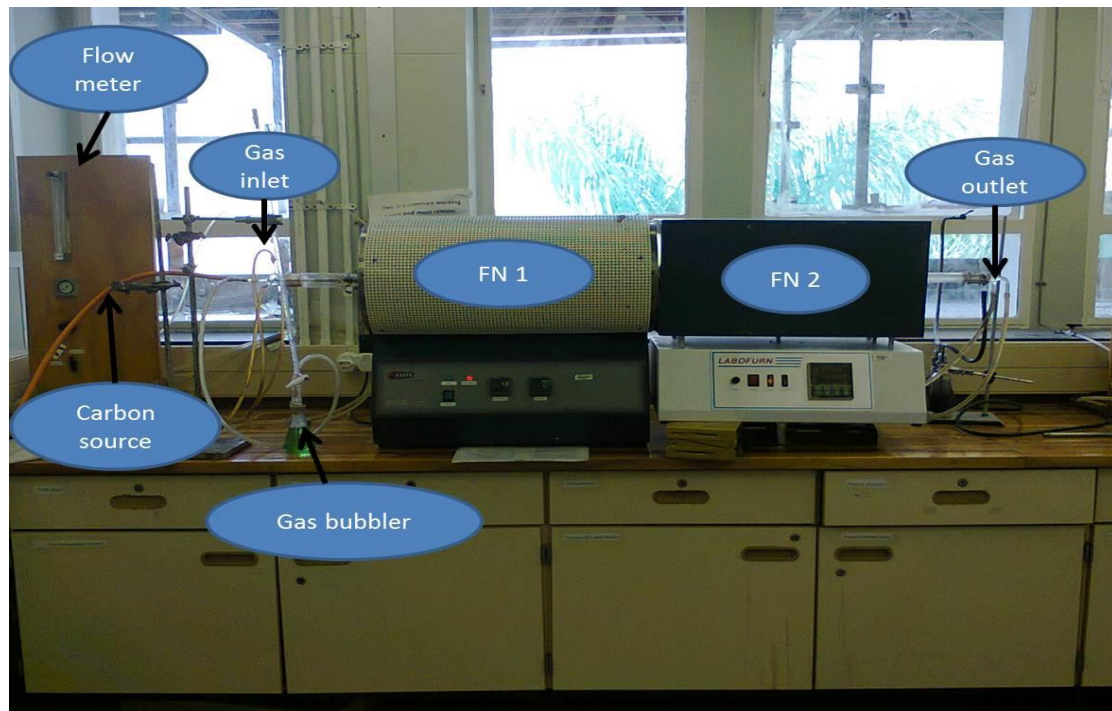


Figure 3.3: Photographic illustration of the double-furnace set-up where FN stands for furnace

3.4.3 Non-equilibrium plasma reactor set-up

Non-equilibrium PECVD apparatus was constructed with commercially available consumables. A simple schematic is provided in **Figure 3.4**. A power supply was connected to copper foils, which were used as the electrodes to provide the spark to initiate the plasma. The reactor was a quartz tube and the system was heated using two ceramic heaters.

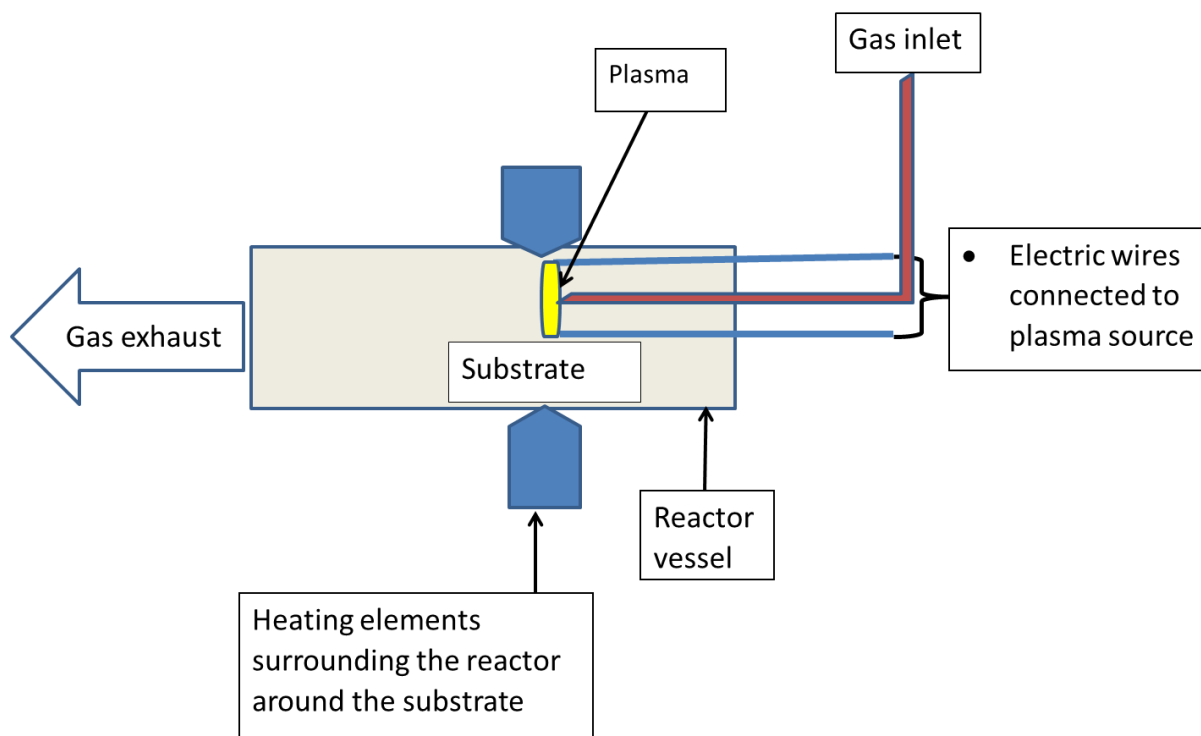


Figure 3.4: Schematic illustration of the non-equilibrium PECVD

Figure 3.5 consists of the complete set-up for non-equilibrium PECVD for MWCNTs. The system consists of an Electrical Supplies Corporation alternator, 0-260 V set at 110 V. The plasma driver, model PVM/DDR, was connected to the alternator. The plasma driver was connected with two 4 mm thick electrical wires which were in turn connected to a 10 mm x 3 mm x 2 mm copper foil. Two Unitemp infra-red ceramic heaters were connected to an RKC FJ02 temperature controller which was connected to a J-type thermocouple. The reactor vessel was a quartz tube with a diameter of 40 mm and a length of 25 mm. The system was closed by connecting the gas and plasma inlet to one end and to the other end was the gas exhaust. The gas flow rates were monitored using Swagelok variable area flow meters, VAF-G4-04S-1-0.

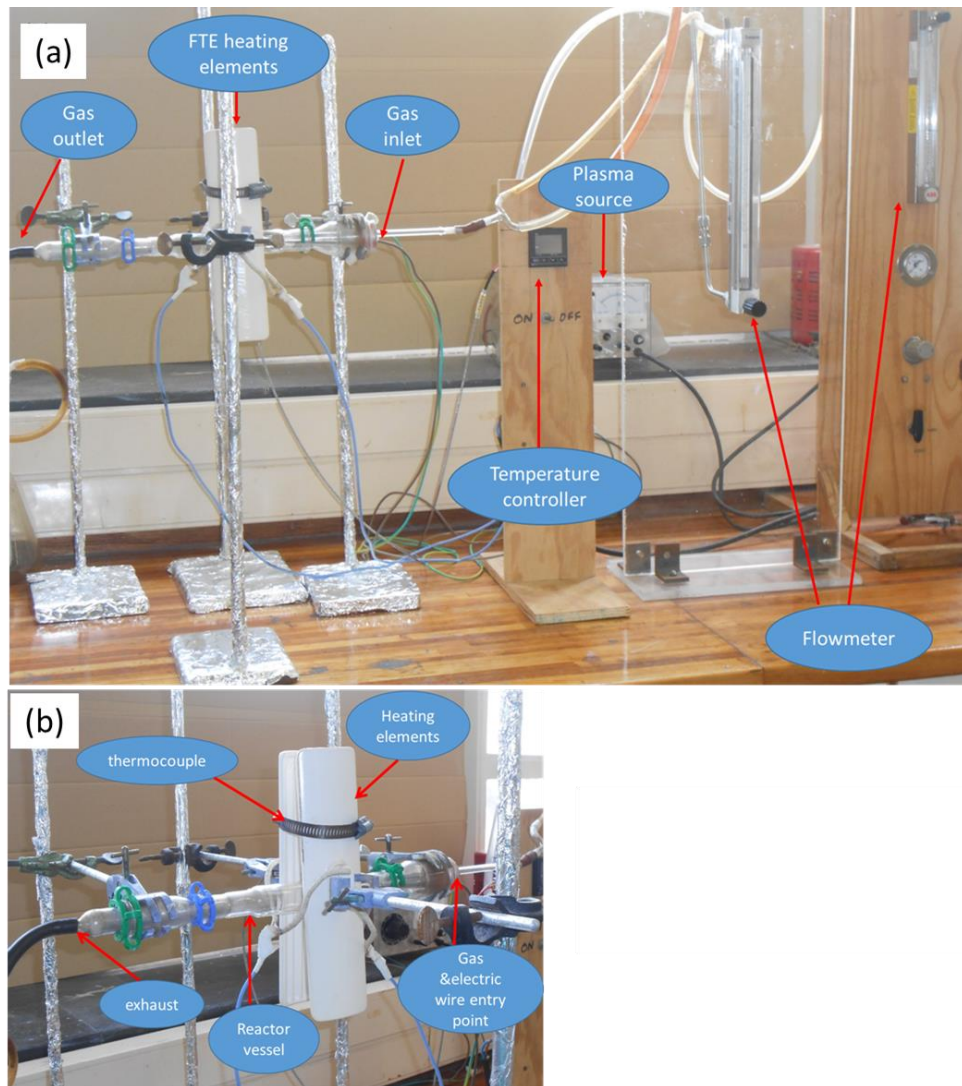


Figure 3.5: (a) whole non-equilibrium PECVD and (b) magnification of the reactor set-up for MWCNTs where full trough element (FTE) ceramic heaters were used

3.5 Synthesis of the MWCNTs

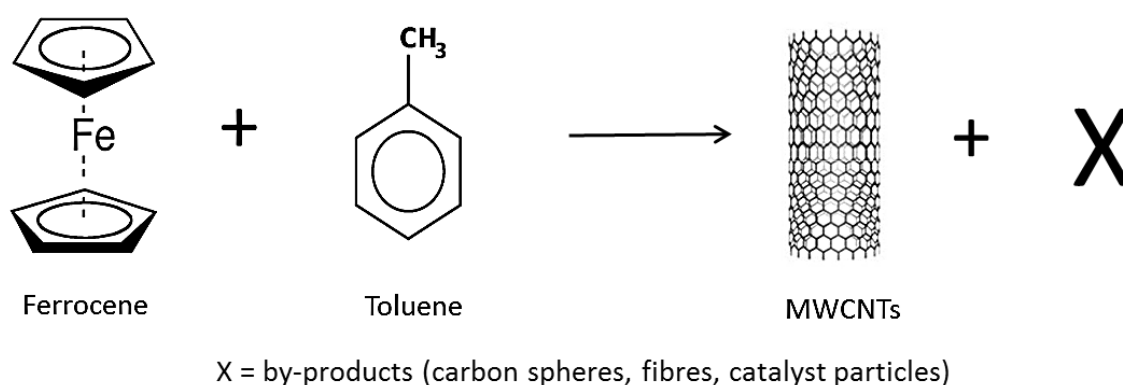
Once the reactors were set-up, the actual synthesis of the carbon nanotubes was carried out. The synthesis methods provided in the following sub-sections are divided according to the reactor designs.

3.5.1 Single-furnace approach

The floating catalyst CVD method was utilised.² The same method was used using different carbon sources. Lighter and heavier hydrocarbon sources were used for independent runs.

3.5.1.1 Ferrocene-toluene

A general thermal floating catalyst CVD synthesis which utilises ferrocene and toluene mixtures was used to produce MWCNTs. The scheme in **Scheme 3.1** shows the typical reaction between the catalyst and the carbon source which occurs during synthesis.



Scheme 3.1: A reaction scheme of MWCNTs synthesis

In this method ferrocene (0.25 g) was mixed with toluene (9.75 g). The mixture (10.00 g) was ultrasonicated using a digital ultrasonic heater, for 2 minutes until all the ferrocene had dissolved. The mixture was put in a 10 mL syringe and placed on the injection port, (**Figure 3.2 (a)**). A mixture of 10% H₂ balanced in Ar (10% H₂/Ar) was introduced into the system at 100 mL/minute, and then the furnace was ramped to 850 °C (T_{MAX}) at a rate of 10 °C/minute. The temperature was then held at T_{MAX}, and the ferrocene-toluene mixture was injected at 0.8 mL/minute using the syringe pump. After complete injection of the mixture, the system was left for a further 30 minutes at T_{MAX}, and then the reaction temperature was allowed to cool under the 10% H₂/Ar buffer gas mixture. The products were scrapped from the quartz tube hot zone region then weighed and characterized.

3.5.1.2 LPG

This method used the catalyst synthesised from the thermal decomposition method where: the catalyst solutions were spread on ITO substrate (**Figure 3.6**). The ITO was then placed in a quartz boat.

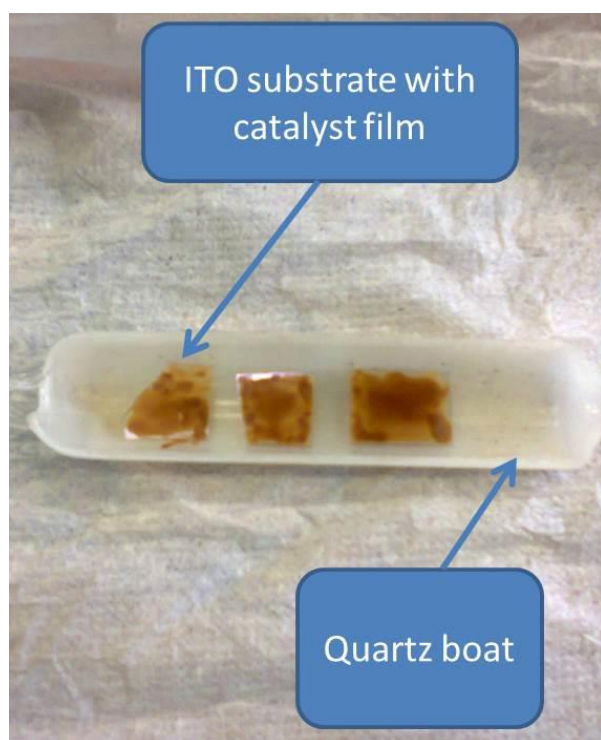


Figure 3.6: ITO substrate in a boat

The quartz boat was placed in the quartz tube reactor vessel before being placed in the hot zone of the furnace (**Figure 3.2 (c)**). To remove air, the system was flushed with LPG for 10 minutes and then flushed with 10% H₂/Ar for 10 minutes. The 10% H₂/Ar was then set to flow at a rate of 100 mL/minutes during the temperature ramps. The temperature of the furnace was ramped from ambient to 80 °C at 5 °C/minute, left to settle for 10 minutes. In the second step the temperature was increased from 80 to 150 °C at a rate of 2 °C/minute and thereafter maintained at 150 °C for 10 minutes. The final temperature stage was from 150 °C at a rate of 20 °C/minute, to T_{MAX} of either 600 °C, 700 °C or 800 °C. The 10% H₂/Ar flow was then terminated once T_{MAX} was reached and LPG was introduced at a rate of 100 mL/minutes. The LPG flow was maintained for 30 minutes. After 30 minutes the LPG flow was terminated and 10% H₂/Ar re-introduced during the cooling phase. The products were scrapped from the substrate and then taken for analysis.

3.5.2 Double-furnace approach

The procedure involved setting the temperatures of the two furnaces at 800 °C and 400 °C respectively.³ The carbon source was first activated in the higher temperature furnace, and the substrate with the catalyst was placed in the lower temperature furnace as illustrated in the schematic diagram (Figure 3.7).

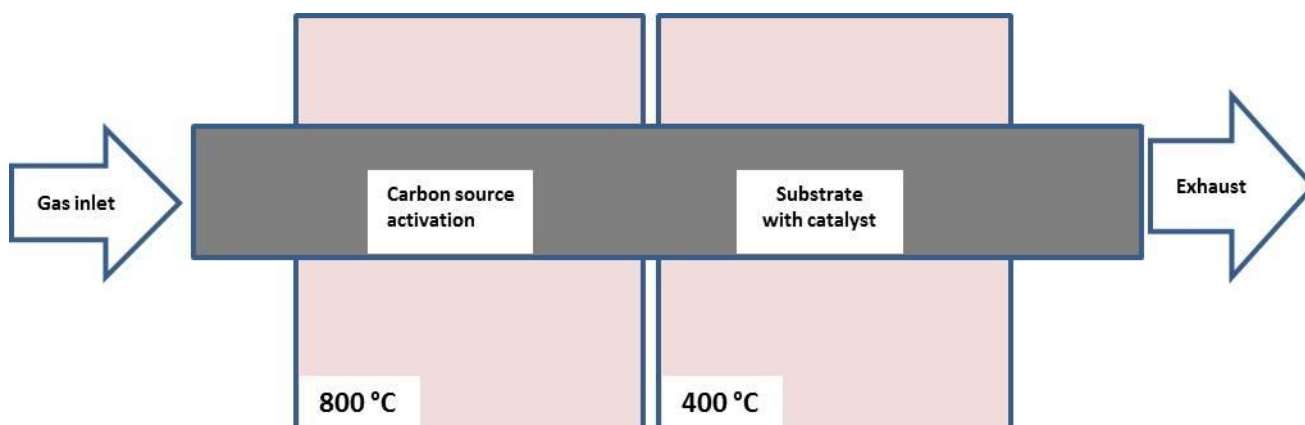


Figure 3.7: Schematic illustration of the double-furnace set-up for MWCNTs

The catalyst was spread on an ITO substrate, placed in a quartz boat, which was then placed in the hot zone of the 400 °C furnace. The carbon source, LPG, was put on the injection port of the 800 °C furnace. The temperature ramps were from ambient to 800 °C (T_{MAX}) at a rate of 10 °C/minute and ambient to 400 °C (T_{MAX}) at 6 °C/minute simultaneously in a flow rate of 10% H₂/Ar at 100 mL/minute. When the respective T_{MAX} was reached the 10% H₂/Ar flow was terminated and the LPG initiated at a rate of 100 mL/minute. The synthesis temperature was 30 minutes, after which the LPG flow was terminated and 10% H₂/Ar re-introduced for inert atmosphere as cooling took place before analysis of products.

3.5.3 Non-equilibrium PECVD approach

In this procedure, to optimise the reaction parameters for synthesis, five different temperatures were investigated i.e. room temperature, 50, 100, 150 to 200 °C as the T_{MAX} . The reaction time was also varied starting from 30 minutes down to 10 minutes. Also the carbon sources were varied from LPG, acetylene, methane to ethylene while the inert atmosphere was kept constant as Ar in all cases. The gas flow rates were kept at a ratio of 3:1 for the carbon source to the inert atmosphere

respectively. The synthesis procedure was divided into two stages, the substrate preparation and the CNT synthesis. Detailed information is provided in respective subsections.

3.5.3.1 Preparation of the substrate

An ITO glass (thermal stability, 666 °C) was used as the substrate. The ITO glass substrates were cleaned and part of ITO etched to give a non-etched: etched partition ratio of 1:3:2 to get 5:15:10 mm division. The ITO was protected from etching by covering the conductive sides with insulation tape which covered an area of 20 mm x 20 mm (**Figure 3.8**). A 200 mL acid solution containing HCl: H₂O:HNO₃ in the ratio 12:12:1 respectively was prepared. The prepared acid solution was heated to 70-90 °C on a hotplate. The ITO substrate (with masked areas) was placed in the solution for 60 seconds to etch the uncovered part. After etching the ITO substrate was rinsed under running tap water to remove and dilute excess acid. The covering insulation tape was then removed and the substrate was ultra-sonicated in a mixture of a detergent (Ajax) and distilled water for 10 minutes. This was followed by the thorough cleaning of the substrate with a cotton ball and acetone. The substrate was then rinsed in pure deionised water to remove the acetone and detergent and further ultra-sonicated for 10 minutes. The substrate was then ultra-sonicated in acetone for another 10 minutes and further ultra-sonicated in isopropanol for an additional 10 minutes. The substrate was left to dry in an oven using a temperature of 120-150 °C for 30 minutes until complete dryness was achieved. The metal NPs prepared by a co-precipitation method (**Section 3.3.2**), were diluted and drop dispersed, 10 µL of respective metal nanoparticle, 1 mg/mL in ethanol using a micro pipette. The MNPs were spread onto the conductive side of the hydrolysed ITO glass substrate covering the 15 mm x 15 mm area in the centre of the substrate (**Figure 3.8**). The other 5 mm x 5 mm and 10 mm x 10 mm ends of the conductive and non-conductive sides respectively were left to be electrode materials.

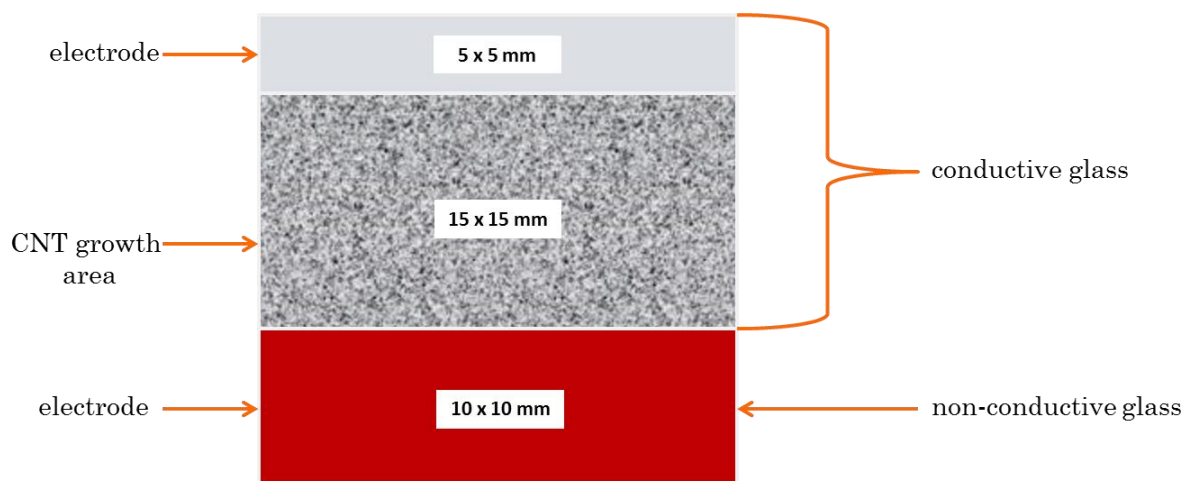


Figure 3.8: Schematic presentation of the 30 x 30 mm treated ITO substrate

3.5.3.2 Non-equilibrium PECVD approach procedure

The ITO substrate with metal NPs (as prepared in **Section 3.5.3.1**) was placed at the centre of the reactor vessel in the PECVD set-up. To remove the air, the system was flushed with the Ar gas for 5 minutes then purged with the carbon source for another 5 minutes. The radio frequency plasma driver was set at 50 W. The current of the plasma was 0.3 A. The substrate was heated up to the synthesis temperatures under Ar flow, at a flow rate of 100 mL/minute before turning off the Ar flow. The power supply was turned on and the current knob adjusted to initiate the plasma. Once the plasma was stable (2 minutes), the hydrocarbon source was slowly increased to a flow rate of 300 mL/minute for 10 minutes. Thereafter, the hydrocarbon flow was terminated and the Ar flow was ramped up. The power supply and the plasma were switched off and the system cooled under Ar flow. In terms of characterisation, two approaches were used (i) substrate including sample upon cooling and (ii) sample was scrapped out off the substrate and taken for analysis.

3.6 Characterisation

The MNP samples used for SEM, IR and TGA were dried in open air at room temperature for 24 hrs before being taken for analysis. All the data obtained from the instruments, which were saved in specific formats per instrument, were saved as ASCII files and then converted to MS Excel™ document format by using the computers connected to the instruments. Further data analysis was done using Origin® software.

3.6.1 Transmission electron microscopy

The structure, dimensions and topography of the MNPs and the MWCNTs were investigated by the use of transmission electron microscopy (TEM). A JEOL JEM 1010 model was used with a Mega view 3 camera attached. The MNP samples were prepared by diluting the catalyst solution, a pipette drop in 1 mL acetone and ultra-sonicated for 5 minutes at room temperature. A lacey or holey carbon-coated copper grid was dipped into the diluted solution and dried under a halogen lamp for 5 minutes. The grid was placed on the sample holder, loaded into the TEM, and images were taken at different magnifications from 80 000X-600 000X using a Mega view 3 camera. The particle sizes and MWCNTs diameter were determined using image J® software. A minimum of 100 particles or tubes were used for statistics.

3.6.2 Scanning electron microscopy

The investigation of the surface morphology of the MNPs and the MWCNTs was investigated by use of a scanning electron microscopy (SEM). The model was JEOL JSM 6100, with Zeiss Smart SEM version 5.03.06 software. An accelerating voltage of 5-10 kV was used. The sample holders used were stubs made of aluminium. A strip of double sided carbon tape was used to cover the top centre of the stub. To observe MNPs, a small sample size, usually a tip full of the spatula was spread on top of a carbon tape. The optimum working distance was 7 mm and the aperture size was 30 μm .

3.6.3 Electron dispersive X-ray spectroscopy

Energy dispersive spectroscopy (EDX) was used as a qualitative technique for the detection of the metals, carbon and oxygen, by showing their atomic ratios. A Bruker X-ray spectrometer attached to the JEOL JSM 6100 SEM instrument was used for EDX. The optimum working distance used was 4 mm. The magnification of images was at 2.5 μm and the scans lasted for 5 min. Bruker Espirit 1.8 software was used for data collection. The elemental mapping was performed on a separate instrument, a JEOL 2100, that was attached to the SEM instrument.

3.6.4 Fourier transform infrared spectroscopy

Fourier transformation infrared spectroscopy (FTIR) analysis was performed using a KBr pellet disk and an FTIR spectrometer. A Perkin Elmer Spectrum 100 instrument was used. Dry potassium bromide (150 mg) powder and 2 mg of respective sample were ground using a motor and pestle. The mixture was pressed into a pellet using 10 Tons of pressure for 2 minutes in a ring press model 00-25 supplied by Research Industrial Company, England. The CO₂ absorption in the background was removed by air scanning. The resolution used was 4 cm⁻¹, in a spectral range of 4000-400 cm⁻¹.

3.6.5 Thermogravimetric analysis

Thermal stability, residual metal and the organic content analysis was confirmed by using a TA Instrument Q series™ Thermal Analyser TGA (Q600). The measurements were done in air at a flow rate of 50 mL/min from ambient temperature to 1000 °C. The isothermal time was 1 min with a ramp temperature of 10 °C/min. To acquire the data, a TA instruments Universal Analysis 2000 software package was used. To re-plot the weight loss curves Origin® software was used.

3.6.6 Raman spectroscopy

The carbon products were analysed with a Raman spectrometer; model Delta Nu Advantage 532™. The grating lines were 1800 per mm. The laser excitation wavelength was 532 nm and the power generally used was medium high according to the software of the instrument. Integration time of 45 s and a resolution 10 cm⁻¹ was set. Spectral analysis was done using an average of three spectra for each MWCNT sample. Background smoothening and baseline correction was done by using the Software 2D CCD detector provided with the Raman instrument.

References

- (1) Choi, G.; Cho, Y.; Son, K.; Kim, D. Mass production of carbon nanotubes using spin-coating of nanoparticles. *Microelectronic engineering* **2003**, *66*, 77-82.
- (2) Oosthuizen, R. S.; Nyamori, V. O. Heteroatom-containing ferrocene derivatives as catalysts for MWCNTs and other shaped carbon nanomaterials. *Applied Organometallic Chemistry* **2012**, *26*, 536.
- (3) Leonhardt, A.; Ritschel, M.; Kozhuharova, R.; Graff, A.; Mühl, T.; Huhle, R.; Mönch, I.; Elefant, D.; Schneider, C. M. Synthesis and properties of filled carbon nanotubes. *Diamond and Related Materials* **2003**, *12*, 790-793.

Chapter Four

SYNTHESIS OF METAL NANOPARTICLES

This chapter focusses on the synthesis of the catalysts, metal nanoparticles. Details of the properties of the products in terms of the metal nanoparticles size, thermal stability and morphology using different characterization techniques are discussed. The main focus is on size and dispersion of the product in relation to the function.

4.1 Introduction

Metal nanoparticles (MNPs) of single metals (Fe, Co, and Ni) and mixed metals (CoFe, NiCo and NiFe) were synthesised using two synthesis methods, i.e. thermal decomposition and co-precipitation. The MNPs results were categorised according to the synthesis methods. The data in all the MNPs synthesis methods were grouped according to the technique used. A comparison of the two synthesis methods was summarised at the end as the last section of synthesis methods to form a conclusion. An ITO coated glass was the substrate of choice in all synthesis steps due to its optical transparency and electrical conductivity properties which are relevant to the energy conversion device application.¹ In nature, ITO coated substrate is an n-type semiconductor. Therefore, the characteristic large band gap (around 4 eV) is recognised. The ITO substrate is predominantly transparent in the visible part of the spectrum.² The surfactant, HDA, was added to stabilise and protect the resultant reduced metal nanoparticles since they are not stable as their respective metal precursors.³ The addition of the surfactant was also necessary to improve the solution homogeneity thereby also reducing light scattering. This is crucial for later and final application.⁴

4.1.1 Thermal decomposition

Thermal decomposition method was performed as a preliminary method to see if MNPs could be synthesised in as few steps as possible. The choice of the method was in comparison with other bottom up synthesis methods which include the sol gel dip coating and spray pyrolysis, where metal precursors undergo hydrolysis and poly-condensation reactions with sedimentation and

centrifugation amongst other steps involved.⁵ The thermal decomposition method entailed dissolving the metal salt precursors and the HDA in alcohol (ethanol). This was carried out to ensure that the surfactant would absolutely dissolve consequently enhancing the solubility of the surfactant. Characteristically, increased solubility enhances the chances of random solvent-surfactant interactions.⁶ The three temperature ramps were in such a way to; dry the solution on the substrate, decompose the resulting metal solution layer and finally ensure that synthesis of the desired metal oxides would be achieved. The temperature ramps were limited to 600 °C to sustain the substrate because higher synthesis temperatures in ignition may lead to destruction.^{2,7} The results presented were for the morphology and surface structure (SEM, EDX and TEM). No further characterisation was ultimately performed for the MNPs synthesised under this method. This was because for instance when XRD was tried on the samples glass (Si) peaks were reflected.

4.1.1.1 SEM and EDX

The morphology of MNPs was studied with SEM after deposition on the surface of the ITO glass substrate. EDX analysis was performed to investigate the presence of the MNPs. The EDX spectra of respective MNPs catalyst were presented as individual figures with respect to the MNP synthesised. SEM and EDX analysis were executed on various parts of the ITO substrate. EDX spectra showed detection of peaks assigned to traces of precursor elements (Cl) and the ITO substrate elements (Sn, In and O₂). Additional peaks detected on the spectra were attributed to peak overlapping due to the resemblance in their energy states. The images in **Figures 4.1, 4.2 and 4.3** show the results observed using the thermal decomposition method for the synthesis of nanoparticles at 400, 500 and 600 °C.

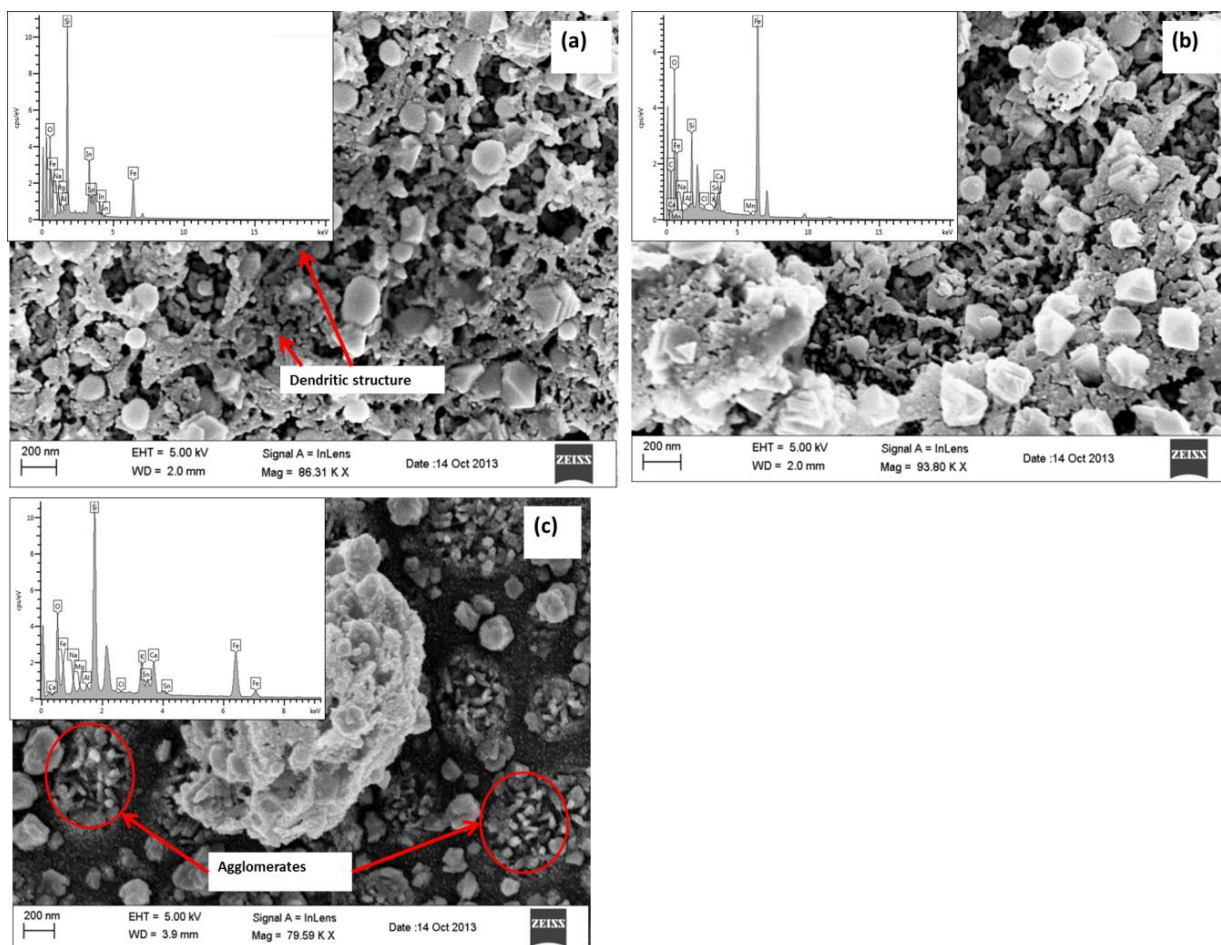


Figure 4.1: Iron nanoparticles on ITO substrates synthesized using the thermal decomposition method at (a) 400, (b) 500 and (c) 600 °C with inserts of respective EDX spectra

The images in **Figure 4.1 (a)** and **(b)** for 400 and 500 °C respectively showed structures that looked like large spherical particles on top of needle like structures or dendritic structures (see arrows). The structures resembles a nano-porous network.⁸ The image in **Figure 4.1 (c)** showed structures that looked like a nano-porous network that has been fragmented into various separate agglomerates (see red circles) possibly due to sintering at the higher temperatures.⁹ Essentially, the observed images showed trends from 400 to 600 °C where Fe NPs and nano-microstructures were synthesised. These structures could be used for CNT synthesis; however, there was poor dispersion of metal particles and more of a rough film formed. A representative EDX spectrum for the Fe nanoparticles is presented as inserts for respective temperatures. The EDX analysis showed a spectrum with traces of substrate elements (In, Sn, O₂) and the other elements (Na, Mg, Al) that were suggested to be a result of overlapping peaks since they were not part of the precursor elements. For instance, in the K group, Mg K_β and Fe K_α forms an overlap. Nanoparticles synthesised from Ni were analysed and the SEM images are presented in **Figure 4.2**.

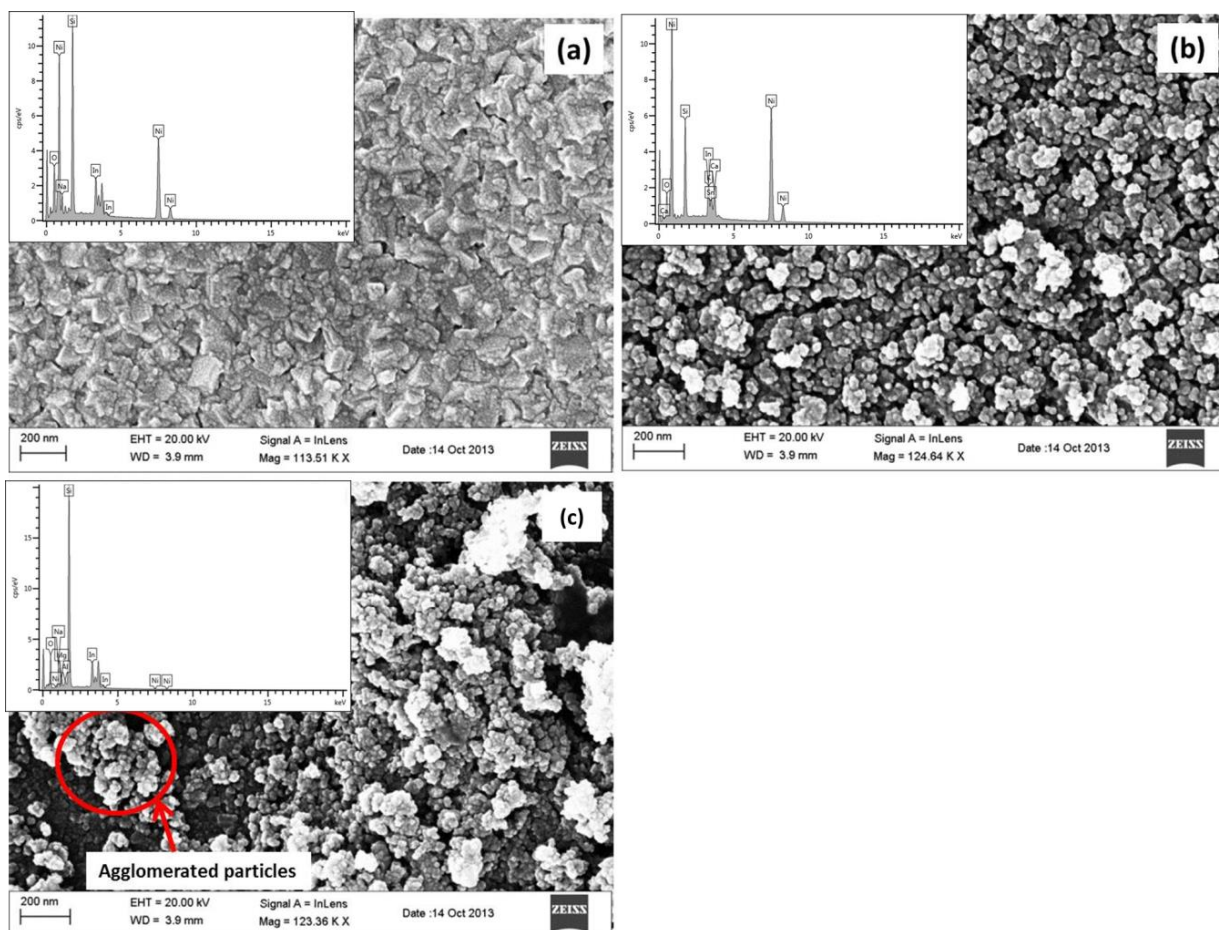


Figure 4.2: Nickel nanoparticles on ITO substrates synthesized using the thermal decomposition method at (a) 400, (b) 500 and (c) 600 °C with inserts of respective EDX spectra

Low temperature images (**Figure 4.2 (a)** and **(b)**) showed a more continuous film, and as the temperature increase to 600 °C (**Figure 4.2 (c)**) the structure changes to agglomerate form and more porous deposit forms. Similar trends were also reported by Miller and co-workers as the synthesis temperature was increased from 400 to 600 °C.¹⁰ EDX analysis was performed and a representative spectrum is presented as an insert in each image. The EDX spectra showed the presence of the traces of the ITO substrate (In, Si, O₂). EDX measurements showed the Si peak as the dominant element and this was attributed to the glass substrate material.¹¹ SEM image analysis of the synthesised Co nanoparticle is represented in (**Figure 4.3**).

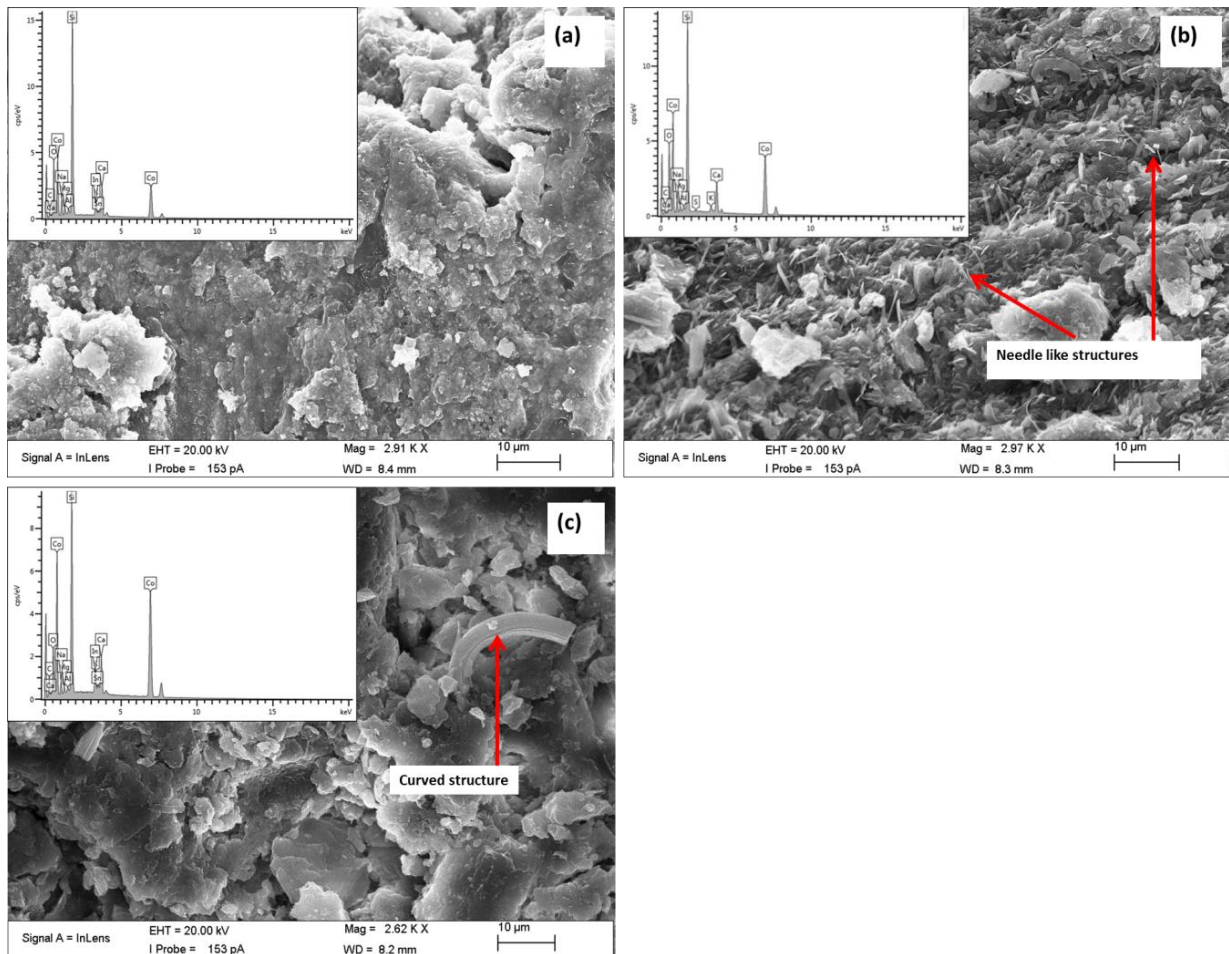


Figure 4.3: Cobalt nanoparticles on ITO substrates synthesized using the thermal decomposition method at (a) 400, (b) 500 and (c) 600 °C with inserts of respective EDX spectra

As observed in the case of Fe and Ni, almost similar trends in terms of the particle agglomeration were observed for Co MNPs, however, the 500 °C image (**Figure 4.3 (b)**) show needle like structures. In **Figure 4.3 (c)**, at 600 °C, structures that appeared curved were observed. Agglomeration of the MNPs was more observed in the highest temperature (600 °C). EDX analysis was carried out to identify the components of the synthesised MNPs. Respective EDX spectra are presented as inserts. The EDX spectra for Co nanoparticles showed the presence of In, Si, Sn and O₂ which were attributed to the nature of the substrate material. The elements Ca, Na, Mg and Al were shown as trace elements. These were attributed to peak overlaps. Mixed metal catalysts were tried for MNPs synthesis. SEM analysis for CoFe mixture is presented in **Figure 4.4**.

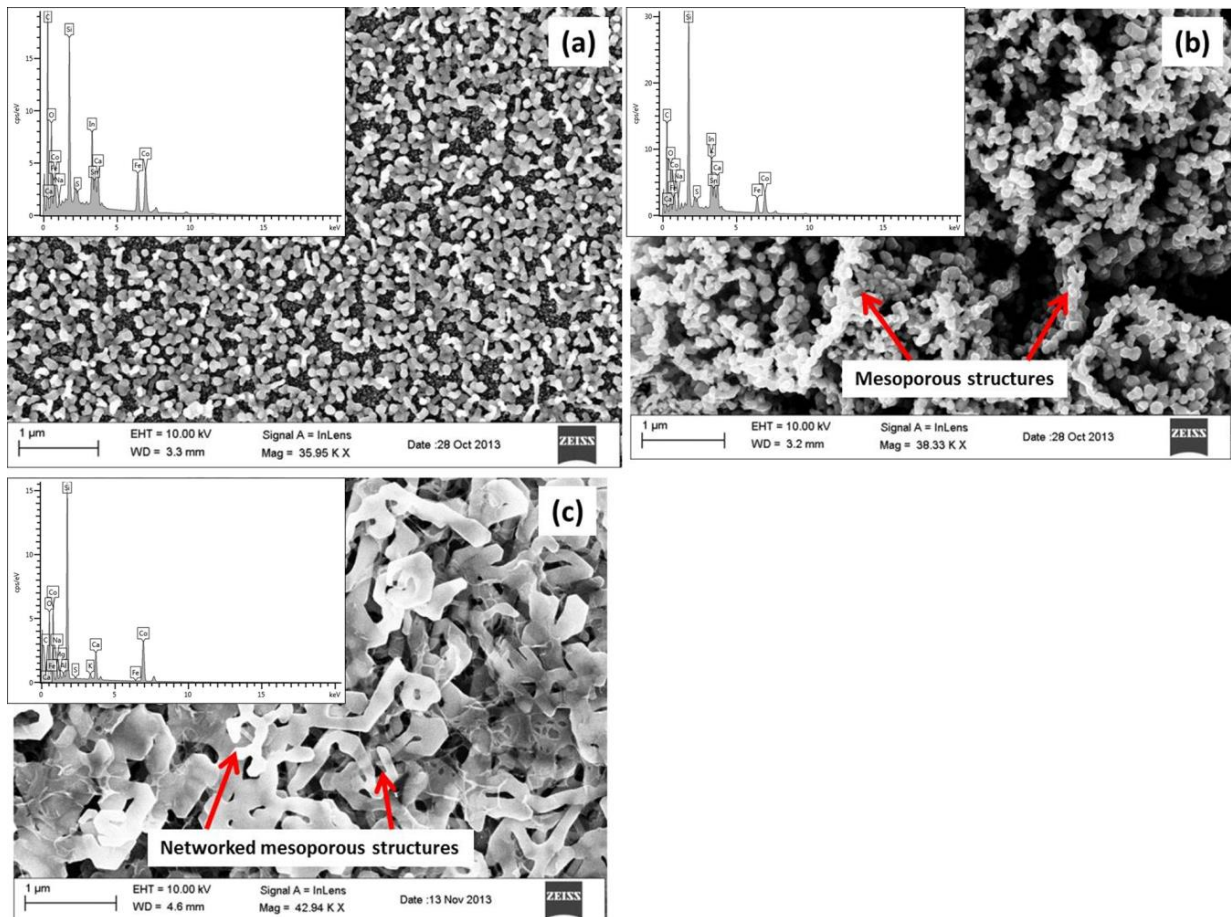


Figure 4.4: Cobalt-iron nanoparticles on ITO substrates synthesized using the thermal decomposition method at (a) 400, (b) 500 and (c) 600 °C with inserts of respective EDX spectra

The image for synthesis at 400 °C (**Figure 4.4 (a)**) showed that a uniform film of CoFe nanostructures was formed. As the temperature was increased to 500 °C (**Figure 4.4 (b)**) morphology changed the particles resembled mesoporous structures. The 600 °C image (**Figure 4.4 (c)**) showed a network of mesoporous structures,¹² that have a rough, dense microstructure due to agglomeration.¹³ Therefore, this showed that as the temperature was increased agglomeration of the nanoparticles became more pronounced.¹⁴ EDX spectrum for CoFe analysis is presented in inserts. The metallic Co and Fe elements were detected. In, Si, Sn and O₂ peaks observed were assigned to the ITO glass substrate.

The effect of temperature on particle size of the metal oxides was investigated at each T_{MAX} (400, 500 or 600 °C) by monitoring the surface changes of the resulting nanoparticles. In this thermal decomposition synthesis method, it was observed that, thick films with rough and dense nano-microstructures were produced due to agglomeration. The observed images showed well defined

respective nanoparticles at low temperatures (400 and 500 °C), while at high temperatures (600 °C) they had continuous undefined mesoporous structures. Nanoparticle clumps were observed as the temperature increased.¹⁵ This observation is also supported in literature which explains the correlation between temperature and aggregation.^{11,14} Higher temperatures are responsible for the aggregation of metal nanoparticles. This is because when the temperature is high there is an increased kinetic energy in the molecules of the nanoparticles hence, high surface tension of the particles is inevitable.¹⁶⁻¹⁸ Therefore, these structures could be used for CNT synthesis. However, there was poor dispersion of metal particles and more rough films were formed. Therefore, for these reasons the thermal decomposition method was not pursued for other mixed metal MNPs (NiCo and NiFe). To further investigate the synthesised MNPs, TEM image analysis was performed.

4.1.1.2 TEM

The TEM analysis determined the dimensions of the MNPs. The data obtained from TEM correlated well with the SEM data. It was observed that there was pronounced agglomeration in the samples. **Figure 4.5** shows the agglomerated MNPs as observed.

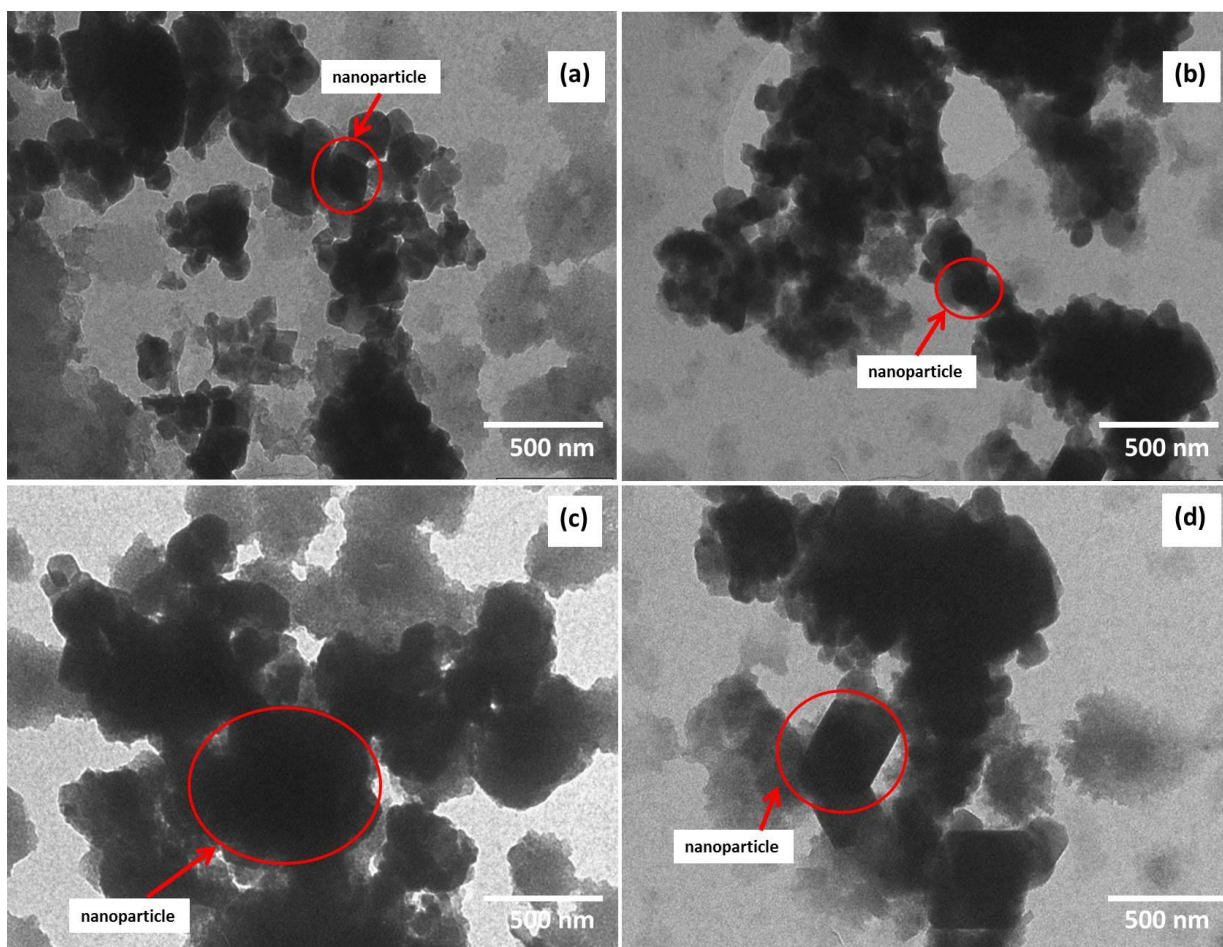


Figure 4.5: TEM images of nanoparticles synthesized when the thermal decomposition method was used at 400 °C; (a) iron, (b) nickel, (c) cobalt and (d) cobalt-iron

The TEM images showed two fused structures, with different colour intensities. The observed dark sections (in red circles) were attributed to the agglomerated MNPs as described by Shen *et al.*¹⁹ Another study by Tabares *et al.* observed similar images and they attributed them to the formation of agglomerated MNPs.²⁰ The grey sections were attributed to the surfactant coating, as similar to core-shells synthesized and reported by Christian *et al.*²¹ Having synthesized agglomerated MNPs using the thermal decomposition method another method, co-precipitation, was employed in an effort to synthesize dispersed MNPs.

4.1.2 Co-precipitation

The electron microscopy studies of the thermally decomposed MNPs show irregularly shaped particles that were agglomerated. Thus, the co-precipitation method was employed. The synthesised MNPs were characterized mainly using SEM and TEM for surface topography and TGA

for residual metal content as well as the determination of the presence of the organic coating. During synthesis, the colloidal solutions were maintained at a pH of ≈ 11 . This optimum pH was based on a study by Mahdavi *et al.* in which iron oxide nanoparticles were synthesised.²² The group used iron chloride hexahydrate and tetrahydrate precursors, using the co-precipitation method and they concluded that particle size of the nanoparticles relied on pH. Therefore, nanoparticle sizes would be reduced with increasing pH from pH8 to pH11 and increased with pH rise from 11.²³ Herranz *et.al* also suggested that a pH of 11 is capable of maintaining the molar ratios of the precursors under a non-oxidative environment.²⁴ The reaction temperature was maintained at 80 °C since the surfactant was added from the beginning of synthesis. Therefore, this temperature would be suitable to assist the prevention of any potential intermediate complexes to form.^{25,26} During the course of the reaction, a vigorous agitation was necessary to help dispersion by inhibiting nanoparticle growth and surface attractions that could lead to agglomeration of the nanoparticles. The surfactant, HDA, was added as aliquots to the metal chloride and ammonia solution such that the surfactant would be able to enclose the surface of the MNPs.²⁷ The first aliquot of HDA acted as the primary surfactant whilst additional aliquots acted as the secondary surfactant. These aliquots had different effects on the growth of the nanoparticles. The polar heads of the first surfactant are bound to adsorb onto the MNP catalyst particles and the nonpolar tails are left floating in the solvent system.²⁸ Van der Waals forces are responsible for the interaction between the additional aliquots of the surfactant and the first surfactant aliquot. The tails of the first surfactant that are left floating around in the solvent system then bind with the nonpolar tails in the additional surfactant. The interaction leaves the polar heads to be solvent and ammonia bound.²⁹ Hou *et al.* synthesised Ni nanoparticles using Ni(acac)₂ precursor and HDA and triocetylphosphine oxide as surfactants to control the metal size.³⁰ They reported that growth of the resulting oxide was dependent on HDA, smaller Ni nanoparticle diameters were related to the addition of HDA. The synthesised MNPs were then characterised using SEM and EDX.

4.1.2.1 SEM and EDX

For analysis, the Co nanoparticles were spread on ITO and dried under heat at 300 °C for 1 hour. SEM image analysis was done on the ITO glass substrate. The resulting MNPs showed that there was sintering of the MNPs. Hence, the adopted procedure was to dry the synthesised metal solutions in an oven at 100 °C for 4 hours without dropping the sample on ITO glass substrate. SEM images observed for each respective MNP are shown in **Figure 4.6**.

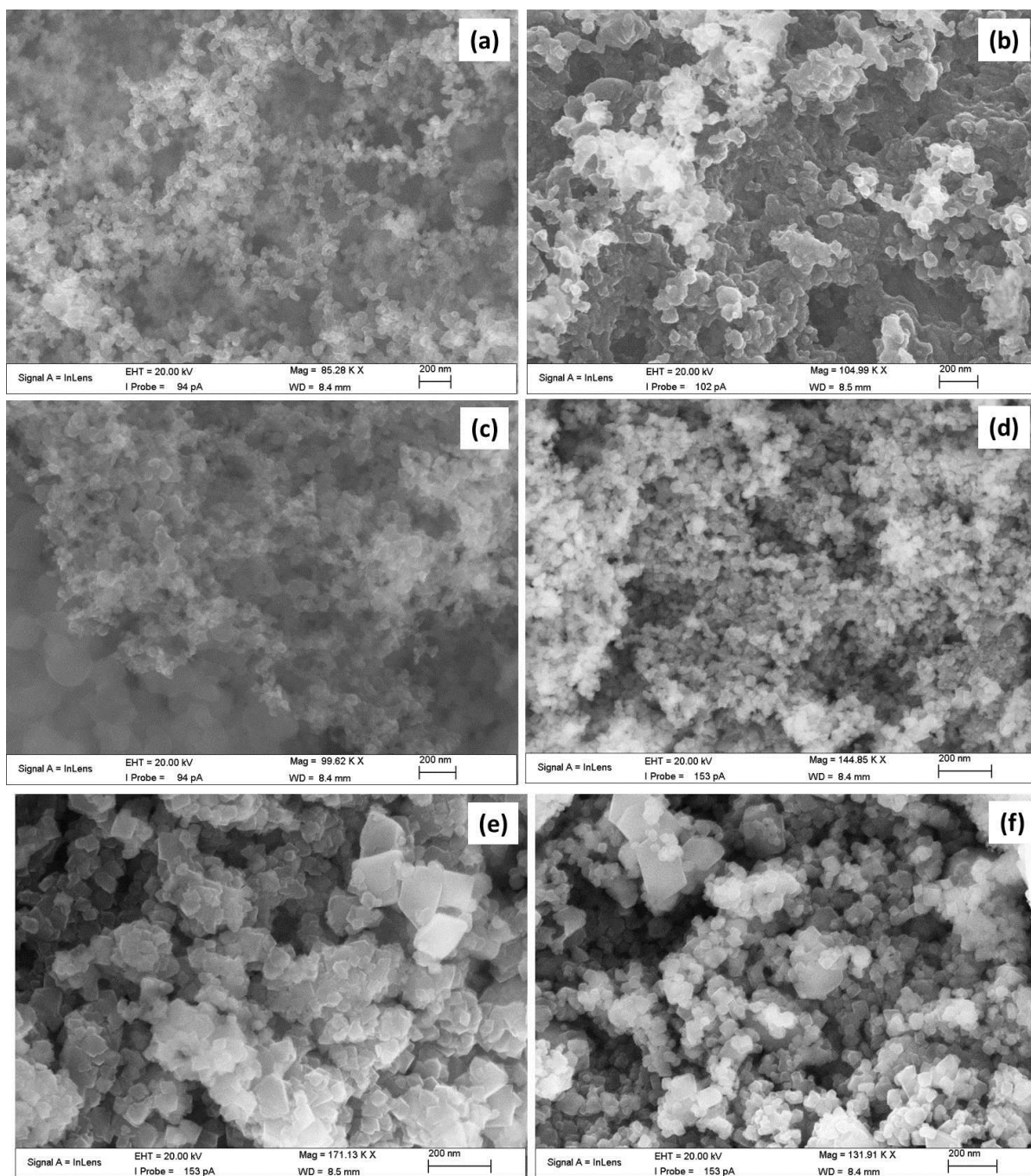


Figure 4.6: SEM images of co-precipitation synthesised metal nanoparticles (a) iron, (b) cobalt, (c) nickel, (d) cobalt-iron, (e) nickel-cobalt and (f) nickel-iron

The SEM images showed well shaped MNPs with almost uniform sizes. Data from SEM images was supported with EDX analysis (**Figure 4.7**) which showed the presence of the metals in the samples.

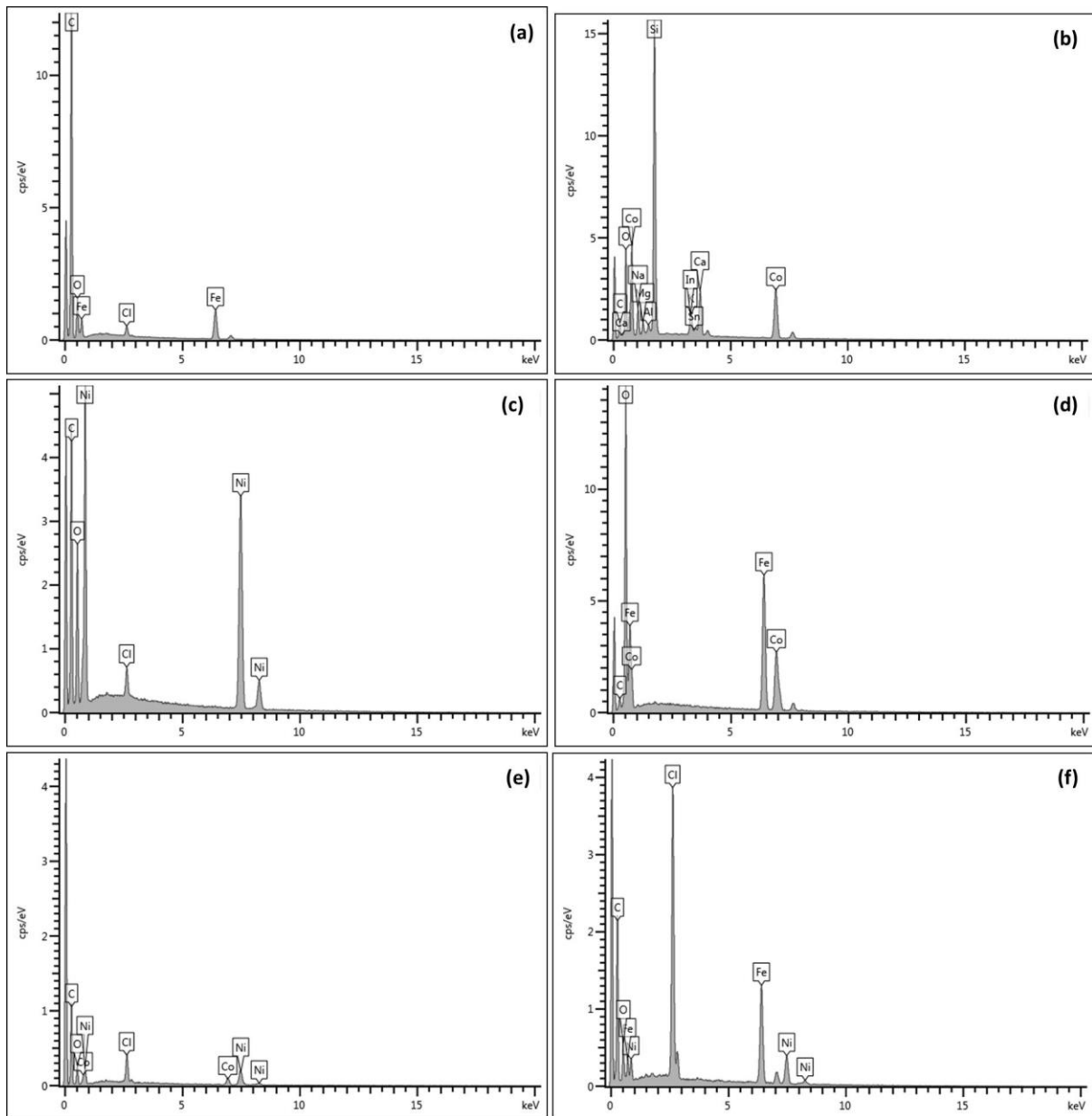


Figure 4.7: EDX spectra of co-precipitation synthesised metal nanoparticles (a) iron, (b) cobalt, (c) nickel, (d) cobalt-iron, (e) nickel-cobalt and (f) nickel-iron

However, the data obtained from EDX was limited to qualitative elemental analysis. The accuracy of the spectrums could have been affected by the nature of the samples. Other contributing factors to the limitations were assigned to the composition of the signal produced (X-rays, secondary and backscattered electrons). During sample bombardment there is characteristic noise interference and the limited alternating number of electrons. In other samples, **(Figure 4.7 (a), (c), (e), and (f))**, the EDX detected traces of other elements including Cl, that were attributed to the residual metal precursor in the samples. As stated earlier, since only the sample of Co was placed on ITO substrate,

in **Figure 4.7(b)** peaks for Si, O₂, Sn and In were attributed to the substrate nature. **Figure 4.8** shows representative atomic weight % ratios for single metal (Fe) and mixed metal (CoFe).

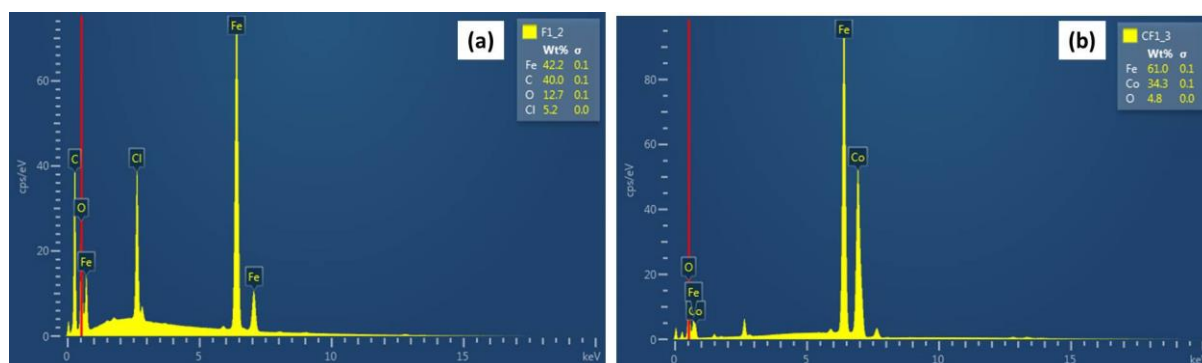


Figure 4.8: EDX spectra of co-precipitation synthesised metal nanoparticles with the atomic weight % of (a) iron, and (b) cobalt-iron

Generally, the EDX spectra for single metal catalysts showed atomic weight % ratio of the metals with the carbon in a 1:1 ratio. **Figure 4.8 (a)** shows a representative spectrum for Fe with insert showing the atomic weight % ratios. The EDX spectrum for mixed MNPs showed that atomic weight % ratios corresponded with the expected molar ratios of the mixed metals for instance, Co to Fe ratios in the CoFe MNPs spectrum (**Figure 4.8 (b)**). The stoichiometric ratio of Co to Fe was 1:2, indicating the ferrite nature of CoFe₂O₄ nanoparticles.³¹ Carbon from the carbon tape was excluded from being detected. Therefore the signal from carbon (C) was attributed to the organic coating (HDA) around the surface of MNPs which prevents aggregation of the nanoparticles.^{32,33} The metal nanoparticles were most likely to be oxides because small diameter MNPs have very huge surface area to volume ratios therefore they get easily oxidised even though they were synthesised under non-oxidative conditions.³⁴ Representative false colour maps of the CoFe analysis are shown in **Figure 4.9**.

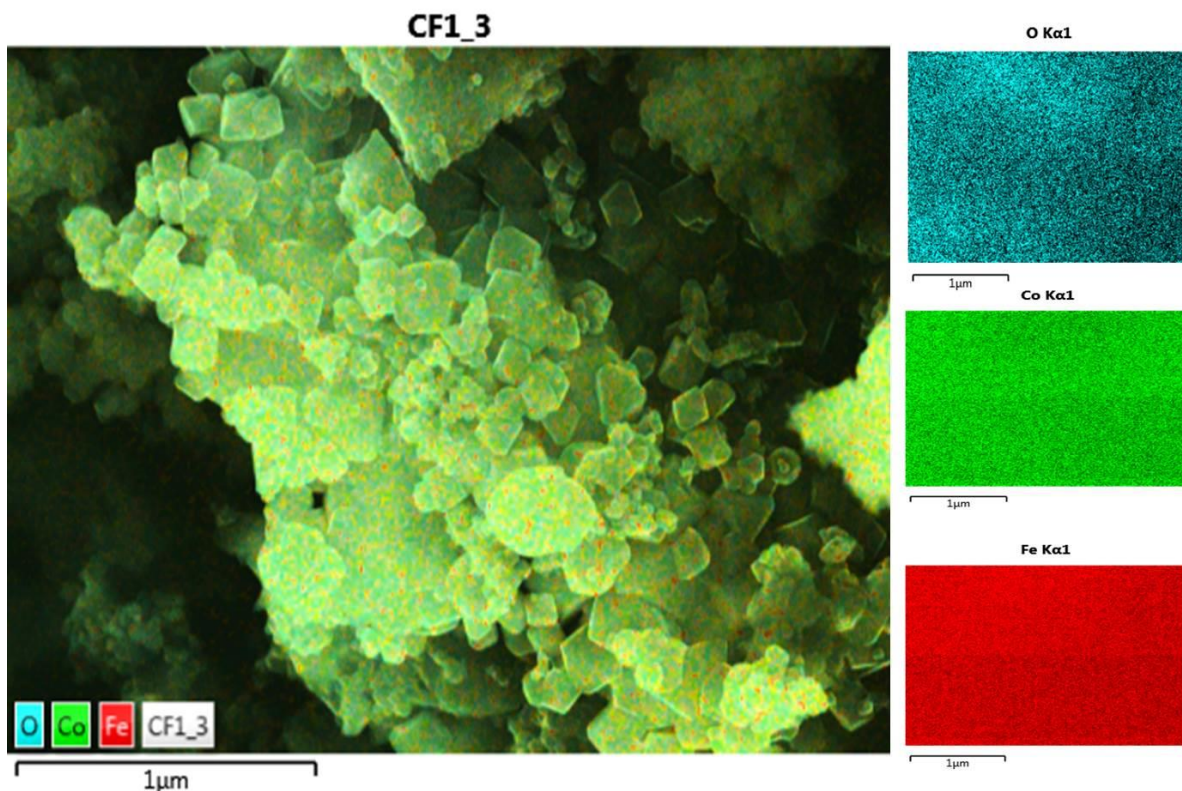


Figure 4.9: Representative CoFe false colour maps indicating the distribution of the metals in the synthesised MNPs using co-precipitation method

The chemical elemental maps of Fe and Co (in the ratio 2:1 respectively) showed a uniform distribution of the atoms which suggests that a homogeneous distribution of nanoparticles on the substrate was obtained.³⁵ TEM image analysis further characterised the morphology of the synthesised MNPs.

4.1.2.2 TEM

In order to ascertain the observations for SEM analysis further characterisation was done using TEM analysis to determine the actual size and structure of the MNPs and their state of agglomeration.

Figure 4.10 shows the TEM images of the respective MNPs.

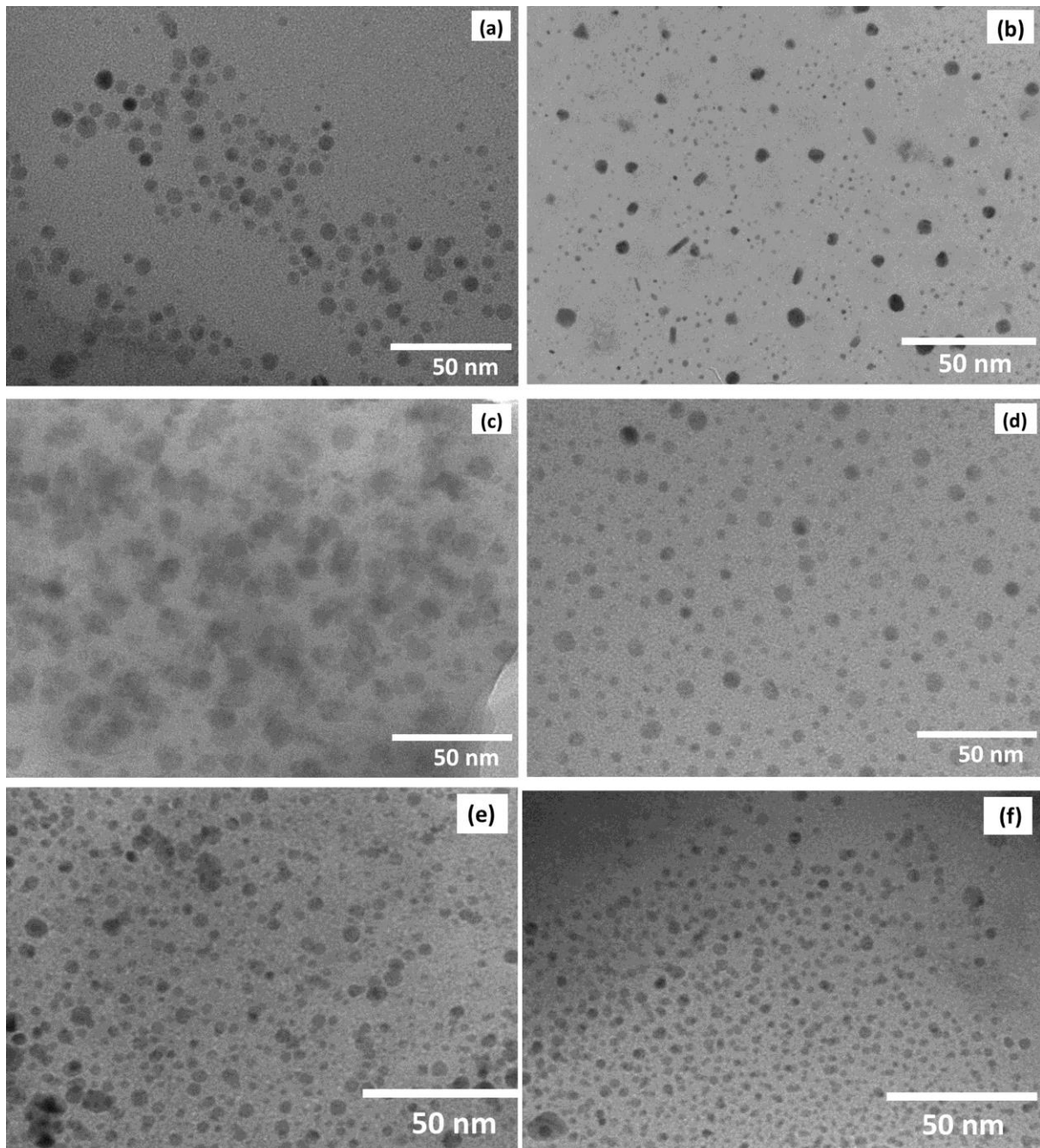


Figure 4.10: TEM images of co-precipitation synthesised metal nanoparticles; (a) iron, (b) cobalt, (c) nickel, (d) cobalt-iron, (e) nickel-cobalt and (f) nickel-iron

The images in **Figure 4.10** show that the metal nanoparticles of Fe **(a)** and CoFe **(d)** had spherical shapes, while those from Co and Ni had shapes that looked like irregular elongated spheres. All nanoparticles synthesised were well dispersed and showed uniform sizes. Hence, histograms showing the particle size distribution can be plotted and the mean particle sizes as well as the standard deviations can be determined (**Figure 4.11**).

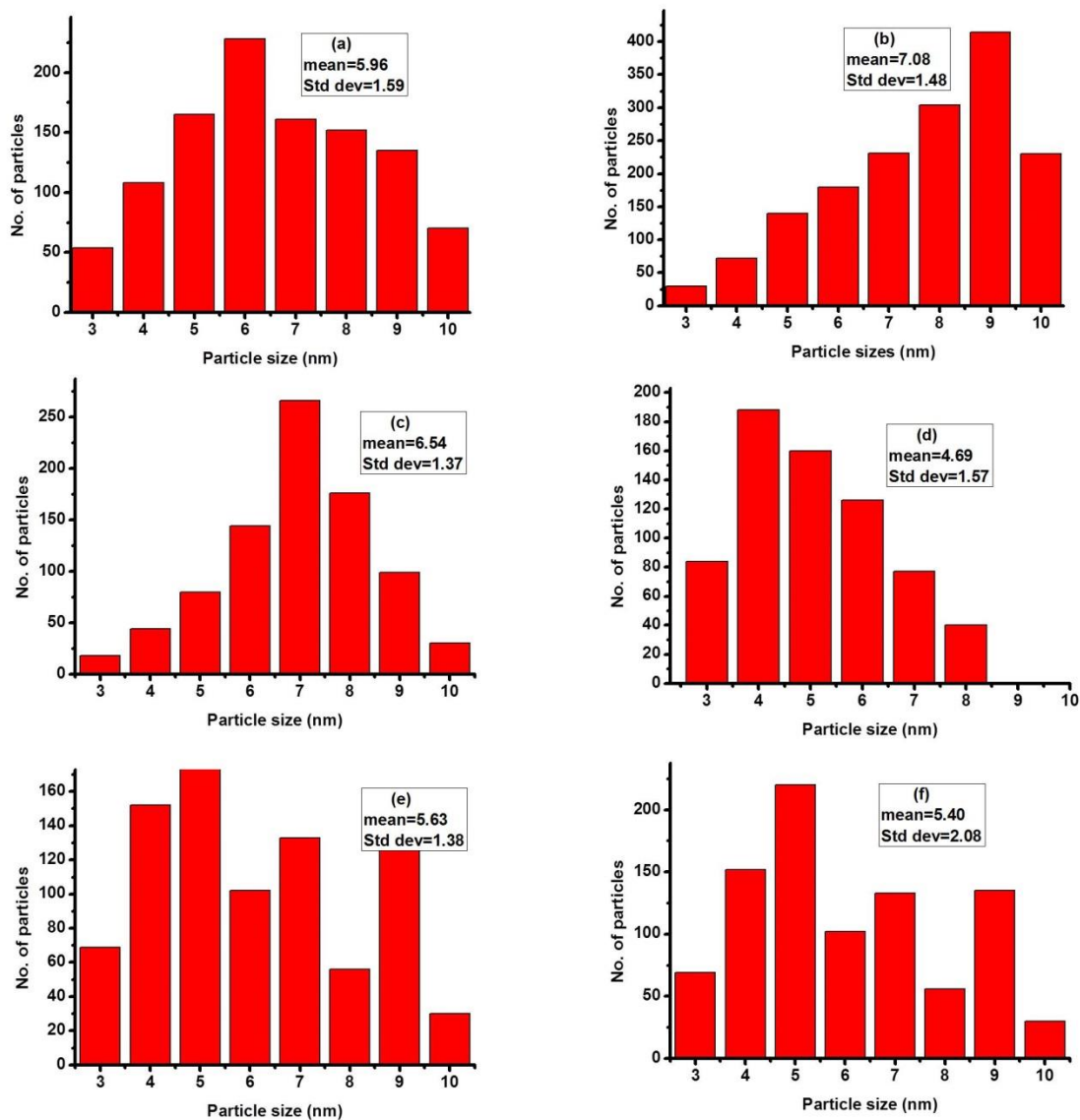


Figure 4.11: Histograms for the sizes of co-precipitation synthesised metal nanoparticles; (a) iron, (b) cobalt, (c) nickel, (d) cobalt-iron, (e) nickel-cobalt and (f) nickel-iron

The particles show a narrow size distribution in the range of 3-10 nm. There is no noticeable difference between the images of single and bimetallic catalysts. Chemical mappings (**Figure 4.9**) show the respective composition of the samples. The co-precipitation synthesised metal nanoparticles were well dispersed. This suggested that HDA played a key role as a surfactant as well as the reducing agent as reported in literature by Li *et al.*²⁷ The metal precursors were reduced from +3, or +2 (Fe, Co and Ni) to their respective zero valence oxidation states. However, the presence of oxygen in EDX could suggest that metal hydroxides were formed. Apart from that, the presence of oxygen signifies metal oxides due to the oxidation by air. This is because the synthesised MNPs have a very large surface area which enhances oxidation.¹⁹ HDA acts by forming co-ordination complexes

with the metal ions in the solution. The amine head surrounds the nanoparticles formed thus reducing sintering.³⁶ To further understand the role of HDA and the chemical environment of the final product, FTIR analysis was done.

4.1.2.3 FTIR spectroscopy

FTIR spectroscopy was used to determine the vibrational and stretching frequencies of the functional groups present in the synthesised MNPs. The formation of the MNPs, through the interaction between the surfactant and the MNPs, was thus further confirmed. The image in **Figure 4.12** shows the IR spectrum for pure HDA.

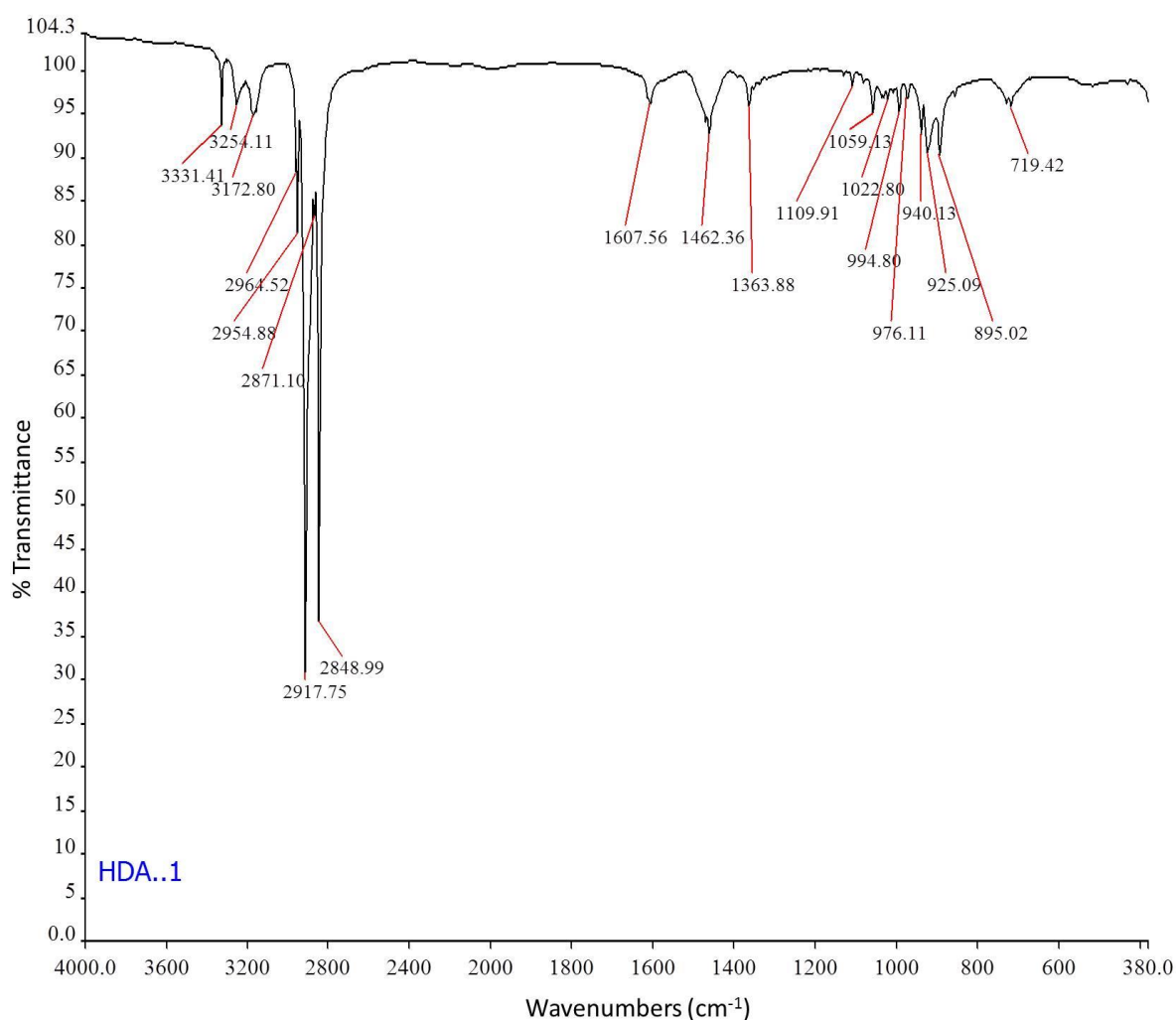


Figure 4.12: Hexadecylamine IR spectrum as analysed using ATR instrument

The peak assignments of the HDA spectrum were given as a summary in **Table 4.1**.

Table 4.1: Summary of the main peaks of the HDA as analysed using FTIR³⁷⁻³⁹

| Peak wavenumber (cm ⁻¹) | Assignment |
|-------------------------------------|-----------------------------------|
| 3354, 3331, 3172 | N-H stretch |
| 2954 | C-H stretching vibration terminal |
| 2917 | C-H stretching |
| 2848 | CH ₂ stretching |
| 1607 | N-H bending |
| 1059 | C-H bending |

A stacked image showing all the MNPs with HDA are provided in **Figure 4.13**. The respective individual spectra of the synthesised metals are presented in **Appendix B**.

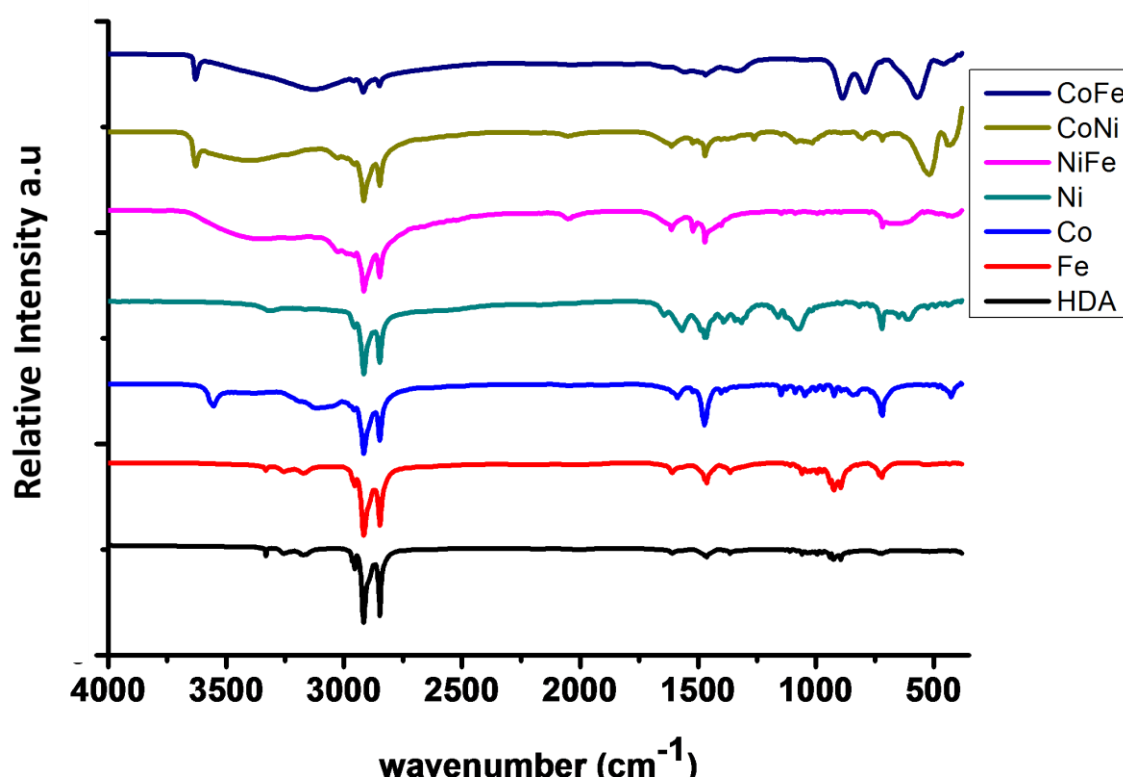


Figure 4.13: Comparison of the IR spectra for HDA and co-precipitation synthesised MNPs

The FTIR spectra of the mixture of HDA and the synthesised MNPs showed that there were some interactions between the surfactant, HDA, and the MNPs. The N-H stretching band at 3331, 3554 and 3172 cm⁻¹ showed a redshift in the synthesised metal nanoparticles. This peak shift indicates that the HDA amine group has bound to the surface of the MNPs.^{37,38} The C-H stretching 2917 cm⁻¹

(symmetric) and 2848 cm^{-1} (anti-symmetric) appeared at 2916 and 2849 cm^{-1} respectively. This also could suggest that HDA had interacted with the MNPs.³⁹ The peak shifts in these oxide molecules are mostly attributed to the constraint of the capping molecular motion which supposedly resulted from surface attachment of the HDA. The peak intensities had differences between the spectra. This was also postulated to be as a result of the HDA molecule on the MNPs forming a relative close-packed HDA layer which constrained the molecular motion.⁴⁰ **Table 4.2** shows how bands of interest were assigned on individual MNPs.

Table 4.2: Summary of FTIR peaks assigned to the co-precipitation synthesised metal nanoparticles^{36,41,42}

| Catalyst | Wavenumber (cm^{-1}) | Assignment |
|----------|---------------------------------|----------------|
| Fe | 422 | Fe-O |
| Co | 516, 481 | O-Co-O |
| Ni | 439 | Ni-O |
| CoFe | 570 | Ferrite MNPs |
| NiCo | 519 | Cobaltite MNPs |
| NiFe | 542, 418 | Ferrite MNPs |

FTIR gave characteristic metal-oxide peaks. To further determine the amount of the metals and the amount of the surfactant present in the MNPs, TGA analysis was done.

4.1.2.4 Thermogravimetric analysis

The residual metal content and thermal stabilities were determined using TGA. The general trend of all the MNPs synthesised using the co-precipitation method showed that the TGA curves had five different steps. A stacked TG curve is shown in **Figure 4.14** where all MNPs are presented.

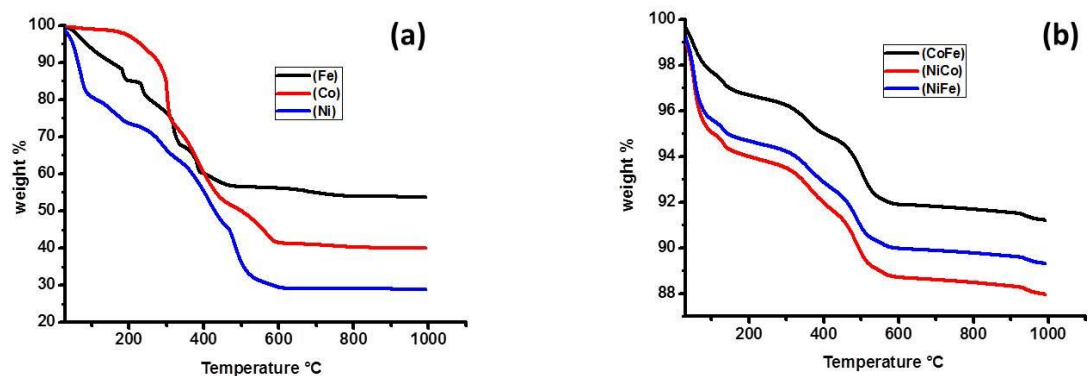


Figure 4.14: TGA curves of all the metal nanoparticles synthesised by the co-precipitation method in nitrogen; (a) single metals and (b) mixed metals

The TGA of the samples run under nitrogen, (**Figure 4.14**), illustrate the loss of water below 150 °C this was attributed to the release of adsorbed water. There was a second and third step effect around 200 and 375 °C respectively. This was attributed to desorption and decomposition of the surfactant, as well as the removal of the unbound HDA on the surface of the metal nanoparticles. Further weight loss around 500 °C was due to de-hydroxylation of the surface and removal of some of the lattice residual HDA. This weight loss suggests that the interaction between the metal nanoparticles and the surfactant was strong. The final weight loss in the TG curve was observed at temperatures around 580 °C. This signified the termination of weight loss associated changes.⁴² The derivative weight loss percentage curves were plotted for each metal sample (**Figure 4.15**).

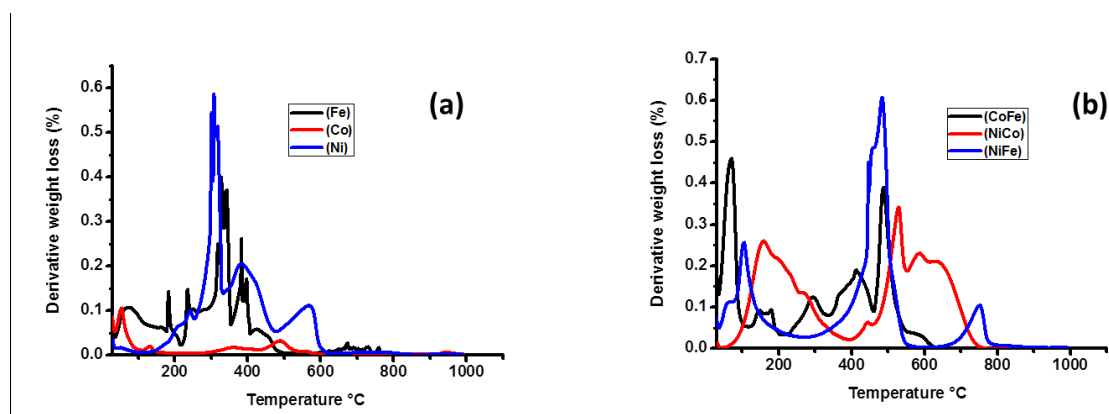


Figure 4.15: DTG profiles of all the metal nanoparticles synthesised by the co-precipitation method in nitrogen; (a) single metals and (b) mixed metals

In these derivative curves, it can be observed that as the thermal events progressed, there was a variation in the weight as a function of temperature. Each metal sample showed an average of five major weight loss peaks. These peaks correlated well with the TG curves. Therefore, the TGA results agreed with the EDX and FTIR results in showing the presence of the organic coating. The TGA curves show that a minimum of 10% weight loss was encountered in mixed MNPs and in single metal catalysts there was a great weight loss around 70%. Therefore, the mixed MNP samples contained more metal than the organic coating while the single MNP samples contained more organic content than metals. This correlated with the EDX spectrum where the single MNPs showed a greater carbon content than the mixed metals. The differences of the metal residual content were attributed to sample inhomogeneity properties. XRD characterisation patterns were not performed. This was based on the data from SEM image analysis where the dried samples showed an increased MNP size, hence all the analysis were done on the synthesised metals in solution.

4.1.3 Summary of the MNPs synthesis methods

From the results obtained with the characterisation techniques SEM, EDX and TEM a comparison of the synthesis methods can be obtained. The MNPs obtained from the thermal decomposition synthesis method were agglomerated whilst those from co-precipitation synthesis method showed mono-dispersion. The resulting nanoparticle showed a narrow size distribution (3-10 nm) and this was suggested to be the random diffusion of the particles due to the increased kinetic energy of the solution.^{15,43} Therefore, the co-precipitation synthesis method was superior to the thermal decomposition method in producing mono-dispersed MNPs which were considerable for the CNT catalysis application. The FTIR and TGA results further confirmed the presence of the HDA in the final MNPs product. Hence the MNPs were successfully coated with the amine.

References

- (1) Hamberg, I.; Granqvist, C. G. Evaporated Sn-doped In_2O_3 films: Basic optical properties and applications to energy-efficient windows. *Journal of Applied Physics* **1986**, *60*, 123-160.
- (2) Kim, H.; Gilmore, C. M.; Piqué, A.; Horwitz, J. S.; Mattoussi, H.; Murata, H.; Kafafi, Z. H.; Chrisey, D. B. Electrical, optical, and structural properties of indium–tin–oxide thin films for organic light-emitting devices. *Journal of Applied Physics* **1999**, *86*, 6451-6461.
- (3) Bönemann, H.; Richards, R. M. Nanoscopic metal particles–synthetic methods and potential applications. *European Journal of Inorganic Chemistry* **2001**, 2455-2480.
- (4) Denayer, J.; Bister, G.; Simonis, P.; Colson, P.; Maho, A.; Aubry, P.; Vertruyen, B.; Henrist, C.; Lardot, V.; Cambier, F.; Cloots, R. Surfactant-assisted ultrasonic spray pyrolysis of nickel oxide and lithium-doped nickel oxide thin films, toward electrochromic applications. *Applied Surface Science* **2014**, *321*, 61-69.
- (5) Xia, Y. W. Bottom-Up and Top-Down Approaches to the Synthesis of monodispersed Spherical Colloids of Low Melting-Point Metals. *Nano Letters* **2004**, *4*, 2047-2050.
- (6) Wang, C.; Shen, E.; Wang, E.; Gao, L.; Kang, Z.; Tian, C.; Lan, Y.; Zhang, C. Controllable synthesis of ZnO nanocrystals via a surfactant-assisted alcohol thermal process at a low temperature. *Materials Letters* **2005**, *59*, 2867-2871.
- (7) Rajpure, K. Y. Exploring structural and magnetic properties of nanocrystalline iron oxide synthesized by autocombustion method. *Superlattices and Microstructures* **2015**, *77*, 181-195.
- (8) Rahman, G.; Joo, O. S. Facile preparation of nanostructured $\alpha\text{-Fe}_2\text{O}_3$ thin films with enhanced photoelectrochemical water splitting activity. *Journal of Materials Chemistry A* **2013**, *1*, 5554-5561.
- (9) Tahir, A. A.; Wijayantha, K. G. U.; Saremi-Yarahmadi, S.; Mazhar, M.; McKee, V. Nanostructured $\alpha\text{-Fe}_2\text{O}_3$ thin films for photoelectrochemical hydrogen generation. *Chemistry of Materials* **2009**, *21*, 3763-3772.
- (10) Mallick, P.; Dash, B. N.; Solanki, V.; Varma, S.; Mishra, N. C. Effect of thermal annealing on the microstructure and surface morphology of nickel oxide (NiO) thin films. *Advanced Science, Engineering and Medicine* **2014**, *6*, 1118-1122.

- (11) Marciuš, M.; Ristić, M.; Ivanda, M.; Musić, S. Formation and microstructure of nickel oxide films. *Journal of alloys and compounds* **2012**, *541*, 238-243.
- (12) Diab, M.; Mokari, T. Thermal decomposition approach for the formation of α -Fe₂O₃ mesoporous photoanodes and an α -Fe₂O₃/CoO hybrid structure for enhanced water oxidation. *Inorganic Chemistry* **2014**, *53*, 2304-2309.
- (13) Chen, W.; Zhu, W. Preparation of cobalt ferrite thick films and their magnetic and electrical properties. *Journal of the American Ceramic Society* **2011**, *94*, 1096-1100.
- (14) Zhu, B.; Yang, C.; Xie, Q.; Zhang, Y.; Li, P. Influence of rapid thermal annealing on the structure and magnetic properties of CoFe₂O₄ films prepared by sol-gel method. *Ferroelectrics* **2013**, *445*, 18-25.
- (15) Sun, S.; Zeng, H.; Robinson, D. B.; Raoux, S.; Rice, P. M.; Wang, S. X.; Li, G. Monodisperse MFe₂O₄ (M = Fe, Co, Mn) nanoparticles. *Journal of the American Chemical Society* **2004**, *126*, 273-279.
- (16) Park, Y. J.; Kim, H. J.; Han, L. T.; Zoukarniev, A. Z.; Min, K. W.; Baek, C. W.; Jeong, T. W.; Chung, D. S.; Park, S. H.; Choi, J. H.; Song, B. K.; Kang, H. S.; Heo, J. N.; Lee, J. H.; Jin, Y. W.; Kim, J. M. Density control of carbon nanotubes for field emission display by control of catalytic layer diffusion. *Vacuum Nanoelectronics Conference, Technical Digest of the 18th International* **2005** 358-359.
- (17) Mahdavi, M.; Ahmad, M.; Haron, M. J.; Rahman, M. Z.; Fatehi, A. Optimized conditions for graft copolymerization of poly (acrylamide) onto rubberwood fibre. *BioResources* **2011**, *6*, 5110-5120.
- (18) Rao, C. N. R.; Ramakrishna Matte, H. S. S.; Voggu, R.; Govindaraj, A. Recent progress in the synthesis of inorganic nanoparticles. *Dalton Transactions* **2012**, *41*, 5089-5120.
- (19) Shen, L.; Laibinis, P. E.; Hatton, T. A. Bilayer surfactant stabilized magnetic fluids: synthesis and interactions at interfaces. *Langmuir* **1999**, *15*, 447-453.
- (20) Tabares, B. J.; Gil, A. A. Z.; Isaza, F. J. Effects of the synthetic method on the particle size and purity of magnetite. *Revista Facultad de Ingenieria*. **2009**, *50*, 9-16.
- (21) Christian, M.; Aguey-Zinsou, K. F. Synthesis of core-shell NaBH₄@M (M = Co, Cu, Fe, Ni, Sn) nanoparticles leading to various morphologies and hydrogen storage properties. *Chemistry Communication* **2013**, *49*, 6794-6796.

- (22) Mahdavi, M.; Ahmad, M. B.; Haron, M. J.; Namvar, F.; Nadi, B.; Rahman, M. Z.; Amin, J. Synthesis, surface modification and characterisation of biocompatible magnetic iron oxide nanoparticles for biomedical applications. *Molecules* **2013**, *18*, 7533-7548.
- (23) Sun, J.; Zhou, S.; Hou, P.; Yang, Y.; Weng, J.; Li, X.; Li, M. Synthesis and characterization of biocompatible Fe₃O₄ nanoparticles. *Journal of Biomedical Materials Research Part A* **2007**, *80A*, 333-341.
- (24) Herranz, F.; Salinas, B.; Groult, H.; Pellico, J.; Lechuga-Vieco, A.; Bhavesh, R.; Ruiz-Cabello, J. Superparamagnetic Nanoparticles for Atherosclerosis Imaging. *Nanomaterials* **2014**, *4*, 408-438.
- (25) Amiens, C.; Chaudret, B.; Ciuculescu-Pradines, D.; Colliere, V.; Fajerweg, K.; Fau, P.; Kahn, M.; Maisonnat, A.; Soulantica, K.; Philippot, K. Organometallic approach for the synthesis of nanostructures. *New Journal of Chemistry* **2013**, *37*, 3374-3401.
- (26) Zhong, Z.; Lin, M.; Ng, V.; Ng, G. X. B.; Foo, Y.; Gedanken, A. A Versatile wet-chemical method for synthesis of one-dimensional ferric and other transition metal oxides. *Chemistry of Materials* **2006**, *18*, 6031-6036.
- (27) Li, Y.; Afzaal, M.; O'Brien, P. The synthesis of amine-capped magnetic (Fe, Mn, Co, Ni) oxide nanocrystals and their surface modification for aqueous dispersibility. *Journal of Materials Chemistry* **2006**, *16*, 2175-2180.
- (28) Li, Y.; Afzaal, M.; O'Brien, P. The synthesis of amine-capped magnetic (Fe, Mn, Co, Ni) oxide nanocrystals and their surface modification for aqueous dispersibility. *Journal of Materials Chemistry* **2006**, *16*, 2175.
- (29) Choi, G.; Cho, Y.; Son, K.; Kim, D. Mass production of carbon nanotubes using spin-coating of nanoparticles. *Microelectronic engineering* **2003**, *66*, 77-82.
- (30) Hou, Y.; Kondoh, H.; Ohta, T.; Gao, S. Size-controlled synthesis of nickel nanoparticles. *Applied Surface Science* **2005**, *241*, 218-222.
- (31) Baliyan, A.; Fukuda, T.; Hayasaki, Y.; Uchida, T.; Nakajima, Y.; Hanajiri, T.; Maekawa, T. CoFe₂O₄ nanoparticles as a catalyst: synthesis of a forest of vertically aligned CNTs of uniform diameters by plasma-enhanced CVD. *Journal of nanoparticle research* **2013**, *15*, 1-9.
- (32) Sanpo, N.; Wang, J.; Berndt, C. C. Influence of chelating agents on the microstructure and antibacterial property of cobalt ferrite nanopowders. *Journal of the Australian Ceramic Society*. **2013**, *49*, 84-91.

- (33) Grass, R. N.; Athanassiou, E. K.; Stark, W. J. Covalently functionalized cobalt nanoparticles as a platform for magnetic separations in organic synthesis. *Angewandte Chemie International Edition* **2007**, *46*, 4909-4912.
- (34) Arita, T.; Hitaka, H.; Minami, K.; Naka, T.; Adschiri, T. Synthesis of iron nanoparticle: Challenge to determine the limit of hydrogen reduction in supercritical water. *The Journal of Supercritical Fluids* **2011**, *57*, 183-189.
- (35) Altavilla, C.; Sarno, M.; Ciambelli, P. Synthesis of ordered layers of monodisperse CoFe_2O_4 nanoparticles for catalyzed growth of carbon nanotubes on silicon substrate. *Chemistry of Materials*. **2009**, *21*, 4851-4858.
- (36) Wang, H.; Jiao, X.; Chen, D. Monodispersed nickel nanoparticles with tunable phase and size: synthesis, characterization, and magnetic properties. *The Journal of Physical Chemistry C* **2008**, *112*, 18793-18797.
- (37) Mishra, T.; Sahu, R. K.; Lim, S. H.; Salamanca-Riba, L. G.; Bhattacharjee, S. Hexadecylamine capped silver and gold nanoparticles: Comparative study on formation and self-organization. *Materials Chemistry and Physics* **2010**, *123*, 540-545.
- (38) Newman, J. D. S.; Blanchard, G. J. Formation of gold nanoparticles using amine reducing agents. *Langmuir* **2006**, *22*, 5882-5887.
- (39) Hou, X.; Zhang, X.; Fang, Y.; Chen, S.; Li, N.; Zhou, Q. 1-Hexadecylamine as both reducing agent and stabilizer to synthesize Au and Ag nanoparticles and their SERS application. *Journal of Nanoparticle Research* **2010**, *13*, 1929-1936.
- (40) Yang, H.; Shen, C.; Wang, Y.; Su, Y.; Yang, T.; Gao, H. Stable cobalt nanoparticles passivated with oleic acid and triphenylphosphine. *Nanotechnology* **2004**, *15*, 70.
- (41) Mohapatra, J.; Mitra, A.; Bahadur, D.; Aslam, M. Surface controlled synthesis of MFe_2O_4 (M = Mn, Fe, Co, Ni and Zn) nanoparticles and their magnetic characteristics. *Royal Society of Chemistry* **2013**, *15*, 524-532.
- (42) Zhao, S.-Y.; Lee, D. K.; Kim, C. W.; Cha, H. G.; Kim, Y. H.; Kang, Y. S. Synthesis of magnetic nanoparticles of Fe_3O_4 and CoFe_2O_4 and their surface modification by surfactant adsorption. *Bulletin of Korean Chemical Society* **2006**, *27*, 237-242.
- (43) Hua, C. C., Sarani Zakaria, R. Farahiyan, and Liew Tze Khong. Size-controlled synthesis and characterization of Fe. *Sains Malaysiana* **2008**, *37*, 389-394.

Chapter Five

MULTI-WALLED CARBON NANOTUBES: SYNTHESIS AND APPLICATION

This chapter presents descriptive findings of the synthesis of multi-walled carbon nanotubes (MWCNTs) and their application in organic solar cells. Fabrication of organic solar cells using the synthesised MWCNTs is presented herein. An explanation of the solar cells and the methods used to fabricate the devices is also provided. Solar cell results obtained and the conclusion are provided in terms of the efficiencies of the cells.

5.1 MWCNTs synthesis using thermal CVD

The MWCNTs were synthesised using two CVD methods, which were, thermal CVD and non-equilibrium PECVD using ITO coated glass as the substrate. During synthesis, 10% H₂/Ar was used as the reducing agent, and this gas mixture was left flowing to maintain a non-oxidative atmosphere. The control was MWCNTs synthesized by CVD floating catalyst using ferrocene as the catalyst and toluene as the carbon source. The MWCNTs synthesized were characterized by use of TEM, SEM and EDX which was attached to SEM. The representative SEM images are shown in **Figure 5.1**.

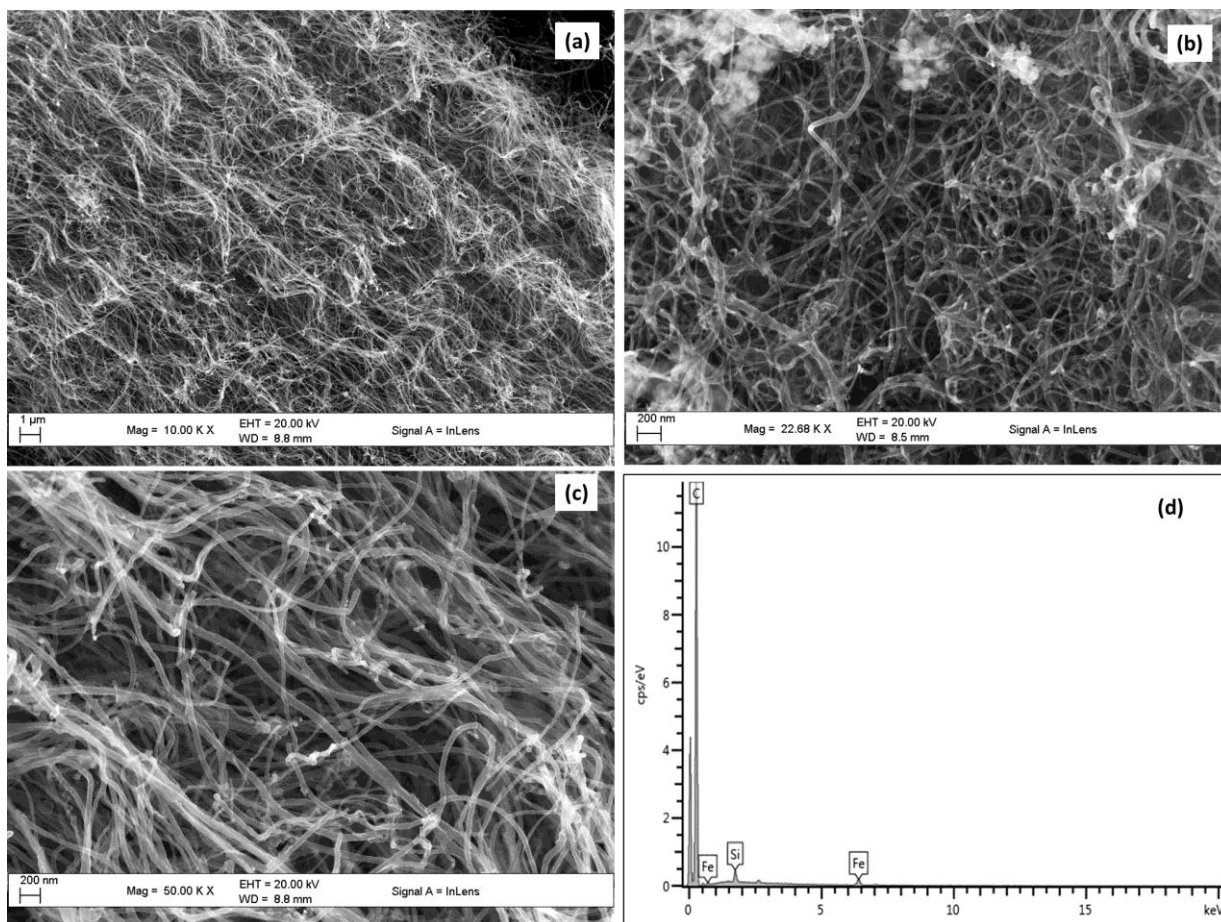


Figure 5.1: The synthesised MWCNTs SEM images at (a) low, (b) medium and (c) high magnification with (d) EDX spectrum at 850 °C with the use of ferrocene and toluene in the thermal CVD method

In this method the coiled interwoven wool like MWCNTs were observed under SEM. The image at low magnification shows structures that looked wavy (**Figure 5.1 (a)**), at intermediate magnification the structures look more inter-twined and at high magnification (**Figure 5.1 (b)**) the images resemble random orientation (**Figure 5.1 (c)**). The EDX spectra showed the presence of the catalyst, Fe, and the C from the tubular structures (**Figure 5.1 (d)**). The Si peak observed was due to the glass substrate particles from the reactor tube. This is a result of the scrapping off of the product from the substrate. The ratio of the catalyst and the carbon showed a higher carbon content which suggested that more tubes were present in the final products. To further confirm the observations, TEM analysis was performed. **Figure 5.2** shows the representative TEM images.

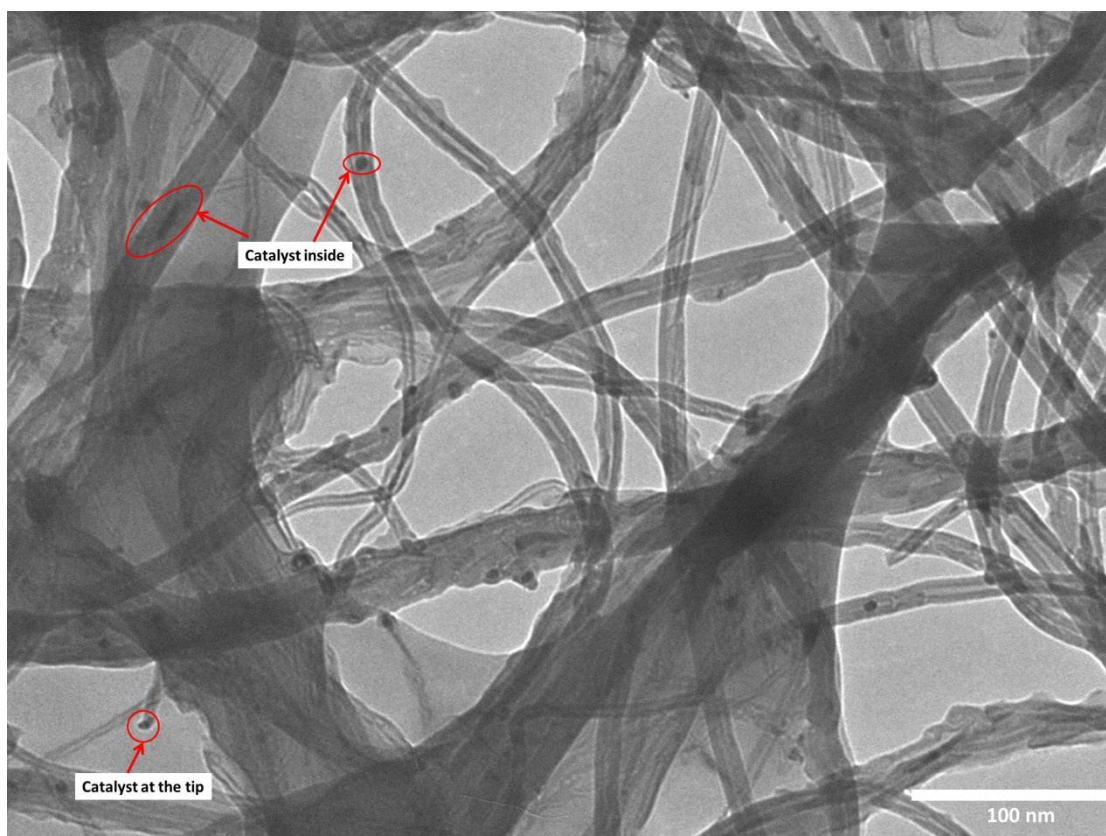


Figure 5.2: Representative TEM image of the synthesised MWCNTs at 850 °C with the use of ferrocene and toluene in the thermal CVD method

The images observed showed typical hollow tubular structures. The catalyst particles were located inside the tube or at the tip of the tubes as shown in **Figure 5.2**. Thick tube walls were observed which suggested successful synthesis of MWCNTs. The walls had variable texture degrees but the most dominant where smooth surfaces. The walls had an average outer diameter of 58 nm. The ITO glass substrate melted due to the choice of reaction temperature which was high, 850 °C. Once the data from the control experiment was obtained and analysed, the synthesis of the MWCNTs continued with different carbon sources. Different carbon sources investigated in the current work are discussed in the following sections.

5.1.1 Single-furnace synthesis of MWCNTs using Liquefied petroleum gas

The synthesis method utilised liquefied petroleum gas (LPG) as the carbon source and Fe as a catalyst. The MWCNTs synthesis temperatures were 600, 700, 800 and 900 °C. The temperature choices were meant to determine the optimum temperature at which maximum MWCNTs production occurred. It was observed that the ITO substrates melted visibly as the temperature increased beyond 600 °C (**Figure 5.3**). This could be attributed to the fact that as the temperatures increased the compactness of the ITO glass components was becoming reduced. The glass components can only be thermally stable below specific temperature ranges. Thus, the melting of ITO was because the ITO glass strain point was exceeded.¹ The photograph in **Figure 5.3** clearly shows that the ITO substrate in quartz boat melted. Hence, a notable transformation of the ITO substrate is evidently highlighted with reference to the initial state before synthesis, (**Figure 5.3** insert).

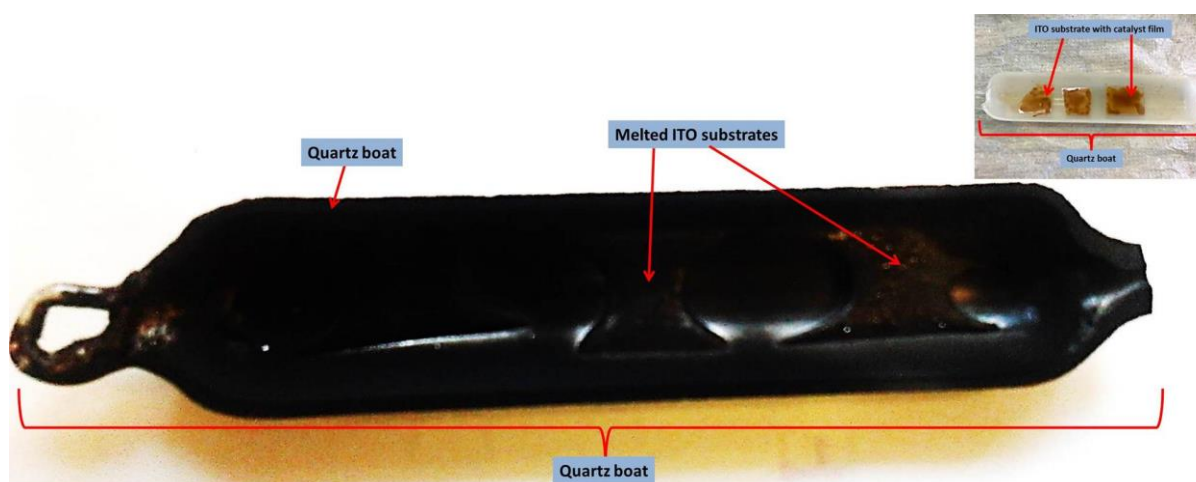


Figure 5.3: ITO melted and stuck substrate in a quartz boat using LPG at 800 °C, the insert shows the state before synthesis

The various carbon-based products, shaped carbon nanomaterials (SCNMs) obtained at each synthesis temperature were critically analysed and are presented as a summary in **Table 5.1**. Basically the summary gives an overall presentation of different observations and challenges faced during synthesis of CNTs using LPG at different maximum temperatures (T_{MAX}). The SCNMs observed included carbon nano-fibres, spheres and tubes. **Table 5.1** shows a strong dependency of carbon nanomaterial products obtained on T_{MAX} when LPG was the carbon source. The temperature at

which a high percentage of CNTs were observed was regarded as the optimum temperature, i.e. 800 °C.

Table 5.1: Summary of the observed SCNMs and the challenges at different LPG synthesis temperatures

| T_{MAX} (°C) | Products | Challenges |
|---|--|---|
| 600 | Solid fibres | - |
| 700 | More fibres, less tubes (60:40) | ITO glass melted |
| 800 | Tubes | ITO glass melted and stuck permanently on the quartz boat |
| 900 (introduced a layer of powder Al_2O_3 in the boat such that the ITO will not stick to the boat) | More spheres and less tubes (80:20) | The ITO melted |

The Al_2O_3 powder was introduced at 900 °C in order to investigate ways in which the substrate would not stick to the boat. The observed images from SEM and TEM representative images are compared in a tabular form in **Table 5.2**.

Table 5.2: Representative SEM and TEM sample images of the LPG SCNMs samples

| T_{MAX} (°C) | SEM | TEM |
|----------------|-----|-----|
| 600 | | |
| 700 | | |
| 800 | | |
| 900 | | |

From the SEM images, it was observed that at 600 °C the structures were thick and the catalyst nanoparticles were noted at the tips of the tubes. This observation correlate with earlier report by Wang *et al.*² In their report, they concluded that at T_{MAX} below 700 °C using LPG source, synthesis of fibres dominantly occurred. At 800 °C the SEM images show twisted structures which were thinner compared to those at 600 and 700 °C. The different SCNMs formed were reported by Huang *et al.* to be as a result of different conformations assumed by the catalysts when exposed to temperature variations.³ These structures showed some bamboo compartments. The bamboo compartments were attributed to the structure of HDA which contains a heteroatom. The T_{MAX} of 900 °C had more carbon spheres produced than tubes. These results agree with what was reported by Songasen *et al.*, that as the temperature increases the decomposition of LPG becomes more enhanced and the formation of the tubes become more pronounced.⁴ The presence of the spheres and the catalyst at the tip contradicted with the report on the LPG effect, a study by Huang *et al.*³ According to their group, LPG inhibits the formation of spheres and the presence of trapped catalyst nanoparticles at the tip of the tubes which are responsible for impurities in the CNT forests.⁵ However, the contradiction could be because LPG quality varies globally.

In summary, synthesis of CNTs using LPG at low temperatures (600 and 700 °C) yields products with more of carbon fibres. Also, increase in T_{MAX} culminated in production of a variety of SCNMs. Apart from destroying the substrate, synthesis at high temperatures produces randomly oriented CNTs instead of the targeted vertically aligned tubes. Therefore, synthesis using LPG was considered unsuitable for direct substrate growth of a vertically aligned forest of tubes. A double furnace synthesis route, which involved the use of two furnaces, was investigated.

5.1.2 Double-furnace synthesis of MWCNTs using Liquefied petroleum gas

The double furnace method involved two furnaces set at different temperatures, i.e. 400 and 800 °C. The choice of the furnace temperatures was based on the temperatures that produced smallest MNPs in terms of size (**Section 4.1.1**), and highest percentage of MWCNTs from the LPG as carbon source (**Section 5.1.1**), respectively. Therefore the carbon source was LPG and the catalyst was CoFe. In this approach, high temperature furnace, (the temperature of the first furnace), was expected to thermally decompose the carbon source and the low temperature furnace was expected

to activate the catalyst. Decomposition of LPG was expected to produce reactive materials such as CH_4^+ , CH_2^+ and CH^+ radicals.⁶ Typical radicals would then react with the metal catalyst in the second furnace. The CNTs were expected to form in the second furnace. Generally this method produced randomly oriented MWCNTs as can be observed in **Figure 5.4**.

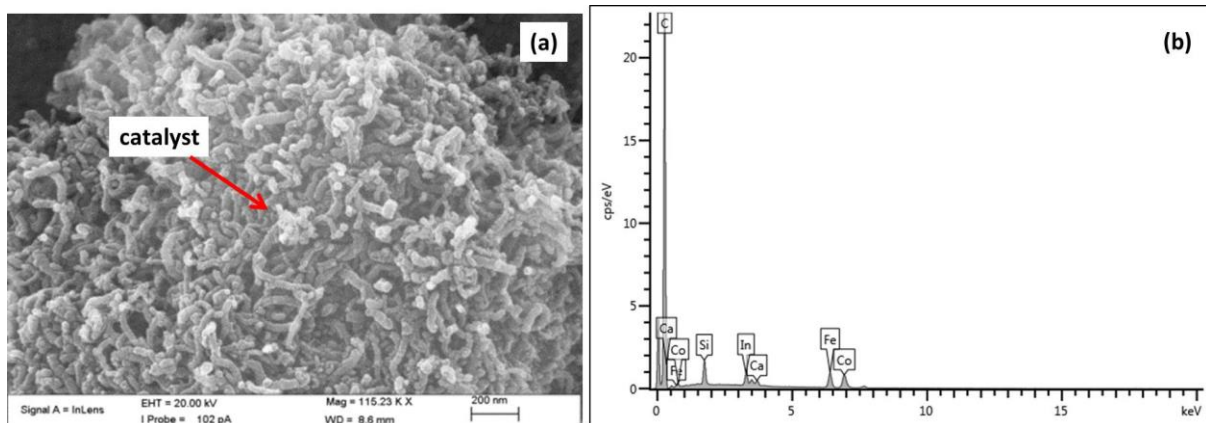


Figure 5.4: Representative SEM-EDX images of MWCNTs synthesised with the double furnace approach using LPG as the carbon source at 800/400 °C; (a) SEM and (b) EDX

The SEM image shows a cluster of short MWCNTs that were randomly oriented with some catalyst residual particles. The random orientation could be attributed to the gas flow rate during the synthesis of the CNTs that could have blown the CNTs as they get deposited. The EDX spectrum showed the presence of carbon attributed to the CNTs and also the catalyst particles (CoFe). Also, other peaks, such as Si and In, assigned to the substrate material were detected. To further characterise the synthesised products TEM image analysis was done (**Figure 5.5**).

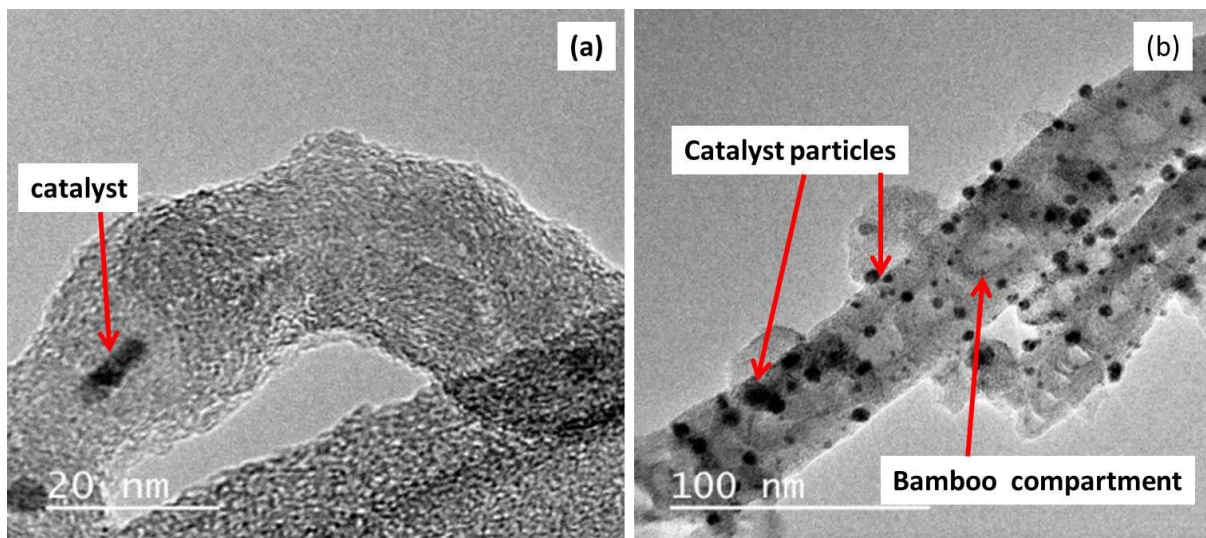


Figure 5.5: Representative TEM images of MWCNTs synthesised with the double furnace approach using LPG as the carbon source at 800/400 °C (a) low and (b) high magnification

The TEM image in **(Figure 5.5 (a))** show the catalyst nanoparticle trapped inside the tube. In other cases, TEM images showed MWCNTs structures with catalyst nanoparticles around the tube walls and the presence of some bamboo compartments **(Figure 5.5 (b))**. The observed bamboo compartments could be due to the use of the LPG carbon source as reported by several researchers.^{3,5,6} The MWCNTs produced were thick and short. This observation correlated well with literature studies which highlighted that the bigger the catalyst particles the thicker and shorter the produced CNTs.⁷⁻⁹ Therefore, a comparison of the observed MWCNTs structures using the thermal CVD methods was inevitable.

5.1.3 Comparison of the thermal CVD approaches

The results obtained using the different types of furnace methods showed some differences in products at the same T_{MAX} . In the single furnace method where toluene was the carbon source, MWCNTs with better surface properties (smooth walls) were produced than those synthesised using LPG (defected walls). The thermal stabilities of the MWCNTs were studied using TGA **(Figure 5.6)**.

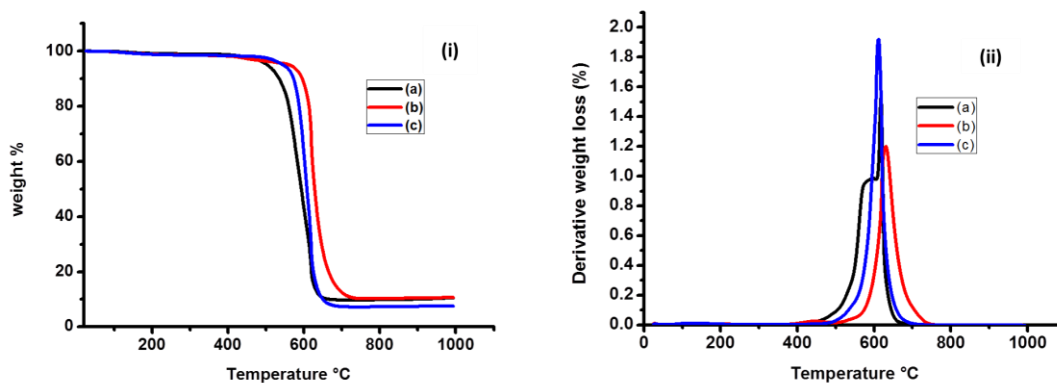


Figure 5.6: Thermal profiles (i) TGA and (ii) DTGA for the thermal CVD approaches using (a) LPG single furnace, (b) LPG double furnace and (c) ferrocene-toluene approach

In the profile of the MWCNTs, minimal water loss is expected below 200 °C however, for these methods there was no water loss observed. There was no noticeable decrease in weight in the range 200-400 °C, a temperature range associated with amorphous carbon decomposition, and in fact loss started around 400 °C (**Figure 5.6 (i)**).¹⁰ This is clearly highlighted by the derivative weight against temperature plot (**Figure 5.6 (ii)**) for toluene and LPG double furnace synthesised MWCNTs. Unlike, LPG single furnace synthesised MWCNTs, characteristic single weight depression peak in **Figure 5.6 (i)** and single peak in derivative weight curve (**Figure 5.6 (ii)**) were noted for LPG in a double furnace and ferrocene-toluene approaches. This suggests that there was no amorphous carbon present and there was only one form of carbon material in the latter.¹¹ This agrees with the microscopy images in **Figures 5.2 and 5.5** respectively. The residual metal weight was least in ferrocene-toluene, with around 7.7 wt. %. This outcome suggest that the mechanism involved in the double furnace, i.e. formation of carbon radicals in the high temperature furnace followed by exposure to metal catalysts in the second furnace, increases the ratio of carbonaceous material in product. Also, it was observed that the MWCNTs synthesized using LPG single furnace were the least stable followed by those from the LPG in a double furnace and the most stable were the ones from ferrocene-toluene (**Figure 5.6 (i) and (ii)**). Therefore, the results suggest that high metal catalyst residual catalyses the decomposition of carbon nanomaterials.¹⁰ To further characterise the products Raman analysis was carried out. **Table 5.3** shows the Raman analysis of the different furnace approaches.

Table 5.3: Comparison of the D- and G-bands from Raman analysis, and average tube diameter of tubes from TEM of the CVD methods

| Method | average diameter (nm) | D-Band | G-Band | I _D /I _G |
|--------------------|--------------------------|--------|--------|--------------------------------|
| Ferrocene-toluene* | 58 | 1342 | 1603 | 0.88 |
| LPG * | 78 | 1361 | 1585 | 0.86 |
| LPG# | 83 | 1376 | 1566 | 0.83 |

*single furnace

double furnace

The general trend observed showed that the ferrocene-toluene method had the MWCNTs with the highest I_D/I_G ratio (**Table 5.3**). This could mean that there was a low degree of crystallinity in these tubes and this could be attributed to greater bond strains. This observation correlated with the smaller mean MWCNTs diameter.¹² Hence, this leads to the conclusion that the ferrocene-toluene method was a reliable method for the synthesis of smaller diameter CNTs. Therefore, all the thermal CVD methods were not suitable for the synthesis of vertically aligned multiwalled carbon nanotubes and severely destroyed the ITO substrate. Equipped with this and the deduction that ferrocene-toluene and LPG single furnace at 800 °C was the most suitable for production of CNTs, non-equilibrium plasma-enhanced chemical vapour deposition (PECVD) approach was used.

5.2 Non-equilibrium PECVD of carbon nanotubes

The non-equilibrium (PECVD) approach was employed to overcome the high temperature problem associated with the thermal CVD. The role of plasma was ionisation of the gaseous feedstock under low temperatures.¹³ The system was optimised in terms of the reaction temperature, time, plasma flame and the deposited CNT layer.

5.2.1 Optimisation

In order to preserve the properties of the ITO coated glass substrate, a purpose built non-equilibrium PECVD apparatus was employed. The reason behind the low temperatures choice is based on a

report Wang and Moore.² Ren *et al.* in their study of synthesis of CNTs on glass substrate, showed that glass electrical resistivity increases by annealing up to 100 °C and decreases above 100 °C.¹⁴ Therefore, temperatures below 300 °C were selected as ideal for the direct deposition of the MWCNTs on ITO glass substrate. The ITO substrates were placed directly below the plasma discharge to maximise the interactions between the plasma and the catalyst as suggested by Somers *et al.*¹⁵ Since the physicochemical properties of the plasma and the catalyst can be modified by their co-existence.¹⁶ **Figure 5.7** shows set-up of the design, i.e. how the ITO was oriented in the reactor.

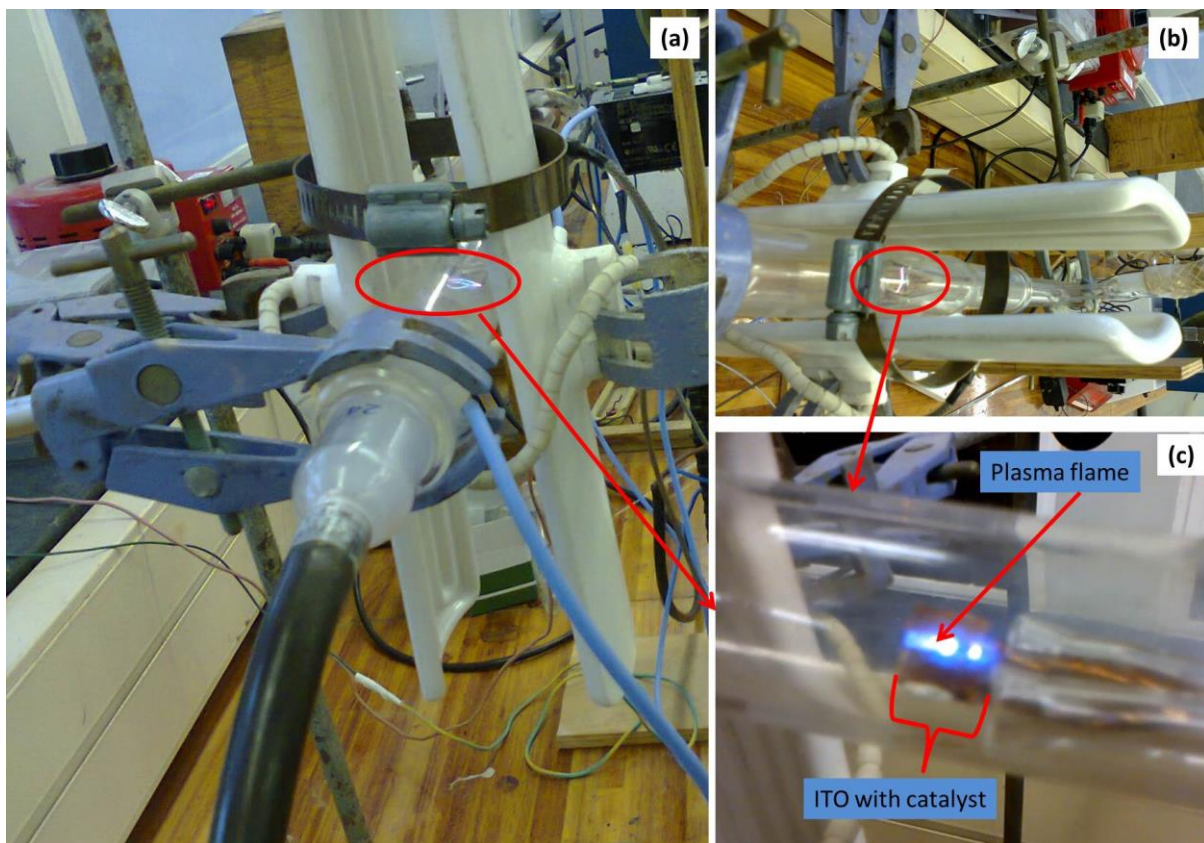


Figure 5.7: Photographic illustration of the ITO-plasma orientation in the reactor chamber where (a) complete set-up, (b) an aerial view and (c) enlarged ITO-plasma area

The synthesis temperatures employed were 25, 50, 100, 150 and 200 °C. The reaction time was 30 and 10 minutes. However, having deduced that ferrocene-toluene was the most suitable for synthesis of CNTs (**Section 5.1.3**), it was not appropriate for the designed non-equilibrium PECVD apparatus. This was because ferrocene requires high temperatures for decomposition to form nanoparticle catalysts and this destroys the substrate. Hence, the LPG and the synthesised catalyst approach was utilised. Also, attempts to use gases such as methane and ethylene as the carbon

sources resulted in blow off of the plasma flame. This was attributed to the differences in the density and vapour pressures of the gases, and the ionisation and dissociation energies. The ignition source would not have been able to provide enough energy to initiate a cascade with the gases thus, the gases requires higher synthesis temperatures which are above 350 °C.¹⁷ Therefore, in this study LPG and acetylene as carbon sources, and the co-precipitation synthesised MNPs as catalysts were investigated. Summary of the results are presented in **Table 5.4**.

Table 5.4: Summary of non-equilibrium variables used for method optimisation

| T_{MAX} (°C) | Reaction time (minutes) | Observations | Results |
|----------------|-------------------------|---|------------------|
| 25 | 30 | No deposits | Amorphous carbon |
| 50 | 30 | No deposits | Amorphous carbon |
| 100 | 30 | Black deposits | fused spheres |
| 150 | 20 | Black deposits | fibres |
| 200 | 10 | CH ₄ /C ₂ H ₄ in Ar blows off the plasma | CNTs |

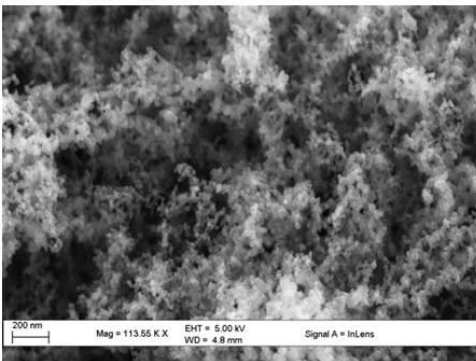
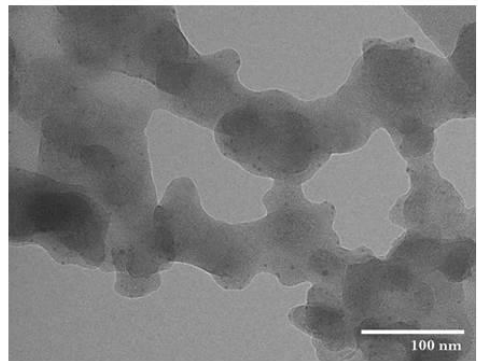
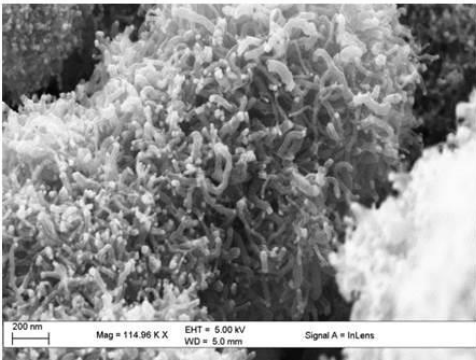
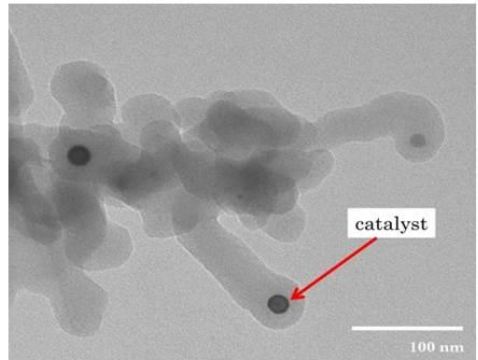
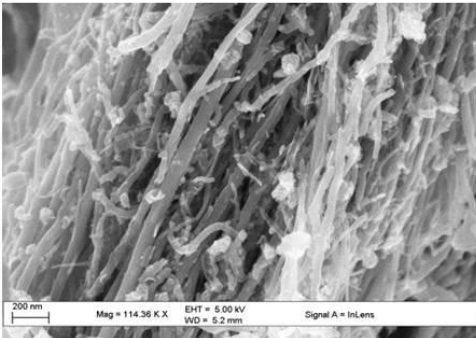
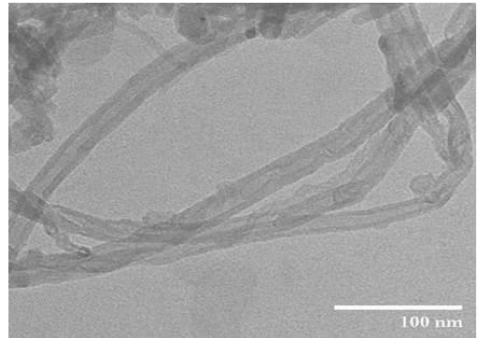
The products were analysed at each respective T_{MAX} in order to investigate changes and trends involved. Amorphous carbon material was observed at 25 and 50 °C for reaction time of 30 minutes. The same reaction time was used for synthesis at 100 and 150 °C and fused spheres and fibres were observed, respectively. At 200 °C MWCNTs were observed however, the products completely obscured the ITO substrate therefore, the time was reduced to 20 and 10 minutes sequentially until an almost transparent film was deposited. The characterisation techniques used for optimisation of the method are discussed in subsequent sections.

5.2.1.1 Structural characterisation

Data analysis for optimisation using SEM, EDX and TEM is presented in this section. The amorphous carbon material observed from 25 to 50 °C is not included as part of the SCNMs. The SCNMs that were observed as the temperature increased from 100 to 200 °C included fibres, spheres and tubes.

Table 5.5 summarizes the SCNMs synthesized at 100 to 200 °C.

Table 5.5: Representative images of the various SCNMs observed at different $T_{(MAX)}$ using Iron catalyst

| $T_{(MAX)}$ °C | SEM | TEM |
|----------------|---|--|
| 100 |  |  |
| 150 |  |  |
| 200 |  |  |

From the SEM and TEM images, it was observed that development of the MWCNTs structures occurred in stages i.e. from sphere, fibres to CNTs. At 100 °C the SEM images showed small spherical shapes. The shapes were better categorised with TEM which showed that they were fused spheres. When the reaction temperature was increased to 150 °C solid carbon structures were observed in the SEM images. This correlated with TEM observations that showed solid fibres. The fibres had the catalyst particles at the tip which suggested that tip growth mechanism was being followed as suggested by Wang *et al.*² As the temperature increased to 200 °C typical aligned CNT structures were observed with SEM. The morphology of these structures was confirmed with TEM. The TEM

images showed hollow tubular structures with thick walls, a description which suits MWCNT structures as reported by Ebbesen *et al.*¹⁸ Therefore, it was concluded that MWCNTs were successfully synthesised at 200 °C using LPG. Hence, the other gases (acetylene, methane and ethylene) were tried for synthesis under the same reaction conditions but methane and ethylene blew off the plasma flame as mentioned before. Therefore, the optimised reactions conditions were used to synthesise MWCNTs using several catalysts (Co, Ni, CoFe, NiCo and NiFe) and LPG and acetylene as the carbon sources.

5.2.2 Synthesis of aligned MWCNTs using LPG and acetylene

The methodology was systematically employed using all the catalysts with one carbon source at a time. In all the samples, characterisation techniques were limited to analysis on the glass substrate except for some SEM and TEM imaging where the samples were scrapped off in an effort to provide the real surface characteristics.

5.2.2.1 Structural characterisation of the synthesised MWCNTs

The as synthesised MWCNTs using different catalysts were viewed under SEM using exceptionally low magnifications to investigate the alignment. **Figure 5.8** shows the variations in the observed structures upon varying catalysts using low magnification.

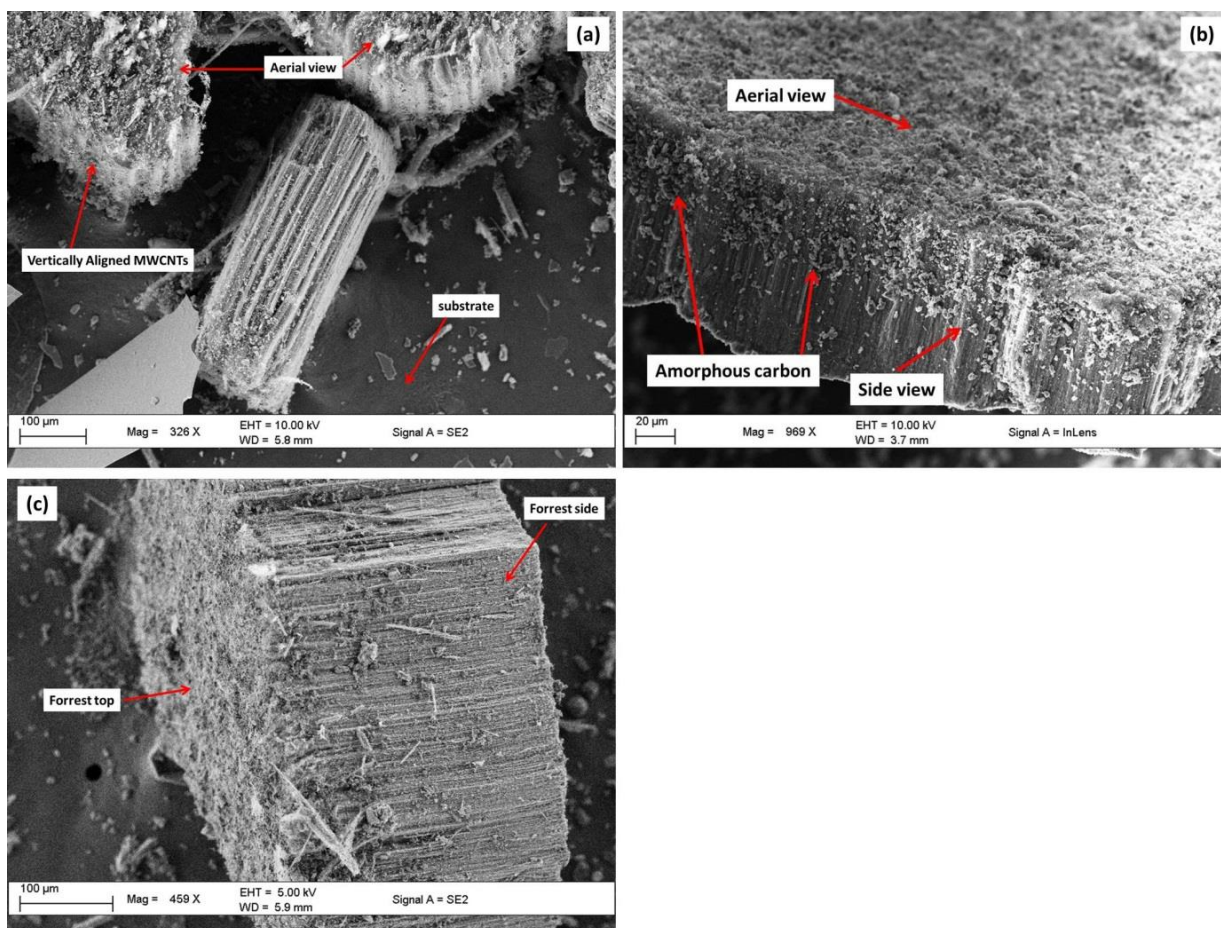


Figure 5.8: Representative images indicating the different views of the MWCNTs as observed using SEM for CoFe catalyst using LPG as the carbon source; (a) aerial view on substrate, (b) scrapped off aerial view and (c) scrapped off side views

Similar images were observed with respect to the different catalyst utilised. The SEM images (**Figure 5.8**) showed vertically aligned MWCNTs were successfully synthesised. Amorphous carbon material was observable from the aerial and side views (**Figure 5.8**). Besides this, no other distinctive observations were noticeable in both mono- and bi-metal catalysts from SEM images. EDX data confirmed the presence to the respective catalysts and carbon in the samples (**Figure 5.9**).

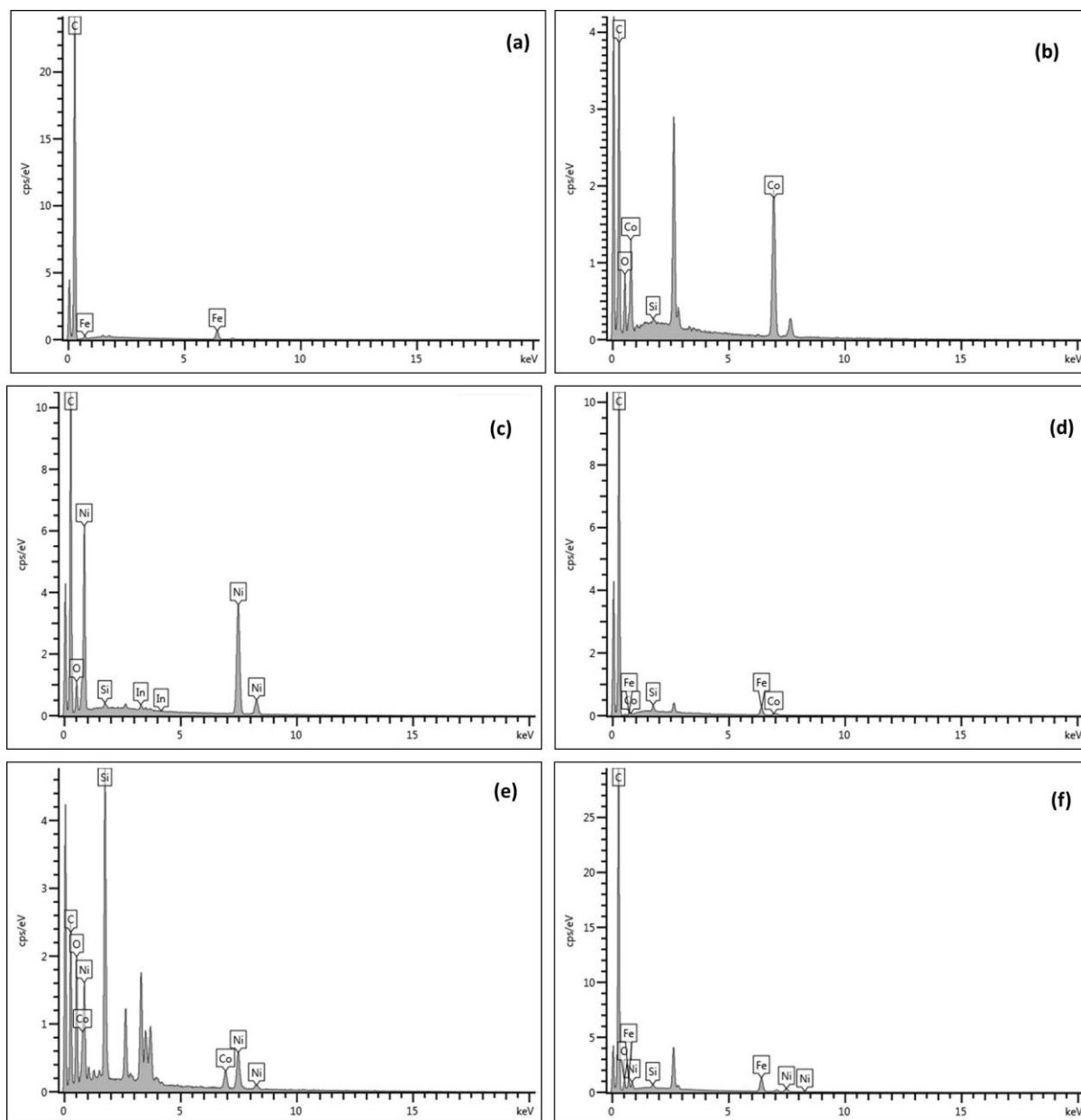


Figure 5.9: EDX spectra of MWCNTs synthesised using various catalysts and LPG as the carbon source (a) Fe, (b) Co, (c) Ni, (d) CoFe, (e), NiCo and (f) NiFe

The EDX spectra in the different catalysts observed showed the peaks of the respective catalysts. The Si, In, Sn and O₂ peaks were also present and they were assigned to the ITO coated glass substrate components. To further characterise in terms of dimensions of the MWCNTs samples, TEM was utilised. **Figure 5.10** shows hollow tubular nanostructures with thick walls from all the catalysts used.

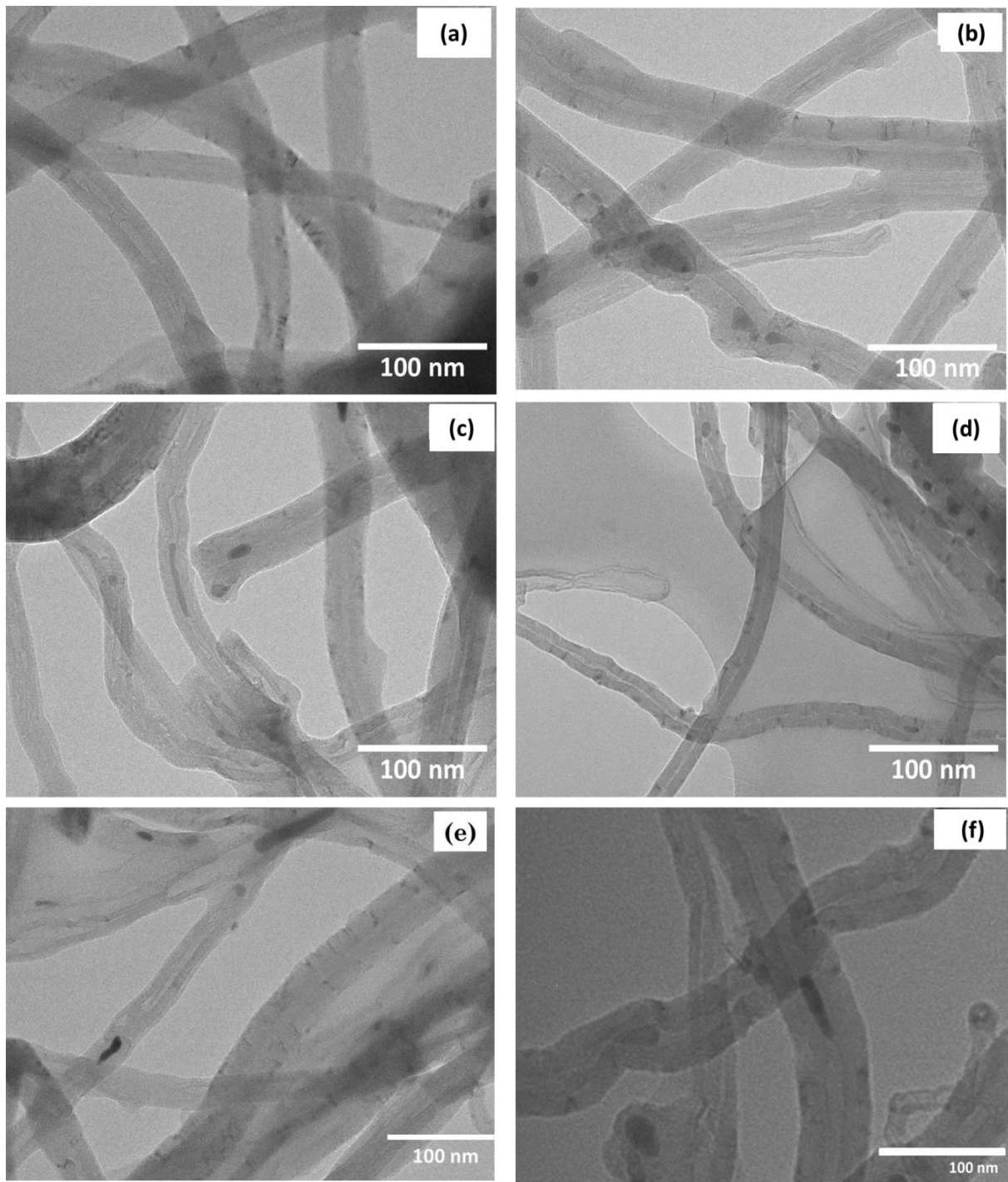


Figure 5.10: TEM images representing the various MWCNT structures using LPG where (a) Fe, (b) Co, (c) Ni, (d) CoFe, (e), NiCo and (f) NiFe are the catalysts used

This means the vertically aligned nanostructures observed by SEM analysis were MWCNTs (**Figure 5.8**). In some images the catalyst materials were observed at the tip end, sides and inside the tube as confirmed by TEM (**Figure 5.10**). In order to investigate whether different carbon sources affects physical properties like alignment of MWCNTs, acetylene was substituted for LPG. However, similar

SEM images were observed and EDX confirmed the presence of the same respective catalysts, as observed in images during LPG investigation. Slightly noticeable size differences were observed with TEM images which showed different MWCNTs dimensions with respect to catalysts used (**Table 5.5**).

5.2.2.2 Comparison of the MWCNTs synthesised

In summary, MWCNTs synthesized by the non-equilibrium PECVD using both LPG and acetylene showed vertical alignment, (**Figures 5.8**). The alignment was attributed mainly to the plasma. The plasma contains positive ions in the cathode sheath. The plasma is responsible for the attracting the MWCNTs to follow a growth towards the source of the ions.¹⁹ To some extent, van der Waals interactions between adjacent MWCNTs could also explain the alignment.²⁰ In the EDX spectra, there were peaks for the respective catalysts and the carbon with some peaks assigned to the substrate components. In most cases the C peaks were more intense than the catalyst peaks. Thus suggesting that MWCNTs were formed the bulk part of the samples than the catalyst particles. All TEM images showed almost similar sizes however, the slight differences were summarised in (**Table 5.6**).

Table 5.6: A summary of the mean diameters of the synthesised MWCNTs using LPG and acetylene with a variety of catalysts

| Catalyst | MWCNT mean diameter (nm) | |
|----------|--------------------------|-----------|
| | LPG | Acetylene |
| Fe | 43 | 40 |
| Co | 65 | 62 |
| Ni | 56 | 53 |
| CoFe | 39 | 38 |
| NiCo | 45 | 42 |
| NiFe | 41 | 40 |

Generally the MWCNTs produced from acetylene had slightly smaller outer diameters compared to those produced using LPG. In both cases, the least tube diameters were achieved with Fe as single catalyst whilst for bi-metal catalyst it was with CoFe. The differences in the mean diameters were attributed to the variations in mean catalyst sizes observed (**Section 4.1.2.2**).^{21,22} Amongst mixed metal-catalysts, NiCo showed the largest CNT diameter and this could be explained using the austenite-phase concept.²³ Where, Co and Ni are common Fe stabilising elements. These austenite-

stabilising elements are responsible for extending the austenite phase thus making the mixture of metals with Fe become stable. It is this stability which is responsible for the enhanced carbon solubility in the mixtures containing Fe.²³ In the case of single metals, it is well known that transition metals have partially filled d shells. Therefore, this property enables interaction with hydrocarbons in order for catalysis to occur. Therefore, the electronic structure of these magnetites of Fe is responsible for catalysing the decomposition of the carbon source.²⁴ This suggests why Fe produced small diameter MWCNTs as compared to Co and Ni.²⁵ Raman analysis was done so as to determine the graphitic nature of the synthesised MWCNTs.

5.2.2.3 Raman analysis

Raman analysis of the MWCNTs synthesized using the six catalysts showed characteristic CNTs disorder band (D band) and graphitic band (G band). The D band due to defects is usually located at 1350 cm^{-1} and the G band, often associate with crystalline nature of the carbon atoms in the MWCNTs, at 1580 cm^{-1} .²⁶ The ratio of the D- to G- band (I_D/I_G) was calculated by dividing the areas under the respective bands. The results presented in **Table 5.7** are for each catalyst in comparison with the respective carbon source.

Table 5.7: Comparison of the I_D/I_G in Raman analysis with respect to the MWCNTs diameters for the LPG and acetylene carbon sources

| Carbon source | Catalyst | Mean tube diameter (nm) | Position (cm^{-1}) | | I_D/I_G |
|---------------|----------|-------------------------|-------------------------------|--------|-----------|
| | | | D-Band | G-band | |
| LPG | Fe | 43 | 1373 | 1617 | 0.94 |
| | Co | 65 | 1381 | 1620 | 0.73 |
| | Ni | 56 | 1376 | 1585 | 0.92 |
| | CoFe | 39 | 1334 | 1618 | 0.99 |
| | NiCo | 45 | 1334 | 1600 | 0.85 |
| | NiFe | 41 | 1350 | 1620 | 0.83 |
| Acetylene | Fe | 40 | 1355 | 1602 | 0.86 |
| | Co | 62 | 1357 | 1602 | 0.59 |
| | Ni | 53 | 1376 | 1619 | 0.85 |
| | CoFe | 38 | 1356 | 1617 | 0.88 |
| | NiCo | 42 | 1377 | 1618 | 0.85 |
| | NiFe | 40 | 1373 | 1602 | 0.82 |

Raman analysis showed that the MWCNTs with smaller mean diameters, from TEM analysis (**Table 5.7**), had higher I_D/I_G . The MWCNTs synthesised using acetylene generally had lower I_D/I_G values than those from LPG. In both cases, when comparing the single metal catalysts, Fe had the least MWCNTs mean diameters and the highest disorder ratios. For mixed metal catalysts, CoFe had the highest disorder ratio. Therefore, the higher I_D/I_G ratios could be attributed to greater carbon bond strains in the MWCNTs due to a low degree of crystallinity.²⁶ This may suggest that different metal catalysts as well as varying their combinations influence the nature of the MWCNTs produced. This ultimately affects the physical characteristics like tube diameters and hence their corresponding graphitic state. The characterisation techniques were substrate dependent; hence, no further investigations of the synthesised samples were further examined.

5.2.2.4 Summary of the synthesised MWCNTs

Synthesis of vertically aligned MWCNTs was successful using both LPG and acetylene as carbon sources at 200 °C in 10 minutes. The MWCNTs diameters are depended on the size of the metal catalyst particles. This in turn affects the graphitic nature of the MWCNTs. LPG, a relatively cheaper carbon source, synthesised MWCNTs that had better properties than the acetylene synthesised MWCNTs. In conclusion the non-equilibrium PECVD was suitable for growing the MWCNTs directly on the substrate without destroying the substrate properties. Hence, these LPG synthesised MWCNTs were tested in organic solar cells as part of the electrode material.

5.3 Organic solar cells

Renewable energy sources that are safe and clean to use are promising eventual sources of sustainable energy. This is especially when considering the direct utilization of solar energy. Organic solar cells (OSC) offer a good alternative to conversion of solar energy into electricity. The energy conversion devices are based on solution-processed, light weight, large-area, and potentially flexible devices.²⁷ The most widely used OSC are the bulk heterojunction as discussed in **Chapter Two**. One of the successful ways to fabricate bulk heterojunction OSC to date has been to use ITO coated substrates, functionalized with a layer of poly(3,4-ethylenedioxythiophene) polystyrene sulfonate (PEDOT:PSS) and an active layer comprising of a mixture of conjugated polymer such as poly(3-hexylthiophene) (P3HT) with a C_{60} derivative such as 6,6-phenyl C_{60} butyric acid methyl ester (PCBM). The current challenges for OSC persist on further enhancing efficiency as well as durability and cost-

effectiveness. Material design through band gap and energy level tuning has been playing a key role in developing new donor materials for efficient OSC.²⁸ Fabrication of the devices to improve properties determines the device performance.

5.3.1 Cell fabrication

The preparation of the devices was performed under ambient conditions. ITO-coated glass substrates which were previously prepared as discussed in **Section 3.5.3.1** and with the MWCNTs as synthesised in **Section 3.5.3.2** were used. The steps involved were divided in three stages namely the preparation of the polymer solution, the coating of the substrate with aluminium and finally the application of the fabricated cell. The main limitations of the study included the absence of a glove box, ideally solar cell experiments are carried in a glove box. The other factors that influence the overall performance of a cell such as the velocity of the wind, cell operating temperature and humidity were not monitored. The focus here was to investigate suitability of the synthesised vertically aligned MWCNTs from various metal catalysts in OSC.

5.3.2 Device preparation

The devices were divided into three main components, i.e. the electron donor, binder and electron acceptor. The hole transport layer used was poly(3,4-ethylenedioxythiophene): poly styrenesulfonate (PEDOT:PSS). The active layer used was a mixture of poly-3-hexyl thiophene (P3HT), and phenyl-C₆₁-butyric acid methyl ester (PCBM), P3HT:PCBM. To level the MWCNT layer, PEDOT:PSS was spin-coated on the MWCNTs synthesised ITO substrate at 3000 rpm for 50 seconds. After spin coating the substrate was annealed at 120 °C for 10 minutes in an oven. P3HT:PCBM was spin-coated at 1500 rpm for 30 seconds, and then annealed for 20 minutes at 120 °C.

The polymer layered substrate was then coated with aluminium (Al). Before vacuum evaporation of the counter electrode, a solution of 0.6 nm of lithium fluoride (LiF) was evaporated on top of the polymer coated substrate, to serve as a hole blocking layer. A 60 nm counter electrode consisting of Al metal was thermally evaporated at 2.22×10^{-7} mbar in an HHV Auto 306 vacuum evaporator equipped with INFICON SQM-160 thin film deposition thickness and rate monitor. Current-voltage characterization was determined by using standard solar simulator model # SS50AAA (Pet

Photoemission Tech. Inc.), with a Keithley 2420 source meter. Where the simulator was operating at AM 1.5 and the power input was 100 mW/cm².

5.3.3 Results and discussion

Bulk heterojunction design was employed for all devices fabricated. **Figure 5.11** illustrates the arrangement of the design.

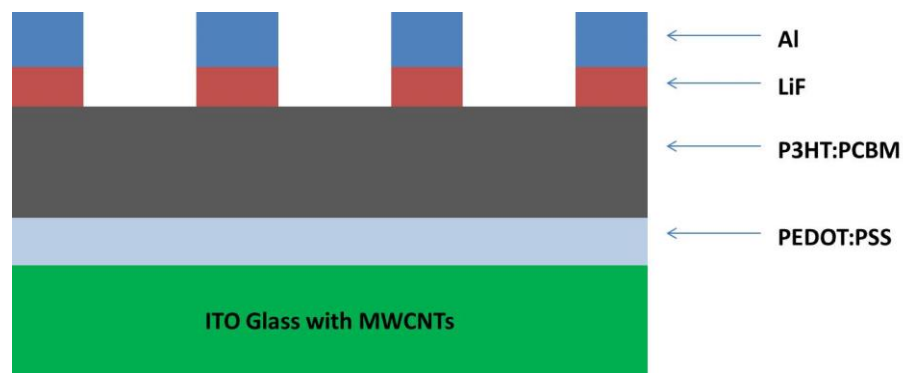


Figure 5.11: Schematic diagram of the layer arrangement in OSC

The diode equation of the J-V characteristics was used to determine values corresponding to the overall device quality and performance. Fill factor (FF) and power conversion efficiency (PCE) represented as in **Equation 5.1** and **5.2** respectively:

$$FF = \frac{J_{Max} \times V_{Max}}{J_{sc} \times V_{oc}} \quad \text{(Equation 5.1)}$$

$$PCE = FF \frac{J_{sc} \times V_{oc}}{P_{in}} \quad \text{(Equation 5.2)}$$

J_{Max} and V_{Max} represent current density and voltage at maximum power point; J_{sc} represent current density; V_{oc} is open circuit voltage and P_{in} stands for incident light power.²⁹

The results presented were performed in the dark and in the illumination. In these devices, some of the OSC diodes showed positive rectification, and others showed good conductivity. The good

conductivity was attributed to MWCNTs which were responsible for the improved electrical conductance due to their internal walls participating in the electrical transportation which enables large current-carrying capacity.³⁰ During the device fabrication, MWCNTs were levelled with a layer of PEDOT:PSS and an active layer comprising of a mixture of conjugated polymer P3HT:PCBM. Preventive procedures of making the devices in a dark room were executed such that the PEDOT:PSS would not degrade.³¹ This was so because when exposed to UV illumination the PEDOT:PSS disintegrates and initiates water into the active layer of the device and thus making it being slightly acidic. LiF/Al was used as the electron collecting contact.

Figure 5.12 illustrates the current versus voltage (J/V) plots obtained using the MWCNTs synthesised using non-equilibrium PECVD with LPG as the carbon source.

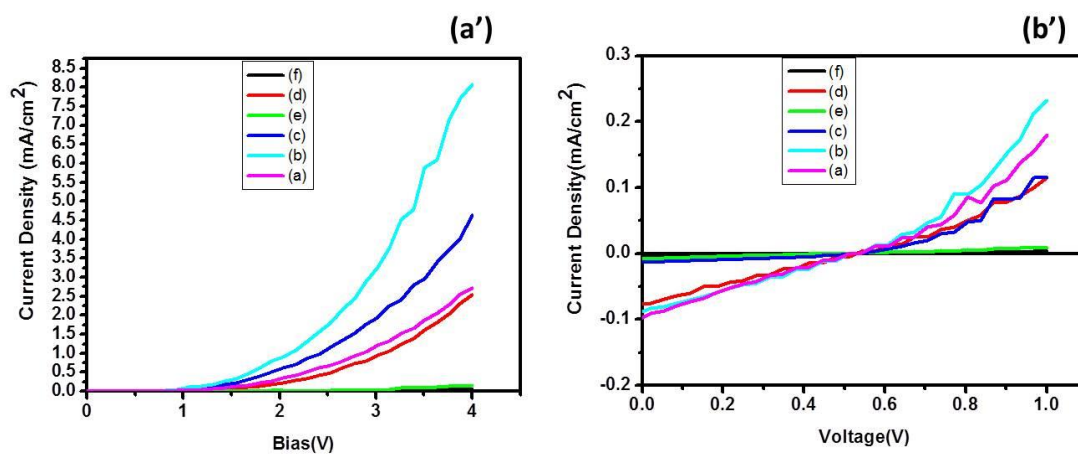


Figure 5.12: Comparison of current against voltage (J/V) plots in (a') dark and (b') illumination using MWCNTs prepared with (a) Fe, (b) Co, (c) Ni, (d) CoFe, (e) NiCo and (f) NiFe as catalysts

The curves for the device in the dark demonstrate a rational rectification for an applied bias of IV. All the samples when tested under illumination the device presented values as presented in **Table 5.8**.

Table 5.8: Measured cell parameters for all MWCNT samples

| MWCNTs sample/catalyst | V _{oc} (V) | J _{sc} (mA.cm ⁻²) | FF | Efficiency (%) | Rectification |
|------------------------|---------------------|--|--------|----------------|---------------|
| a (Fe) | 0.5159 | 0.0950 | 0.2355 | 0.1160 | Yes |
| b (Co) | 0.5040 | 0.0880 | 0.2695 | 0.0119 | Yes |
| c (Ni) | 0.4900 | 0.0164 | 0.3328 | 0.0029 | Yes |
| d (CoFe) | 0.5131 | 0.0741 | 0.2324 | 0.0088 | Yes |
| e (NiCo) | 0.4390 | 0.0588 | - | - | No |
| f (NiFe) | - | - | - | - | No |

The highest V_{oc} recorded was 0.5159 V corresponding to the FF of 0.2355 for the Fe synthesised MWCNTs. NiCo and NiFe had no FF and efficiency values due to constraints associated with series resistance. Several factors account for the series resistance and these include; extreme contact resistance and poor optimisation of the P3HT:PCBM film thickness.³⁰ The low efficiency could be due to the electronic nature of the respective catalysts in the synthesis of the MWCNTs. The trend observed showed that in the single metal catalysts, Fe synthesised MWCNTs showed the highest efficiency, 0.116%, followed by Co and Ni. While a combination of CoFe showed better efficiency amongst the mixed metal catalyst. This could suggest that the catalytic nanoparticles were participating in the electronic transfer processes in devices. Therefore, it can be concluded that LPG synthesised MWCNTs are suitable electrode components. Also, catalytic nanoparticles used in the synthesis of the MWCNTs influences the ultimate activity of the MWCNTs in the OSC device. This was attributed to the size of the MNPs, the smaller the size the smaller the diameter of the MWCNTs.^{21,22} Hence, for this case, the small sized MWCNTs are better electron transporters.

5.3.4 Summary of the OSC

The performance of the MWCNTs synthesised using different catalysts were compared in OSCs. The devices fabricated using MWCNTs synthesised by all the catalysts, except NiCo and NiFe, showed positive rectification. Single metal catalysts exhibited best efficiencies as compared to bimetallic counterparts. The observation was attributed to the nature of the catalyst particles. MWCNTs synthesised using LPG had better efficiencies than those synthesised using acetylene.

References

- (1) Kim, H.; Gilmore, C. M.; Piqué, A.; Horwitz, J. S.; Mattoussi, H.; Murata, H.; Kafafi, Z. H.; Chrisey, D. B. Electrical, optical, and structural properties of indium–tin–oxide thin films for organic light-emitting devices. *Journal of Applied Physics* **1999**, *86*, 6451-6461.
- (2) Wang, H.; Moore, J. J. Low temperature growth mechanisms of vertically aligned carbon nanofibers and nanotubes by radio frequency-plasma-enhanced chemical vapor deposition. *Carbon* **2012**, *50*, 1235-1242.
- (3) Huang, C. W.; Wu, H. C.; Lin, W. H.; Li, Y. Y. Temperature effect on the formation of catalysts for growth of carbon nanofibers. *Carbon* **2009**, *47*, 795-803.
- (4) Songsasen, A.; Pairgreethaves, P. Preparation of carbon nanotubes by nickel catalyzed decomposition of liquefied petroleum gas (LPG). *Kasetsart University, Bangkok, Thailand* **2001**, 354-359.
- (5) Huang, J.; Zhang, Q.; Wei, F.; Qian, W.; Wang, D.; Hu, L. Liquefied petroleum gas containing sulfur as the carbon source for carbon nanotube forests. *Carbon* **2008**, *46*, 291-296.
- (6) Wang, W.; Turn, S. Q.; Keffer, V.; Douette, A. Parametric study of autothermal reforming of LPG. *American Chemical Society* **2004**, *49*, 142-143.
- (7) Lee, C. J.; Park, J.; Yu, J. A. Catalyst effect on carbon nanotubes synthesized by thermal chemical vapor deposition. *Chemical Physics Letters* **2002**, *360*, 250-255.
- (8) Wei, Y. E. G.; Merkulov, V. I.; Lowndes, D. H. Effect of catalyst filmthickness on carbon nanotube growth by selective area chemical vapor deposition. *Applied Physics Letters* **2001**, 1394–1396.
- (9) Bu, I. Y.; Hou, K.; Engstrom, D. Industrial compatible re-growth of vertically aligned multiwall carbon nanotubes by ultrafast pure oxygen purification process. *Diamond and Related Materials* **2011**, *20*, 746-751.
- (10) McKee, G. S. B.; Vecchio, K. S. Thermogravimetric analysis of synthesis variation effects on CVD generated multiwalled carbon nanotubes. *The Journal of Physical Chemistry B* **2006**, *110*, 1179-1186.
- (11) Bom, D.; Andrews, R.; Jacques, D.; Anthony, J.; Chen, B.; Meier, M. S.; Selegue, J. P. Thermogravimetric analysis of the oxidation of multiwalled carbon nanotubes: evidence for the role of defect sites in carbon nanotube chemistry. *Nano Letters* **2002**, *2*, 615-619.

- (12) Datsyuk, V.; Kalyva, M.; Papagelis, K.; Parthenios, J.; Tasis, D.; Siokou, A.; Kallitsis, I.; Galiotis, C. Chemical oxidation of multiwalled carbon nanotubes. *Carbon* **2008**, *46*, 833-840.
- (13) Ahmadzade, F.; Safa, S.; Balashabady, P. Growth of vertically aligned carbon nanotubes by DCPECVD system and the effects of C₂H₂ concentration and plasma current on the growth behavior of CNTs. *Arabian Journal for Science and Engineering* **2011**, *36*, 97-103.
- (14) Ren, Z. F.; Huang, Z. P.; Xu, J. W.; Wang, J. H.; Bush, P.; Siegel, M. P.; Provencio, P. N. Synthesis of large arrays of well-aligned carbon nanotubes on glass. *Science* **1998**, *282*, 1105-1107.
- (15) Somers, W.; Bogaerts, A.; van Duin, A. C. T.; Neyts, E. C. Interactions of plasma species on nickel catalysts: A reactive molecular dynamics study on the influence of temperature and surface structure. *Applied Catalysis B* **2014**, *154-155*, 1-8.
- (16) Chen, H. L.; Lee, H. M.; Chen, S. H.; Chao, Y.; Chang, M. B. Review of plasma catalysis on hydrocarbon reforming for hydrogen production-Interaction, integration, and prospects. *Applied Catalysis B* **2008**, *85*, 1-9.
- (17) Chen, M.; Chen, C. M.; Shi, S. C.; Chen, C. F. Low-temperature synthesis multiwalled carbon nanotubes by microwave plasma chemical vapor deposition using CH₄-CO₂ gas mixture. *Journal of Applied Physics, Part 1* **2003**, *42*, 614-619.
- (18) Ebbesen, T.; Ajayan, P. Large-scale synthesis of carbon nanotubes. *Nature* **1992**, *358*, 220-222.
- (19) Maschmann, M. R.; Amama, P. B.; Goyal, A.; Iqbal, Z.; Fisher, T. S. Freestanding vertically oriented single-walled carbon nanotubes synthesized using microwave plasma-enhanced CVD. *Carbon* **2006**, *44*, 2758-2763.
- (20) Dai, H. Carbon nanotubes: opportunities and challenges. *Surface Science* **2002**, *500*, 218-241.
- (21) Kim, N. S.; Bae, S. Y.; Park, J. The catalytic effect on vertically aligned carbon nanotubes. *Materials Review Society* **2003**, *800*, 105-110.
- (22) Altavilla, C.; Leone, C.; Sannino, D.; Sarno, M.; Ciambelli, P. Synthesis of monodispersed MFe₂O₄(M=Fe, Co, Ni) ferrite nanoparticles: effect of reaction temperature on particle size. *CRC Press* **2009**, *1*, 143-146.
- (23) Raravikar, N. R.; Schadler, L. S.; Vijayaraghavan, A.; Zhao, Y. P.; Wei, B. Q.; Ajayan, P. M. Synthesis and characterization of thickness-aligned carbon nanotube-polymer composite films. *Chemistry of Materials* **2005**, *17*, 974-983.

- (24) Casillas, P. E. G.; Gonzalez, C. A. R.; Pérez, C. A. M. Infrared spectroscopy of functionalized magnetic nanoparticles. *Infrared Spectroscopy-Materials Science, Engineering and Technology*, **2012**, 405.
- (25) Dupuis, A. C. The catalyst in the CCVD of carbon nanotubes—a review. *Progress in Materials Science* **2005**, *50*, 929-961.
- (26) Costa, S.; Borowiak-Palen, E.; Kruszynska, M.; Bachmatiuk, A.; Kalenczuk, R. J. Characterization of carbon nanotubes by Raman spectroscopy. *Mater Science* **2008**, *26*, 433-441.
- (27) Hoppe, H.; Sariciftci, N. S. Organic solar cells: An overview. *Journal of Materials review* **2004**, *19*, 1924-1945.
- (28) Rowell, M. W.; Topinka, M. A.; McGehee, M. D.; Prall, H.-J.; Dennler, G.; Sariciftci, N. S.; Hu, L.; Gruner, G. Organic solar cells with carbon nanotube network electrodes. *Applied Physics Letters* **2006**, *88*, 2335061-2335063.
- (29) Günes, S.; Neugebauer, H.; Sariciftci, N. S. Conjugated polymer-based organic solar cells. *Chemical reviews* **2007**, *107*, 1324-1338.
- (30) Zhu, L.; Sun, Y.; Hess, D. W.; Wong, C.P. Well-aligned open-ended carbon nanotube architectures: an approach for device assembly. *Nano letters* **2006**, *6*, 243-247.
- (31) van de Lagemaat, J.; Barnes, T. M.; Rumbles, G.; Shaheen, S. E.; Coutts, T. J.; Weeks, C.; Levitsky, I.; Peltola, J.; Glatkowski, P. Organic solar cells with carbon nanotubes replacing $\text{In}_2\text{O}_3:\text{Sn}$ as the transparent electrode. *Applied Physics Letters* **2006**, *88*, 233503.

Chapter Six

CONCLUSIONS AND FUTURE WORK

This chapter gives a summary and overall conclusion of the work. It also highlights possible ways in which the study can be further developed.

6.1 Summary of thesis chapters

Chapter One emphasis is on the relevance of studying the MWCNTs synthesised directly on the substrate and their associated physical-chemical properties from the literature. A detailed background of the study which addresses the importance of energy and the problems associated with the current energy supply resources is provided. Factors contributing to the energy strain such as population increase are also discussed. This energy strain in the current primary energy sources brings about the need for sustainable and alternative renewable resources of energy. Justifications of the choice of substrates and the method employed for synthesis are highlighted. The aims and objectives are also stated in this chapter. A general thesis overview in terms of the outline is provided at the end of Chapter One.

In Chapter Two, a literature review of the study is provided. The use of energy and the implementation of various energy sources are described in greater detail in this chapter. The current energy consumption with respect to each source of energy supply is further explained. A brief history of some of the renewable energy forms and their associated disadvantages are presented. The chapter further points out how nanotechnology has opened up new lines of study to meet the looming energy crisis. The carbon nano-forms that cover various carbon allotropes are discussed herein. Properties of CNTs in relation to their functions are also described. A descriptive study on the various synthesis methods available for CNT production and the factors affecting the CNT synthesis, growth and mechanisms involved are presented. The application of the synthesised CNTs in organic solar cells and the types of organic solar cells are described. Characterisation techniques available for the investigation of the synthesised CNTs are also discussed in this chapter.

The experimental details are provided in Chapter Three. Here, details concerning the metal precursors, solvents, gases and other chemicals involved in the synthesis of MNPs and MWCNTs are presented. The instrumental details, models, software versions and the procedure used in data collection are provided. Different methods involved in the synthesis of MNPs and MWCNTs are evaluated. A descriptive design of a non-equilibrium plasma-enhanced CVD and the parts involved are provided.

Chapter Four and Five discusses the MNPs and MWCNTs results, respectively. These two chapters form the core of the study. Characterisation and comparison of the synthesis methods involved in synthesis are evaluated thoroughly. Representative SEM and TEM images of the observed structures showing the morphology and nature of the synthesised catalysts and MWCNTs are presented. In the case of MNPs, images that indicate the nature and state of agglomeration are provided. FTIR of the MNPs showed the presence of the characteristic metal-oxide bonds and TGA showed the characteristic TG profiles for the organic capped MNPs.

In Chapter Five, the MWCNT images that show alignment and the structure of the synthesised tubes are provided. The graphitic nature of the MWCNTs was examined with Raman analysis. The application of the synthesised MWCNTs in OSCs, experimental procedure and the solar cell performances are reported herein. In this chapter it was apparent that the aligned MWCNTs are suitable for OSC applications.

Chapter six provides the summary, conclusions and future prospective of the work involved.

6.2 Conclusions

Two synthesis methods, thermal decomposition and co-precipitation, were employed. From the data evaluations, in terms of suitability of size and dispersion, co-precipitation was superior than thermal decomposition method. In the *thermal decomposition* method, agglomerated MNPs were synthesised. The method involved the use of high temperatures which destroyed the substrate morphology resulting in the melting of the substrate. These MNPs synthesised in this method were large and therefore were not suitable for MWCNT synthesis application.

Whereas in the *co-precipitation method*, mono-dispersed MNPs of Co, Fe, Ni, a mixture of NiCo, NiFe and CoFe were successfully synthesised in a homogeneous aqueous solution. The average particle sizes were varied in the range 3-10 nm. The EDX, FTIR and TGA techniques confirmed the presence of the organic coating in the final MNPs product. The FTIR showed characteristic metal oxide bonds for the respective metal elements. The oxide nature of the MNPs was attributed to the smaller size of the MNPs thus an easy oxidation of the metals could have occurred. The general trend observed in the TG curves showed the presence of the organic coating from HDA. This coating was concluded to be effective for the dispersion of the MNPs. According to the comparison of the TEM images for the two methods, it can be concluded that the co-precipitation preparation method successfully overcame the problem of agglomeration and was appropriate to obtain the metal nanoparticles with smaller crystalline sizes. Therefore the co-precipitation method was superior to the thermal decomposition method.

In terms of vertically aligned MWCNT synthesis, *ferrocene-toluene*, the mixture of ferrocene and toluene produced MWCNTs with relatively smaller tube diameters with the least thermal stabilities and a higher degree of graphitization. For *LPG single furnace* method, productions of fibres were at low temperatures of 600 °C, whilst MWCNTs synthesis at intermediate temperatures of 800 °C, and mixtures of spheres and tubes as the temperature increased to 900 °C. ITO substrate melted as the temperature was increased above 600 °C. This method was not suitable for the project, direct substrate growth of MWCNTs. In the *LPG double furnace*, ITO properties were maintained in the low temperature furnace. However, the double furnace method produced short and thick randomly oriented MWCNTs. Based on the targeted orientation, vertical alignment, this approach was again not suitable for the work.

In *non-equilibrium PECVD*, methane and ethylene could not be able to synthesise any CNTs since they blew off the plasma (glow discharge). In this approach, low temperature synthesis of the MWCNTs was successful in achieving vertical alignment using LPG and acetylene. The system produced amorphous carbon as by-products. Also, based on data obtained, it can be concluded that the activity of the alloy was better than the activity of the single metals in production of high quality MWCNTs with reduced defects. The vertically aligned MWCNTs synthesised by the non-equilibrium LPG showed positive results during testing in OSC. MWCNTs synthesised using iron-based catalyst showed the highest efficiencies followed by Co, and lastly Ni. Based on this, it can be concluded that MWCNTs synthesised by this system decreases with change of the transition metal catalysts used

from left to right. In the MWCNTs from mixtures of metals, CoFe showed the highest efficiencies, which suggested that a combination of Fe and Co is most suitable compared to the NiCo and NiFe combinations.

6.3 Future work

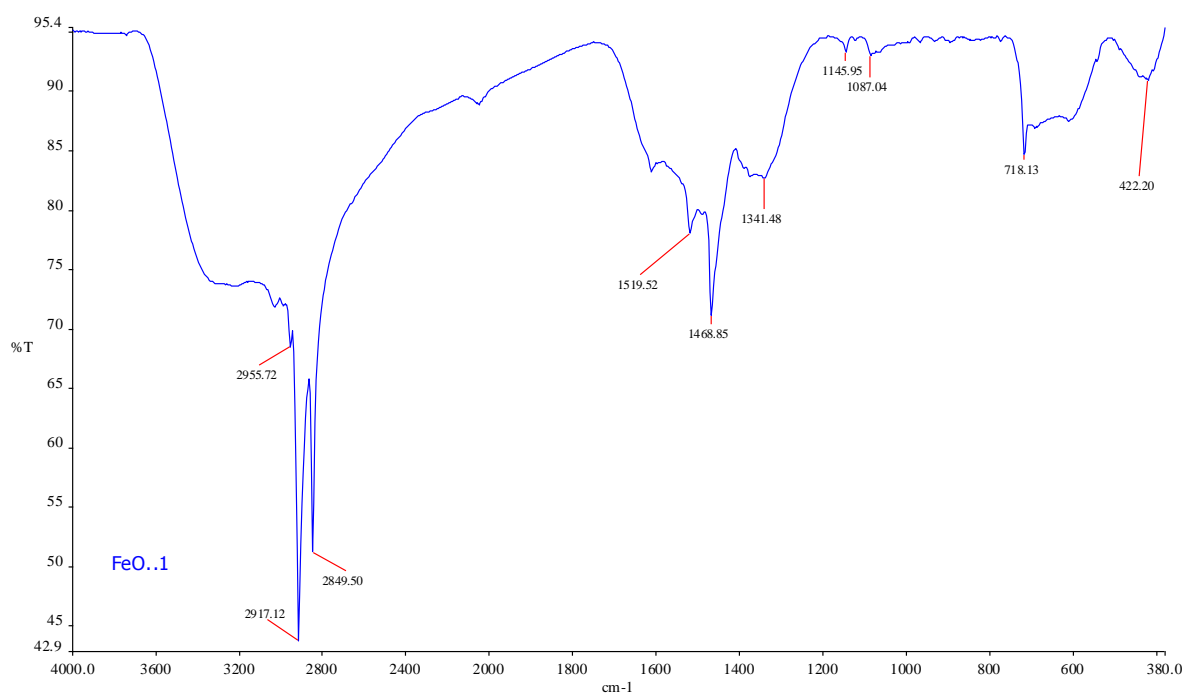
Several possible ways are inevitable to further study the current work. Firstly, synthesis of the combined tri-metallic mixture of the catalysts involved and a comparison of the different catalytic mixtures. The use of techniques such as AFM and XRD on the deposited MNPs would assist in the investigation of the size, crystallinity and layer thickness of the metal nanoparticles (MNPs). Secondly, an investigation of the effect of several ways in which the MNPs can be deposited on the ITO coated glass substrate. This involves techniques like spin coating which aids the understanding of the ideal morphology of the MNPs on the substrate. This also improves the dispersion of the MNPs on the substrate and in turn brings about a way to control the density of the synthesised MWCNTs. An investigation of the ways in which the MWCNTs density can be controlled, including introduction of polymers or dendrimers to enhance the optical transparency as well as the conductivity studies of the electrode for fabrication of OSC. The use of other diluents such as ammonia can be incorporated so as to increase the etching ability of the plasma. Synthesis of the MWCNTs on other substrate materials with higher strain points such as FTO, plastics, polymers and rubber. Larger area synthesis of the MWCNTs can be done so as to enhance optical transparency, thus being able to measure transmittance, and improve characterisation with the use of XRD measurements. The system can also be used to synthesise doped MWCNTs using the same carbon sources and lower nitrogen or boron containing precursors for applications in OSCs. Electrochemical characterisation in order to quantify the absorption efficiencies, exciton dissociation efficiency, charge transfer efficiency and charge collection efficiency separately at respective interfaces since these factors have a substantial effect on the overall performance of the OSC device. A different way to fabricate the OSC by either removing PEDOT:PSS or removing P3HT:PCBM and test the efficiency of the device. In addition, the utilization of a glove box to ensure that possible environmental consequences are eradicated during solar cell experiments.

APPENDICES

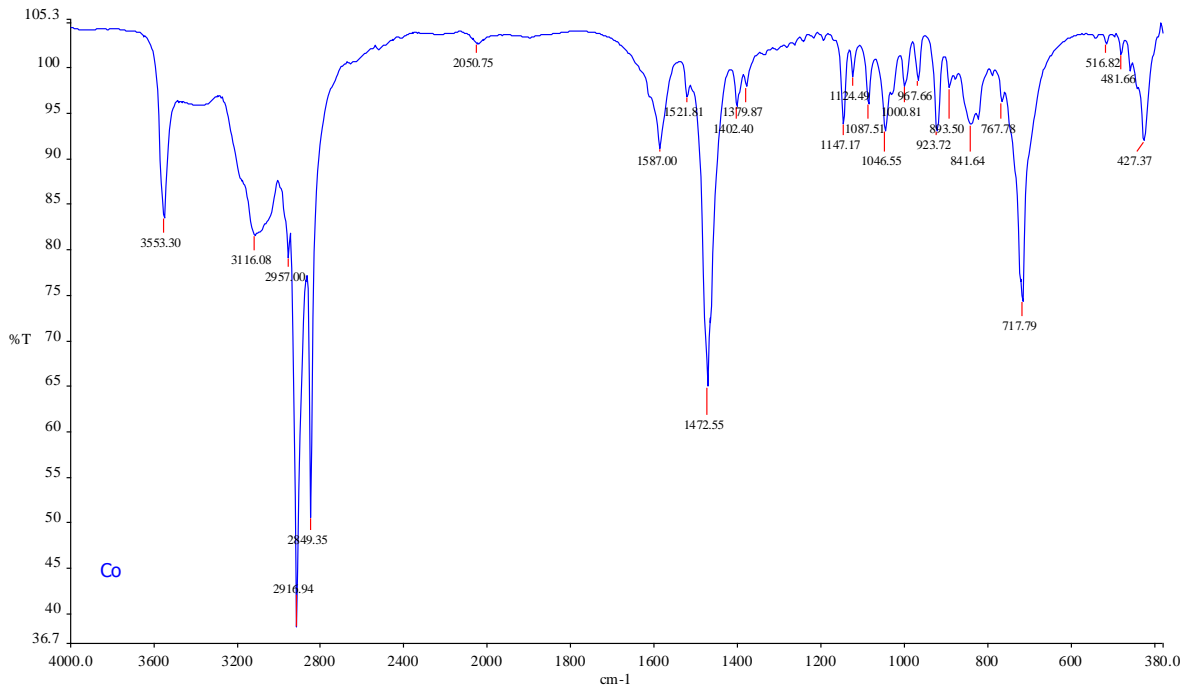
A. Laboratory apparatus

| | | |
|---------------------|--------------|-----------------------|
| Spatula | stirrer bar | round bottomed flasks |
| watch glass | quartz boats | quartz tube |
| measuring cylinders | forceps | thermometers |
| burette | pipettes. | 10 ml syringe |

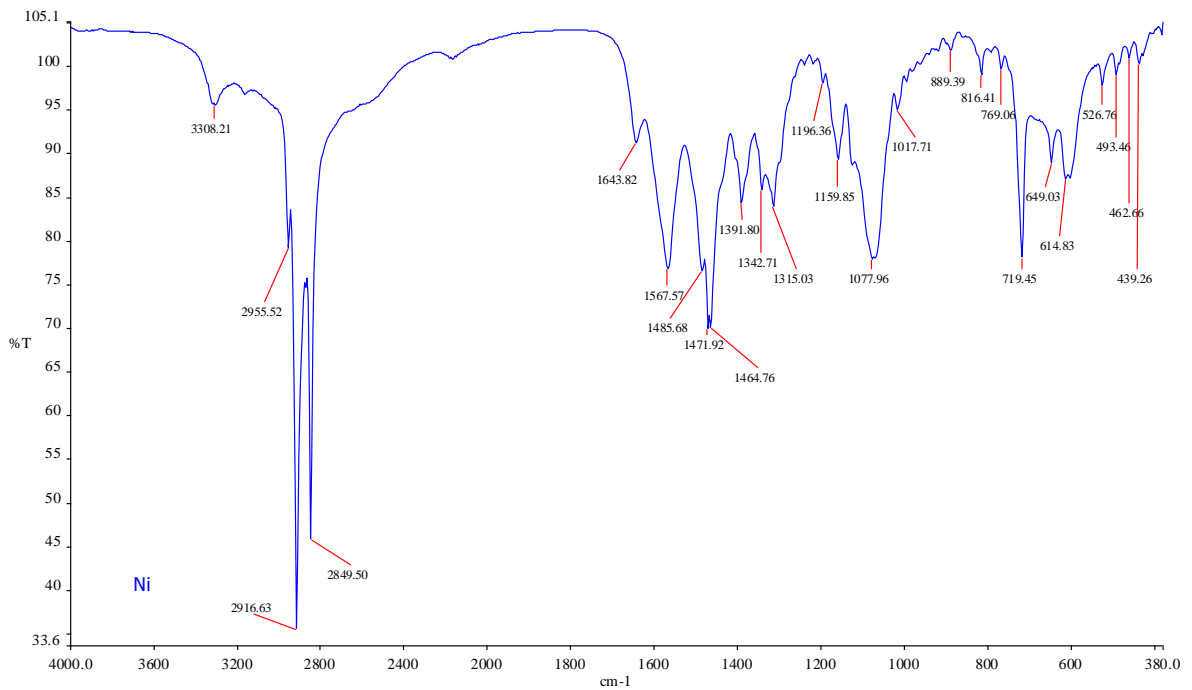
B. FTIR



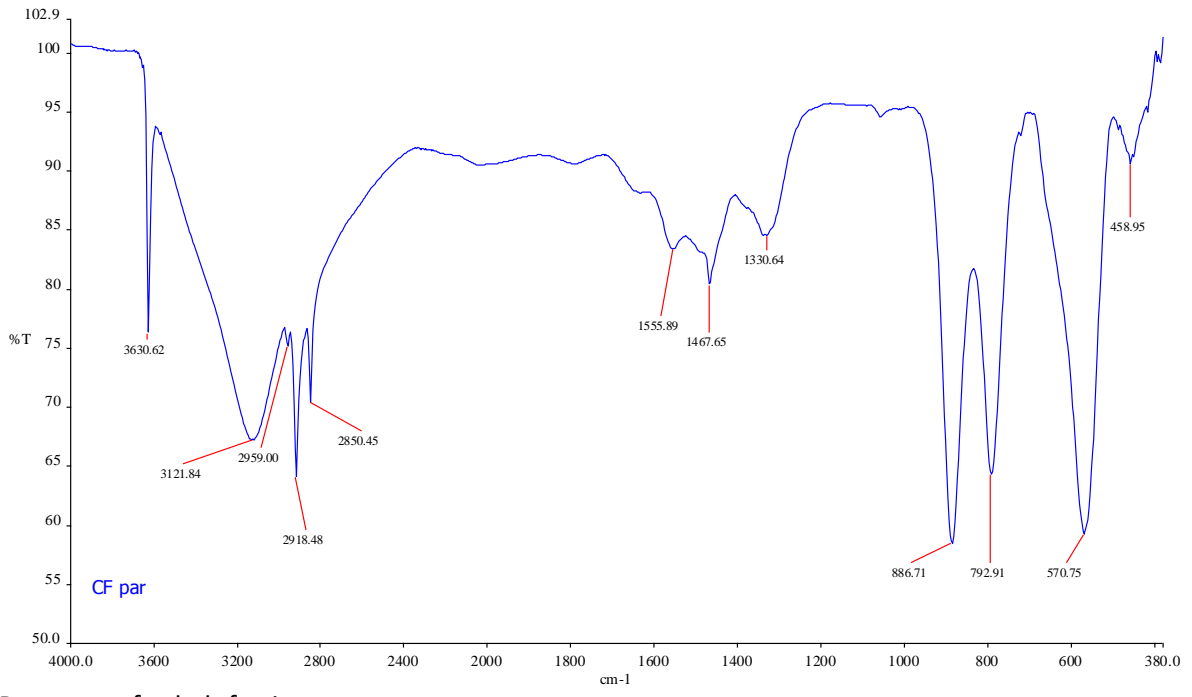
IR spectra of iron oxide



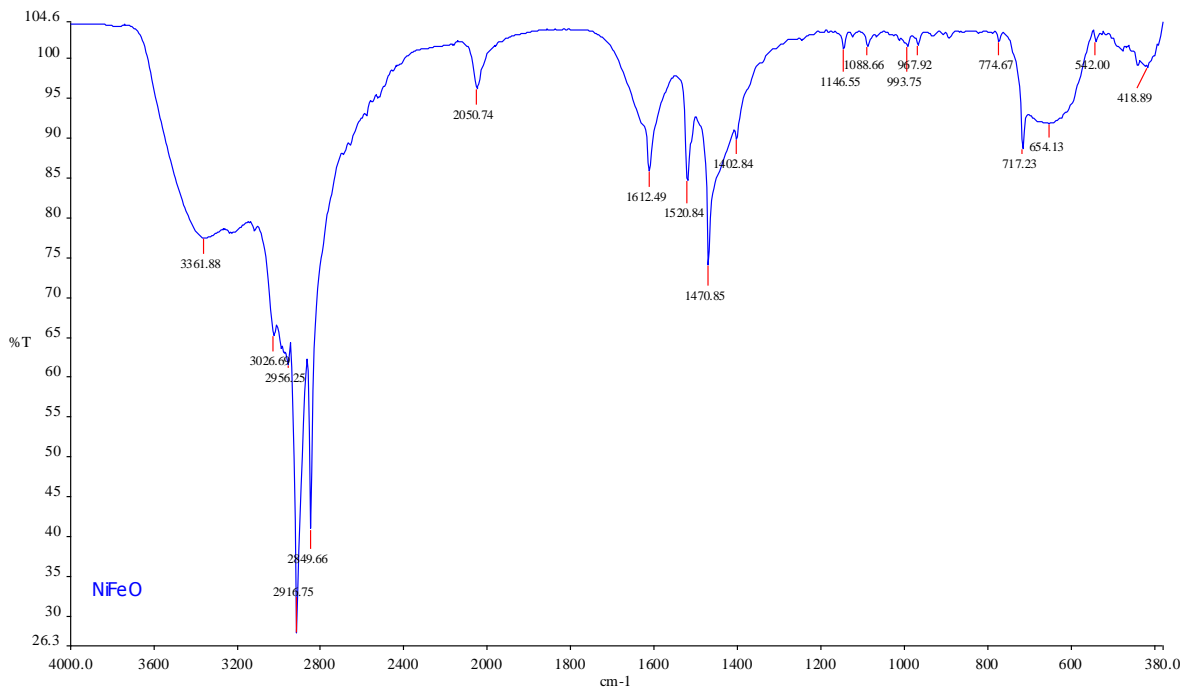
IR spectra of cobalt oxide



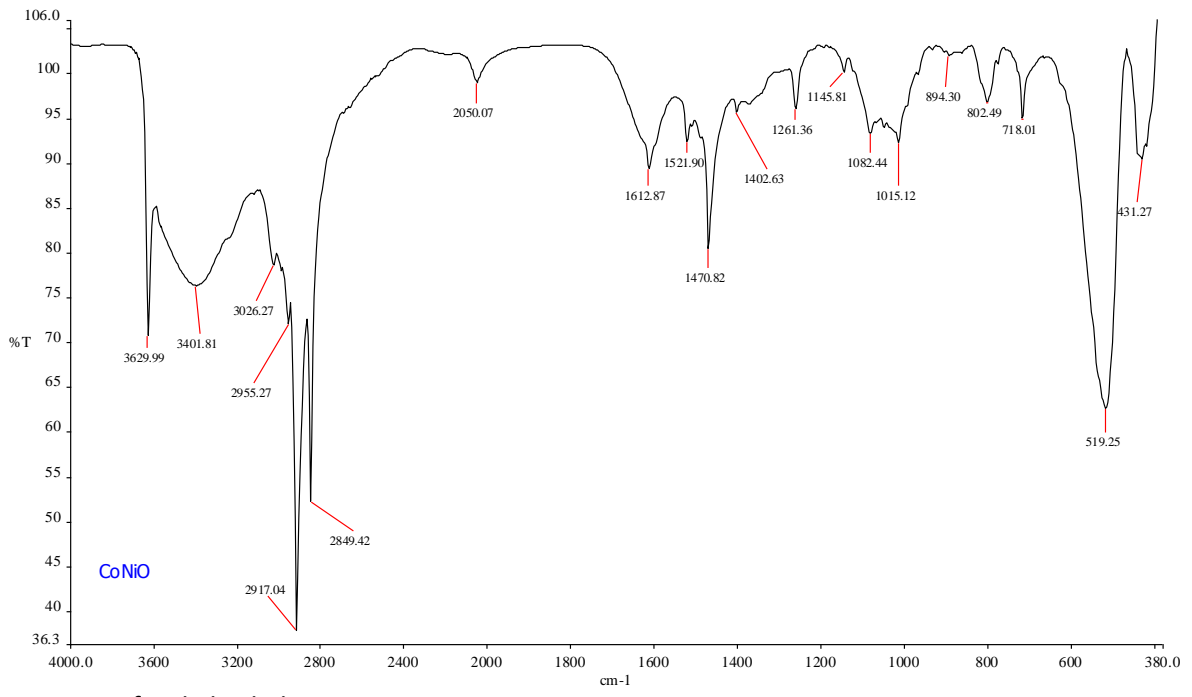
IR spectra of nickel oxide



IR spectra of cobalt ferrite



IR spectra of nickel ferrite



IR spectra of nickel cobaltite